Universitat Politècnica de València
Departamento de Máquinas y Motores Térmicos

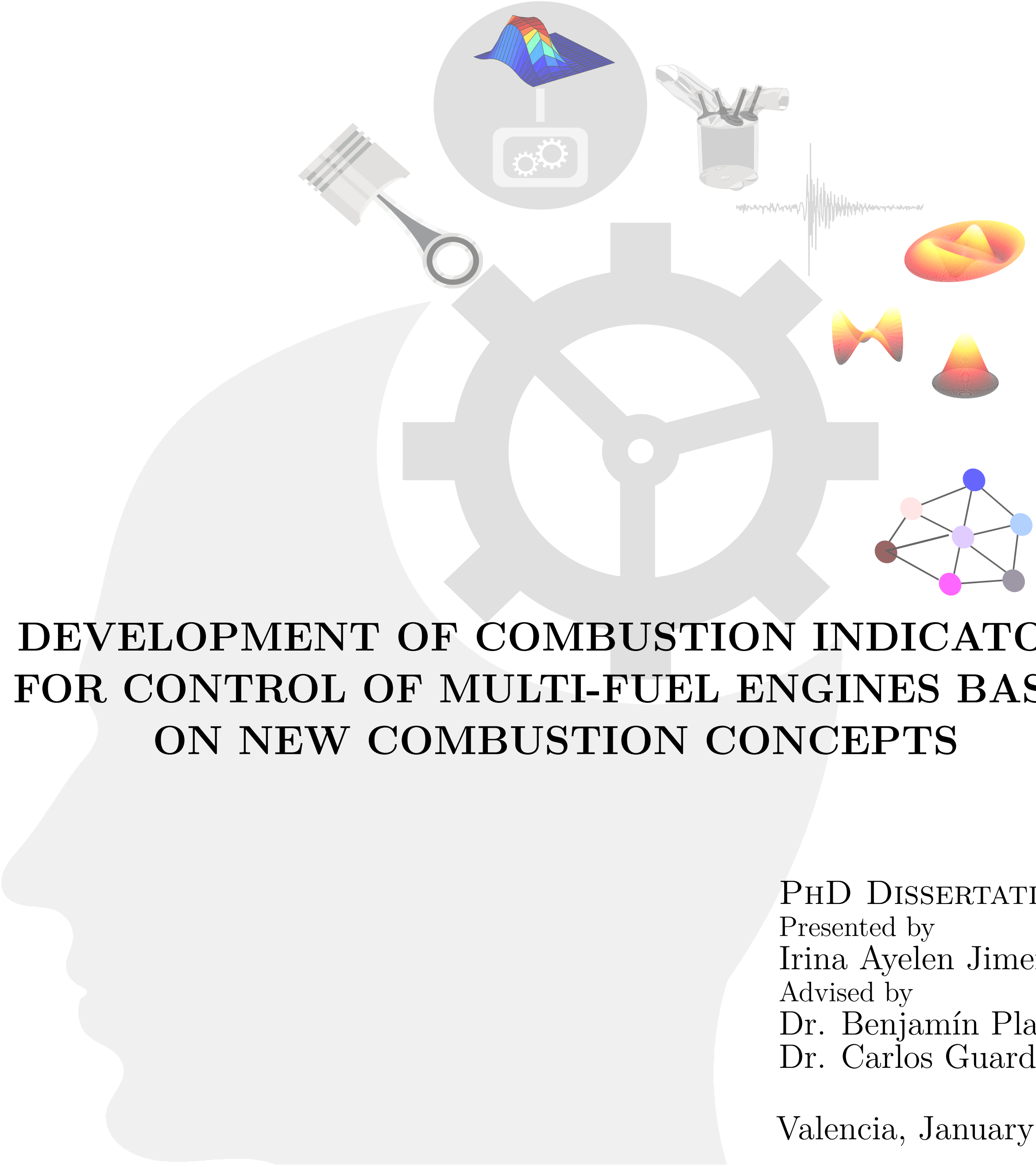

DEVELOPMENT OF COMBUSTION INDICATORS FOR CONTROL OF MULTI-FUEL ENGINES BASED ON NEW COMBUSTION CONCEPTS

PhD Dissertation
Presented by
Irina Ayelen Jimenez
Advised by
Dr. Benjamín Pla
Dr. Carlos Guardiola

Valencia, January 2022

Universitat Politècnica de València
Departamento de Máquinas y Motores Térmicos

DEVELOPMENT OF COMBUSTION INDICATORS FOR CONTROL OF MULTI-FUEL ENGINES BASED ON NEW COMBUSTION CONCEPT

PhD Dissertation
Presented by
Irina Jimenez
Advised by
Dr. Carlos Guardiola
Dr. Benjamin Pla

Valencia, January 2022

Resumen

Debido a las regulaciones en materia de emisiones y CO2 la industria automotriz a desarrollado diferentes tecnologías inovadoras. Estas tecnologias incluyen combustibles alternativos y nuevos modos de combustión, entre otros.

De aquí surge la necesidad del desarrollo de nuevos métodos para el control de la combustión en estas condiciones mencionadas. Por este motivo, en este trabajo se han desarrollado diferentes modelos e indicadores orientados al diagnóstico y control de la combustión tanto en condiciones normales como anormales.

Para los casos de combustion normal, se ha desarrollado un modelo de combustion, cuyo objetivo es estimar la media de la evolución de la fracción de la masa quemada y la presión dentro del cilindro. Se implementó un observador, basado en la señal de knock, con la finalidad de mejorar la estimación en condiciones transitorias y poder aplicar así el modelo a diferentes tipos de combustibles. También se presenta un modelo de variabilidad cíclica, en el cual, a partir del modelo de combustión, se propaga una distribución en dos de los parametros de dicho modelo. Ambos modelos han sido aplicados para un motor de encendido provocado y un motor de combustión de encendido por chorro turbulento.

En los casos de combustion anormal, se ha includo un analisis de la resonancia dentro de la cámara de combustion, en donde también se desarrollaron dos modelos capaces de estimar la evoluación de la resonancia.

Estos modelos, tanto para condiciones normales como anormales, se utilizaron para el diagnóstico de la combustión. Por una parte, para la detección de knock, en donde tres estrategias de detección de knock fueron desarrolladas: dos basadas en el sensor de presión en cámara y una en el sensor de knock. Por otra parte, se realizó una aplicación de un modelo de resonancia para la mejora de la estimación de la masa atrapada a partir de la resonancia.

Finalmente, para mostrar el potencial de los modelos de diagnóstico, dos aplicaciones a control se desarrollaron: una para el control de knock a través de la actuación de la chispa, y otra para el control de gases residuales, a través de la actuación de la distribución variable, realizando paralelamente una optimización de la combustión a través de la actuación de la chispa.

Resum

Impulsada per les regulacions en matèria d'emissions i CO2 la indústria automotriu a desenvolupat diferents tecnologies inovadore. Aquestes tecnologies inclouen combustibles alternatius i nous modes de combustió, entre altres.

D'ací sorgix la necessitat posar en pràctica nous mètodes per al control de la combustió. En aquest context, el present trevall proposa diferents models i indicadors orientats al diagnòstic i control de la combustió tant en condicions normals com anormals.

Per als casos de combustió normal, es proposa un model de combustió, l'objectiu del qual és estimar la mitjana de l'evolució de la fracció de la massa cremada i la pressió dins del cilindre. Es va implementar un observador, basat en la senyal de knock, amb la finalitat de millorar l'estimació en condicions transitòries i poder aplicar així el model a diferents tipus de combustibles. També es presenta un model de variabilitat cíclica, en el qual, a partir del model de combustió, es propaga una distribució en dos dels parametres del dit model. Ambdós models han sigut aplicats a un motor d'encesa provocada i un motor de combustió d'encesa per doll turbulent.

Als casos de combustió anormal, s'ha inclos un anàlisi de la ressonància dins de la cambra de combustió, on també es van desenvolupar dos models capaços d'estimar l'evolució de la ressonància.

Aquests models, tant per a condicions normals com anormals, s'utilitzen per al diagnòstic de la combustió. Per una part, per a la detecció de knock, on tres estratègies de detecció de knock s'han desenvolupat: dues basades en el sensor de pressió a la cambra de combustió i una altra basada en el sensor de knock. Per altra part, es va realitzar una aplicació d'un model de ressonància per a la millora de l'estimació de la massa atrapada a partir de la ressonància.

Finalment, per a mostrar el potencial dels models de diagnòstic, dos aplicacions de control es van desenvolupar: una per al control de knock a través de l'actuació de l'espurna, i una altra per al control de gasos residuals, a través de l'actuació de la distribució variable, realitzant paral · lelament una optimització de la combustió a través de l'actuació de l'espurna.

Abstract

The need to satisfy emissions and CO_2 regulations is pushing the automotive industry to develop different innovative technologies. These technologies include alternative fuels and new modes of combustion, among others.

Therefore, the need for the development of new methods for combustion control in these mentioned conditions arises. For this reason, in this work different models and indicators have been developed aimed at the diagnosis and control of combustion in both normal and abnormal conditions.

For normal combustion cases, a combustion model has been developed, the objective of this model is to estimate the mean of evolution of the mass fraction burned and the in-cylinder pressure. An observer had been implemented, based on knock sensor signal, in order to improve the estimation in transient conditions and also to be able to make use of the model with different fuels. A cyclic variability model is also presented, where from the combustion model, a probability distribution is propagated over two of the parameters of such model. Both models had been applied for a spark ignition engine and a turbulent jet ignition combustion engine.

For the abnormal combustion cases, an analysis of the resonance within the combustion chamber had been included, where two models capable of estimating the evolution of the resonance were also developed.

These models, for both normal and abnormal conditions, were used for the diagnosis of combustion: on the one hand, for knock recognition, where three knock detection strategies were developed: two based on the in-cylinder pressure sensor and one on the knock sensor. On the other hand, an application of a resonance model was carried out in order to improve the estimation of the trapped mass from the resonance excitation.

Finally, to show the potential of such models and applications, two control strategies were developed: one for the control of knock through the actuation of the spark advance, and a second for the control of residual gases, through the actuation of the variable valve timing, while optimizing the combustion through the actuation of the spark advance.

Agadecimientos

La elaboración de esta tesis no podría haber sido posible sin la colaboración y el soporte de muchas personas a quienes quiero mostrar mis agradecimientos en las siguientes líneas.

En primer lugar, quiero agradecer a mis directores de tesis: *Carlos Guardiola* y *Benjamín Pla*, también tutor, sin ellos esta tesis no podría haber sido posible. Gracias *Carlos*, tu puerta siempre estuvo abierta para cualquier inquietud o problema que me surgiera, tu experiencia y conocimiento han sido de gran ayuda para la elaboración de esta tesis. Y que es de un alumno/a de doctorado sin su tutor... *Benja*, qué decirte, muchas gracias... trabajar con vos es un placer, gracias por siempre estar ahí cuando necesitaba ayuda, ya sea relacionado con la investigación como en lo personal; y por sobre todo, gracias por confiar en mi y siempre darme libertad a la hora de elegir caminos a explorar.

Por otra parte, quería agradecer a *Pau Bares*, con quien desde el primer día he trabajado, gracias a su buena predisposición y conocimiento lo desarrollado en este documento fue posible. También gracias a todos los compañeros que han hecho cada día mas ameno y divertido, *Alvin, Alexandra, André* ... quienes no solo siempre estaban dispuestos a dar una mano, sino también a hacer que las horas sean un poco más divertidas.

Sin ninguna duda esta tesis tuvo lugar gracias al apoyo del departamento de Máquinas y Motores Térmicos: a las personas de secretería, quienes siempre estuvieron atentos ante cualquier incoveninte; a la dirección; a los técnicos, en especial a *Vicente Esteve* con quien compartí muchas horas de trabajo experimental y siempre estuvo dispuesto a dar una mano; a los profesores e investigadores, quienes siempre estaban dispuestos a ayudar; en particular a *Joaquin De La Morena*, quien siempre me ha facilitado acceso a la parte experimental y así poder obtener gran parte de los resultados de esta tesis.

También quiero agradecer a *Teresa* y *Micaela*, quienes siempre estuvieron a mi lado desde que llegué a Valencia y fueron un gran soporte y ayuda en el ambito personal.

Por último, y no por ello menos importante, quería dedicar esta tesis a mi familia: mis padres *Marta* y *Eduardo*, quienes desde siempre me han apoyado en todo lo que he querido hacer en la vida, y hoy a la distancia no deja de ser así. En especial a mi mamá, quien desde siempre fue ese rayo de luz que ilumnina el camino y me guia en esto que llamamos vida. Y por supuesto a vos, *Soraya*, que gracias a tu apoyo y paciencia durante estos años este camino ha sido aún mas placentero.

Agadecimientos institucionales

El trabajo desarrollado en esta tesis ha sido posible gracias a la financiación de la Generalitat Valenciana y el fondo social europeo a través de la beca 132GRISOLIAP/2018/132 y BEFPI/2021/042.

Contents

Nomenclature

Acronyms

ATDC	After top dead center
BTDC	Before top dead center
BMEP	Break mean effective pressure
CAD	Crank angle degrees
CFD	Computational fluid dynamics
CI	Compression ignition
CL	Closed loop
CN	Natural gas
CNG	Compressed natural gas
CO	Carbon monoxide
CO_2	Carbon dioxide
DI	Direct injection
DoF	Degree of freedom
DOI	Duration of injection
ECU	Electronic control unit
EGR	Exhaust gases re-circulation
EKF	Extended Kalman filter
EMD	Empirical mode decomposition
EOC	End of combustion
EU	European union
EV	Electric vehicles
EVC	Exhaust valve closing
EVO	Exhaust valve opening
FFT	Fast Fourier transform
FPGA	field-programmable gate array
HCCI	Homogeneous charge compresison ignition
HEV	Hybrid electric vehicles
HRL	Heat release law
HRR	Heat release rate
IC	Internal combustion
IMAO	Integral of modulus of accelerometer oscillations
IMEP	Indicate mean effective pressure
IMPO	Integral of modulus of pressure oscillations
IVC	Intake valve closing
IVO	Intake valve opening

KF	Kalman filter
KO	Knock onset
LPG	Liquefied petroleum gas
LSM	Least square method
MAPO	Maximum amplitude pressure oscillation
MFB	Mass fraction burnt
MPC	Model predictive control
NA	Naturally aspirated
NEDC	New European driving cycle
NI	National instruments
NO	Nitric oxide
NO2	Nitric dioxide
NOx	Oxides of nitrogen
NVO	Negative valve overlap
OECD	Organization for economic cooperation and development
OL	Open loop
OPEC	Organization of the petroleum exporting countries
PEMS	Portable emission measurement system
PM	Particulate matter
PN	Particulate number
PPCI	Partially premixed compression ignited
RCCI	Reactivity controlled compression ignited
RDE	Real driving emissions
RGF	Residual gas fraction
RON	Research Octane Number
SA	Spark advance
SI	Spark ignited
STFT	Short time Fourier transform
SOI	Start of injection
SOC	Start of combustion
TDC	Top dead center
TJI	Turbulent jet ignited
TOC	Time of combustion
VGT	Variable geometry turbocharged
VVT	Variable Valve Timing
WD	Wigner Distribution

Variables

$CA10$	Crank angle at which 10 % of the heat from combustion has been released	CAD
$CA50$	Crank angle at which 50 % of the heat from combustion has been released	CAD
$CA90$	Crank angle at which 90 % of the heat from combustion has been released	CAD
Q_c	Heat released in the combustion chamber	MJ
κ	Polytropic coefficient	-
T	Temperatures	°C

V	Volume	l
f	Frequency	Hz
a	Sound speed	m/s
n	Engine speed	rpm
R	Gas constant	J/kg/K
Re	Reynolds number	-
γ	Heat capacities ratio	-
ρ	Density	kg/m^3
V_{dis}	Displaced Volume	l
m_{air}	Air mass	mg/str
m_f	Injected fuel mass	mg/str
m_{cyl}	Cylinder mass	mg/str
m_{int}	Intake mass	mg/str
m_{res}	Residual gas mass	mg/str
p_{cyl}	In-cylinder pressure	bar
p_{int}	Boost pressure	bar
p_m	Motored pressure	bar
p_k	Knock probability	-
p_{th}	Knock probability threshold	-
T_{air}	Air temperature	°C
T_{exh}	Exhaust gases temperature	K
T_{int}	Intake gases temperature	K
T_{cyl}	In-cylinder temperature	K
T_s	Sampling period	s
I_r	Resonance index	bar
η_v	Volumetric efficiency	-
θ	Crankshaft angle	°
y	Sensor measurements	-
x	State-vector	-
u	Input	-
u_C	Combustion resonance excitation	-
u_A	Autoignition resonance excitation	-
τ	Sensor delay	s
α_{up}	Discrete time response parameter for a first order filter	-
F_s	Sampling frequency	Hz
Δt_{cic}	Cycle duration	s
t	time	s
k	Discrete instant	-
s	s transform variable	-
w	Window function	-
μ	Dynamic viscosity	Pa s

PART

I

Overview

Chapter

1

Introduction

Contents

1.1 Background

Internal combustion (IC) engines are the main propulsion systems in road transport, since they represent the 99 % of global transport [1]. In the past decades, the number of vehicles produced has increased, being the passenger cars the ones with the highest percentage compared to the commercial ones. The word production of IC engines is illustrated in Figure 1.1.

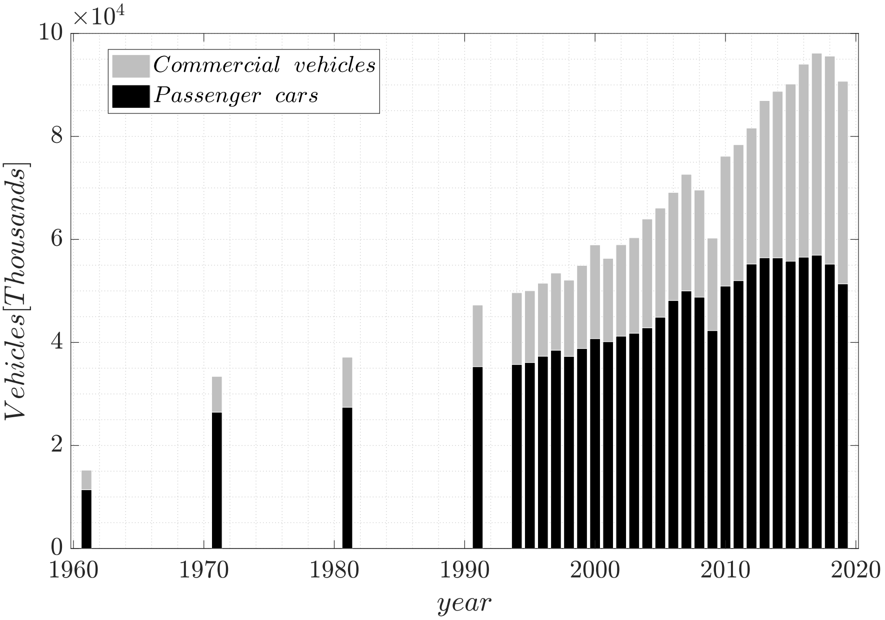

Figure 1.1: *Word vehicles production. Data extracted from [2].*

Nerveless, environment is of great concern these days due to the climate changes and one of the main challenges of the industry is to generate a low environmental impact. Climate changing is producing global warming on the earth surface, since 1980 the mean global temperature has increased over 1 ° C, as illustrated in Figure 1.2, where the distribution over the years of the temperature anomaly is shown.

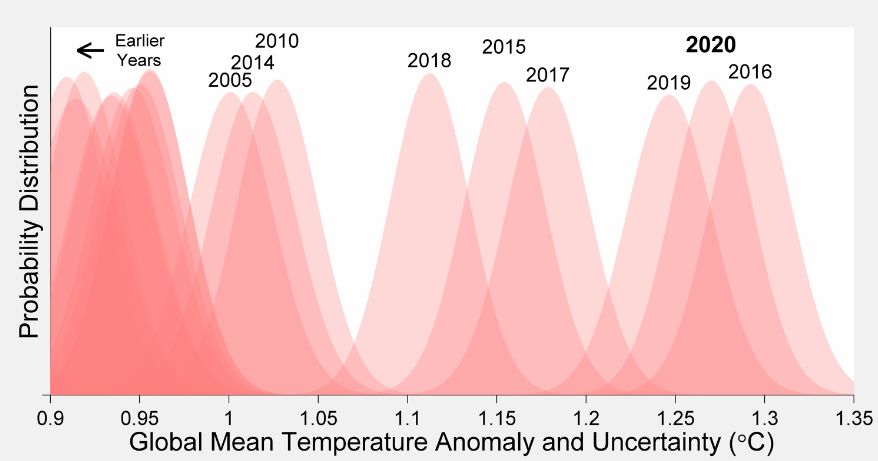

Figure 1.2: *Global Temperature probability distributions. Data extracted from [3].*

As a consequence, states have translated society concerns into policies set to keep global warming below 2 °C [4]. Global warming in mainly caused by human activity, the concentrations of some of greenhouse gases is increasing in the atmosphere, especially: carbon dioxide (CO_2), methane(CH_4), nitrous oxide (N_2O) and fluorinated gases, among others. Being CO_2 the responsible for 64% of global warming related with human activity [5]. Because of the impact of CO_2 emissions on climate change, a reduction on greenhouse gas emissions more than 55% below 1990 levels is expected by 2030 [5].

Passenger cars transport contributes around 23 % of global CO_2 emissions [6], as is shown in Figure 1.3and road transport is responsible for more than 70 % of the CO_2 emissions from transport [5].

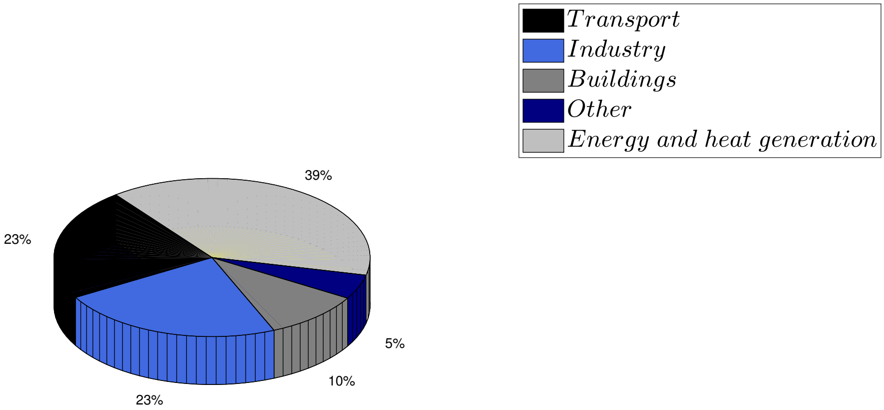

Figure 1.3: *CO_2 emissions produced by different economic sectors. Data extracted from [6].*

Currently, IC engine future is on discussion, and as a consequence, the evaluation of various powertrain solutions is underway, e.g Electrical Vehicles (EV) and Hybrid Electrical Vehicles (HEV). But the benefits in CO_2 emissions of EV is associated to the electricity production emissions [7]. Regarding the future of IC technology, OPEC considers that, by 2045, a 16% of vehicles will be operating with non-oil fuels, as shown in Figure 1.4.

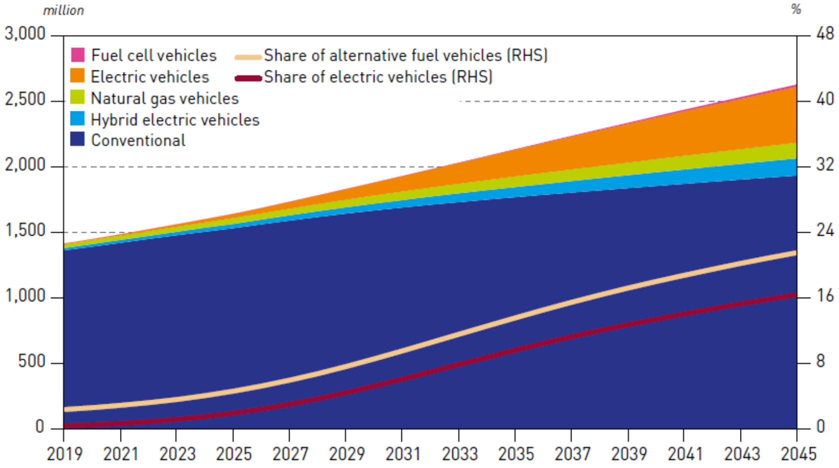

Figure 1.4: *Composition of the global vehicle fleet, 2019–2045 million. Source OPED [8].*

As is shown in Figure 1.4, IC engines will continue to be dominant in the road transport sector, being HEV and Natural Gas (NG) vehicles the third highest percentage.

In this context, and with the aim of controlling transport emissions, governments legislated the emission targets limits in the last two decades. The current pollution emissions values for the European Union (EU), the United States (USA) and Japan are illustrated in Figure 6.6. The emissions shown are: carbon monoxide (CO), non-methane organic gases (NMOG), CO_2, particulate matter (PM) and particle number (PN).

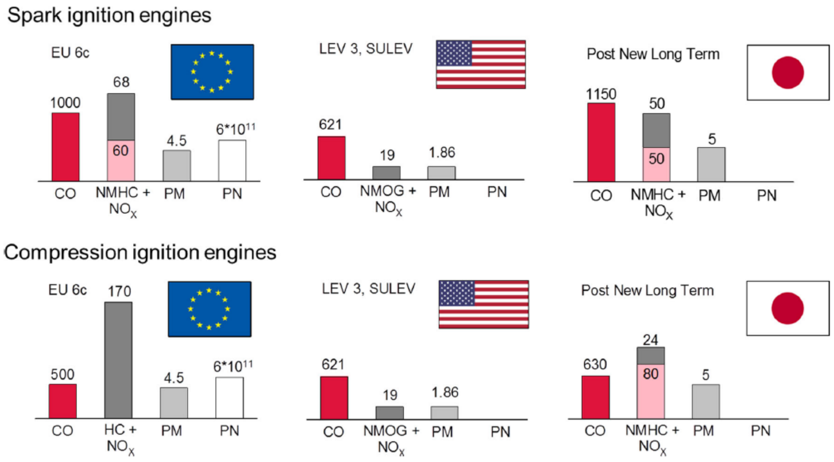

Figure 1.5: *Pollutant emission limits for EU, USA and Japan (mg/km, PN/km). Source [9].*

Regarding the future of IC engines technology, the main target is to increase the efficiency and fulfill the emissions regulations. In this sense, fuel consumption of compression ignition engines (CI) compared to spark-ignited (SI) demonstrated important benefits. But in terms of emissions, the after treatment system for CI engines is more complex and costly than for SI engines [10]. In this sense, several alternatives fuels had been studied in order to improve CI engines emissions performance [11, 12].

Regarding SI technology, according to [13], the registration of new gasoline cars during 2020 in the EU is about the 47 %, as is shown in Figure 6.7.

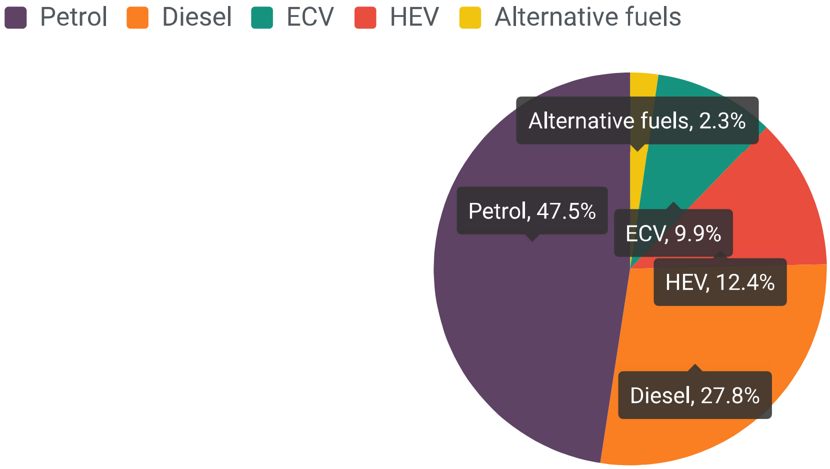

Figure 1.6: *EU New passenger cars classified by fuel type. Source [13].*

For this reason, in the last years new technologies raised in SI in order to reduce the gap in terms of fuel consumption, and maintaining the advantages in exhaust emissions. These new technologies included direct injection (DI), exhaust gas re-circulation (EGR), turbocharging and downsizing, diversification of fuels, lean combustion, among others [9].

In recent years, EGR became a good alternative to achieve similar efficiency levels to CI engines. With EGR the engine is kept at stoichiometric conditions ($\lambda = 1$) while diluting the oxygen concentration. One advantage of cooled EGR is the mitigation of knock phenomena at high load conditions [14]. The main problem with EGR in SI combustion, is that high EGR rates are not possible to achieve due to misfire and stability [15, 16].

Respecting the engine operation at lean conditions ($\lambda > 1$), the main problem is that the after-treatment in SI engine is not compatible with this combustion concept [17], and then NO_x emissions will not satisfy the target limits. An alternative to implement lean combustion for SI combustion is the Turbulent Jet Ignition concept (TJI), which make used of a pre-chamber connected to the main combustion chamber across a set of orifices [18].

Nowadays, downsizing is a design trend in SI engine, on the one hand small volume engines allows to reduce heat, pump and friction losses [19]. The reduction of the displacement in downsizing engines needs the increase of

Brake Mean Effective Pressure (BMEP) to keep equal engine torque, in order to cope this problem turbocharging seem to be the best solution [19].

Regarding diversification of fuels, other alternatives to petroleum based fuels are being analyzed: Bio-fuels, Liquefied Petroleum Gas (LPG), alcohols (e.g ethanol), Compressed Natural Gas (CNG) are alternative fuels which can be used in IC engines [20, 21]. Concerning ethanol as fuel, it has an octane number (RON) higher than gasoline, which improves thermal efficiency by using higher compression ratios [22]. LPG is comparatively easier to implement than CNG, but because is a refinery product it is not suitable on future applications [23]. SI engine fueled with CNG exhibit a performance drop, but shows better emissions compared with gasoline [24] due to its low carbon content. According to OPEC, CNG it is one of the key fuels as an alternative to conventional fuels due to its lower emission of greenhouse gasses [8].

1.2 Engine control

In this context, engine control optimization has an important role in IC engine development. The engine control can be divided in combustion, air-path and after-treatment controls [25]. Actually, IC engines are controlled by Electronic Control Units (ECUs), which stores Open Loop (OL) maps on memory in order to manage some of the different control variables of the engine, and different control oriented models [26]. OL control exhibit good results since is predictable and robust because of the extensive knowledge in this field. The problem with this approach is the extensible calibration experiments necessary for each operating condition. In addition, some variables, e.g lambda or knock, are controlled by CL controls in order to correct the control variable with the feedback information [27].

In recent years, evolution of computational capabilities of ECUs presents an opportunity in order to implement more advanced control strategies based in more complex models [27]. On-board diagnosis of combustion were implemented over the last few years, and due to the increasing functions of IC engines, the development of the control electronic management has become more complex.

In order to improve engine performance, the process needs to be precisely controlled, so model-based control is required, not only to estimate off-line parameters but to be implemented in real-time. Progressively, control oriented models have been included in ECUs in order to provide more information to the system and for a more efficient operation [28].

Recently, more complex control techniques have been published: online learning [29–31], Model Predictive Control (MPC) [32] or on-board calibrations [33,34], all of them aimed to adapt the engine control to a wider spectrum of conditions at the expense of the increase in control complexity.

1.3 Scope of the work

Future IC engine technologies focused on combustion efficiency will need accurate combustion indicators for on-board diagnosis and control. This dissertation presents a set of combustion diagnosis indicators, some of them based on the extensive use of information from the in-cylinder pressure sensor, and some of them relying on conventional sensors currently used in state-of-the-art engines. These indicators aim to model the engine operation condition under normal and abnormal combustion, being able to adapt to different fuels.

The work is divided in modeling and diagnosis part, which includes an average and variability combustion model, resonance characterization of in-cylinder pressure signal, and knocking recognition methods based on in-cylinder pressure and knock sensor. And a second part which includes the control applications of the diagnosis and models developed in the first part of the work, showing the potential of such models and indicators.

1.4 Objectives

The main objective of this work is the development of combustion indicators for combustion diagnosis and control. This objective is implemented in the following partial objectives:

- Developing a control oriented combustion model able to predict the average of the combustion in a SI engine. (Chapter 4)
- Identification and modeling of the combustion variability in SI engine. (Chapter 5)

- Providing a model able to predict resonance evolution of the in-cylinder pressure for different combustion modes. (Chapter 6)
- Designing different knock recognition methods, in-cylinder pressure based, and knock sensor based. (Chapter 7)
- Proposal of two control applications for knock control and combustion optimization. (Chapter 8)

1.5 Methodology

In order to achieve such objectives, this dissertation is divided in 5 parts which consist of 9 different chapters as is shown in Figure 1.7.

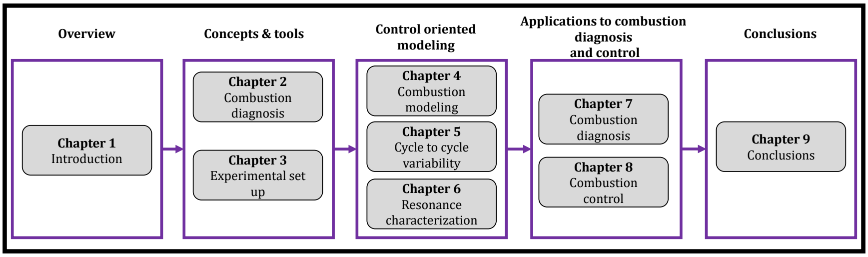

Figure 1.7: *Chapters organization.*

The second part, concepts and tools, is composed of two chapters: the state of the art in combustion and control topic, and the experimental facilities used to carry out experimental activities, where the engines and test benches configurations are described.

The third part, control oriented modeling, is organized in three chapters: Chapter 4, the combustion modeling, where a control oriented model to represent the combustion in an average sense, i.e. without considering cycle-to-cycle dispersion is presented. The model makes use of available signals on the ECU as input variables. An observer is designed in order to improve the estimation of such model under transient conditions. Chapter 5, where the variability causes in IC engines is analyzed. Previous analysis have led to the development of a model able to capture cycle-to-cycle dispersion in an statistical way. And Chapter 6, a resonance analysis of in-cylinder pressure is performed, where two models are developed. This models aims to reproduce the amplitude evolution of resonance in the combustion chamber. These models can improve control oriented analysis of resonance for applications such as knock recognition or trapped mass estimation.

The fourth part, applications to combustion diagnosis and control, is organized in two chapters: in Chapter 7 offline applications of the modeling block for trapped mass estimation and knock recognition methods are developed, where knock recognition methods are two in-cylinder pressure based, and one knock sensor based. Chapter 8 presents two control applications to point out the potential of such models. In the first control application, a map-based knock control which makes use of in-cylinder pressure sensor is described. In the second control application, a residual gas fraction control with combustion optimization based on the combustion model developed in Chapter 4 is presented. Both controllers are validated on a SI engine.

Finally, the last part, Chapter 9 which includes main conclusions of the work and future implementation in industry of the methods and models presented.

1.6 Publications

Most of the contents included in this dissertation have been published in international journals and conferences. In this section, the publications by the author are listed with the chapter which include the publication information.

Journal papers

1. Pla, B., De la Morena, J., Bares, P., & Jiménez, I. (2020). Cycle-to-cycle combustion variability modelling in spark ignited engines for control purposes. International Journal of Engine Research, 21(8), 1398-1411. (Chapter 4 and 5)

2. Novella, R., Pla, B., Bares, P., & Jiménez, I. (2020). Acoustic characterization of combustion chambers in reciprocating engines: An application for low knocking cycles recognition. International Journal of Engine Research, 1468087420980565. (Chapters 6 and 7)

3. Pla, B., Bares, P., Jiménez, I., Guardiola, C., Zhang, Y., & Shen, T. (2020). A fuzzy logic map-based knock control for spark ignition engines. Applied Energy, 280, 116036. (Chapter 8)

4. Pla, B., De La Morena, J., Bares, P., & Jiménez, I. (2021). Adaptive in-cylinder pressure model for spark ignition engine control. Fuel, 299, 120870. (Chapter 8)

5. Pla, B., Bares, P., Jiménez, I., Guardiola, C. (2022). Increasing knock detection sensitivity by combining knock sensor signal with a control oriented combustion model. Mechanical Systems and Signal Processing (MSSP) (Chapter 7).

Conference papers

1. Pla, B., De La Morena, J., Bares, P., & Jiménez, I. (2020). Knock Analysis in the crank angle domain for low-knocking cycles detection (No. 2020-01-0549). SAE Technical Paper. (Chapter 7)

2. Pla, B., Bares, P., Jiménez, I. & Guardiola, C. (2021). Model-based residual gas fraction control with spark advance optimization. Engine and Powertrain Control, Simulation and Modeling, E-COSM 2021, Tokyo, Japan. (Chapter 8)

References

[1] Leach Felix, Kalghatgi Gautam, Stone Richard and Miles Paul. “The scope for improving the efficiency and environmental impact of internal combustion engines”. *Transportation Engineering*, p 100005, 2020. (cited in p. 3)

[2] (cited in p. 4)

[3] Earth Berkeley. “Global Temperature Report for 2020”. http://berkeleyearth.org/global-temperature-report-for-2020/. Accessed: 2021-03-12. (cited in p. 5)

[4] (cited in p. 5)

[5] comission European. “2030 Climate target plan”. https://ec.europa.eu/info. Accessed: 2021-03-16. (cited in p. 5)

[6] Agency International Energy. “Global Energy Review: CO2 Emissions in 2020”. https://www.iea.org/. Accessed: 2021-03-12. (cited in pp. 5 and 6)

[7] Serrano Jose Ramon, Novella Ricardo and Piqueras Pedro. “Why the development of internal combustion engines is still necessary to fight against global climate change from the perspective of transportation”, 2019. (cited in p. 6)

[8] of the Petroleum Exporting Countries Organization. “2020 World Oil Outlook 2045”. https://www.opec.org/. Accessed: 2021-03-12. (cited in pp. 6 and 9)

[9] Pischinger Stefan. “Current and future challenges for automotive catalysis: engine technology trends and their impact”. *Topics in Catalysis*, Vol. 59 n^o 10, pp. 834–844, 2016. (cited in pp. 7 and 8)

[10] Sjeric Momir, Taritas Ivan, Tomi Rudolf, Bla Mislav, Kozarac Darko and Luli Zoran. “Efficiency improvement of a spark-ignition engine at full load conditions using exhaust gas recirculation and variable geometry turbocharger–Numerical study”. *Energy conversion and management*, Vol. 125, pp. 26–39, 2016. (cited in p. 7)

[11] Armas Octavio, Yehliu Kuen and Boehman André L. “Effect of alternative fuels on exhaust emissions during diesel engine operation with matched combustion phasing”. *Fuel*, Vol. 89 n^o 2, pp. 438–456, 2010. (cited in p. 7)

[12] Armas Octavio, Ballesteros Rosario and Cardenas María Dolores. “Thermodynamic diagnosis of diesel and biodiesel combustion processes during load-increase transient sequences”. *Applied energy*, Vol. 97, pp. 558–568, 2012. (cited in p. 7)

[13] Association European Automobile Manufacturers. “Fuel types of new cars 2019-2020”. https://www.acea.be/. Accessed: 2021-03-17. (cited in pp. 7 and 8)

[14] Yu Shui and Zheng Ming. “Future gasoline engine ignition: A review on advanced concepts”. *International Journal of Engine Research*, p 1468087420953085, 2020. (cited in p. 8)

[15] Galloni E, Fontana G and Palmaccio R. “Effects of exhaust gas recycle in a downsized gasoline engine”. *Applied Energy*, Vol. 105, pp. 99–107, 2013. (cited in p. 8)

[16] Maldonado Bryan P and Kaul Brian C. “Control-oriented modeling of cycle-to-cycle combustion variability at the misfire limit in SI engines”. In *Dynamic Systems and Control Conference*, volume 84287, p V002T26A001. American Society of Mechanical Engineers, 2020. (cited in p. 8)

[17] Yeo GwonKoo, Kil JeongKi, Youn YoungKee, Kim ChangDae and Kim NamHyuk. “Three-way catalysts for partial lean-burn engine vehicle”. Technical report, SAE Technical Paper, 2000. (cited in p. 8)

[18] Benajes J, Novella R, Gomez-Soriano J, Martinez-Hernandiz PJ, Libert C and Dabiri M. “Evaluation of the passive pre-chamber ignition concept for future high compression ratio turbocharged spark-ignition engines”. *Applied Energy*, Vol. 248, pp. 576–588, 2019. (cited in pp. 8 and 30)

[19] Police Giuseppe, Diana Salvatore, Giglio Veniero, Iorio Biagio and Rispoli Natale. “Downsizing of SI engines by turbo-charging”. In *Engineering Systems Design and Analysis*, volume 42517, pp. 463–476, 2006. (cited in pp. 8 and 9)

[20] Göktaş Meltem, Balki Mustafa Kemal, Sayin Cenk and Canakci Mustafa. “An evaluation of the use of alcohol fuels in SI engines in terms of performance, emission and combustion characteristics: A review”. *Fuel*, Vol. 286, pp. 119425, 2021. (cited in p. 9)

[21] Gómez Arántzazu, Fernández-Yáñez Pablo, Soriano José A, Sánchez-Rodríguez Luis, Mata Carmen, García-Contreras Reyes, Armas Octavio and Cárdenas M Dolores. “Comparison of real driving emissions from Euro VI buses with diesel and compressed natural gas fuels”. *Fuel*, Vol. 289, pp. 119836, 2021. (cited in p. 9)

[22] Costa Rodrigo C and Sodré José R. “Compression ratio effects on an ethanol/gasoline fuelled engine performance”. *Applied Thermal Engineering*, Vol. 31 n^o 2-3, pp. 278–283, 2011. (cited in p. 9)

[23] Demirbas Ayhan. “Fuel properties of hydrogen, liquefied petroleum gas (LPG), and compressed natural gas (CNG) for transportation”. *Energy Sources*, Vol. 24 n^o 7, pp. 601–610, 2002. (cited in p. 9)

[24] A Aziz A Rashid, Firmansyah Firmansyah and Raja Shahzad Raja Shahzad. “Combustion analysis of a CNG direct injection spark ignition engine”. *International Journal of Automotive and Mechanical Engineering (IJAME)*, Vol. 2, pp. 157–170, 2010. (cited in p. 9)

[25] Payri F, Luján José M, Guardiola Carlos and Pla B. “A challenging future for the IC engine: new technologies and the control role”. *Oil & Gas Science and Technology–Revue d’IFP Energies nouvelles*, Vol. 70 n^o 1, pp. 15–30, 2015. (cited in p. 9)

[26] Zhang Yahui and Shen Tielong. “On-Board map learning-based combustion phase control in spark ignition engines”. In *2017 IEEE Conference on Control Technology and Applications (CCTA)*, pp. 287–292. IEEE, 2017. (cited in p. 9)

[27] Isermann Rolf. “Engine modeling and control”. *Berlin: Springers Berlin Heidelberg*, Vol. 1017, 2014. (cited in p. 9)

[28] Butts Kenneth Roy and Jaikamal Vivek. “Model-based verification and validation of electronic engine controls”. Technical report, SAE Technical Paper, 2012. (cited in p. 10)

[29] Gao Jinwu, Zhang Yahui, Zhang Jiangyan and Shen Tielong. “Adaptive Internal Model Based Control of the RGF Using Online Map Learning and Statistical Feedback Law”. *IEEE/ASME Transactions on Mechatronics*, Vol. 25 n^o 2, pp. 1117–1128, 2019. (cited in pp. 10 and 186)

[30] Zhang Yahui, Shen Xun, Wu Yuhu and Shen Tielong. “On-board knock probability map learning–based spark advance control for combustion engines”. *International Journal of Engine Research*, Vol. 20 n^o 10, pp. 1073–1088, 2019. (cited in pp. 10, 34, 188, and 190)

[31] Zhao Kai and Shen Tielong. “Boundary Learning for Spark-Ignition Engine Control”. In *2020 15th IEEE Conference on Industrial Electronics and Applications (ICIEA)*, pp. 241–246. IEEE, 2020. (cited in p. 10)

[32] Del Re Luigi, Allgöwer Frank, Glielmo Luigi, Guardiola Carlos and Kolmanovsky Ilya. *Automotive model predictive control: models, methods and applications*, volume 402. Springer, 2010. (cited in p. 10)

[33] Hellström Erik, Lee Donghoon, Jiang Li, Stefanopoulou Anna G and Yilmaz Hakan. “On-board calibration of spark timing by extremum seeking for flex-fuel engines”. *IEEE Transactions on control systems technology*, Vol. 21 n^o 6, pp. 2273–2279, 2013. (cited in p. 10)

[34] Eguchi Makoto, Fukuda Naoki, Ohmori Hiromitsu, Takahashi Motoki, Yamasaki Yudai and Kaneko Shigehiko. “Diesel Engine Combustion Control with Onboard Calibration by Using Feedback Error Learning”. Technical report, SAE Technical Paper, 2019. (cited in p. 10)

PART

II

Concepts and tools

Chapter 2

State of the art: Combustion modeling and control

Contents

2.1 Introduction

In-cylinder pressure is the most important variable to analyze the combustion process in IC engines, and can be used used as feedback signal for closed-loop combustion control and diagnostics. In-cylinder pressure sensors are the most precise measurement for combustion analysis [1], by providing a direct measurement of the combustion process. These sensors are widely used for combustion detection, to evaluate different combustion parameters such as the crank angle where the 50 % of the heat release (CA50), knock recognition, thermal efficiency, Indicated Mean Effective Pressure (IMEP), cycle-to-cycle variability, cylinder-to-cylinder dispersion, among others.

In-cylinder pressure signal of IC engine can be decomposed into three different frequency bands: motored, combustion and resonance [2]. The motored pressure, which corresponds to compression and expansion, is associated with the piston movement, so the frequency depends on the engine speed, and its energy depends mainly on the load. Combustion is also affected by engine speed and injection settings, and in-cylinder resonance depends on the resonant modes excitation, and load.

Different types of in-cylinder pressure transducers can be found, such as balanced disk type, variable inductance or resistance, piezoelectric with different levels of accuracy, being piezoelectric transducers the most widely used for in-cylinder pressure measurement in modern engines, due to the high frequency response and small size [3]. Despite their high accuracy, in-cylinder pressure sensors, still suffer from cost and durability issues, and also require modifications in the cylinder head to be installed. Even though in-cylinder pressure sensors are extensively used in the engine research field or in some engines brands, the application on production engines is not so extended [4].

For this reason, model-based control has become an interesting tool for IC engine control [5]. Virtual sensors can be used to improve the estimation of in-cylinder pressure by obtaining information about combustion characteristics, such as ignition delay, peak cylinder pressure and its location.

The first part of the chapter presents a survey of the use of the in-cylinder pressure sensors for engine diagnosis and control. Then, in order to replace the used of in-cylinder pressure sensors, indirect combustion diagnosis methods are presented. After, knock recognition methods based in both, in-cylinder pressure and knock sensor, are introduced. Finally, combustion control techniques for combustion optimization and knock control are presented.

2.2 Direct combustion diagnosis

In-cylinder pressure is the most direct signal for combustion diagnosis, since provides an accurate information about the thermodynamic process during combustion and engine power [6], for this reason, is widely used to study combustion phenomena in IC engine. During this section, some of the information that can be extracted from in-cylinder pressure sensors to evaluate combustion development will be presented.

2.2.1 In-cylinder pressure modeling

Otto Thermodynamic cycle is divided in four stages: intake, compression, combustion, and combustion stoke [7]. In Figure 2.1 the Otto cycle stages are represented.

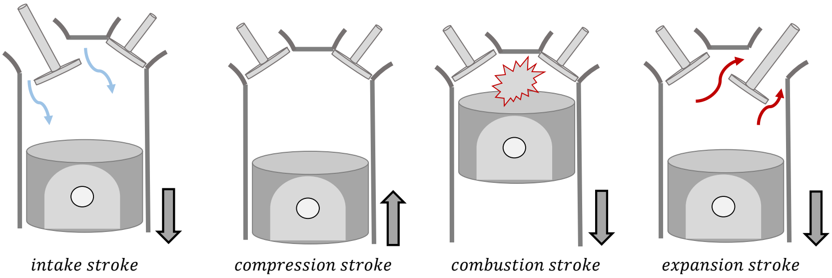

Figure 2.1: *Otto thermodynamic cycle stages.*

The compression and expansion stages can be represented by a polytropic evolution, which assumes an adiabatic process [8]: where the realtion between the pressure p_{cyl} and the volume V is computed as :

$$p_{cyl}V^{\kappa} = K \tag{2.1}$$

where K is a constant and κ the polytropic coefficient, which considered the discrepancies with the adiabatic assumption, i.e. wall heat transfer. In most of the application κ is one or two constant values: one for compression (κ_c) and an additional for expansion (κ_e). Once κ is determined, the compression and expansion pressures can be obtained through:

$$p_{comp}(\theta) = p(\text{IVC}) \left(\frac{V(\text{IVC})}{V(\theta)} \right)^{\kappa_c} \tag{2.2}$$

$$p_{exp}(\theta) = p(\text{EOC}) \left(\frac{V(\text{EOC})}{V(\theta)} \right)^{\kappa_e} \tag{2.3}$$

where IVC is the Intake Valve Closing, θ the crank angle, and EOC the End Of Combustion. In Figure 2.2, the polytropic pressure modeled during compression and expansion is represented with the measured in-cylinder pressure.

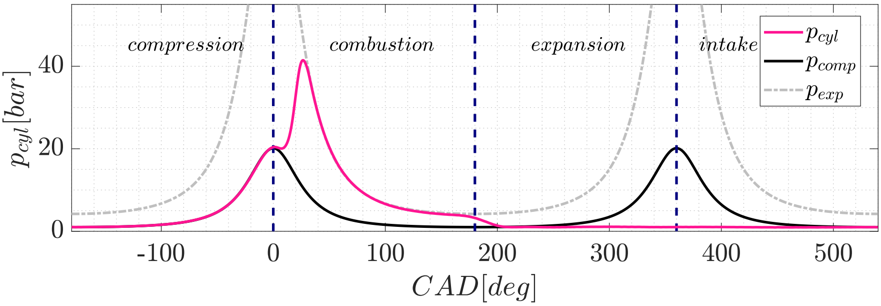

Figure 2.2: *Adiabatic in-cylinder pressure evolution during compression and expansion compared with the in-cylinder pressure measured.*

During combustion, the in-cylinder gas can be described by an open thermodynamic system, where the combustion chamber represents the system boundary as is shown in Figure 2.3.

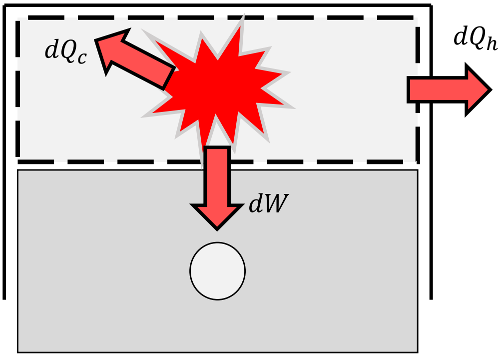

Figure 2.3: *Combustion model system.*

The first law of thermodynamic for this system is as following:

$$\mathrm{d}U = \mathrm{d}Q - \mathrm{d}W + \sum h^i \mathrm{d}m^i_{cyl} \tag{2.4}$$

where $\mathrm{d}Q$ is the heat added to the system (combustion), $\mathrm{d}U$ represents the change in system internal energy, $\mathrm{d}W$ is the work performed by the system, and the enthalphy flux is represented by $\sum h^i dm^i_{cyl}$. The combustion is modeled as a release of heat given by the difference between the chemical energy, $\mathrm{d}Q_c$, and the heat transferred to the cylinder walls $\mathrm{d}Q_{h-w}$, such as:

$$\mathrm{d}Q = \mathrm{d}Q_c - \mathrm{d}Q_{h-w} \tag{2.5}$$

Then, Equation (2.4) can be written as:

$$\mathrm{d}U = \mathrm{d}Q_c - \mathrm{d}Q_{h-w} - \mathrm{d}W + \sum h^i \mathrm{d}m^i_{cyl} \tag{2.6}$$

Assuming ideal gas conditions in the combustion chamber during conditions:

$$p_{cyl}V = m_{cyl}RT \tag{2.7}$$

$\mathrm{d}U$ can be expressed as following:

$$\mathrm{d}U = m_{cyl}c_v\mathrm{d}T + u\mathrm{d}m_{cyl} \tag{2.8}$$

where m_{cyl} represents the trapped mass, c_v the heat-capacity at constant volume and u is the specific internal energy.

From the ideal gas law presented in Equation (2.7) differential of T can be expressed as following:

$$\mathrm{d}T = \frac{1}{m_{cyl}R}(V\mathrm{d}p_{cyl} + p_{cyl}dV - RT\mathrm{d}m_{cyl}) \tag{2.9}$$

Assuming R to be a constant, replacing Equations (2.6) and (2.9) in Equation (2.6). Substituting $c_v = \frac{R}{\gamma T}$, where γ is the ratio of specific heat, the following differential in p_{cyl} can be obtained:

$$\mathrm{d}p_{cyl} = -\frac{\gamma}{V}p_{cyl}dV + \frac{\gamma-1}{V}(\mathrm{d}Q_c - \mathrm{d}Q_{h-w} + \sum h^i \mathrm{d}m^i_{cyl}) + \frac{1}{V}(RT - (\gamma-1)u)\mathrm{d}m_{cyl} \tag{2.10}$$

The simplified differential equation of p_{cyl} by assuming m_{cyl} constant is expressed as:

$$\mathrm{d}p_{cyl} = -\frac{\gamma}{V}p_{cyl}dV + \frac{\gamma-1}{V}(\mathrm{d}Q_c - \mathrm{d}Q_{h-w}) \tag{2.11}$$

The evolution of the heat in the control volume of the combustion chamber is expressed as:

$$Q_c = \frac{\gamma}{\gamma-1}p_{cyl}\mathrm{d}V + \frac{1}{\gamma-1}V\mathrm{d}p_{cyl} + \mathrm{d}Q_{h-w} \tag{2.12}$$

where Q_c is the evolution of the heat in the combustion chamber, p_{cyl} represents the in-cylinder pressure, V is the instantaneous volume in the combustion chamber which can be derived from geometrical data of the engine, γ the specific heat capacities ratio, and $\mathrm{d}Q_{h-w}$ the wall heat transfer.

The value of the specific heat capacities ratio, γ, can be estimated through semi-empirical models. In order to determine gases properties, in lean mixtures some models used the air to fuel ratio, the Mass Fraction Burned (MFB), and the temperature of the gases (T) [9, 10]. But in stoichiometric conditions, as SI combustion, γ can be approximated with much more simple functions, such as in [11], where γ is proportional to the temperature. In SI combustion, the model presented in [12] can be used:

$$\gamma = 1.38 - 0.2e^{\frac{900}{T}} \tag{2.13}$$

The wall heat transfer should be modeled in order to obtain the heat release from fuel, as:

$$Q_w = hA_w(T - T_w) \tag{2.14}$$

where T_w the temperature, A_w represents the area of the walls, and h is the convective coefficient. One of the most widely used models was developed in [13], and modeled the evolution of h as a function of pressure, temperature, and engine speed, as following:

$$h = C_1 D^{-0.2} p^{0.8} T^{-0.53} \left[C_2 \overline{c} + C_3 K_h (p - p_m)\right]^{0.8} \tag{2.15}$$

where p_m is the motored in-cylinder pressure, $\overline{c}$ the mean piston speed, C_1, C_2, and C_3 are constants, and K_h is obtained from the volume displace, V_{dis}, at the Intake Valve closing (IVC), as following:

$$K_h = \frac{V_{dis} T_{IVC}}{p_{IVC} V_{IVC}} \tag{2.16}$$

2.2.1.1 Cylinder geometry

The instantaneous volume evolution V of the combustion chamber is modeled as a slider-crank-mechanism as:

$$V(\theta) = V_{cc} + \frac{\pi D^2}{4}\left[L_c + L_r\left(1 - \cos(\theta)\right) - \sqrt{L_c^2 - L_r^2 \sin(\theta)^2}\right] \tag{2.17}$$

where L_r is the rod length, D is the bore, L_c is the crank length, and V_{cc} is the minimum combustion chamber volume. Expression of Equation (2.17) neglected pressure deformations, which can be assumed for practical applications.

2.2.1.2 In-cylinder temperature

The in-cylinder temperature evolution, T_{cyl}, can be modeled by estimating the exhaust temperature, T_{exh}, and fitted during the end of the expansion. The exhaust temperature can be calculated using polytropic expansion as suggested in [14]:

$$T_{exh} = k_1 p_{cyl}^{\frac{\kappa-1}{\kappa}} \tag{2.18}$$

where the temperature to pressure ratio k_1 is fitted considering that T_{exh} = T_{cyl} during the end section of the expansion stroke, where T_{cyl} can be approximated from the perfect gas law as:

$$T_{cyl} = \frac{p_{cyl} V}{R m_{cyl}} \tag{2.19}$$

where m_{cyl} is the trapped mass, V the volume, and R the constant of the gases.

2.2.1.3 Mass fraction burned

The MFB describes the process of chemical energy liberate as a function of the Crank Angle Degree (CAD), and the determination of MFB is frequently based on the burning rate analysis. In the present text, we will consider the normalized version of the MFB (between 0 and 1) by dividing by the total fuel Heat Release Rate per crank angle(HRR), $\frac{dQ_c}{d\theta}$, is a difficult parameter to model due to the complexity of the phenomena, and the dependency on several factors such as fuel-injection, chemical combustion rates, among others. Some authors use an alternative formulation of Equation (2.12), which enforces to represent the losses with a single parameter, κ, such as:

$$\mathrm{HRR} = \frac{dQ}{\mathrm{d}\theta} = \frac{\kappa}{\kappa-1} p_{cyl} \frac{\mathrm{d}V}{\mathrm{d}\theta} + \frac{1}{\kappa-1} V \frac{\mathrm{d}p_{cyl}}{\mathrm{d}\theta} \tag{2.20}$$

$$MFB_Q = \frac{HRR}{max(HRR)} \tag{2.21}$$

The approximation in Equation (2.20), named apparent heat release, is widely employed in control applications due to the low computational burden. A commonly value used for κ in SI combustion is 1.3, which is used to compensate the errors of the estimation due to the underestimating HRR at compression stroke, and the overestimating HRR at the expansion.

The expression in Equation (2.20), is usually precise enough in combustion phase estimation for control purposes but exhibits significant inconsistency in total HRR. In addition, the prediction of EOC by analyzing this expression is one of the major issues. One way to compensated this error is assuming that HRR before the Spark Advance (SA) is zero. Another solution is the approximation of the MFB evolution at SI combustion by one combustion event with a vibe function shape [15], as following:

$$MFB_w = 1 - exp\left(-k_1 \frac{\theta - SOC}{EOC - SOC}\right)^{m_w+1} \tag{2.22}$$

where k_1 and m_w are relate to the duration and shape of the heat-release profile.

An alternative to computed the MFB is the pressure ratio procedure presented in [16, 17]. Where, the MFB is computed by comparing the actual pressure with the motored one, such as:

$$MFB_p = \frac{\frac{p_{cyl}(\theta)}{p_m(\theta)} - 1}{\max\left(\frac{p_{cyl}}{p_m}\right) - 1} \tag{2.23}$$

Figure 2.4 shows the MFB obtained through Equations (2.21),(2.23) and (2.22).

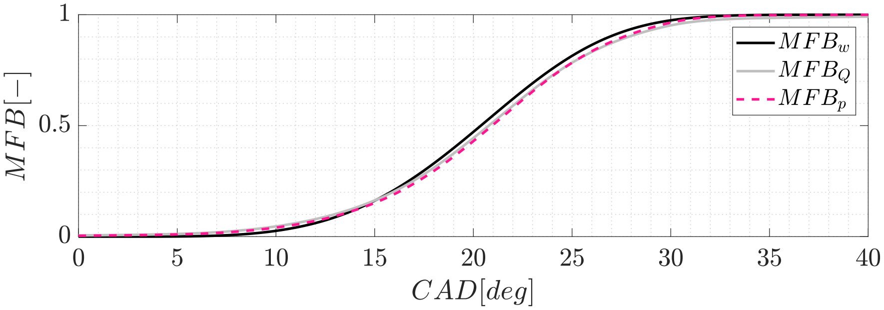

Figure 2.4: *Mass fraction burned of a cycle of SI combustion.*

2.2.2 Combustion indicators definitions

Pressure peak amplitude: The maximum pressure amplitude is an important variable of combustion which is restricted by the structural limitations of the engine. Maximum peak pressure amplitude and location can be calculated as:

$$p_{max} = max(p_{cyl}(\theta)) \tag{2.24}$$
$$\theta_{p_{max}} = arg_{\theta}max(p_{cyl}(\theta)) \tag{2.25}$$

Start of combustion (SOC): Is the point where combustion is initiated, which gas an impact on the combustion evolution, and affects the engine efficiency [7]. The SOC position can be estimated by identifying the point where the HRR curve starts to rapidly increase, without heat released.

CAx The evolution of the combustion is studied by analyzing the crank angle position (CAx) where a determined percentage of the energy released is achieved, which accomplishes:

$$\int^{\alpha=CA_x} \mathrm{HRR}d\alpha = \frac{x\mathrm{HR}}{100} \tag{2.26}$$

where x is a value comprised between 0 ant 100. Note that CA_0 = SOC and CA_{100} = EOC. The $CA10$ is usually used to indicated the SOC, due to noise and inaccuracies near to zero.

Time Of Combustion (TOC): The time of combustion is defined as the duration in angle or time between 0% and 100% of MFB. In practice, is expressed as the angular distance between CA10 and CA90.

Indicate Mean Effective Pressure (IMEP): Defined as the engine work normalized with the cylinder displacement volume V_d, such as:

$$IMEP = \frac{1}{V_d}\oint p_{cyl}dV \tag{2.27}$$

If the pressure is integrated over the entire four-stroke cycle, the net IMEP is obtained, conversely, if the pressure is integrated only in the compression and expansion strokes, the gross IMEP is computed.

Efficiency: The total thermal efficiency is the relation between the work output of the engine cycle and the chemical energy stored in the injected fuel, as:

$$\eta = \frac{W}{q_{LHV} m_f} \tag{2.28}$$

where m_f is the injected fuel mass, q_{LHV} is the lower heating value of the fuel, and W the work. Depending on the work involve in this relation will be the efficiency obtained: mechanical, thermal, etc.

2.3 Indirect combustion diagnosis

In-cylinder pressure sensors provide a direct measurement of combustion process, as is shown in section 2.2 can be used to estimate parameters such as the SOC, TOC, CAx, IMEP, among others. In-cylinder pressure sensors disadvantages are durability and high cost, which makes its application limited in large scale production engines. Therefore, virtual sensors to estimate combustion parameters for diagnosis and control are developed. Some of these virtual sensing strategies are based on the analysis of engine vibration [18, 19], engine speed fluctuation [20–22], in-cylinder ion current [23, 24] and engine acoustic emission [25, 26].

The relation between crankshaft speed fluctuations and the combustion process has been widely explored, several works aim to model the in-cylinder pressure signal from instantaneous speed signal measured by a crankshaft speed sensor [27–29].

It was found that among ion current, crankshaft speed fluctuations and knock sensor signals, the most utilized signal for combustion metric estimation is knock sensor or accelerometer signal [1]. This is due to the low cost, high reliability, durability and easy mounting. In the present work, knock sensor signal will be used in further chapters to estimate combustion metrics.

2.3.1 Combustion diagnosis through vibration signal

Knock sensors are mounted externally on the engine block or the engine head, and measure the vibration signal which is transferred from the in-cylinder oscillations to the engine structure [1]. Nevertheless, other noise sources, such as valve dynamics, must to be eliminated in order to obtained combustion metric from this sensor. From vibration signal different combustion metrics can be computed, such as SOC [30], the CA50 [31], pressure peak location [4, 32], among others.

In order to evaluate the correlation between the information contained in knock sensor signal the signal is analyzed in frequency domain in Figure 2.5, where the vibration signal and in-cylinder pressure are illustrated for 200 cycles in SI combustion.

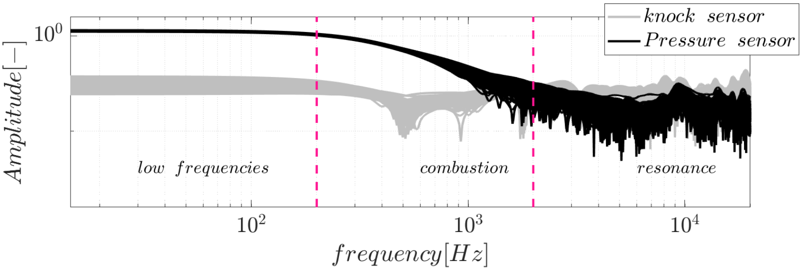

Figure 2.5: *In-cylinder pressure and vibration signal in frequency domain.*

Three frequency bands are highlighted, low frequencies associated with the piston movement, combustion frequencies and resonance frequencies. In order to evaluate the relation in a fixed frequency band, the coherence function is used [33]. Frequencies above 20 kHz can be considered background and sensor noise. As shown in Figure 2.5, the combustion pressure trace has higher energy concentrated in the combustion zone than knock sensor trace. The coherence function computes the ratio between the cross power spectral density of the in-cylinder pressure $P_{p,p}(f)$ and knock sensor signals $P_{k,k}(f)$, to the product of the power spectral density of each signal $P_{p,k}(f)$, as:

$$C_{p,k}(f) = \frac{|P_{p,k}(f)|^2}{P_{p,p}(f)P_{k,k}(f)} \tag{2.29}$$

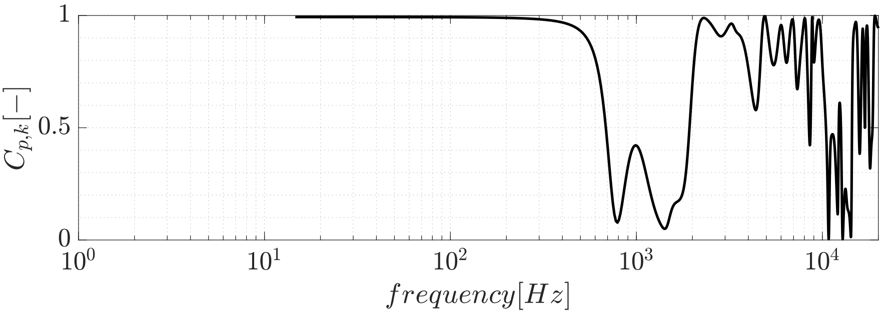

Figure 2.6: *Coherence between vibration signal and in-cylinder pressure for a given cycle.*

Analyzing Figure 2.6, specific points have a high coherence function value, indicating a strong relationship between the spectral components. These points corresponds to the combustion and the resonance frequencies. For this reason, from the vibration signal analysis is possible to extract combustion parameters.

One of the combustion parameters that can be estimated through the vibration signal is the pressure peak location. In [32] a method which consists on band-pass filter the signal is suggested. The band-pass filter is used to separate the harmonic components, which is used to find the zero-crossing acceleration angle, that is characteristic of the pressure peak location, because the zero-crossing represents the beginning of the negative vibration oscillation, which is characterized by the maximum amplitude from in-cylinder pressure [34].

Based on previous results, the vibration signal has been band-pass filtered in a frequency range of 200-1400 Hz. In Figure 2.7 the in-cylinder pressure signal of each cylinder and the filtered knock sensor signal are represented as example.

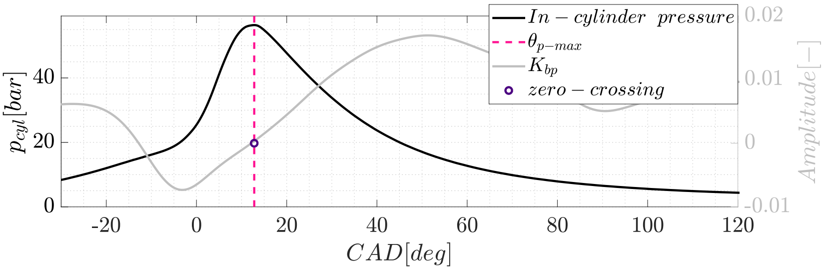

Figure 2.7: *Pressure peak location estimation: Low-pass in-cylinder pressure compared with band-pass knock sensor signal.*

Note that the pressure peak location is significantly correlated to the zero-crossing position of band-pass vibration signal K_{bp} after the first peak. A blue circle shows the zero-crossing angle, which represents the maximum of the pressure peak location obtained through the vibration signal, and in grey hatched line the maximum pressure peak location measurement from in-cylinder pressure signal is also highlighted.

2.4 Abnormal combustion: knock recognition methods

Knock phenomenon is an abnormal combustion which is caused by the spontaneous auto ignition of the end gas [35], this rapid auto-ignition heavily excites resonance in the combustion chamber. The auto-ignition process causes a reduction of the engine efficiency, noise and if oscillations are heavily excited can damage the engine [36]. Knock research is important, since is directly associated with fuel consumption, emissions, engine durability and performance [37].

In new combustion modes, such as TJI combustion, normal combustion heavily excites resonance, so knock cannot be easily identified from normal combustion [38, 39].

Knock recognition techniques can be divided in three groups: ion current signal based [40], methods based on vibration signal [41,42], and methods based on in-cylinder pressure signal. The most reliable technique for knock recognition are in-cylinder pressure based, since provides accurate information about pressure oscillations [43]. Because of it simplicity, vibration signal is the most employed signal for knock recognition in production engines, the issue with knock sensors is the quality of recognition since is usually affected by noise [35].

During this section knock recognition methods based on in-cylinder pressure measurement and knock sensor signal are introduced.

2.4.1 In-cylinder pressure based

In recent years, several knock recognition techniques based on in-cylinder pressure sensors have been published. Several authors quantify pressure oscillations to compute knock [43, 44]. Other works analyzes HRR, in [45] a 0D model is presented, where a heat transfer correlation is used to predict knock event. Additional methods employ frequency domain to compute knock indexes, as for example wavelet transform or Fourier transform [46, 47]. Low-knocking cycle recognition is important, since substantially improves controller performance [48].

One of the most widely employed indicator for knocking recognition is the Maximum Amplitude Pressure Oscillation (MAPO). This indicator is obtained by filtering the in-cylinder pressure within the resonance frequency band ($f_{min} - f_{max}$) and computing the maximum, such as:

$$MAPO = max(|p_{cyl-bp}^{f_{min}-f_{max}}|) \tag{2.30}$$

Another knock indicator is the Integral of Modulus of Pressure Oscillations (IMPO), which is computed as:

$$IMPO = \int_{\theta_0}^{\theta_{end}} |p_{cyl-bp}^{f_{min}-f_{max}}| \tag{2.31}$$

where (θ_0, θ_{end}) is the integration interval in the crank angle space.

In order to apply this indicators for knock recognition, a pre-selected threshold should be provided, so if the limit is not properly established, normal combustion will not be differentiated from knock.

A more accurate method can be found in [49], where a low-knocking cycle recognition method is presented. Here, the excitation produced by combustion is compared with that associated with knock by windowing the band-pass pressure. The problem with this method is if combustion and knock have similar amplitudes or location in CAD, the method is not able to differentiate them. This can be crucial for knock recognition in new combustion modes [50].

2.4.2 Knock sensor based

Sensing vibrations caused by knock is the most widespread method for knock recognition in automotive industry [51]. The mechanical vibrations is transformed into an electrical signal by a piezoelectric element. This signal contain complex information, and it is difficult to detect low knock [52].

Several works have been developed for vibration signal processing and knock recognition: traditional frequency analysis such as Short Time Fourier Transform (STFT) [53, 54], Empirical Mode Decomposition (EMD) [55, 56], or Wavelet transform [57].

A similar IMPO and MAPO knock index definitions for vibration signal are proposed in [52] and [58] respectively, where the Integral of Modulus of Accelerometer Oscillations (IMAO) is defined as:

$$IMAO = \int_{\theta_0}^{\theta_{end}} |K_{s-bp}^{f_{min}-f_{max}}| \tag{2.32}$$

where K_{s-bp} is the band-pass knock sensor signal. And The maximum amplitude of knock sensor oscillating signal (KS) is defined as:

$$KS = max(|K_{s-bp}^{f_{min}-f_{max}}|) \tag{2.33}$$

Both, KS and IMAO are compared with MAPO and IMPO respectively in Figure 2.8 over 5000 cycles in SI combustion, in hatched line a linear model between both indexes is represented.

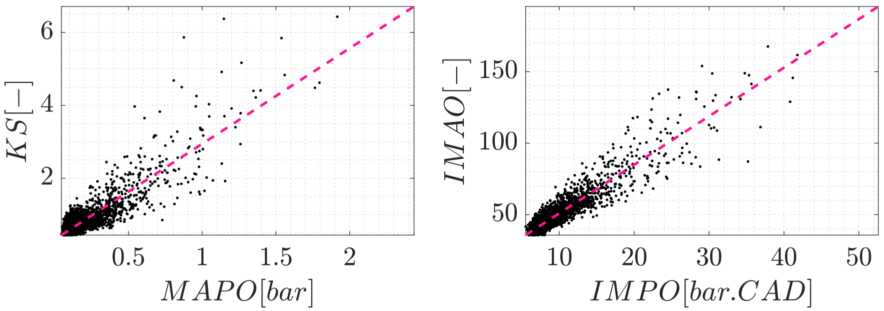

Figure 2.8: *In-cylinder pressure index compared with knock sensor. Left: MAPO and KS ($R^2 = 0.74$). Right: IMPO and IMAO ($R^2 = 0.85$).*

As can be seen in Figure 2.8, both knock sensor based method show a linear relation with the corresponding in-cylinder pressure indicators. But for the case of IMAO index, R^2 value is higher, being a stronger linear dependence.

2.4.3 Knock control

Spark advance is often controlled by look up tables stored at the ECU. These look up tables are initially calibrated for all the engine map operating points [59]. The main disadvantage with this control strategy is the absence of feedback information, since knock phenomena is influenced by the operating condition, hence a CL control is usually necessary [60]. One of the most employed feedback signal is vibration measurement, but as discussed above this method lacks precision.

Regarding CL strategies, two groups can be identified: model-based controls and stochastic controls [49]. The former tend to predict the SA of knock onset, while the latter group aim to keep knock probability below a desired value by controlling the SA. The most extensively knock controller employed in literature is the conventional deterministic strategy [61], consists on advancing the SA by a quantity K_{adv} in order to achieve higher efficiency, and retard a higher quantity K_{ret} when a knock is recognized. The strategy can be expressed as:

$$SA^{k}_{conv} = \begin{cases} SA^{k-1}_{conv} - K_{ret} & if \quad knock \\ SA^{ki-1}_{conv} + K_{adv} & otherwise \end{cases} \tag{2.34}$$

where k is the cycle number. K_{adv} and K_{ret} are the controller gains, which are associated by the knock probability, such as:

$$K_{ret} = \frac{1 - p_{th}}{p_{th}} K_{adv} \tag{2.35}$$

Higher values of K_{adv} permits the controller to achieve the optimal SA faster, but the variability of the SA will be also higher. Because its easy implementation, this strategy is extensively used in industry applications, but the issue with this strategy is high variance associated with the SA, and hence high variability on IMEP.

Other stochastic methods use the likelihood ratio to control the SA. In [62], the controller gains are scaled by the likelihood ratio between the observation and the desired knock probability. In [63], knock probability estimation is conducted by a beta distribution and the likelihood ratio test is used adjust the SA. Despite stochastic methods for SA control exhibit good results in steady operating conditions, during transient have a delayed response due to the estimation of statical properties of knock phenomena [64,65].

The objective of model-based knock control strategies is to predict the SA of knock onset. Some strategies makes uses of physical models, as for example the auto-ignition prediction model presented in [66]. Other strategies can be map based models, which are easily calibrated, however these methods are not flexible, and can lead to explore dangerous SA zones [67]. In order to cope this issue, map learning techniques have been developed recently [68,69]. But these methodologies need a prior calibration and the probability set is around 1%, what means that under transient conditions a large number of cycles are necessary to achieve the 1 % with adequate precision. This can be solved by working with a low-knocking cycle recognition method, in order to update faster the models.

2.5 Conclusions

From in-cylinder pressure and knock sensor signals different combustion parameters can be estimated by combining them with the instantaneous volume, which is obtained from the crank angle evolution. This information can be used as an input for closed-loop controls or control oriented combustion models, such as knock recognition, in-cylinder pressure models, in order to control variables like the spark advance, the variable valve timing, among others.

References

[1] Jia Libin, Naber Jeffrey D and Blough Jason R. “Review of sensing methodologies for estimation of combustion metrics”. *Journal of Combustion*, Vol. 2016, 2016. (cited in pp. 18, 27, and 28)

[2] Payri F, Broatch A, Tormos B and Marant V. “New methodology for in-cylinder pressure analysis in direct injection diesel engines—application to combustion noise”. *Measurement Science and Technology*, Vol. 16 n^o 2, pp. 540, 2005. (cited in p. 18)

[3] Maurya Rakesh Kumar. “In-cylinder pressure measurement in reciprocating engines”. In *Reciprocating Engine Combustion Diagnostics*, pp. 37–121. Springer, 2019. (cited in p. 18)

[4] Taglialatela F, Cesario N, Porto M, Merola SS, Sementa P and Vaglieco BM. “Use of Accelerometers for spark advance control of SI engines”. *SAE International Journal of Engines*, Vol. 2 n^o 1, pp. 971–981, 2009. (cited in pp. 18 and 28)

[5] Finesso Roberto, Hardy Gilles, Mancarella Alessandro, Marello Omar, Mittica Antonio and Spessa Ezio. “Real-time simulation of torque and nitrogen oxide emissions in an 11.0 L heavy-duty diesel engine for model-based combustion control”. *Energies*, Vol. 12 n^o 3, pp. 460, 2019. (cited in p. 18)

[6] Caton Jerald A. “The thermodynamics of internal combustion engines: examples of insights”. *Inventions*, Vol. 3 n^o 2, pp. 33, 2018. (cited in p. 19)

[7] Heywood John B. *Internal combustion engine fundamentals*. McGraw-Hill Education, 2018. (cited in pp. 19, 26, 64, 66, 90, and 186)

[8] Bares Moreno Pau. *In-cylinder pressure resonance analysis for trapped mass estimation in automotive engines*. PhD Thesis, Universitat Politècnica de València, 2017. (cited in pp. 19, 115, and 122)

[9] Lapuerta Magin, Armas Oy and Hernández JJ. “Diagnosis of DI Diesel combustion from in-cylinder pressure signal by estimation of mean thermodynamic properties of the gas”. *Applied Thermal Engineering*, Vol. 19 n^o 5, pp. 513–529, 1999. (cited in pp. 22 and 116)

[10] Ceviz MA and Kaymaz I. “Temperature and air–fuel ratio dependent specific heat ratio functions for lean burned and unburned mixture”. *Energy Conversion and Management*, Vol. 46 n^o 15-16, pp. 2387–2404, 2005. (cited in p. 22)

[11] Gatowski JA, Balles En N, Chun Kwang Min, Nelson FE, Ekchian JA and Heywood John B. “Heat release analysis of engine pressure data”. *SAE Transactions*, pp. 961–977, 1984. (cited in p. 22)

[12] Egnell R. “Combustion diagnostics by means of multizone heat release analysis and NO calculation”. *SAE Technical Papers*, 1998. (cited in p. 23)

[13] Woschni G. “A universally applicable equation for the instantaneous heat transfer coefficient in the internal combustion engine”. *SAE Technical Papers*, 1967. (cited in p. 23)

[14] Guardiola Carlos, Olmeda P, Pla B and Bares P. “In-cylinder pressure based model for exhaust temperature estimation in internal combustion engines”. *Applied Thermal Engineering*, Vol. 115, pp. 212–220, 2017. (cited in p. 24)

[15] Vibe Ivan I and Meißner Franz. *Brennverlauf und kreisprozess von verbrennungsmotoren*. Verlag Technik, 1970. (cited in p. 25)

[16] Giglio V., Iorio B., Police G. and Rispoli N. “In-cylinder Pressure Measurement for Control and Diagnostics in Spark Ignition Engines”. *SAE Technical Papers*, 2005. (cited in p. 25)

[17] Brunt M. F. J. and Emtage A. L. “Evaluation of burn rate routines and analysis errors”. *SAE Technical Papers*, 1997. (cited in p. 25)

[18] Rugland Christian and Stenlaas Ola. “Knock Sensor Based Virtual Cylinder Pressure Sensor”. Technical report, SAE Technical Paper, 2019. (cited in p. 27)

[19] Narayan S, Milojevic Sasa and Gupta Vipul. “Combustion monitoring in engines using accelerometer signals”. *Journal of Vibroengineering*, Vol. 21 n^o 6, pp. 1552–1563, 2019. (cited in p. 27)

[20] Ponti Fabrizio, Ravaglioli Vittorio, Serra Gabriele and Stola Federico. “Instantaneous engine speed measurement and processing for MFB50 evaluation”. *SAE International Journal of Engines*, Vol. 2 n^o 2, pp. 235–244, 2010. (cited in p. 27)

[21] Mocanu Florin and Taraza Dinu. “Estimation of main combustion parameters from the measured instantaneous crankshaft speed”. Technical report, SAE Technical Paper, 2013. (cited in p. 27)

[22] Tong Qiang, Xie Hui, Song Kang and Zou Dong. “A Control-Oriented Engine Torque Online Estimation Approach for Gasoline Engines Based on In-Cycle Crankshaft Speed Dynamics”. *Energies*, Vol. 12 n^o 24, pp. 4683, 2019. (cited in p. 27)

[23] Hellring Magnus and Holmberg Ulf. “An ion current based peak-finding algorithm for pressure peak position estimation”. Technical report, SAE Technical Paper, 2000. (cited in p. 27)

[24] Yoshiyama Sadami, Tomita Eiji and Hamamoto Yoshisuke. “Fundamental study on combustion diagnostics using a spark plug as ion probe”. Technical report, SAE Technical Paper, 2000. (cited in p. 27)

[25] Jiang J, Gu Fengshou, Gennish R, Moore DJ, Harris G and Ball AD. “Monitoring of diesel engine combustions based on the acoustic source characterisation of the exhaust system”. *Mechanical Systems and Signal Processing*, Vol. 22 n^o 6, pp. 1465–1480, 2008. (cited in p. 27)

[26] Gu Fengshou, Li W, Ball AD and Leung AYT. “The condition monitoring of diesel engines using acoustic measurements part 1: acoustic characteristics of the engine and representation of the acoustic signals”. Technical report, SAE Technical Paper, 2000. (cited in p. 27)

[27] Ponti Fabrizio, Ravaglioli Vittorio, Moro Davide and Serra Gabriele. “MFB50 on-board estimation methodology for combustion control”. *Control Engineering Practice*, Vol. 21 n^o 12, pp. 1821–1829, 2013. (cited in p. 27)

[28] Ponti Fabrizio, Ravaglioli Vittorio and De Cesare Matteo. “Development of a methodology for engine performance investigation through double crankshaft speed measurement”. *Journal of Engineering for Gas Turbines and Power*, Vol. 138 n^o 10, 2016. (cited in p. 27)

[29] Saraswati Samir and Chand Satish. "Reconstruction of cylinder pressure for SI engine using recurrent neural network". *Neural Computing and Applications*, Vol. 19 n^o 6, pp. 935–944, 2010. (cited in p. 27)

[30] Arnone L, Manelli S, Chiatti G and Chiavola O. "In-cylinder pressure analysis through accelerometer signal processing for diesel engine combustion optimization". Technical report, SAE Technical Paper, 2009. (cited in p. 28)

[31] Chiavola Ornella, Chiatti Giancarlo and Recco Erasmo. "Accelerometer measurements to optimize the injection strategy". Technical report, SAE Technical Paper, 2012. (cited in p. 28)

[32] Businaro Andrea, Cavina Nicolò, Corti Enrico, Mancini Giorgio, Moro Davide, Ponti Fabrizio and Ravaglioli Vittorio. "Accelerometer Based Methodology for Combustion Parameters Estimation". *Energy Procedia*, Vol. 81, pp. 950–959, 2015. (cited in pp. 28, 29, and 71)

[33] Chiavola Ornella, Chiatti Giancarlo, Arnone Luigi and Manelli Stefano. "Combustion characterization in diesel engine via block vibration analysis". Technical report, SAE Technical Paper, 2010. (cited in p. 28)

[34] Chiatti Giancarlo, Chiavola Ornella, Recco Erasmo, Magno Agnese, Mancaruso Ezio and Vaglieco Bianca M. "Accelerometer measurement for MFB evaluation in multi-cylinder diesel engine". *Energy*, Vol. 133, pp. 843–850, 2017. (cited in p. 29)

[35] Zhen Xudong, Wang Yang, Xu Shuaiqing, Zhu Yongsheng, Tao Chengjun, Xu Tao and Song Mingzhi. "The engine knock analysis–An overview". *Applied Energy*, Vol. 92, pp. 628–636, 2012. (cited in pp. 30 and 31)

[36] Guardiola Carlos, Pla B, Bares P and Barbier A. "An analysis of the in-cylinder pressure resonance excitation in internal combustion engines". *Applied Energy*, Vol. 228, pp. 1272–1279, 2018. (cited in pp. 30 and 114)

[37] Netzer Corinna, Seidel Lars, Ravet Frederic and Mauss Fabian. "Assessment of the validity of RANS knock prediction using the resonance theory". *International Journal of Engine Research*, Vol. 21 n^o 4, pp. 610–621, 2020. (cited in p. 30)

[38] Desantes Jose Maria, Novella Ricardo, De La Morena Joaquin and others. "Achieving ultra-lean combustion using a pre-chamber spark ignition system in a rapid compression-expansion machine". Technical report, SAE Technical Paper, 2019. (cited in p. 30)

[39] Benajes J, Novella R, Gomez-Soriano J, Martinez-Hernandiz PJ, Libert C and Dabiri M. "Evaluation of the passive pre-chamber ignition concept for future high compression ratio turbocharged spark-ignition engines". *Applied Energy*, Vol. 248, pp. 576–588, 2019. (cited in pp. 8 and 30)

[40] Lagana Armando AM, Lima Leonardo L, Justo João F, Arruda Benedito A and Santos Max MD. "Identification of combustion and detonation in spark ignition engines using ion current signal". *Fuel*, Vol. 227, pp. 469–477, 2018. (cited in p. 30)

[41] Bi Fengrong, Li Xin, Liu Chunchao, Tian Congfeng, Ma Teng and Yang Xiao. "Knock detection based on the optimized variational mode decomposition". *Measurement*, Vol. 140, pp. 1–13, 2019. (cited in p. 30)

[42] Bi Fengrong, Ma Teng and Wang Xu. "Development of a novel knock characteristic detection method for gasoline engines based on wavelet-denoising and EMD decomposition". *Mechanical Systems and Signal Processing*, Vol. 117, pp. 517–536, 2019. (cited in p. 30)

[43] Shu Gequn, Pan Jiaying and Wei Haiqiao. “Analysis of onset and severity of knock in SI engine based on in-cylinder pressure oscillations”. *Applied Thermal Engineering*, Vol. 51 n^o 1-2, pp. 1297–1306, 2013. (cited in pp. 30 and 31)

[44] Galloni Enzo. “Dynamic knock detection and quantification in a spark ignition engine by means of a pressure based method”. *Energy conversion and management*, Vol. 64, pp. 256–262, 2012. (cited in p. 31)

[45] Parra Andres Felipe Sierra and Torres Adalberto Gabriel Diaz. “Improvement of a knock model for natural gas SI engines through heat transfer evaluation”. *International Journal on Interactive Design and Manufacturing (IJIDeM)*, Vol. 12 n^o 4, pp. 1423–1433, 2018. (cited in p. 31)

[46] Park Sung Tae and Yang Jinguo. “Engine knock detection based on wavelet transform”. In *Proceedings. The 8th Russian-Korean International Symposium on Science and Technology, 2004. KORUS 2004.*, volume 3, pp. 80–83. IEEE, 2004. (cited in p. 31)

[47] Gerardin Rodrigo Ceccatto, Alves Marco Aurélio Faleiros, de França Arruda Jose Roberto and others. “Analysis of Spark Ignition Engine Knock Signals using Fourier and Discrete Wavelet Transform”. Technical report, SAE Technical Paper, 2009. (cited in p. 31)

[48] Peyton Jones James C, Spelina Jill M and Frey Jesse. “Optimizing knock thresholds for improved knock control”. *International Journal of Engine Research*, Vol. 15 n^o 1, pp. 123–132, 2014. (cited in p. 31)

[49] Bares Pau, Selmanaj DONALD, Guardiola Carlos and Onder Christopher. “A new knock event definition for knock detection and control optimization”. *Applied Thermal Engineering*, Vol. 131, pp. 80–88, 2018. (cited in pp. 31, 33, 148, and 153)

[50] Attard William P, Blaxill Hugh, Anderson Eric K and Litke Paul. “Knock limit extension with a gasoline fueled pre-chamber jet igniter in a modern vehicle powertrain”. *SAE International Journal of Engines*, Vol. 5 n^o 3, pp. 1201–1215, 2012. (cited in pp. 32 and 114)

[51] Dues Steven M, Adams Joseph M and Shinkle George A. “Combustion knock sensing: Sensor selection and application issues”. *SAE transactions*, pp. 1192–1202, 1990. (cited in p. 32)

[52] Siano Daniela, Bozza Fabio, D’Agostino Danilo and Panza Maria Antonietta. “The use of vibrational signals for on-board knock diagnostics supported by in-cylinder pressure analyses”. Technical report, SAE Technical Paper, 2014. (cited in p. 32)

[53] Zadnik Martin, Vincent François, Vingerhoeds R and Galtier Frederic. “SI engine knock detection method robust to resonance frequency changes”. Technical report, SAE Technical Paper, 2007. (cited in p. 32)

[54] Akimoto Kenji, Komatsu Hirotaka and Kurauchi Atsushi. “Development of pattern recognition knock detection system using short-time Fourier transform”. *IFAC Proceedings Volumes*, Vol. 46 n^o 21, pp. 366–371, 2013. (cited in p. 32)

[55] Moshrefi Amirhossein. “Weighted-EMD to Increase Knock Detection Accuracy”. (cited in p. 32)

[56] Li Ning, Yang Jianguo, Zhou Rui and Liang Caiping. “Determination of knock characteristics in spark ignition engines: An approach based on ensemble empirical mode decomposition”. *Measurement Science and Technology*, Vol. 27 n^o 4, pp. 045109, 2016. (cited in p. 32)

[57] Kurihara N, Suzuki J, Shirayama Y, Borg J and Oho S. "An accurate method of knock detection using wavelet transform for spark-ignition (SI) engine". In *14th International Congress on Sound and Vibration*, 2007. (cited in p. 32)

[58] Chao Yuedong, Lu Haifeng, Dong Guangyu, Deng Jun and Li Liguang. "Abnormal Combustion Diagnosis and Combustion Period Based Phase Estimation with a Modified Form Tandem Ion Current Detection System on SI Gasoline Engines". *Energy Procedia*, Vol. 158, pp. 2098–2105, 2019. (cited in p. 32)

[59] Corti Enrico, Forte Claudio, Mancini Giorgio and Moro Davide. "Automatic combustion phase calibration with extremum seeking approach". *Journal of Engineering for Gas Turbines and Power*, Vol. 136 n^o 9, pp. 091402, 2014. (cited in pp. 33 and 46)

[60] Shen Tielong, Kang Mingxin, Gao Jinwu, Zhang Jiangyan and Wu Yuhu. "Challenges and solutions in automotive powertrain systems". *Journal of Control and Decision*, Vol. 5 n^o 1, pp. 61–93, 2018. (cited in p. 33)

[61] Jones James C Peyton, Frey Jesse and Shayestehmanesh Saeed. "Stochastic simulation and performance analysis of classical knock control algorithms". *IEEE Transactions on Control Systems Technology*, Vol. 25 n^o 4, pp. 1307–1317, 2016. (cited in p. 33)

[62] Jones James C Peyton, Shayestehmanesh Saeed and Frey Jesse. "A Bayesian knock event controller". *IEEE Transactions on Control Systems Technology*, Vol. 28 n^o 5, pp. 1627–1637, 2019. (cited in p. 34)

[63] Zhao Kai, Wu Yuhu and Shen Tielong. "Stochastic Knock Control with Beta Distribution Learning for Gasoline Engines". *IFAC-PapersOnLine*, Vol. 51 n^o 31, pp. 125–130, 2018. (cited in p. 34)

[64] Thomasson Andreas, Shi Haoyun, Lindell Tobias, Eriksson Lars, Shen Tielong and Jones James C Peyton. "Experimental validation of a likelihood-based stochastic knock controller". *IEEE Transactions on Control Systems Technology*, Vol. 24 n^o 4, pp. 1407–1418, 2015. (cited in p. 34)

[65] Selmanaj Donald, Panzani Giulio, Van Dooren Stijn, Rosgren Jonatan and Onder Christopher. "Adaptive and unconventional strategies for engine knock control". *IEEE Transactions on Control Systems Technology*, Vol. 27 n^o 4, pp. 1838–1845, 2018. (cited in p. 34)

[66] Livengood JC and others. "Correlation of autoignition phenomena in internal combustion engines and rapid compression machines". 1955. (cited in p. 34)

[67] Corti Enrico and Forte Claudio. "A statistical approach to spark advance mapping". *Journal of Engineering for Gas Turbines and Power*, Vol. 132 n^o 8, 2010. (cited in p. 34)

[68] Zhang Yahui, Shen Xun and Shen Tielong. "A survey on online learning and optimization for spark advance control of SI engines". *Science China Information Sciences*, Vol. 61 n^o 7, pp. 70201, 2018. (cited in p. 34)

[69] Zhang Yahui, Shen Xun, Wu Yuhu and Shen Tielong. "On-board knock probability map learning–based spark advance control for combustion engines". *International Journal of Engine Research*, Vol. 20 n^o 10, pp. 1073–1088, 2019. (cited in pp. 10, 34, 188, and 190)

CHAPTER 3

System set-up

Contents

3.1 Introduction

Several engines with different combustion modes were used in this dissertation. During the first part of the chapter, the experimental facilities and acquisition system of each engine are described. After, the main characteristics of experimental tests are summarized, for steady and transient conditions.

3.2 Experimental set-up

3.2.1 Engines

In this dissertation, three engines, one commercial SI engines, and two research engines working with new combustion concepts, i.e. Reactivity Controlled Compression Ignited (RCCI) and TJI, are used. Each engine is identified with a letter, from A to C, with which it will be labeled in future sections.

Table 3.1: *Main characteristics of engines.*

	A	B	C
Combustion mode	SI	TJI / SI	RCCI
Cylinders [-]	4	1	6
Bore length [mm]	72	80	110
Stroke length [mm]	81.2	80.5	135
Rod length [mm]	128	133.8	212.5
Compression ratio	10.6:1	13.4:1	12.2:1
V_{dis} [cc]	1300	404	7700
Injection	GDI	PFI	PFI/DI

Engine A

A four cylinder Euro 6 SI production engine fueled with gasoline was used to analyze and characterize in-cylinder pressure evolution during normal and knocking combustion. The engine is equipped with Variable Geometry Turbocharger (VGT), Variable Valve Timing (VVT) system, and direct gasoline injection (GDI) system.

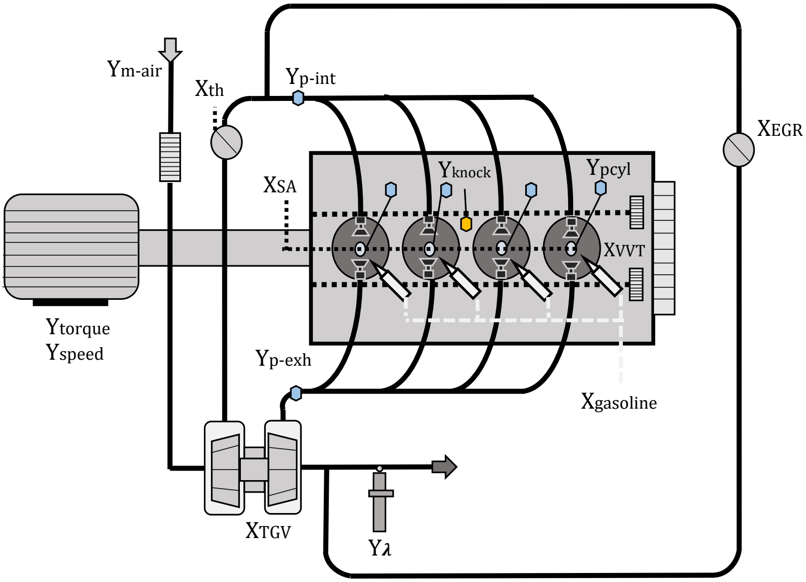

Figure 3.1: *Experimental set-up of Engine A: Control variables (X) and sensors (Y).*

The control of the test bench was performed by AVL-PUMA software, allowing speed (Y_{speed}) and engine torque (Y_{torque}) control by the use of a dynamo-metric brake. A prototyping system from National Instruments (PXI) was used to acquire, process and control the engine. Intake and exhaust pressure (Y_{p-int} and Y_{p-exh}) was measured by a piezo-resistive pressure sensor, a fuel balance was used for fuel mass flow metering, the air-to-fuel ratio was estimated from a lambda sensor at the exhaust (Y_{λ}), and a knock sensor was mounted in the engine block (Y_{knock}). In-cylinder pressure was collected with a sampling accuracy of 0.2 CAD with a spark-plug integrated pressure sensors (Y_{pcyl}). The SA (X_{SA}), VVT system (X_{VVV}), gasoline mass ($Y_{gasoline}$) and throttle valve (X_{th}) were controlled by ECU by-pass, while the VGT position (X_{VGT}) was directly controlled with a Field Programmable Gate Array (FPGA) full pass system.

Regarding the VVT system, it is a hydraulic system and enables to advance or delay the camshaft timing in a range of 40 for both intake and exhaust sides, while keeping constant the valve lift and opening duration. In Figure 3.2, the VVT lift law for intake and exhaust are shown.

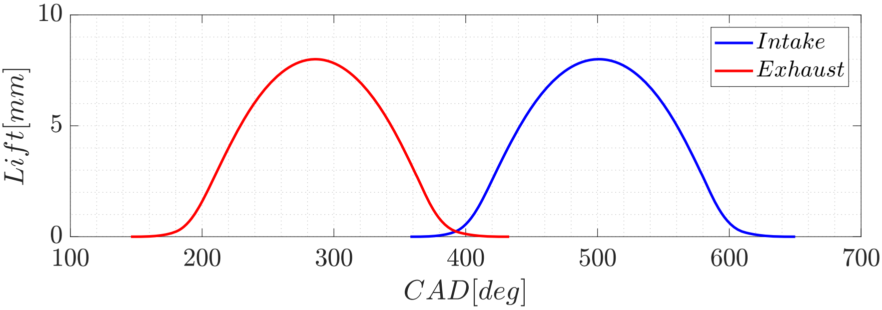

Figure 3.2: *VVT lift law.*

Engine B

Engine B is a single cylinder research version of a 4-stroke SI engine modified to operated in SI and TJI combustion. The boost pressure was provided by an external compressor, the engine is equipped with intake and exhaust manifold piezo-resistive pressure sensors, an in-cylinder pressure sensor with a resolution of 0.5 CAD per sample. The scheme of the experimental set-up of engine B is shown in Figure 3.12.

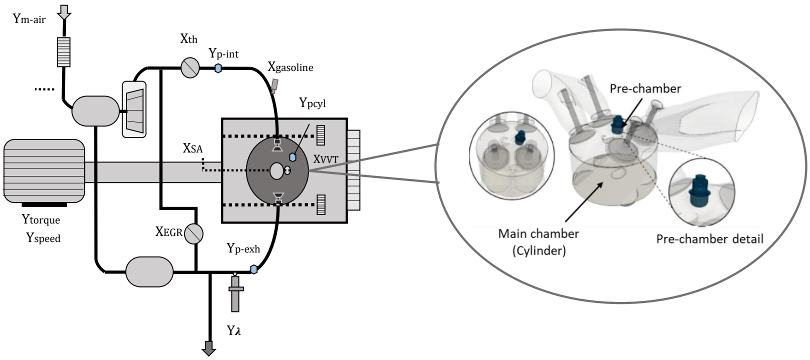

Figure 3.3: *Experimental set-up of Engine B.*

As can be seen in Figure 3.3, the conventional spark plug and the prechamber are located at the cylinder head, facilitating the change of operation between SI and TJI combustion.

Engine C

Engine C is a six cylinder heavy-duty diesel engine, modified to run in dual-fuel combustion by adding a port fuel injector (PFI) at each cylinder

($Y_{gasoline}$). The engine is equipped with VGT (X_{TGV}), with intake and exhaust piezo-resistive pressure sensors, and in-cylinder pressure sensors with a sampling frequency function of the engine speed using a research encoder set with a resolution of 0.2 CAD per sample. Figure 3.4 shows the scheme of the experimental set-up of engine C.

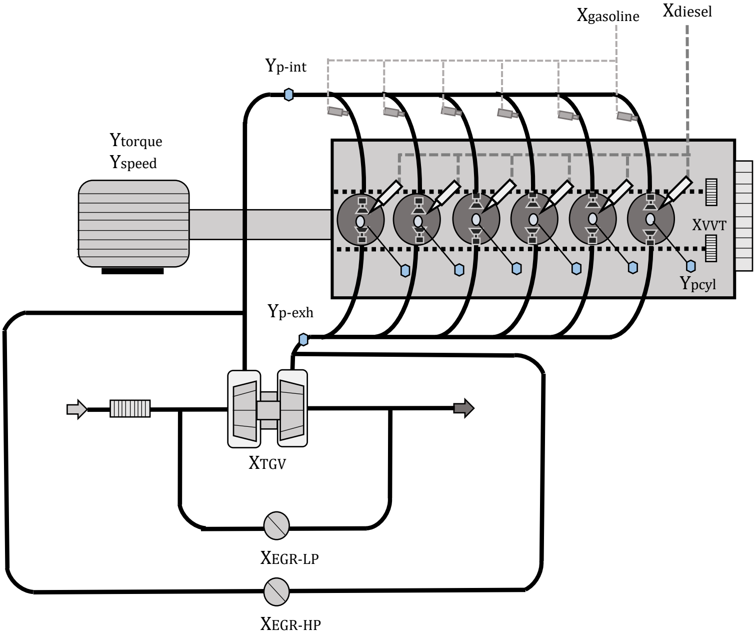

Figure 3.4: *Experimental set-up of Engine C.*

3.2.2 Acquisition and control structure

Regarding the engine control approach for engine testing, two main alternatives can be found, full-pass and by-pass. In figure 3.5, a general scheme of these control and acquisition structures are shown.

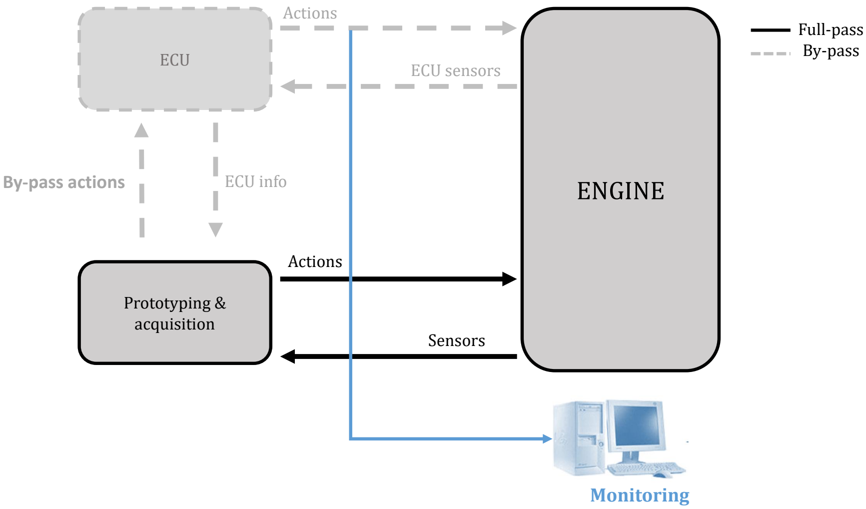

Figure 3.5: *General scheme for sensor acquisition and engine control.*

- **By-pass acquisition and control:** Usually, in production engines, the ECU controls the engine by open-loop 2D tables in function of the intake pressure and engine speed previusly calibrated [1]. These OL tables in some cases are combined with grey box models [2, 3], or with low-complexity feed-back controls [4]. The bypass approach consists of replacing ECU control signals by their equivalent implemented in the prototyping system.

  In order to send and receive information from/to the ECU, an interface system is required. The interface system requires of a representation of the ECU structure, which is included in an ASAP2 description file (a2l file), and a detailed information of the calibration of the engine, which is in a hexadecimal source file (hex) file [5].

- **Full-pass acquisition and control:** For some applications in research engines field, the ECU can be total or partially replaced by directly sending the information to the actuators. These information is send by a prototyping and acquisition systems, such as real-time PXI (programmed with Labview).

3.2.2.1 Engine A acquisition and control layout

Engine A acquisition and control layout is shown in Figure 3.6. The engine was controlled with a real-time system National Instrument (NI) PXI-8110 embedded controller with a 2.26 GHz quad-core processor. A NI-9759 module was used with a PXI 7813R for programming in FPGA the full-pass control of the VGT and EGR valves.

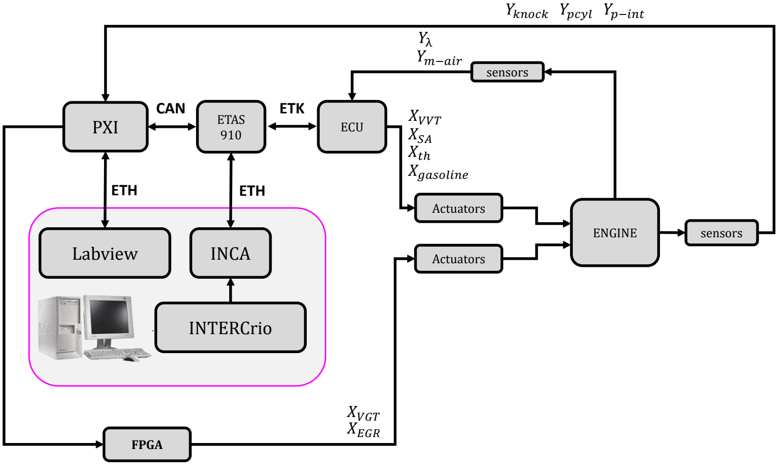

Figure 3.6: *Acquisition and control layout of engine A.*

Three ECU control variables are used in this work: SA, VVT, and throttle, which are controlled by modifying the ECU commands through Ethernet by pass.

3.2.2.2 Engine B acquisition and control layout

Engine B acquisition and control layout is shown in Figure 3.7. The control of the engine has been implemented with a FPGA chasis and modules for analog acquisition up to 16kHz, and the control of port fuel injection, spark, throttle and EGR valves control. A parallel system has been used for high frequency acquisition and pressure processing (PXI), which allows an acquisition up to 1 MHz and computation capabilities of a 3.06 GHz, Quad-Core PXI Controller in real time. Both systems, FPGA and PXI, are connected by Ethernet and monitored by an external computer.

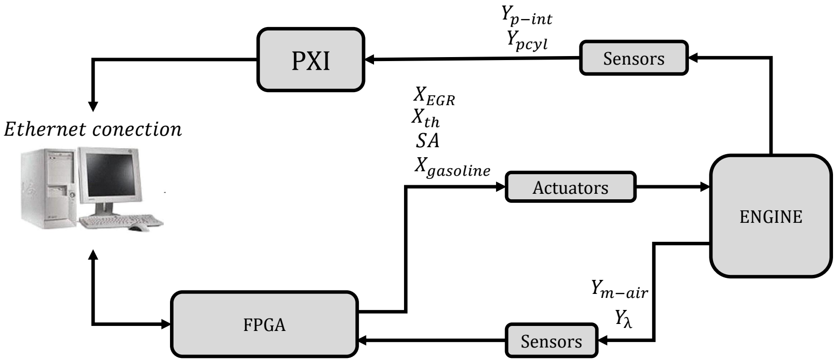

Figure 3.7: *Acquisition and control layout of engine B.*

3.2.2.3 Engine C acquisition and control layout

Engine C acquisition and control layout is shown in Figure 3.8. The injection settings control at each cylinder, the Duration Of Injection (DOI) and the Start Of Injection (SOI), was carried out using a FPGA chassis compactRIO and modules of NI. The VGT is controlled by the ECU, and both low pressure and high pressure, EGR valves are controlled by the Controller Area Network (CAN). The acquisition of the in-cylinders pressure and intake pressure different signals was handled by a 16 analog channels acquisition card connected to the real-time controller (PXI), which was used to process and save the cycle-to-cycle data.

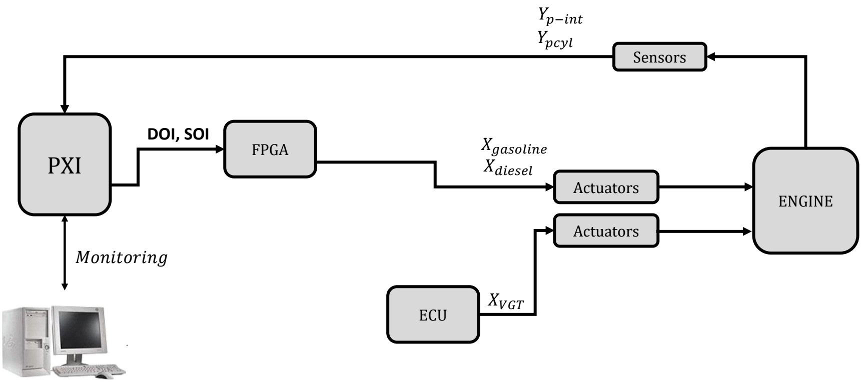

Figure 3.8: General scheme control structure of engine C.

Main characteristics of controllers and sensors for engines A, B and C are summarized in Table 3.2.

Table 3.2: *Main characteristics of acquisition and control systems.*

Engine	A	B	C
Make Y_{pcyl}	AVL	Kistler	Kistler
Model Y_{pcyl}	ZI33	6061B	6125C
Make Y_{knock}	Bosch	-	-
Model Y_{knock}	KS4-R2	-	-
Sampling accuracy Y_{pcyl} [CAD]	0.2	0.5	0.2
f_{low} [Hz]	4500	4000	2500
f_{high} [Hz]	20000	15000	15000
Make Y_{p-int}	Kistler		Kistler
Model Y_{p-int}	4045A5		4045A10
Sampling accuracy Y_{p-int} [CAD]	0.2	0.5	0.2
Make Y_{p-exh}	Kistler	-	-
Model Y_{p-exh}	4045A5		-
Sampling accuracy Y_{p-exh} [CAD]	0.2	0.5	0.2
Amplifier	-	-	-
Controller	PXI-8110	PXIe8133	PXIe-8135
Acquisition module	PXI-6123 / PXI-6251		PXIe-6358
FPGA controller	cRIO 9114	PXI cRIO 9024	PXI cRIO 9024
FPGA module	NI-9759 / PXI 7813R		NI 9152/ NI 9751/ NI 9758
CAN interface	PXI-8513	-	PXI-8512

3.2.2.4 Real time combustion analysis

The real-time combustion analysis computations was run in LabVIEW RT inside timed loops on the real-time system. The in-cylinder pressure was measured with piezo-electric transducers, where the signal given by these sensors is as:

$$p_{cyl} = C_s p_c + \Delta p \tag{3.1}$$

where p_{cyl} is the sensor signal, p_c the actual pressure, C_s the sensor conversion factor and Δp the sensor offset.

In Figure 3.9 the in cylinder pressure processing scheme for the different parameters calculation is shown.

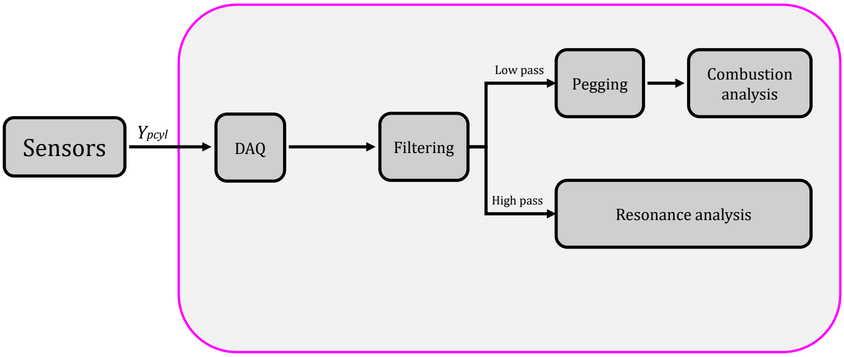

Figure 3.9: *In-cylinder pressure acquisition and processing.*

The in-cylinder pressure analog signal from sensors (Y_{cyl}) is digitized by DAQmx module. Then, the in-cylinder pressure is filtered in order to eliminate non-desired components: a low pass filter is set in order to extract information from combustion and a band pass filter used for resonance analysis. The cutoff frequency was selected according to the resonant frequency of the first circumferential mode in a cylindrical volume such as [6]

$$f_{low-pass}^{cut-off} = a\frac{B_{10}}{\pi D} \tag{3.2}$$

where a is the sound speed, B_{10} Bessel constant of the first circumferential mode, and D the engine bore.

After, the low-pass in-cylinder pressure pegging was done using the intake pressure at IVC. The in-cylinder pressure signal is collected at constant angular sampling by an external digital signal provided by an encoder.

3.3 Experimental tests

In this section, experimental tests conducted on the engines A, B and C will be described. Various test campaigns were performed to calibrate models, and to analyze resonance excitation within the combustion chamber and also the response of the control applications. Experimental tests are divided in two parts: in the first part the steady test carried out on each engine are introduced. And in the second part, the transient tests are presented.

3.3.1 Steady tests

Each engine was used to analyze the combustion evolution and resonance excitation at different operating conditions. Steady-state test campaigns, which will be used in later sections, are explained below.

Engine A

Figure 3.10 illustrates the 14 operating conditions (OP_A), characterized by intake pressure (and hence air mass flow) and engine speed, are represented. At each steady-state operating condition, various SA settings were performed, lambda has been maintained at 1 to ensure stoichiometric conditions.

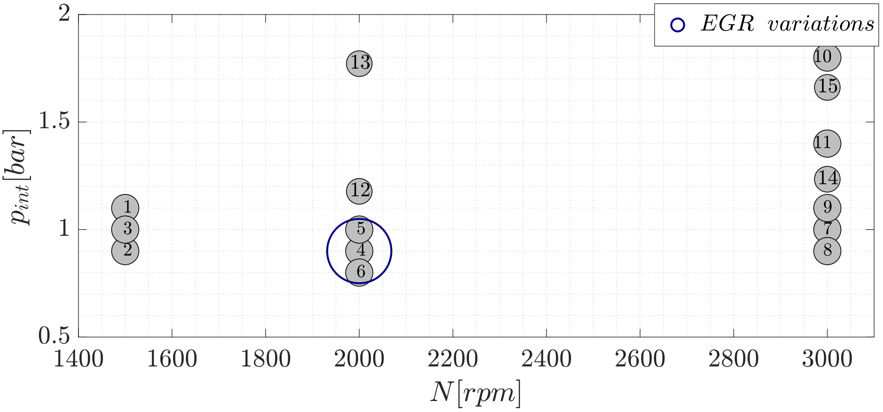

Figure 3.10: *Operating conditions tested in Engine A.*

Steady test performed in engine A were conducted without EGR, except for those cases highlighted in Figure 3.10. In Figure 3.11 the variations in SA performed at each operating condition (OP_A) are shown. Each SA step have been maintained until the number of cycles recorded was enough for knock probability estimation, ensuring in each set a minimum of 500 cycles.

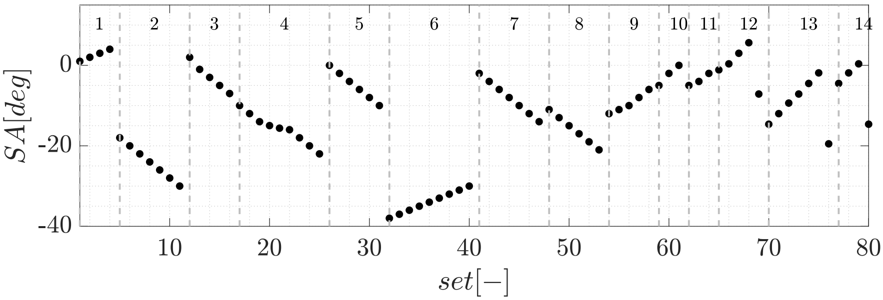

Figure 3.11: *SA variations for each operating condition tested in engine A.*

Engine B

Engine B data set was included 39 operating conditions shown in Figure 3.12 (left). Different colors have been used to highlight the fuel used for each test.

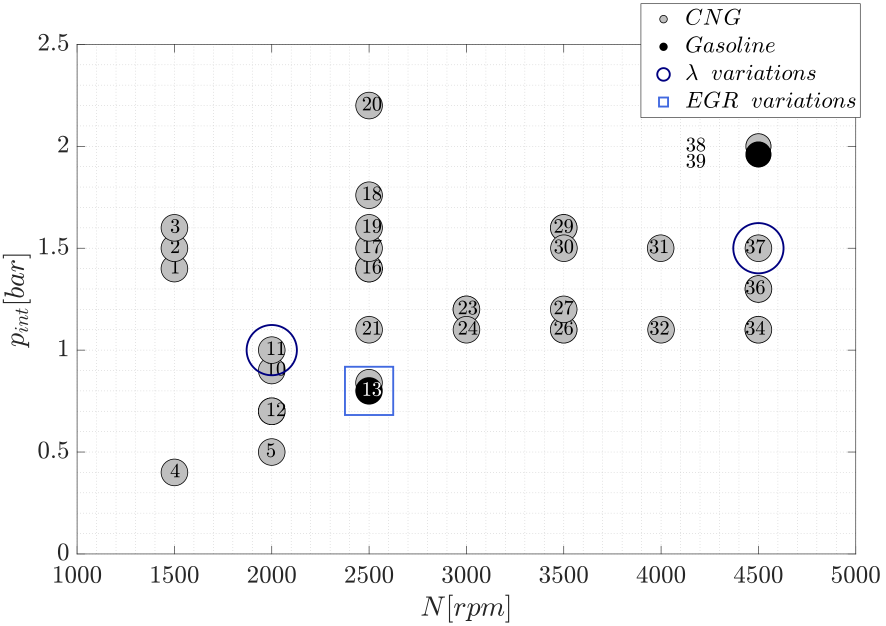

Figure 3.12: *Operating conditions tested in Engine B.*

The SA variations for each operating condition (OP_B) are represented in Figure 3.13.

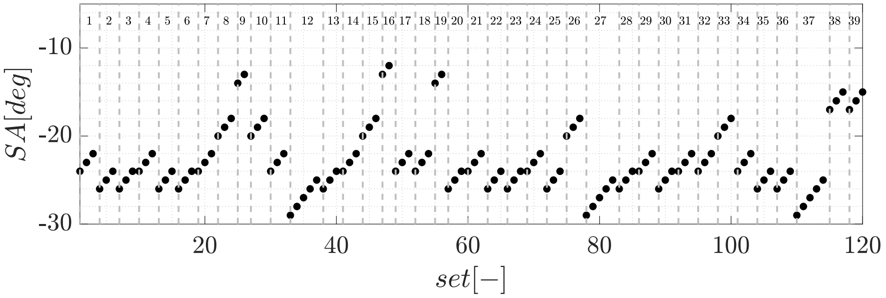

Figure 3.13: *SA variations for each operating condition tested in engine B.*

All the operating points (OP_B) were ignited with TJI combustion, and a few of them with SI combustion: 5, 38 and 19. During all steady tests lambda was maintained at stochoimetric conditions and without EGR, only at the indicated OP_B conditions variations of λ between 1 and 1.5 and EGR between 0 and 5 % were performed. Fuel Research Octane Number (RON) are shown in Table 3.4.

Engine C

Operating conditions tested in engine C are summarized in Table 3.3. Each operating condition is characterize by the speed and IMEP. For each operating condition, the EGR, SOI of pilot and main injection setting are shown.

Table 3.3: *Operation points tested in engine C.*

OP_C	N [rpm]	IMEP [bar]	SOI_{pilot}	SOI_{main}	EGR [%]
1	1200	6.28	60	50	0
2	1200	6.62	60	50	0
3	1200	6.43	40	30	0
4	1100	5.9	60	50	0
5	1200	6	60	50	0
6	1200	5.72	60	50	0
7	1200	6.84	60	50	0
8	1200	6.87	60	50	11
9	1200	5.69	60	50	0
10	1200	4.45	60	50	0
11	1200	5.19	30	15	0
12	1200	5	30	15	0
13	1200	5.1	30	15	0
14	1200	4.8	35	15	0
15	2000	3.7	21	10	54
16	2000	3.77	23	12	55
17	2000	3.2	20	10	48
18	1800	4.35	23	12	50
19	1500	4.63	22	11	46
20	2200	4.61	27	17	43
21	1500	2.9	28	16	52
22	1500	3	24	13	54
23	2200	3	28	16	48
27	1800	3.8	29	18	53

Please notice that the subindex with the engine letter and numbers are used to label every steady-state operating condition for each engine, which will be used for identifying them in future sections.

Table 3.4: *Fuel specifications for Engines A, B & C.*

Fuel	Gasoline	CNG	Diesel
RON	95	120	-

3.3.2 Transient tests

To analyze the combustion and resonance models, and control application of knock recognition and combustion model, several transient tests have been designed. Transient tests are labeled by letter T and the number of the test from 1 to 13.

3.3.2.1 Close loop knock control

In order to validate two novel detection methodologies, which will be described in Chapter 7, the conventional knock controller strategy, explained in Chapter 2, was selected. Four tests were performed, two for each novel methodology, by varying the controller gains K_{adv} and K_{ret}. These two gains are related by the knock probability (p_k), as following:

$$K_{ret} = \frac{1 - p_k}{p_k} K_{adv} \tag{3.3}$$

the time response of the controller is characterize by K_{adv}: high values allow the controller to reach the optimal value faster, but with a high SA variation and hence, higher knock amplitudes are also expected. K_{ret} is greater than K_{adv} so the SA slowly advances during non-knocking cycles, but it is rapidly retarded if a knock event is recognized.

The main characteristics of the controller at four tests are summarized in Table 3.5.

Table 3.5: *Test performed in engine A with conventional knock control.*

	MAPO		Method 1		MAPO		Method 2	
Test	T1	T2	T1	T2	T3	T4	T3	T4
$Time[s]$	600	800	600	800	600	800	600	800
$K_{adv}[CAD]$	0.01	0.02	0.01	0.02	0.01	0.02	0.01	0.02
$p[\%]$	0.6	0.6	2	2	1	1	8	8
$K_{ret}[CAD]$	1.99	3.98	0.49	0.98	0.99	1.98	0.115	0.23

3.3.2.2 Load transient

For validation purposes different throttle transients were performed. In Figure 3.14, the intake pressure and the throttle actuation are represented.

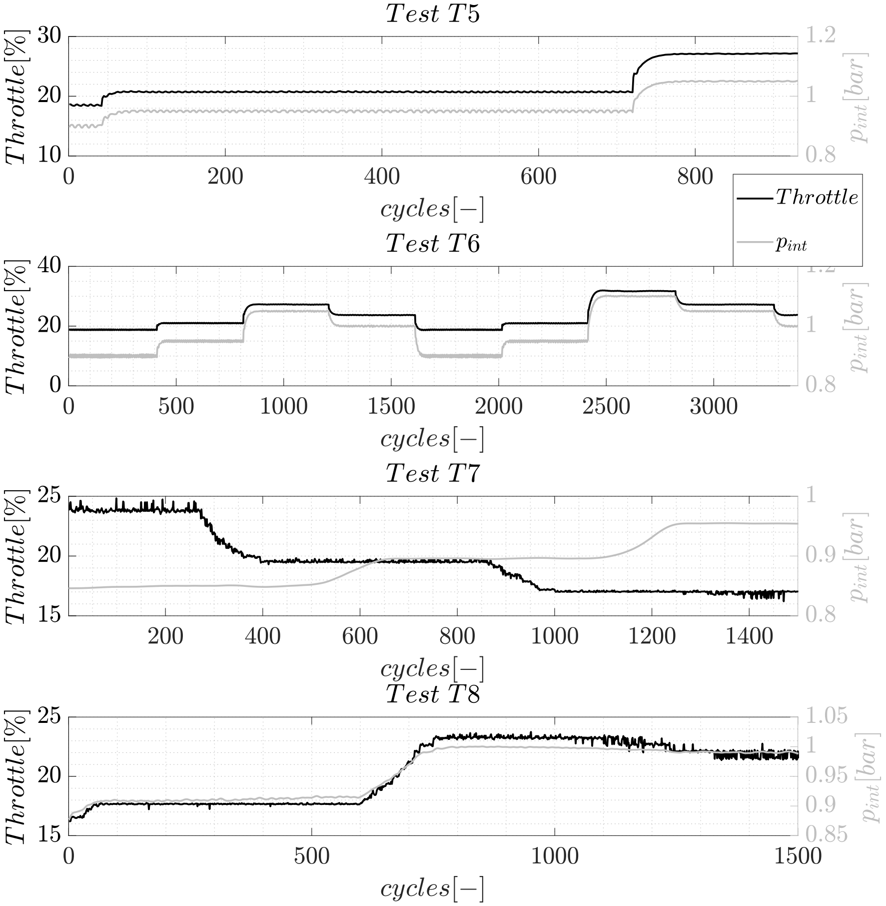

Figure 3.14: *Throttle transients performed in Engine A*

3.3.2.3 Speed transient

For validation purposes different throttle transients were performed. In Figure 3.15, the speed and intake pressure evolution are shown.

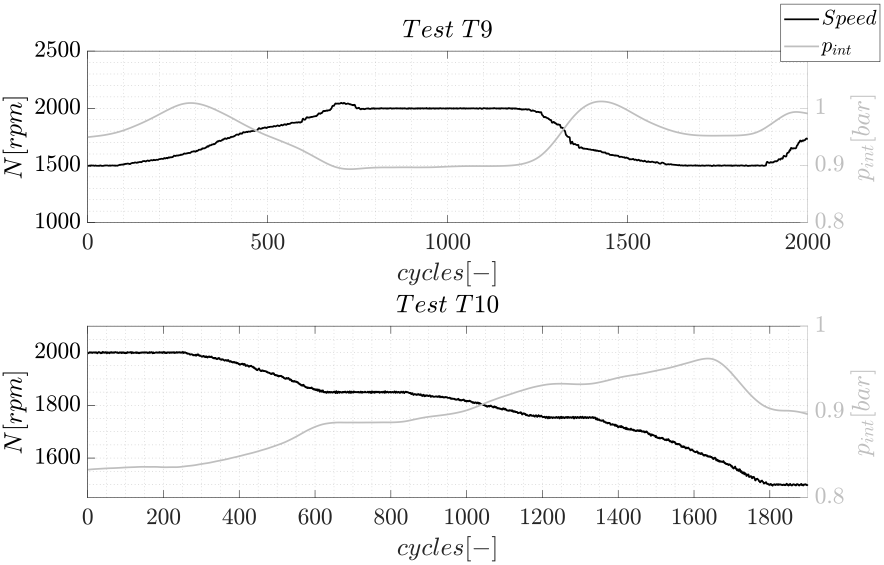

Figure 3.15: *Speed transients performed in Engine A.*

3.3.2.4 Tip in-tip out

Next, a tip-in test was performed in Engine A in order to evaluate the model dynamics. This test is shown in Figure 3.16, where the pedal demand and the intake pressure is plotted.

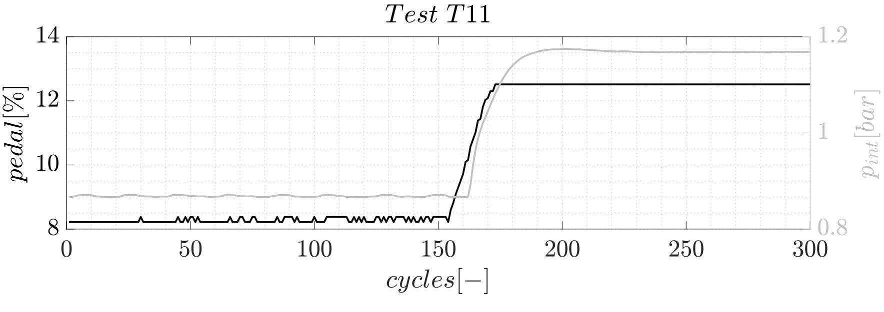

Figure 3.16: *Short tip-in test Engine A.*

3.3.2.5 Cycles

Two different transients, in which more than two control variables were changed, in order to evaluate model dynamics. First, in Figure 3.17, a transient test of 990 s has been recorded for validation purposes. The transient test consist in step variations at various conditions (different of those used for training) in order to validate the method at diverse operating conditions and in transient operation.

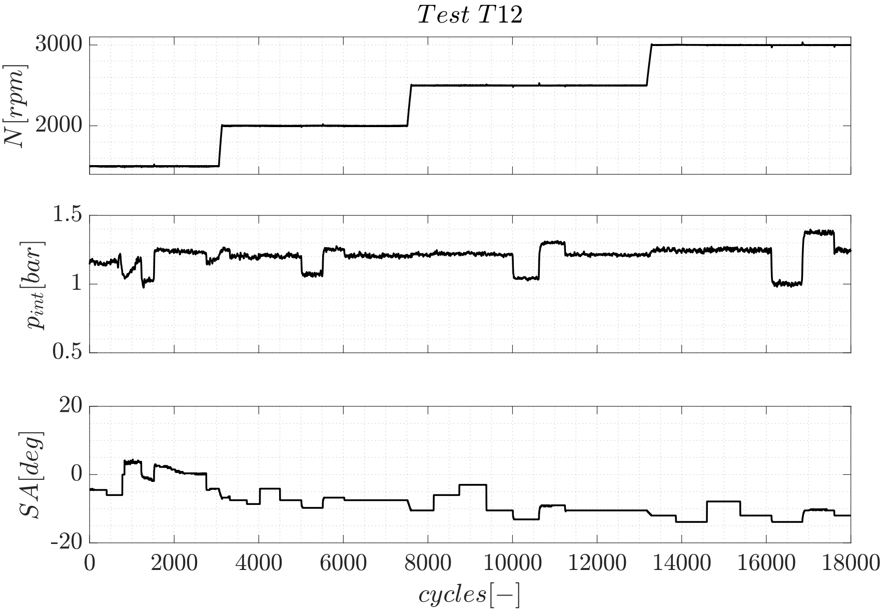

Figure 3.17: *Tip-in and tip-out test Engine A.*

Finally, a SA and throttle valve transient is performed in Engine B, with the engine running at 2500 rpm.

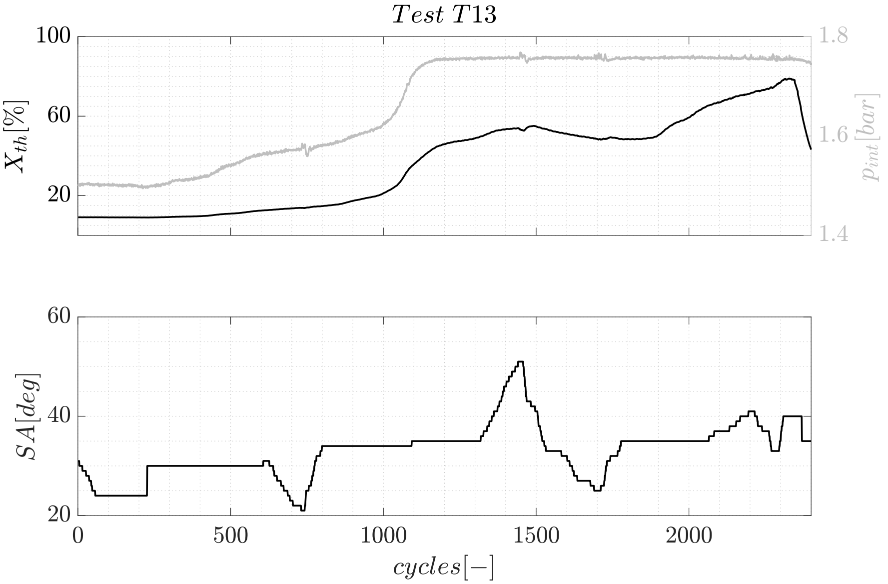

Figure 3.18: *Tip-in and tip-out test Engine A.*

References

[1] Guardiola Carlos, Pla Benjamin, Bares Pau and Stefanopoulou Anna. “Cylinder charge composition observation based on in-cylinder pressure measurement”. *Measurement*, Vol. 131, pp. 559–568, 2019. (cited in pp. 46 and 74)

[2] Gundlapally Santhosh R, Papadimitriou Iakovos, Wahiduzzaman Syed and Gu Tian. “Development of ECU capable Grey-box models from detailed models—application to a SCR reactor”. *Emission Control Science and Technology*, Vol. 2 n^o 3, pp. 124–136, 2016. (cited in p. 46)

[3] Hirsch Markus, Alberer Daniel and Del Re Luigi. “Grey-box control oriented emissions models”. *IFAC Proceedings Volumes*, Vol. 41 n^o 2, pp. 8514–8519, 2008. (cited in p. 46)

[4] Corti Enrico, Forte Claudio, Mancini Giorgio and Moro Davide. “Automatic combustion phase calibration with extremum seeking approach”. *Journal of Engineering for Gas Turbines and Power*, Vol. 136 n^o 9, pp. 091402, 2014. (cited in pp. 33 and 46)

[5] Mauss Jakob and Simons Matthias. “Chip simulation of automotive ECUs”. In *9th symposium Steuerungssysteme fur automobile Antriebe*, 2012. (cited in p. 46)

[6] Draper Charles Stark. “The physical effects of detonation in a closed cylindrical chamber”. 1935. (cited in pp. 50 and 115)

PART

III

Control oriented modeling

Chapter 4

Control oriented combustion model

Contents

4.1 Introduction

In-cylinder pressure is the most accurate variable to analyze the combustion process in IC engines, since is used to analyze the evolution of the different combustion parameters such as HRR, and it can be considered the most direct measured of the combustion evolution. These sensors can be implemented as feedback signal for CL combustion control and diagnostics. However, pressure sensors are still affected by issues such as durability and cost, which limit their application in production vehicles [1].

This chapter presents a control oriented model for SI combustion engines. The model inputs are available signals in the ECU, such as SA, air mass, intake pressure, lambda, among others, aims to predict the mean value of the combustion evolution. Additionally, in order to provide a better estimation of in-cylinder pressure, an observer is proposed by using the vibration signal in an Extended Kalman Filter (EKF).

First part of the chapter is devoted to present the combustion model. Then, with the aim of improving the model estimation, an observer design is presented. After, both, the combustion model and the model with the observer are compared. Next, an application to different fuels is examined in engine B, where the potential of the observer is analyzed. And finally, main conclusion of this chapter are discussed.

4.2 Combustion model

The combustion model presented in this section was introduced in [2]. Which consists of a quasi-stationary two-zone physic-based turbulent combustion model [3], where the laminar flame speed (S_l) and the turbulence intensity (u_t) are used to predict the MFB during combustion.

The model separates the combustion chamber in two zones during combustion: burned and un-burned zones. It assumes that the entrained mass can be modeled by the following Equation (4.1), which is later burned in a time τ according to Equation (4.2).

$$\begin{aligned}\frac{\delta m_e}{\delta t} &= \rho_{ub} A_f (u_t + S_l) && (4.1)\\ \frac{\delta m_b}{\delta t} &= \frac{m_e - m_b}{\tau} + \rho_{ub} A_f S_l && (4.2)\end{aligned}$$

where m_e represents the entrained mass, m_b the mass burnt, ρ_{ub} the density of un-burnt gases, A_f the flame front area, u_t the turbulent intensity, and S_l the laminar flame speed.

4.2.1 Combustion variables

Three parameters have a significant influence in this model: Laminar flame speed, turbulence intensity and the characteristic burning time, which will be following introduced.

Laminar flame speed: The laminar flame speed has been extracted from the semi-empirical expressions suggested in [4], such as:

$$S_l = X_1 S_{l,0}(\lambda) \left(\frac{T_{ub}}{T_{int}}\right)^{\alpha(\lambda)} \left(\frac{p_{cyl}}{p_{int}}\right)^{\epsilon(\lambda)} (1 - 2.06 RGF^{0.77}) \tag{4.3}$$

where X_1 represents a calibration factor, T_{int} and p_{int} the temperature and pressure at the inlet. The initial flame speed (S_{l0}) and the coefficients α and ϵ depends on the fuel properties, in [4] proposed $S_{l,0} = 0.281$, $\alpha = 2.129$, and $\epsilon = -0.217$, for gasoline and stoichiometric conditions ($\lambda = 1$).

Turbulence intensity: Is the main component of the flame propagation speed, which has an important impact in the burning rate. The turbulent flow is assumed isotropic in the combustion chamber, and was estimated from an expression suggested in [5], as following:

$$u_t = u_{t0} \left(\frac{\rho_{ub}}{\rho_{ub}(SOC)}\right)^{\frac{1}{3}} \tag{4.4}$$

where u_{t0} is the initial value of turbulent intensity, and can be computed as is proposed in [6]:

$$u_{t0} = X_2 \overline{u_p} \sqrt{\frac{\rho(SOC)}{\rho(IVC)}} \tag{4.5}$$

where $\overline{u_p}$ is the medium piston velocity, and X_2 is a calibration parameter.

Characteristic time (τ): is the time taken to burn-up an eddy at the laminar flame speed, and can be as expressed as suggested in [5]:

$$\tau = \frac{\lambda_m}{S_l} \tag{4.6}$$

where λ_m is the microscale length.

The microscale length can be computed from the integral length scale (L) as:

$$\frac{\lambda_m}{L} = C\sqrt{Re} \tag{4.7}$$

where Re is the Reynolds number. L can be obtained from the distortion theory [7], concluding with an expression as follows:

$$\lambda_m = X_3 \sqrt{\frac{\mu h_c(SOC)}{u_{t0}}} \left(\rho_{ub}(SA)\right)^{\frac{1}{3}} \left(\frac{1}{\rho_{ub}}\right)^{\frac{5}{6}} \tag{4.8}$$

where X_3 is a constant particular of each engine, and μ is the dynamic viscosity. μ is assumed to be the viscosity of the air for un-burned gases, following:

$$\mu = (3.3.10^{-7}) T_{ub}^{0.7} \tag{4.9}$$

4.2.2 Flame geometry

In this model, the flame geometry is assumed spherical until reaches the piston wall, after a semi-spherical geometry is assumed as suggested in [8]. The corresponding scheme is shown in Figure 4.1. The burned radius (r_b) and flame front area (A_f) can be calculated as:

$$A_f = \begin{cases} 2\pi r_b^2 & \text{if } r_b \leqslant h_c \\ 2\pi r_b h_c & \text{otherwise,} \end{cases} \tag{4.10}$$

where h_c is the chamber height, r_b is the radius of the burned gases. The burning radius is computed by assuming that $4\rho_b \approx \rho_{ub}$ [9], and estimating the volume from the previously mentioned geometries as:

$$V_f = \begin{cases} \frac{2}{3}\pi r_b^3 & \text{if } r_b \leqslant h_c \\ \pi r_b^2 h_c - \frac{1}{3}\pi h_c^3 & \text{otherwise,} \end{cases} \tag{4.11}$$

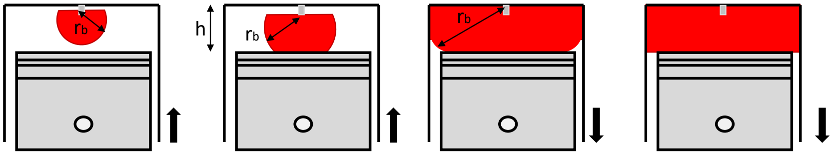

Figure 4.1: *Flame geometry.*

4.2.3 Model execution

To implement the combustion model, two zones of the combustion chamber have to be characterized; moreover, gas properties will also depend on the phase of the cycle. From intake valve closing (IVC) to ignition (SOC), the in-cylinder pressure can be computed by assuming no heat transfer, therefore, γ is replace by a single constant parameter: κ. In that conditions, the pressure evolution, p_{cyl}, follows:

$$p_{cyl}(k) = p(IVC)\left(\frac{V(IVC)}{V(k)}\right)^{\kappa} \tag{4.12}$$

where k is the discrete instant of the time-step, that for the model is the time corresponding to the Δt step considered.

The rest of thermodynamic variables can be computed as following:

$$T_{cyl}(k) = \tfrac{p_{cyl}(k)}{\rho(k)R} \tag{4.13}$$

$$\rho(k) = \frac{m}{V(k)} \tag{4.14}$$

$$m_{cyl} = \frac{m_{air} + m_{fuel}}{1 - RGF} \tag{4.15}$$

$$\lambda = \frac{\frac{1}{14.6}}{\frac{m_{fuel}}{m_{air}}} \tag{4.16}$$

where m_{cyl} is the trapped mass, m_{air} and m_{fuel} mass flows from sensors, RGF the residual gas fraction.

The SOC is assumed at the SA, and the initial burning radius has to be determined. Therefore, after studying the experimental data, the initial burned radius was assumed to be a constant of value 0.5 mm. After, the two volumes, namely burned and un-burned, can be computed as:

$$V_b = V_f \tag{4.17}$$

$$V_{ub} = V - V_f \tag{4.18}$$

Then, the un-burned mass (m_{ub}), burned mass (m_b), and un-burned density (ρ_{ub}) values can be obtained according to [9] by solving:

$$\rho_{ub}(k) = \frac{m_{cyl} + 3m_b(k)}{V(k)} \tag{4.19}$$

$$m_{ub}(k) = m_{cyl} - m_b(k) \tag{4.20}$$

$$m_{ub}(k) = \frac{\rho_{ub}(k)}{V_{ub}(k)} \tag{4.21}$$

The instantaneous heat released (Q_b) can be computed from the fuel burned mass (m_{b-fuel}), and the lower calorific value (H_f):

$$Q_b(k) = (m_{b-fuel}(k) - m_{b-fuel}(k-1))H_f\eta_c \tag{4.22}$$

$$Q_b(k) = (\frac{m_b(k) - m_b(k-1)}{1 + 14.6\lambda})(1 - RGF)H_f\eta_c \tag{4.23}$$

where H_f is 46.6 MJ/kg for gasoline, and η_c is a correction factor of the combustion efficiency, which will be calibrated in following section.

At $k = SOC$, the in-cylinder pressure can be computed by Equation (2.12), as:

$$p_{cyl}(k) = p_{cyl}(k-1)Q_b(k-1) - p_{cyl}(k-1)dV(k-1)\frac{\kappa}{\kappa - 1} \tag{4.24}$$

At the ignition time (SOC), the un-burned temperature can be computed as Equation (4.14). After, A_f and μ can be obtained from Equations (4.10) and (4.9), respectively. With these parameters, S_l: Equation (4.3), u_t: Equations (4.5) and (4.4), Taylor microscale: Equation (4.8) can be calculated at SOC. With these values defined, the combustion process can be solved at each time step t.

4.2.4 Residual Gas Fraction estimation

The RGF is a required input of the combustion model. In this work, the in-cylinder pressure model of previous cycle is used to estimated the RGF of the forthcoming cycle, following:

$$RGF^{k+1} = \frac{m^k_{res}}{m^{k+1}_{cyl}} \tag{4.25}$$

where m_{res} represents the residual gas mass, and m_{cyl} the cylinder trapped mass, notice that the time step of k is one cycle. The residual gas mass of the forthcoming cycle can be computed as:

$$m^{k+1}_{res} = \frac{p^k_{cyl}(EVC)V(EVC)}{RT^k_{exh}} \tag{4.26}$$

where $p(EVC)$ and $V(EVC)$ are the in-cylinder pressure and volume at the EVC, R is the gas constant, a value for a mixture of air and burned gases R = 286 J/Kg.K, and T_{exh} is the exhaust temperature which can be obtained from Equation (2.18) as introduced in Chapter 2. The cylinder mass in the cycle k can be calculated as:

$$m_{cyl}^{k} = m_{fuel}^{k} + m_{air}^{k} + m_{res}^{k-1} \tag{4.27}$$

where m_{air} and m_{fuel} are obtained from sensors and models at the ECU.

An initial RGF has to be assumed, in this work an initial value of 4 % is used to initialized the model.

4.2.5 Model calibration

The model has been calibrated by using the training data presented in Chapter 3, operating points: OP_A. In order to improve the combustion model, three parameters have been mapped as a function of the engine speed and the intake pressure. Two parameters related with the HRR calculation (Q_b), namely the combustion efficiency η_c, and κ, and a one degree of freedom for the combustion model, X_2.

4.2.5.1 Calibration of combustion parameters

Two combustion parameters need to be calibrated: κ, which is associated with the compression stroke, and η_c, which is associated with the combustion efficiency and with additional phenomena which are not included in the combustion model (blow-by, SOC, etc).

Figures 4.2 shows the OL maps obtained for κ (left) and η_c (right). The training operating points used for calibration are highlighted with circles.

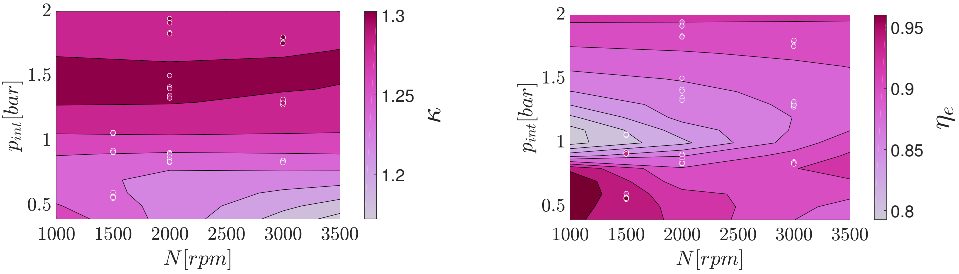

Figure 4.2: *Open loop maps for HRR calculations.*

4.2.5.2 Calibration of model constants

After η_c and κ can be obtained from the operating conditions defined by p_{int} and n, as:

$$\kappa = f_\kappa(p_{int}, n) \tag{4.28}$$

$$\eta_c = f_\eta(p_{int}, n) \tag{4.29}$$

the parameters X_1, X_2, and X_3 from the laminar flame speed, turbulent intensity and microscale length can be calibrated.

In Figure 4.3 (top plot) the mean value of burning rate at operating condition $OP_A = 12$ is represented in dashed line, and in continuous line the modeled value for three possible fittings values of X_1 and X_2 are plotted. The magenta line is the optimal calibration value obtained by least square method: $X_1 = 0.67$ and $X_2 = 0.91$, in blue the effect of decreasing X_2 is shown, while in grey line the fitting value of X_1 when decreasing X_2. The medium plot and top plot shows the effect of the calibration constant variations in the laminar flame speed and turbulent intensity evolution.

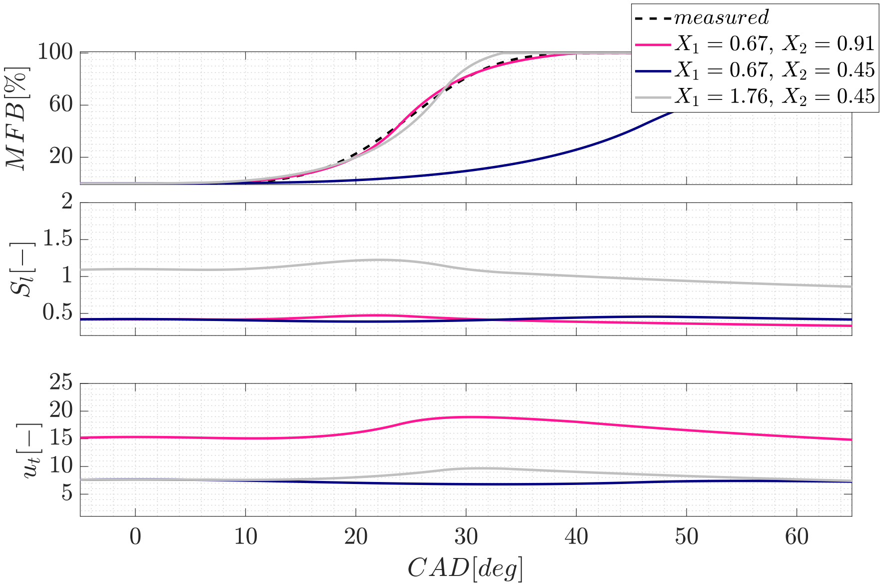

Figure 4.3: *Values of X_2 obtained as a function of SA.*

As it can be seen in Figure 4.3, X_1 is directly associated with S_l, while X_2 and X_3 are associated with the evolution of the u_t and with the effect in the burning rate. If X_1 or X_2 are increased, the combustion rate will be accelerated, and the opposite effect is expected from X_3.

The main parameter to calibrate in the combustion model is X_2, since the turbulent intensity is modeled by assuming the SOC at SA, and in consequence the inconsistencies of the model will depend on the operating conditions and with the SA.

In Figure 4.5 the best fitting of X_2 value is represented as a function of the SA, when setting $X_1 = 0.5$ and $X_3 = 10$. Eight tests groups with different intake pressure and engine speed are represented.

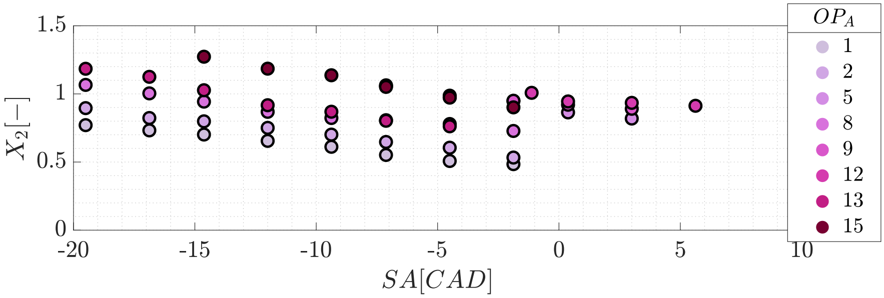

Figure 4.4: *Values of X_2 against SA values.*

As it is shown in Figure 4.5, X_2 seems to have a linear dependence with the SA, where the slope is 0.02 per CAD. Therefore, an adaptation of the calibration constant X_2 is proposed as follows:

$$X_2 = X_{20}(n, p_{int}) + 0.02SA \tag{4.30}$$

where X_{20} is mapped as a function of the operating condition (p_{int} and n). In Figure 4.5 the values of the final map of X_{20} is shown.

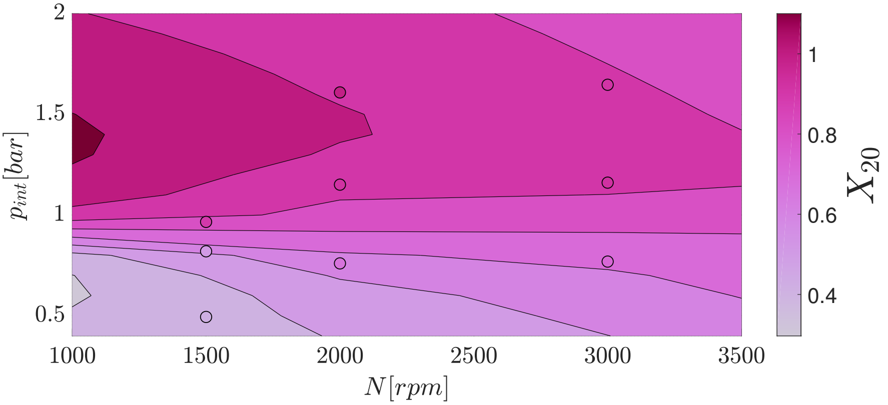

Figure 4.5: *Values of X_2 obtained as a function of SA.*

4.3 Observer design

In order to provide to the combustion model a permanently estimation of the laminar burning velocity (S_l) an observer is designed in this section. The observer objective is to update a bias in the pressure peak location in order to estimate X_1. The pressure peak location will be estimated cycle-to-cycle through the structural vibration sensor signal.

4.3.1 Pressure peak location estimation

As already explained in Chapter 2, the pressure peak location can be estimated through the vibration signal, by making use of the signal from the vibration signal, as suggested in [10]. This method band-pass filter the vibration signal in order to separated the harmonic components, which is used to find the zero-crossing acceleration angle, characteristic point of the maximum pressure location.

In Figure 4.6 the location computed from vibration signal is compared with the measured from in-cylinder pressure sensor during transient $T6$. On the left plot, the pressure peak location of each of the cycles during the test are represented, and on the right plot the correlation of both pressure peak locations.

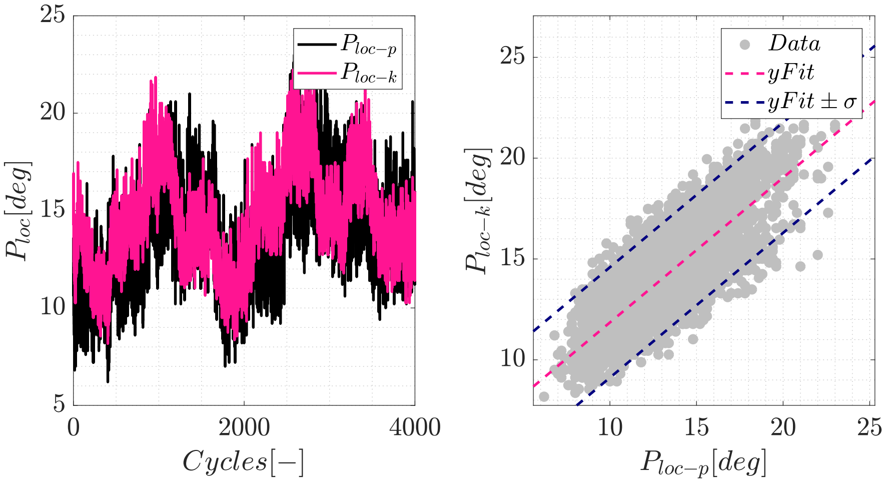

Figure 4.6: *Pressure peak location computed from in-cylinder pressure sensor and vibration signal during transient* $T6$.

As it can be seen in Figure 4.6, most of the points computed from the vibration signal are within the range $yFit \pm \sigma$ during the transient test.

The maximum pressure location was also estimated over SA sweeps at operating condition $OP_A = 2$. The histogram of the estimated values from vibration signal (P_{loc-k}) and from in-cylinder pressure signal (P_{loc-p}) and the cumulative distribution function (cdf) are shown in Figure 7.28 over 2000 cycles.

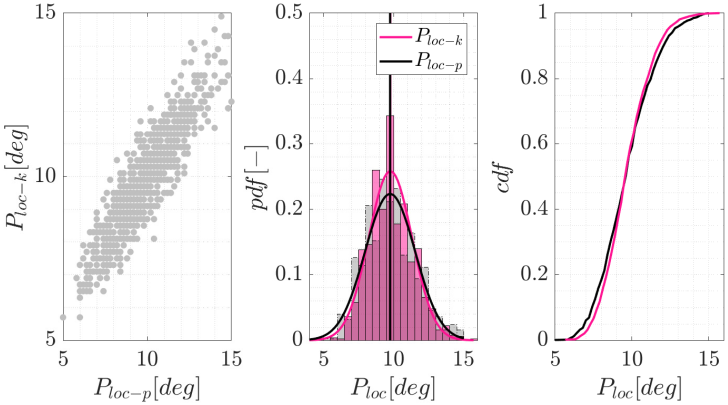

Figure 4.7: *Pressure peak location computed from in-cylinder pressure sensor and vibration signal.* $R^2 = 0.84$*: Left plot: Histogram. Right plot: Cumulative distribution function of both measurements.*

As is illustrated in Figures 4.6 and 4.7, the values computed through the vibration signal are good estimations of the maximum pressure location. Thereby, for each cylinder, cycle by cycle, a feedback of P_{loc} is obtained from the vibration signal, and used to design an observer. In Figure 4.8 the pressure peak location is computed from vibration signal for all four cylinders during 500 cycles of transient test $T12$.

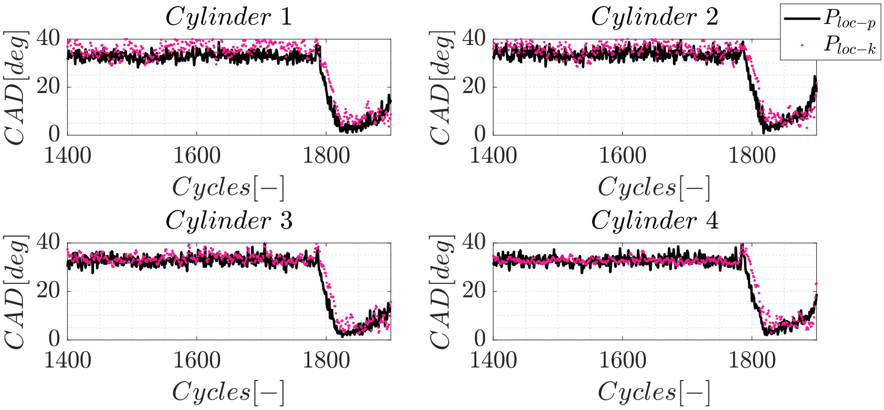

Figure 4.8: *Pressure peak location computed from in-cylinder pressure sensor and vibration signal for all cylinders during 500 cycles of test* $T12$*.*

As is shown in Figure 4.8, the vibration signal is able to capture the evolution of the pressure peak location for each one of the four cylinders, hence, the pressure peak location computed from the vibration signal can be in an observer in order to improve the model estimation.

4.3.2 Observer: Extended Kalman Filter

In order to provide the system a estimation of the maximum in-cylinder pressure location P_{loc}, an Extended Kalman Filter (EKF) is used. The EKF is a data fusion technique which combines data obtained from different sources, in this case model and vibration measurement, through the EKF an optimal estimation for a Gaussian noise can be obtained [11]. In this case, an EKF is applied to estimate the optimal value of the calibration value X_1 in a cycle-by-cycle basis in order to minimize the difference between the maximum pressure location computed from vibration measurement and model. The EKF is designed with a cycle step (k) as:

$$x^{k+1} = f(x^k, u_k) + w^k \tag{4.31}$$

$$y^k = h(u, x_k) + v^k \tag{4.32}$$

where x is the state, and y the outputs of the model described by the combustion model h, u represents the inputs of the combustion model, v the noise related to y, and v the noise related to x.

This system is composed from the following state x and measurement y:

$$\begin{array}{rcl} X_1 & = & X_1 \\ y & = & P_{loc-k} \end{array} \tag{4.33}$$

An state vector of the EKF can be defined as:

$$\begin{array}{rcl} \hat{x}^{k|k-1} & = & f(\hat{x}^k) \\ e^k & = & y^k - h(u_k, \hat{x}^{k|k-1}) \\ \hat{x}^k & = & \hat{x}^{k|k-1} + K^k e^k \end{array} \tag{4.34}$$

A gain value (K_k) is updated cycle-by-cycle, such as:

$$\begin{array}{rcl} P^{k|k-1} & = & F^k P^{k-1} F^{k^T} + W^k \\ K_k^k & = & P^{k|k-1} H^{k^T} (H^k P^{k|k-1} H^{k^T} + R^k)^{-1} \\ P^k & = & (I - K_k^k H^k) P^{k|k-1} \end{array} \tag{4.35}$$

where W_k and R_k are Gaussian distribution matrices which modeled w and v. F^k and H^k are the linear state matrices, and these equations are linearized as following:

$$F^k = \frac{d(f(u, x_k))}{dx_k} = \frac{f(u, x^k) - f(u, x^k + \Delta_{x^k})}{\Delta_{x^k}} \tag{4.36}$$

In Figure 4.11 the complete combustion model with the observer proposed is shown. From the vibration signal (K_{signal}) the location of the pressure peak (P_{loc-k}) is estimated, and the calibration parameter X_1 is updated by making use of the combustion model presented in section 4.2. From the in-cylinder pressure model and signal the following combustion parameters can be extracted: CA10, CA50, CA90, IMEP, or RGF.

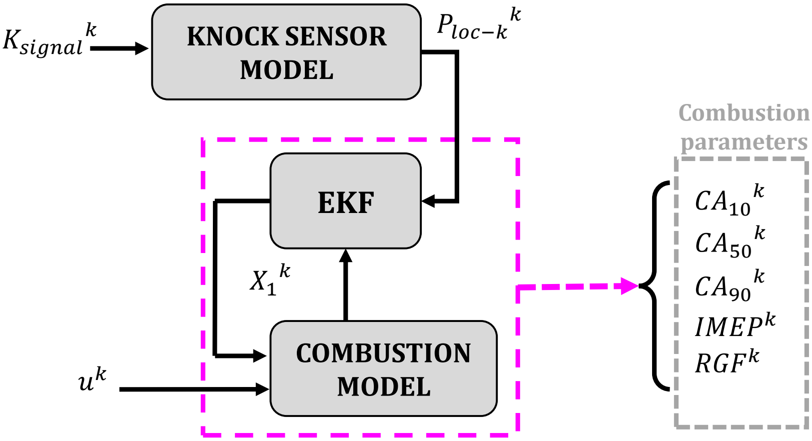

Figure 4.9: *Model observer scheme.*

The performance of the EKF is characterized by the noises, where low noises related to the measured signal (P_{loc-k}) show a fast adaptation, and low noises related to the combustion model shows a more filtered signal of the output. In Figure 4.10, P_{loc} computed from the observer is represented when two combination of noises v and w (Noise A and Noise B) are used during transient test $T9$. Noise A values are collected in Table 4.1, and Noise B shows the effect of applying a lower noise at the prediction of X_1.

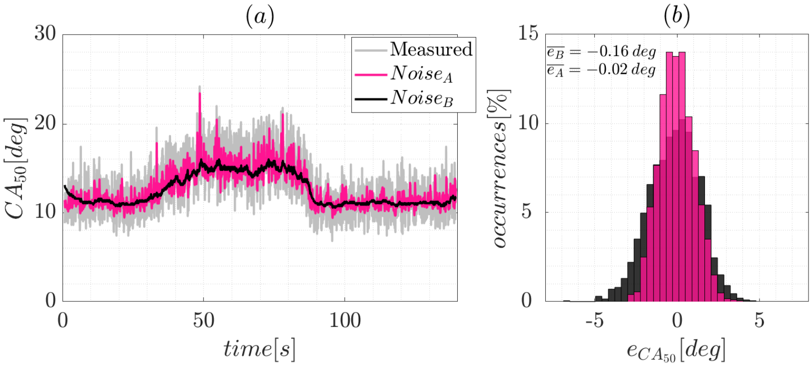

Figure 4.10: *EKF response under different noises.*

Table 4.1: *Noise suggested for EKF*

Variable	Type	Value [unit]
X_1	state	0.005 [-]
P_{loc}	output	1[deg]

In order to fix the initial value of X_1 the combustion model with observer is applied in steady condition to evaluated the convergence in Figure 4.11: left plot shows the X_1 value when different initial values are considered, and right plot presents the measured pressure peak location and the output of the combustion model with the observer. As it can be seen in Figure 4.11, regardless of the initial value of X_1, the observer converges to the solution in between 5 and 6 seconds regardless on the initial conditions.

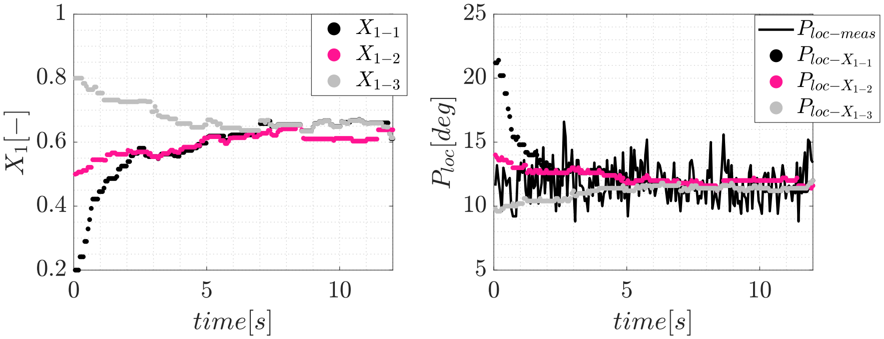

Figure 4.11: *Convergence of X_1 parameter for different initial values: X_1 values (left) and pressure peak location measured and model (right).*

In order to analyzed the adaptation of the calibration constant X_1 during transient conditions, the load transient $T11$ is analyzed in Figure 4.12, where the state X_1 is shown for each one of the four cylinders of engine A.

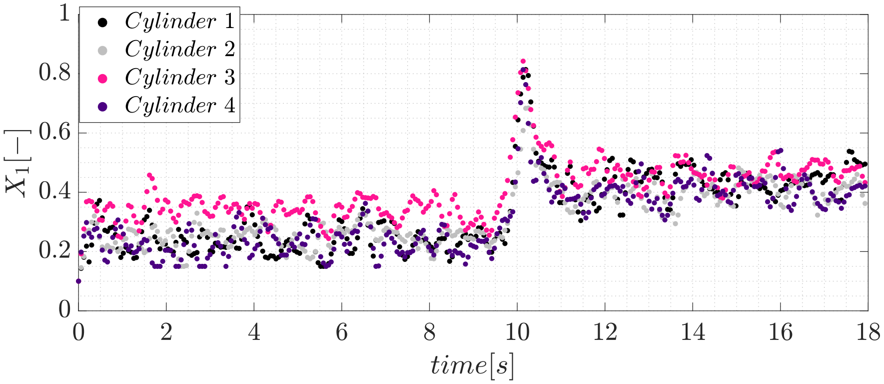

Figure 4.12: *X_1 value during test $T11$ for all cylinders*

As it is shown in Figure 4.12, at steady state condition (before 10 s) each cylinder calibration constant X_1 estimated by the observer is almost constant. After 10 s, when the transient starts, the observer estimates the calibration value from the pressure peak location estimated from the vibration signal. Once steady state conditions are reached, after 12 s, the calibration value for each cylinder is almost constant in a different value. In summary, the model with observer allows the calibration of each cylinder separately, i.e. during a transient and through the estimation of the pressure peak location of each cylinder, the observer is able to re-calibrate cycle-by-cycle the constant parameter of the combustion model X_1 for a better estimation of the in-cylinder pressure.

4.4 Results and discussion

In this section, both the combustion model and the model with the observer will be validated over two data sets: training data set (OP_A) and validation data set.

4.4.1 Training data set

Figure 4.13 shows the combustion model pressure evolution compared with the observer and the in-cylinder measured pressure. On the top plot, the in-cylinder pressure evolution is shown. In continuous grey line the 150 cycles are represented and in continuous black line the mean value, dashed line is used to represent both mean modeled pressure, in pink the observer and in grey the combustion model. On the bottom plot the mean relative error over 150 cycles ($OP_A = 6$) of both models is represented.

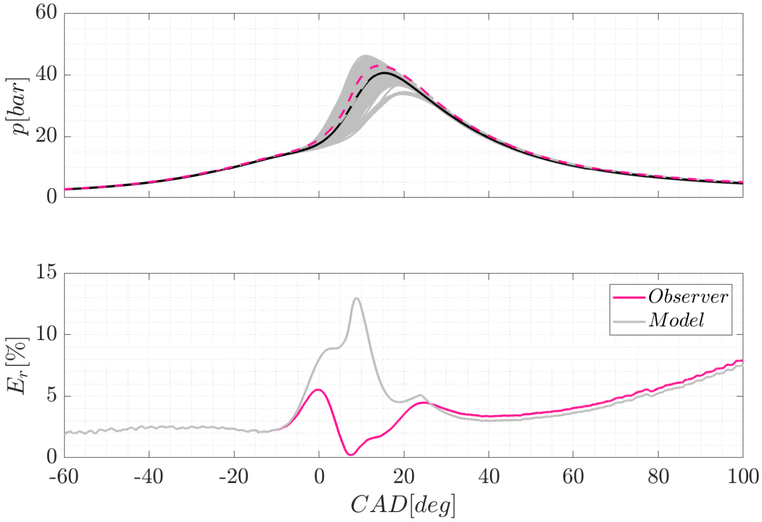

Figure 4.13: *Combustion model results at* $OP_A = 6$*: In-cylinder pressure. Top plot: In-cylinder pressure in grey 150 cycles and black line mean value, in dashed line both models. Bottom plot: Mean relative error evolution for both: combustion model and observer.*

As shown in Figure 4.13, the relative error during the steady test is lower for the observer case. For combustion model case, the relative error grows significantly at the end of the combustion. In Figure 4.14 (top), the mean MFB over the 150 cycles represented in Figure 4.13 is shown. On the bottom plot, the absolute error of both,the combustion model and the observer, are represented.

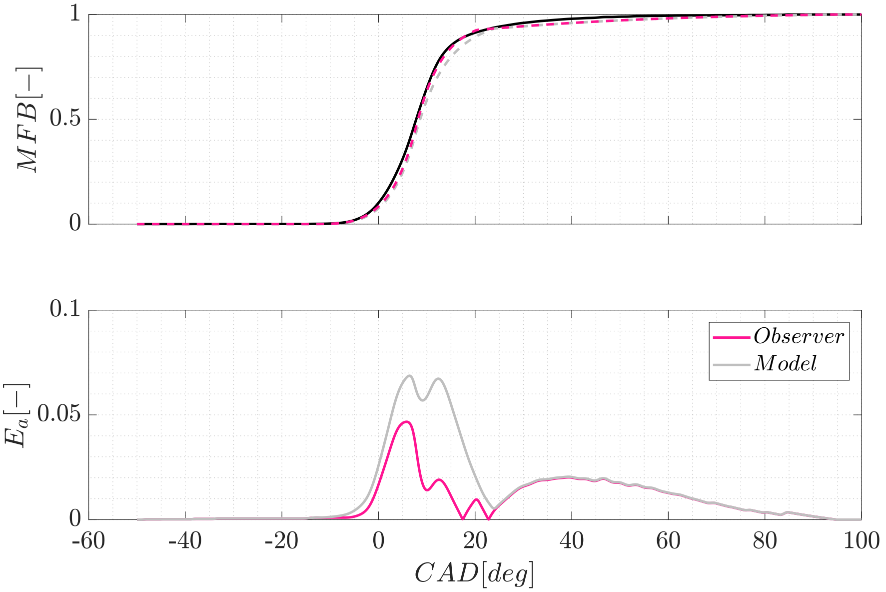

Figure 4.14: *Combustion model results at* $OP_A = 6$*: MFB. Top plot: in black line mean MFB over 150 cycles, in dashed line both models. Bottom plot: Mean absolute error evolution for both: combustion model and observer.*

The mean relative error of the in-cylinder pressure is computed over all operating points OP_A in cylinder 2, in Figure 4.15, the mean relative error for each engine speed group: 1500, 2000 and 3000 rpm is shown. Different markers are used to identify the different engine speeds, and different colors to identified the model: lighter grey the combustion model and magenta the observer.

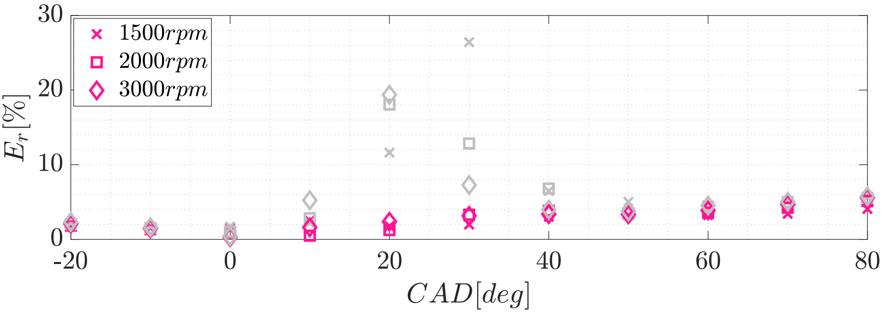

Figure 4.15: *Relative error over all training points divided in three engine speed groups: 1500, 2000 and 3000 rpm.*

As shown in Figure 4.13, before combustion the relative error of both models is similar, but after TDC the observer clearly outperforms the model results, specially in crank angle interval where combustion appears.

4.4.2 Validation data set

In order to compare the results of the model and the observer, two perspectives are used to analyzed data: the cycle-to-cycle combustion parameters for one cylinder, and the cylinder to cylinder modeling.

Cycle-to-cycle: First, the cycle-to-cycle combustion parameters will be compared for one cylinder (cylinder 3 as example). The CA10, CA50, CA90, IMEP, and RGF will be compared during a load transient test ($T6$) in Figure 4.16, for the model and the observer.

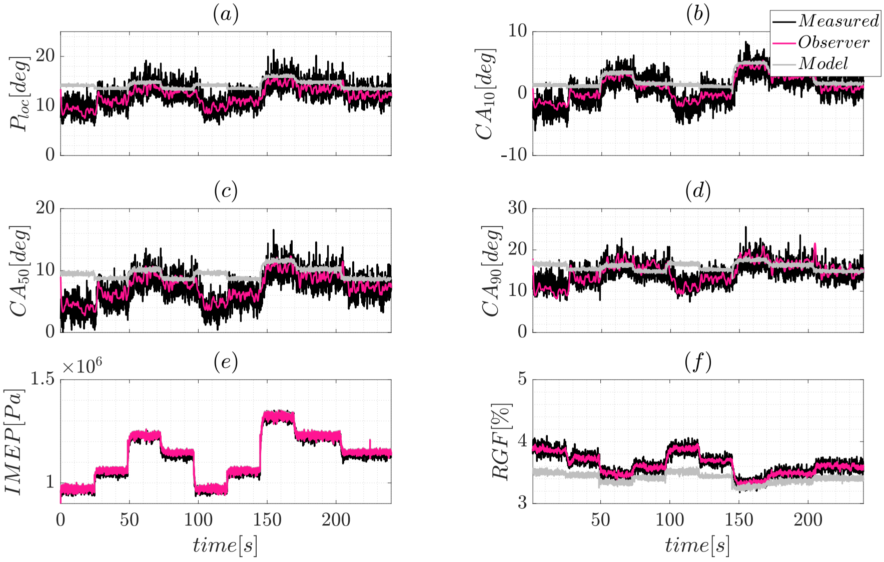

Figure 4.16: *Combustion model results at transient test $T6$ for cylinder 3. (a) : pressure peak location, (b) : CA10 (c) : CA50, (d): CA90, (e): IMEP and (f): RGF.*

Analyzing Figure 4.16, the improvement of the observer in terms of the peak pressure location (P_{loc}) is translated to noticeable improvements in the combustion indicators (CA_x, IMEP or RGF). The absolute error histograms of the combustion indicators represented in Figure 4.16 are exhibit in Figure 4.17.

The values of both methods, combustion model and observer, are compared with the obtained from the measured from in-cylinder pressure signal.

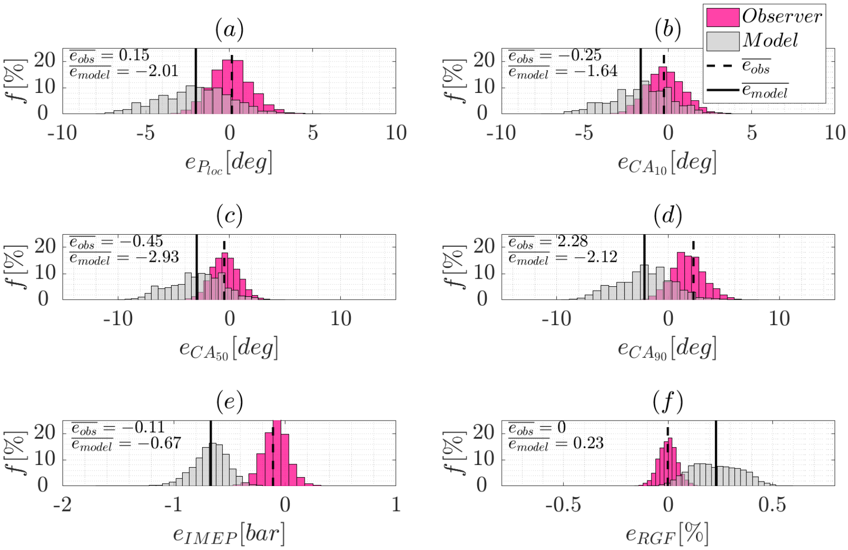

Figure 4.17: *Error histograms of estimation from combustion model and observer. (a) : pressure peak location, (b) : CA10, (c) : CA50, (d): CA90, (e): IMEP and (f): RGF*

As it can be seen in Figure 4.17, mean absolute error and maximum error obtained through observer are lower than combustion model, showing a better estimation of the combustion parameters under transient conditions.

Cylinder to cylinder: The models are also compared over the different cylinders during test $T6$. In Table 4.2 the mean error between the measurement and the models for the parameters represented in Figure 4.17 are summarized.

Table 4.2: *Mean absolute error of both models combustion parameters for the four cylinders during test $T6$.*

Cylinder	1		2		3		4	
	Observer	Model	Observer	Model	Observer	Model	Observer	Model
P_{loc} [deg]	1.3	5.6	0.8	3.5	0.15	2.1	0.8	2.8
CA10 [deg]	1.7	2.22	1.67	2.19	0.25	1.64	0.95	3.5
CA50 [deg]	5.4	8.64	5.55	8.6	0.45	2.93	1.26	4.3
CA90 [deg]	3.5	8.25	3.4	07.05	2.28	2.12	1.2	3.5
IMEP [bar]	0.16	0.33	0.58	1.14	0.3	0.78	0.5	1.29
RGF [%]	0.55	0.98	0.11	0.21	0.23	0.9	0.3	0.65

The in-cylinder pressure evolution of a given cycle is shown in Figure 4.18, where the in-cylinder pressure for each cylinder corresponding to cycle $t = 13s$ of the tip-in shown in Figure 4.12 is analyzed. Where the measured in-cylinder pressure, the pressure obtained through the observer, and the combustion model are represented.

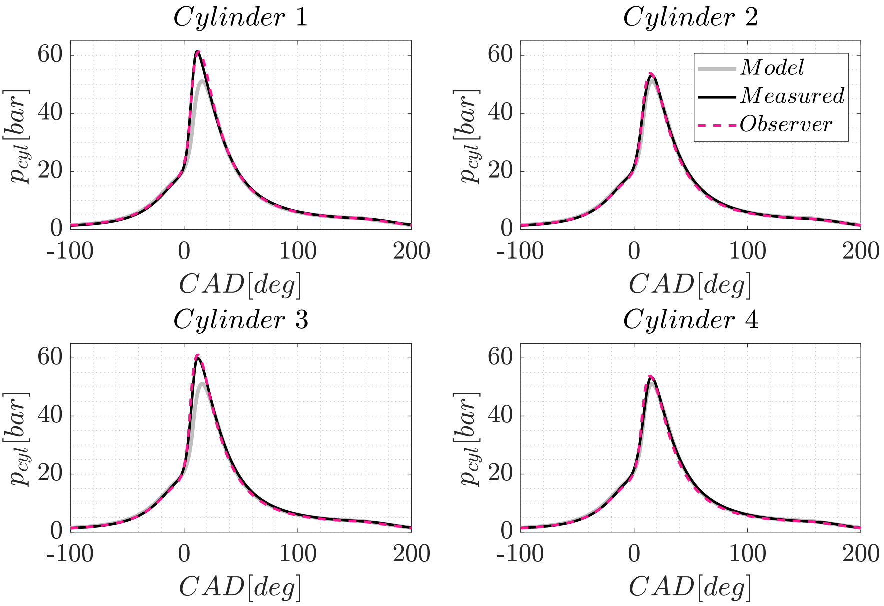

Figure 4.18: *In-cylinder pressure evolution measured compared with combustion model and observer during test $T11$ cycle labeled in Figure 4.11.*

As shown in Figure 4.18, the model with the observer is able to better predict the in-cylinder pressure evolution.

In Figure 4.19 P_{loc} for both models, are compared with the pressure peak location from the in-cylinder pressure sensors during the tip-in $T11$.

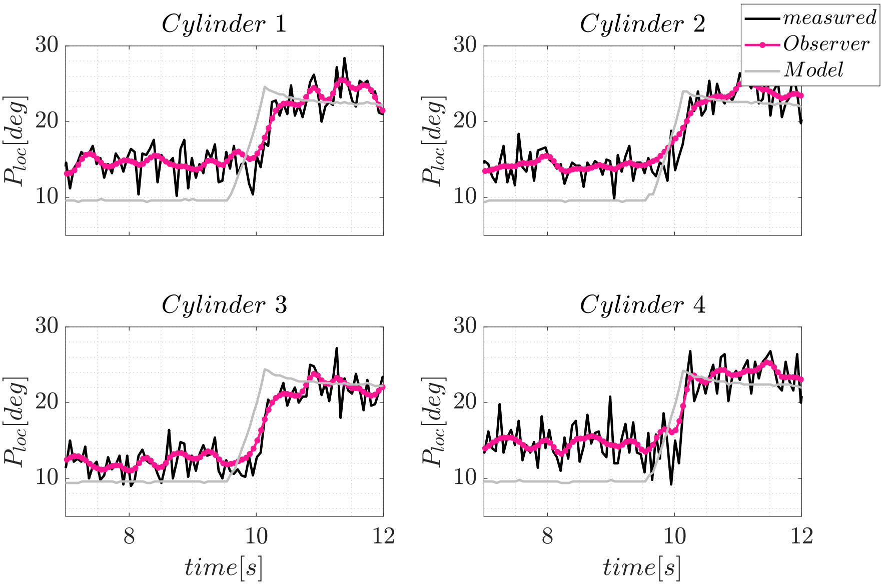

Figure 4.19: *Combustion parameters obtained from in-cylinder pressure, combustion model and observer during test $T11$. Left top: cylinder 1, right top: cylinder 2, bottom left: cylinder 3, bottom right; cylinder 4.*

In the case of the combustion model the output is the same for all cylinders, since the inputs (cycle operating conditions) are the equal for all cylinders. Furthermore, in the case of the observer, the output from each cylinder is different, being able to better represent each cylinder.

In Figure 4.20 the mean absolute error of the pressure peak location, CA10, CA50 and CA90 are shown for each cylinder. Different colors are used to differentiate the combustion model and observer.

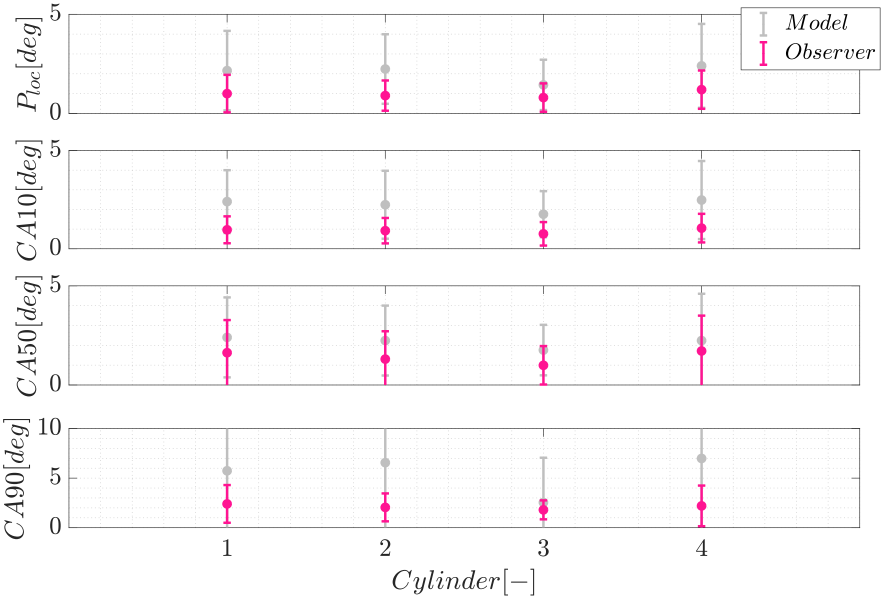

Figure 4.20: *Combustion parameters absolute error of combustion model and observer during test $T11$. From top to bottom: pressure peak location, CA10, CA50 and CA90.*

As it can be seen in Figure 4.20, the error in the estimation for each cylinder is remarkable higher for the combustion model case than for the observer.

4.5 Application to different fuel types

The last section was devoted to compared the combustion model and the observer. It was demonstrated that the in-cylinder pressure and the combustion parameters estimated though the observer shows better results than the combustion model, being able to reproduce the combustion under steady and transient operating conditions. In this section, the observer benefits for two types of fuels will be presented on Engine B. The combustion model was calibrated for engine B with SI combustion fueled with gasoline.

As explained above, X_1 is the calibration factor of the laminar flame speed. The initial laminar flame speed S_{l0} and the temperature and pressure exponents of the laminar flame speed correlation presented in Equation (4.3) depend on fuel properties. In particular, In order to compensate the exponents effect on the laminar flame speed, the cycle-to-cycle calibration of X_1 was proposed in previous section. In this section, the effect on the value X_1 for different fuel types is analyzed by fitting the combustion model for each cycle.

Two operating points, $OP_B = 13$ and $OP_B = 38$, will be compared by fitting the calibration constant X_1 stating from the same calibration value. In this case, at each cycle, the value of the calibration constant was obtained by finding the minimum of constrained nonlinear multi-variable function (fmincon Matlab function) with the same starting value x_0.

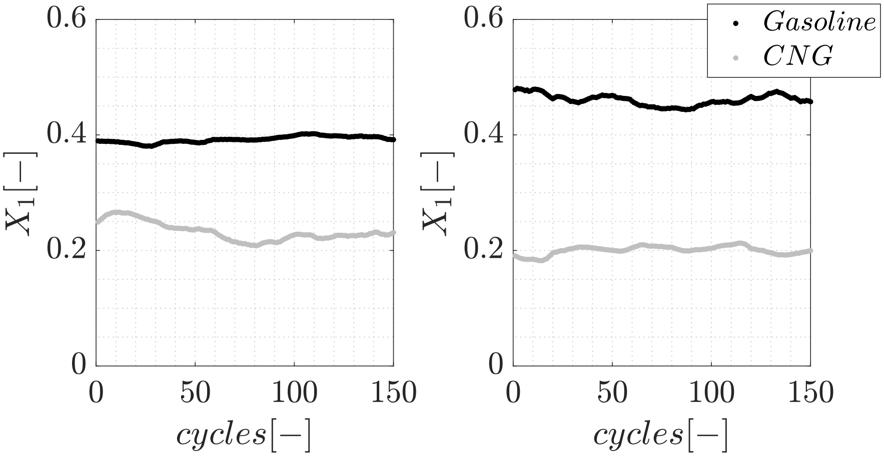

Figure 4.21: *X_1 fitting value impact for different fuels in engine B for two operating points: $OP_B = 13$ (left) and $OP_B = 38$ (right).*

As shown in Figure 4.21, for both operating conditions X_1 for gasoline cases is higher than CNG cases, which corresponds with experimental studies which demonstrates that at equal equivalence ratio the laminar flame speed is lower for CNG than gasoline [12]. In Figure 4.22, the mean in-cylinder pressure from the model and sensor is represented in operating condition $OP_B = 38$, in grey the in-cylinder pressure of all cycles is also shown. On left plot for gasoline case, and on right plot for CNG case.

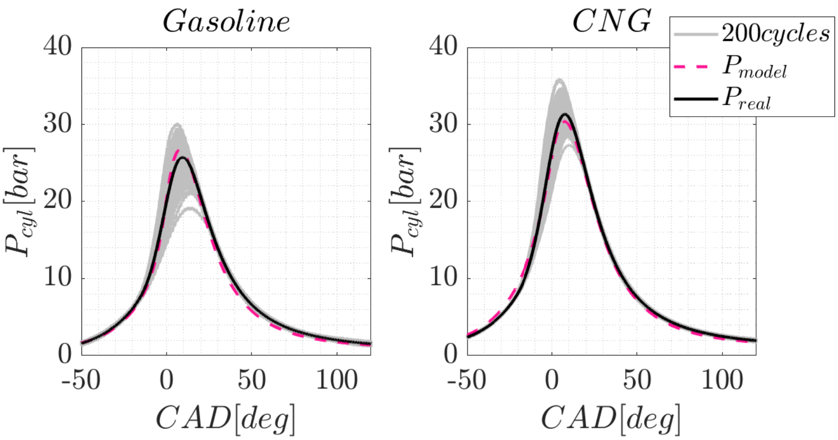

Figure 4.22: *In-cylinder pressure evolution over $OP_B = 38$ for two fuels: Gasoline (left) and CNG (right).*

As it can be seen in Figure 4.21, the model is capable of reproducing the mean in-cylinder pressure for both cases by fitting the calibration constant X_1, which means that with the observer the model is able to compensate the effect of the fuel type without a complete re-calibration of the model for each fuel type.

For this reason, and taking into account what is shown in Figure 4.11 about the convergence of the X_1 parameter for different initial values, from the observation of the pressure peak location is possible to capture the fuel effect and to model the in-cylinder pressure by updating the X_1 constant.

4.6 Conclusions

A two-phase 0D control oriented model has been presented in this chapter, the model is able to predict the mean combustion phase evolution. In order to improve the model under transient conditions, an observer has been designed to provide the model feedback information from vibration signal. A calibration parameter of the laminar flame speed is updated cycle-to-cycle by using an EKF. The observer is able to improve the model prediction, not only for the estimation of combustion indicators, but also to provide more information to analyze each engine cylinder.

An application for two different fuels was performed in engine B, showing that the observer is also able to adapt the model to different fuels by re-calibrating the constant X_1 of the combustion model.

References

[1] Siano D and D'agostino D. "Knock detection in SI engines by using the discrete wavelet transform of the engine block vibrational signals". *Energy Procedia*, Vol. 81, pp. 673–688, 2015. (cited in p. 62)

[2] Blizard Norman C and Keck James C. "Experimental and theoretical investigation of turbulent burning model for internal combustion engines". *SAE Transactions*, pp. 846–864, 1974. (cited in p. 62)

[3] Wang Shu, Zhu Qilun, Prucka Robert, Prucka Michael and Dourra Hussein. "Input adaptation for control oriented physics-based SI engine combustion models based on cylinder pressure feedback". *SAE International Journal of Engines*, Vol. 8 n^o 4, pp. 1463–1471, 2015. (cited in p. 62)

[4] Poulos Stephen G and Heywood John B. "The effect of chamber geometry on spark-ignition engine combustion". *SAE transactions*, pp. 1106–1129, 1983. (cited in p. 63)

[5] Tabaczynski Rodney J, Ferguson Colin R and Radhakrishnan Krisna. "A turbulent entrainment model for spark-ignition engine combustion". *SAE transactions*, pp. 2414–2433, 1977. (cited in pp. 63 and 64)

[6] Keck James C. "Turbulent flame structure and speed in spark-ignition engines". In *Symposium (International) on Combustion*, volume 19, pp. 1451–1466. Elsevier, 1982. (cited in p. 63)

[7] Wong Victor W and Hoult David P. "Rapid distortion theory applied to turbulent combustion". *SAE Transactions*, pp. 1243–1262, 1979. (cited in p. 64)

[8] Wu Hao. "Study of spark ignition engine combustion model for the analysis of cyclic variation and combustion stability at lean operating conditions". 2013. (cited in p. 64)

[9] Heywood John B. *Internal combustion engine fundamentals*. McGraw-Hill Education, 2018. (cited in pp. 19, 26, 64, 66, 90, and 186)

[10] Businaro Andrea, Cavina Nicolò, Corti Enrico, Mancini Giorgio, Moro Davide, Ponti Fabrizio and Ravaglioli Vittorio. "Accelerometer Based Methodology for Combustion Parameters Estimation". *Energy Procedia*, Vol. 81, pp. 950–959, 2015. (cited in pp. 28, 29, and 71)

[11] Guardiola Carlos, Pla Benjamin, Bares Pau and Stefanopoulou Anna. "Cylinder charge composition observation based on in-cylinder pressure measurement". *Measurement*, Vol. 131, pp. 559–568, 2019. (cited in pp. 46 and 74)

[12] Ben Livier, Raud-Ducros Nathalie, Truquet Remy and Charnay Georges. "Influence of air/fuel ratio on cyclic variation and exhaust emission in natural gas SI engine". Technical report, SAE Technical Paper, 1999. (cited in p. 86)

CHAPTER

5

Cycle-to-cycle variability modeling

Contents

5.1 Introduction

The cyclic and cylinder-to-cylinder variability can cause a decrease in efficiency and uncomfortable noise due to vibration [1], which makes variability one of the major challenges to optimize combustion in SI engines. In addition, cycle-to-cycle variability produces undesired noise in combustion indicators, which makes combustion control challenging in IC engines.

Some of the cycle-to-cycle combustion variability causes have been identified in SI engines [1,2], such as variations of the in-cylinder mixture, turbulent intensity, difference of the mean flow speed, among others. In addition, many factors such as the spark timing, the dilution of the mixture, the spark plug, do not cause cyclic variability in combustion themselves, however affect the extent of cycle-to-cycle variability caused by other factors [3]. In recent years, different control strategies had been developed in order to reduce cycle-to-cycle variability under lean conditions in SI engines by controlling the SA and EGR valve [4,5], the SA and the throttle valve [6] among others. In addition, in [7] the IMEP and its variability is model in order to control the cycle-to-cycle variability under transient conditions.

The first part of the chapter is devoted to analyze the impact of the combustion phasing, type of ignition and stratification on the combustion variability for two different fuels: gasoline and CNG. The second part of the chapter aims to characterize the distribution of the variability over the HRR pattern in engine A. Then, a cycle-to-cycle variability model of the HRR pattern for SI combustion is presented, the model aims to reproduce the causes of cycle-to-cycle variation by introducing a probability distribution on the combustion model presented in Chapter 4, particularly at the laminar speed, S_l, and at the turbulent speed, u_t. Finally, conclusions are discussed.

5.2 Experimental analysis of fuel effect on combustion variability

In this section the cycle-to-cycle variability will be analyzed by examining the HRR pattern in engine B. The impact on the variability of the combustion phasing, the type of combustion and the dilution will be analyzed for different fuels.

Combustion phasing impact

The first part of the experimental analysis includes four SA sweeps performed in engine B (Operating point: $OP_B = 12$). In Figure 5.1 the impact of the combustion phasing is shown for gasoline (left) and CNG (right). On the top plot the average of the combustion location at each percentage of combustion over 200 cycles is represented, and on the bottom plot the standard deviation. Different grey scale colors are used to exhibit each SA.

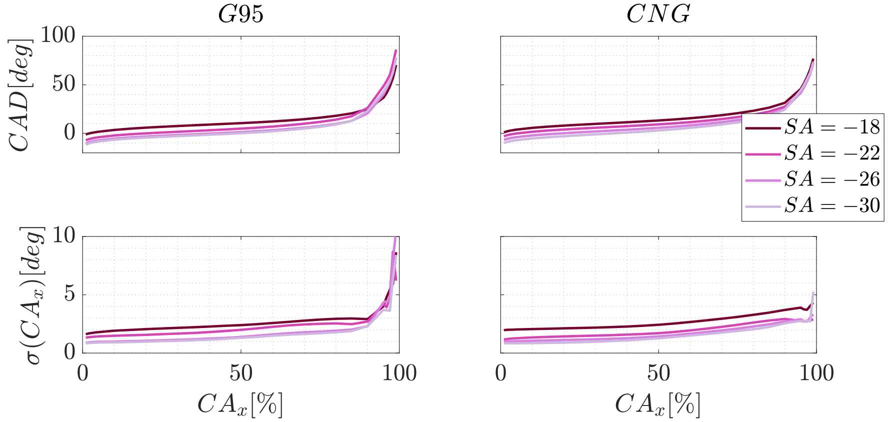

Figure 5.1: *Combustion phasing effect for TJI combustion fueled with gasoline 95 (left) and CNG (right). Average (top plot) and the standard deviation (bottom plot) of the CA_x over each percentage. Operating point: $OP_B = 12$ 200 cycles*

As it can be noticed in Figure 5.1, the combustion variability over the heat release pattern is affected by the combustion location. In both cases, gasoline and CNG, the cycle-to-cycle variability decreases as the SA, and therefore the combustion phasing, moves into compression stroke, as it is experimentally studied in [8, 9].

When comparing the effect of the fuel at equal SA, it can be noticed that at the end of the combustion, i.e. between the 85-100 % of the MFB, the variability is increased for gasoline case is higher than the rate for CNG case. This is due to the slow burning rate observed for gasoline case, which increases significantly the variability at this stage.

Ignition method

SI and TJI ignition methods are analyzed in Figure 5.2, where the HRR pattern over two different operating conditions are shown. In Figure 5.2 (top) the CA_x at each percentage of combustion is shown, in black for SI combustion and in pink for TJI combustion. On the bottom plot the standard deviation for each test group is represented.

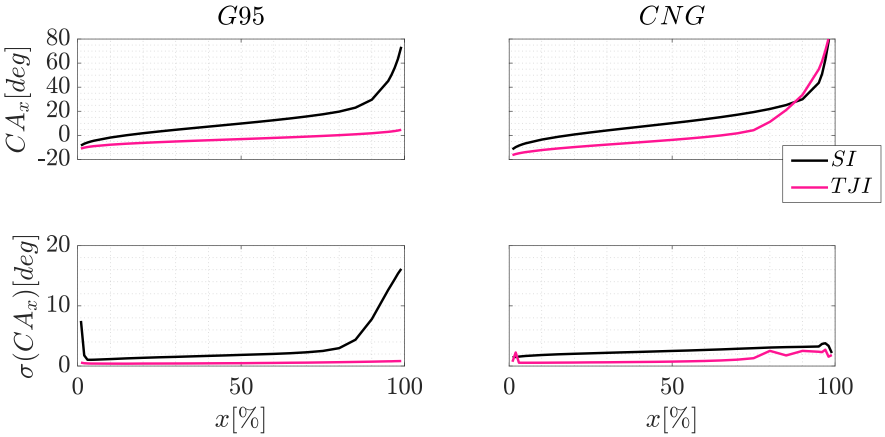

Figure 5.2: *Ignition method effect in engine B fueled with gasoline 95 (left) and CNG (right). Average (top plot) and the standard deviation (bottom plot) of the* CA_x *over each percentage. Operating point:* $OP_B = 31$ *(left)* $OP_B = 11$ *(right) 200 cycles.*

As it can be seen in Figure 5.2, the cycle-to-cycle variability for both operating conditions, and hence fuels, is lower for TJI combustion. As it can be noticed, for the SI combustion fueled with gasoline (left), the variability at the end of the combustion is increased due to the slow burning rate that is observed on the top plot. The cycle to cycle variability in both operating conditions is lower in TJI combustion due to the fast burning rate induced by the jet flame [10].

Lean combustion:

TJI combustion engines extend the lean burn limitations of gasoline engines and show an improvement in burning rates [10]. Lean combustion consist in diluting the air-fuel mixture with air or EGR [9], which leads to a reduction of pumping losses, and an improvement of thermal efficiency. The cycle-to-cycle variability sensitivity to λ is shown in Figure 5.3 for two fuels in engine B fueled with gasoline (left) and CNG (right).

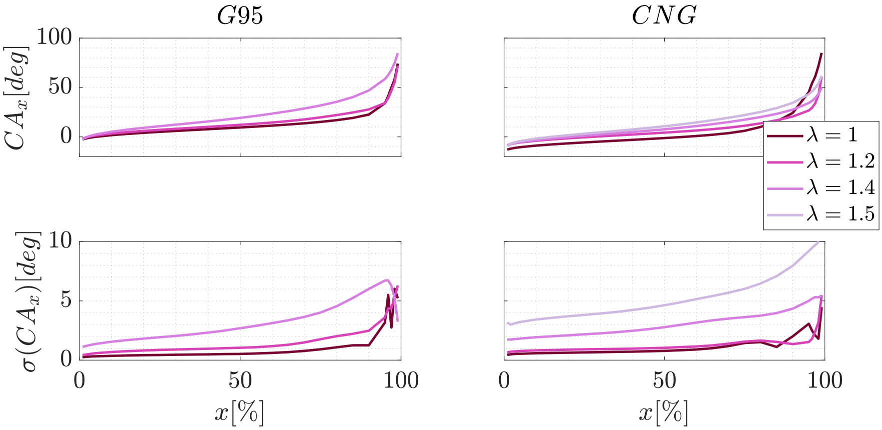

Figure 5.3: *Lambda effect in engine B TJI combustion fueled with gasoline 95 (left) and CNG (right). Average (top plot) and the standard deviation (bottom plot) of the* CA_x *over each percentage. Operating point:* $OP_B = 11$ *200 cycles*

As it can be seen in Figure 5.3, for cases with more diluted combustion the cycle-to-cycle variability over the HRR pattern is higher, but for CNG cases the exhibit variability is lower than for gasoline cases.

The EGR dilution impact on combustion variability for TJI combustion is shown in Figure 5.4 for two cases with the engine running at the same operating condition: On the left side the engine in fueled with gasoline, and on the right side with CNG.

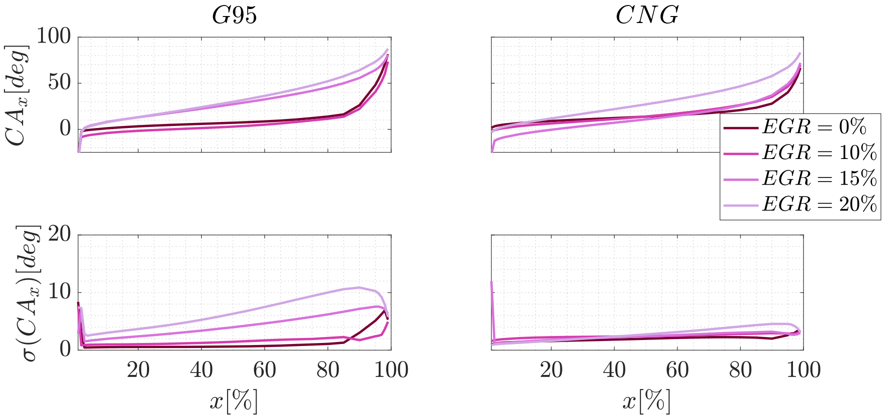

Figure 5.4: *EGR effect in engine B TJI combustion fueled with gasoline 95 (left) and CNG (right). Average (top plot) and the standard deviation (bottom plot) of the* CA_x *over each percentage. Operating point:* $OP_B = 13\ 200$ *cycles.*

It is noticeable that combustion fueled with CNG has more tolerance to air diluted conditions from the point of view of cycle-to-cycle variability.

As shown in this section, the sources of combustion variability are various and complex. Because of the different event that triggers the cycle-to-cycle combustion variability, for every operating tested condition the combustion flame characteristics might have a different probabilistic distribution [3], whose modeling will be the focus of the next section.

From this study four points may be highlighted:

- The delay between the spark and the SOC introduces certain variability as the combustion does not start always at the same point. This can be attributed to both the local turbulence and air-to-fuel ratio near the spark plug.
- The TJI ignition method has less variability than SI, which can be associated to the fast burning rate of TJI combustion.
- Lean combustion increases the cycle to cycle variability in TJI combustion.
- The effect on the combustion variability under lean combustion is higher when the engine is fueled with gasoline in TJI combustion

5.3 Cycle-to-cycle variability distribution

In order to model the combustion variability in SI combustion, a previous analysis from experimental data was performed in engine A fueled with gasoline. With the aim to obtain information about the distribution of the variability, the crank angle values at 10 %, 50% and 90% of the total MFB were collected on for each cycle, the data is represented in histograms in Figure 5.5.

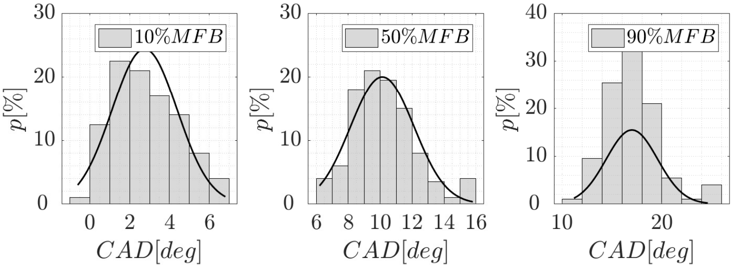

Figure 5.5: *Crank angle histograms for 10 % (left), 50 % (middle) and 90 % (right) of the MFB for operating test* $OP_A = 6$*.*

To evaluate if all operating points adjust to a normal distribution, two hypothesis tests algorithms were selected: Lilliefors and Anderson-Darling. These tests are used to check the statistical characteristic of the crank angle values at each percentage of combustion. Detailed information about the hypothesis tests can be found in Appendix 5.A.

These hypothesis tests were performed over 12 operating conditions OP_A at 4 SA settings, which leads to 48 sets, results are shown in Figure 5.6. Where, H = 0 indicates that the distribution is normal and H = 1 otherwise.

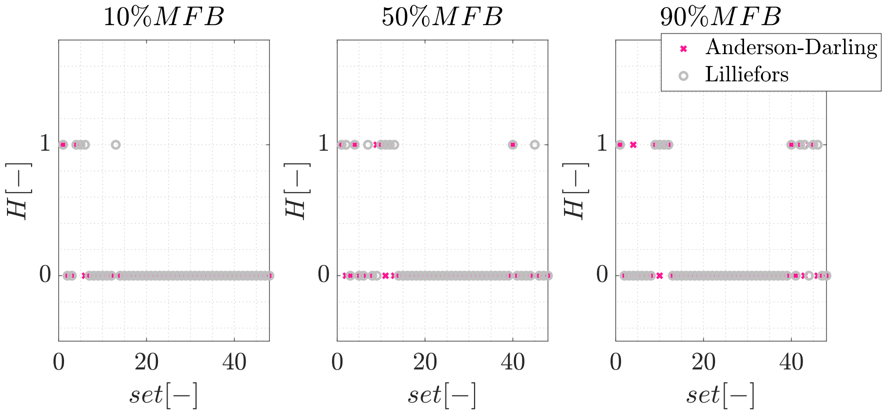

Figure 5.6: *Hypothesis tests performed over OP_A operating points for 10 % (left), 50 % (middle) and 90 % (right) of the MFB.*

As it can be seen in Figure 5.6, although some sets are not normally distributed, most sets from experimental data can be described as a normal distribution (see Table 5.1). In next section the variability will be modeled by a normal probability distribution, regardless of the disturbance it is triggering the variability.

Table 5.1: *Percentage of H = 0 cases for each CAx.*

Test	CA10	CA50	CA90
Anderson Darling	93.87	87.75	81.63
Lilliefors	89.79	79.6	79.56

5.4 Cycle to cycle variability model

In previous sections was shown that the cycle-to-cycle variability in IC engines depends on several factors such as combustion phasing, fuel type, λ, EGR or ignition system, and that the distribution of such variability can be described by a normal distribution in most of the cases for engine A. In this section, a cycle-to-cycle variability model for SI engines running at stochiometric conditions without EGR is presented.

The combustion model presented in Chapter 4 has been calibrated to reproduce the mean engine performance in steady conditions. However, in SI combustion important cycle-to-cycle variability can be observed, even during steady state conditions. For this reason, the combustion parameters can not be calculated in a deterministic manner [11]. The procedure to analyze the cycle-to-cycle variability is based on computing the standard deviations of the CAD at different percentages of the MFB, CAx where x represents the combustion percentage. The MFB will be divided every 5% in this analysis.

The modeling process of the combustion variability will be divided into two different parts: first, the description of the variability model by using the error propagation theory. Then, the calibration procedure of the constants standard deviation. It was decided not to include X_3 constant to model the cycle-to-cycle variability, because as it was discussed in Chapter 4, X_3 is a constant that is calibrated for a given engine, and it is independent on the operating condition point.

5.4.1 Variability model

In Figure 5.7 (top plot) the combustion phase evolution over 30 cycles is shown in grey line, the average over 200 cycles is represented in black line. In bottom plot the standard deviation of the CA_x for these 200 cycles at each combustion location is also represented.

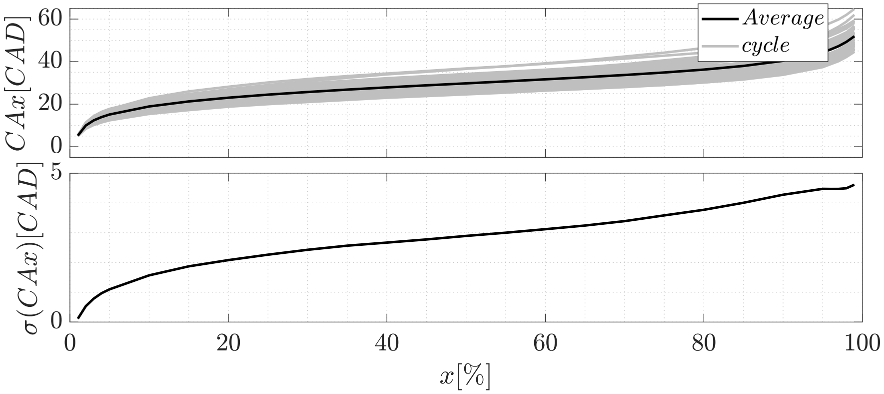

Figure 5.7: *Average (top plot) and the standard deviation (bottom plot) of the* CA_x *at each percentage of combustion over 200 cycles at* $OP_A = 16$ *with the SA at -2 CAD-ATD.*

The combustion phase variability shown in Figure 5.7, and hence the combustion phase location, are directly related with the IMEP variability, and in consequence with the combustion efficiency. For this reason, the combustion efficiency is also affected by the cycle-to-cycle variability.

Because in the combustion model there is no expression to be able to compute the variance, i.e. an expression to compute the derivative, the variability will be modeled by the error propagation theory, by assuming that, no matter which is the disturbance triggering the variability, it can be modeled by a normal probability distribution at S_l and u_t. Such as:

$$\sigma_{CAx}(\%) = f_\sigma\left(\mathcal{N}_1(\overline{X_1}, \mathrm{CV}_1), \mathcal{N}_2(\overline{X_2}, \mathrm{CV}_2)\right) \tag{5.1}$$

where f_σ is the function which propagates two distributions, namely $\mathcal{N}_1$ and $\mathcal{N}_2$, on the combustion model presented in Chapter 4.

Normal distributions are characterized by a mean value that represent the mean combustion phase evolution, $\overline{X_1}$ and $\overline{X_2}$, and a variability, which can be defined as the coefficient of variation CV as:

$$\mathrm{CV}_1 = \frac{\sigma(X_1)}{\overline{X_1}}100, \mathrm{CV}_2 = \frac{\sigma(X_2)}{\overline{X_2}}100 \tag{5.2}$$

In Figure 5.8 the experimental variability found in $OP_A = 16$ at each CAx location is shown in dashed line, three cases of CV_1 and CV_2 are also represented in continuous line: the optimal one, only CV_2, and only CV_1.

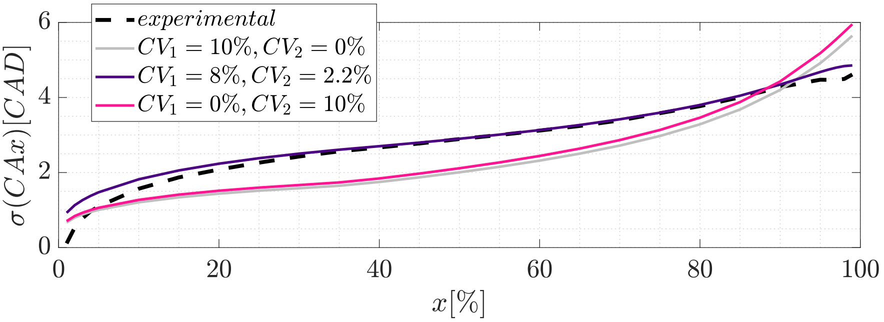

Figure 5.8: *Variability found with experimental data and 3 combinations of CV_1 and CV_2. Operating condition: $OP_A = 16$.*

All possible values for X_1 and X_2 should be analyzed, as:

$$MFB(i,j,\theta) = f_c(X_{1i}, X_{2j}) \tag{5.3}$$

where MFB(i,j,θ) is the mas fraction burned at CAD $= \theta$ when S_l and u_t are modeled by constants X_{1i} and X_{2j} respectively. Subsequently, the position at each % of the combustion (CA_{xij}) is computed, and then, the mean $(\overline{CA_x})$ and the standard deviation $(\sigma(CA_x))$ can be obtained as following:

$$\overline{CA_x} = \sum_i \sum_j CA_{xij} P_{ij} \tag{5.4}$$

$$\sigma(CA_x) = \sqrt{\sum_i \sum_j P_{ij} \left(CA_{xij} - \overline{CA_x}\right)^2} \tag{5.5}$$

where P_{ij} represents the probability density function of each possible combination of X_{1i} and X_{2j}, which must satisfy that the sub-indexes i and j are used for each execution at each constants, and note that the axis are normalized in order to represent the proportional effect at each constant. Henceforth:

$$A_{1i} = X_{1i}/\overline{X_1}, A_{2j} = X_{2j}/\overline{X_2} \tag{5.6}$$

$$\sum_i \sum_j P_{ij} = 1 \tag{5.7}$$

The problem with this model is that computing all the possible variations leads to a high computational burden. Figure 5.9 (left) shows the normalized probability density functions, in right plot for the optimal solution, namely CV$_1$ = 8% and CV$_2$ = 2.2% is represented. For a sufficient precision, 100 values are used at each dimension: CV$_1$ and CV$_2$. These implies that to compute all the possible combustion phase combinations the model should be executed 100x100 times.

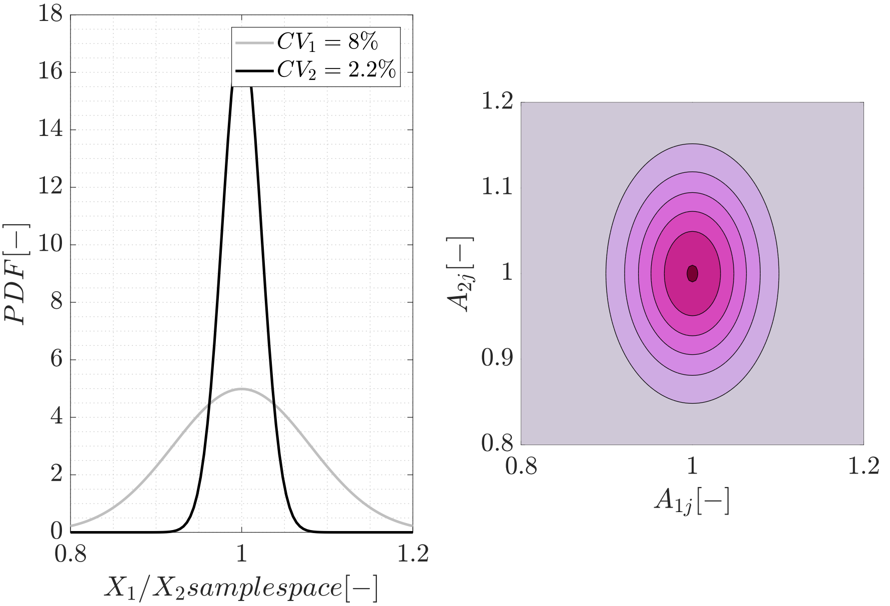

Figure 5.9: *Left: Probability density function for* $CV_1 = 8\%$ *and* $CV_2 = 2.2\%$*. Right: Optimal probability function* P_{ij} *:* $CV_1 = 8\%$ *and* $CV_2 = 2.2\%$*.*

In order to develop a model with lower computational burden, two hypothesis have been made:

- The cross effects between the two dimensions, namely A_1 and A_2, can be neglected, and the following assumption may be done:

$$CA_x(A_1, A_2) = \sigma(A_1, 1) + \sigma(1, A_2) \tag{5.8}$$

- A quadratic dependence of CA_x with each parameter is assumed, i.e. the second derivatives of the CA_x with respect to X_1 and X_2 variations are constant:

$$\frac{\mathrm{d}CA_x^2}{\mathrm{d}^2\Delta X_1} = X_{12} \tag{5.9}$$

$$\frac{\mathrm{d}CA_x^2}{\mathrm{d}^2\Delta X_2} = X_{22} \tag{5.10}$$

$$\tag{5.11}$$

Integrating and combining Equations (5.9):

$$CA_x = \frac{m_i^2}{2}\Delta x_i + dX_{i0}\Delta x_i + CA_{x0} \tag{5.12}$$

where CA_{x0} is the mean CA_x, m_i and dx_{i0} are constants values for each parameter which define the dependence of CA_x respect to the dimensions: A_1 and A_2.

Making these assumptions, the variability can be computed by executing the model 5 times. In Figure 5.10 the five iterations selected are marked with crosses: one at the mean value value (X_1 and X_2) and the remains using a 20% variation ($A_1 = [0.8, 1.2]$ and $A_2 = [0.8, 1.2]$). The derivatives are computed by Euler finite differences. Finally, a projection from these points of the evolution of the derivative is done (pointed out by circles in Figure 5.10).

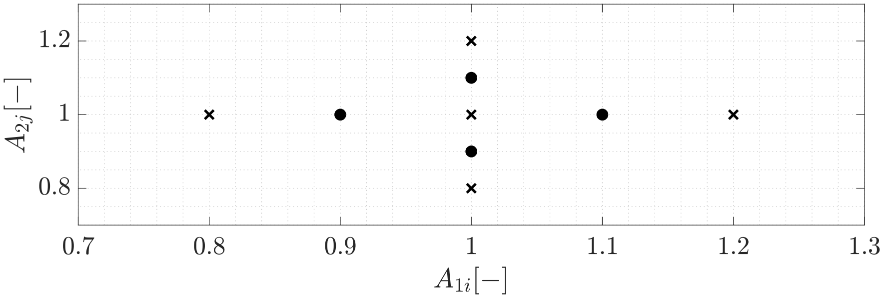

Figure 5.10: *Proposed simulations to obtain the variability at all the range.*

The estimations must be updated cycle by cycle, since the model inputs (intake pressure, air mass flow, SA, and engine speed) lead to modify the function (5.1).

In Figure 5.11 the impact on the CA50 when A_1 and A_2 are modified is represented. In black, the value computed at 100 iterations along A_1 and A_2 is shown, and in grey the linear interpolation is represented.

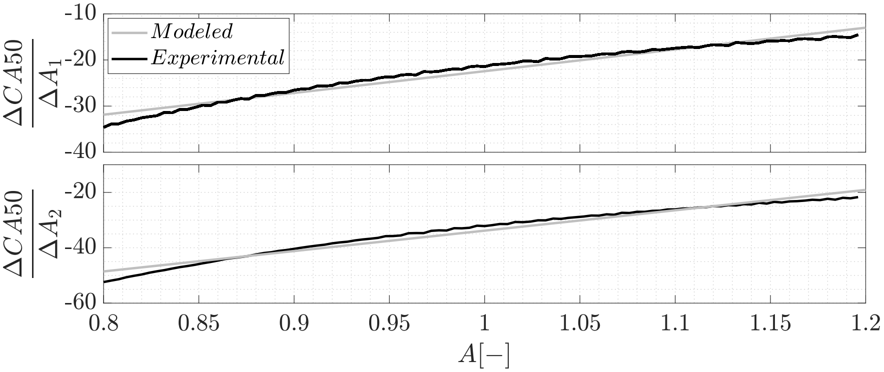

Figure 5.11: *Variation of CA50 as a function of X_1 and X_2.*

Note that increasing A_1 by 0.1, i.e. increasing X_1 by a 10%, then the CA50 increases 1 CAD (combustion advanced). When reducing A_1 by 0.1, the combustion is retarded 1.5 CAD. Hence, the effect is lower near the SOC, while the effect leads to increase near the EOC. Even though the function is not linear, the linear approximation behaves with sufficient accuracy, values below 15%.

In Figure 5.12 the discrepancies between the complete model (100x100) and the 5 iteration simulation is represented: on top the variability and bottom plot the error between both simulations. As can be seen, the error of the five-points approximation is below the 4 % for all the combustion evolution. But the time consumed for 100x100 case was 51 s, while for 5 iteration case less than 0.1 s.

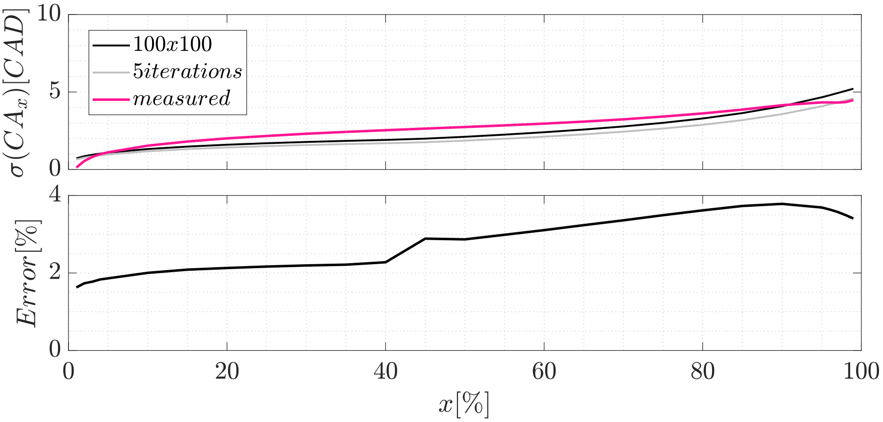

Figure 5.12: *Probability calculation* $OP_A = 16$. *Top plot: Variability measured compared with 100x100 and 5 iteration model. Bottom plot: Differences in percentage between the 100x100 calculation and the five-point iterative method.*

5.4.2 Calibration of the variability model

The combustion variability model calibration is performed by least-squares adjustment between the variability model curve and the experimental data curve. These curves represent the CAD standard deviation values at a certain CAx. Figures 5.13 shows the calibration of such functions over the conditions tested (OP_A).

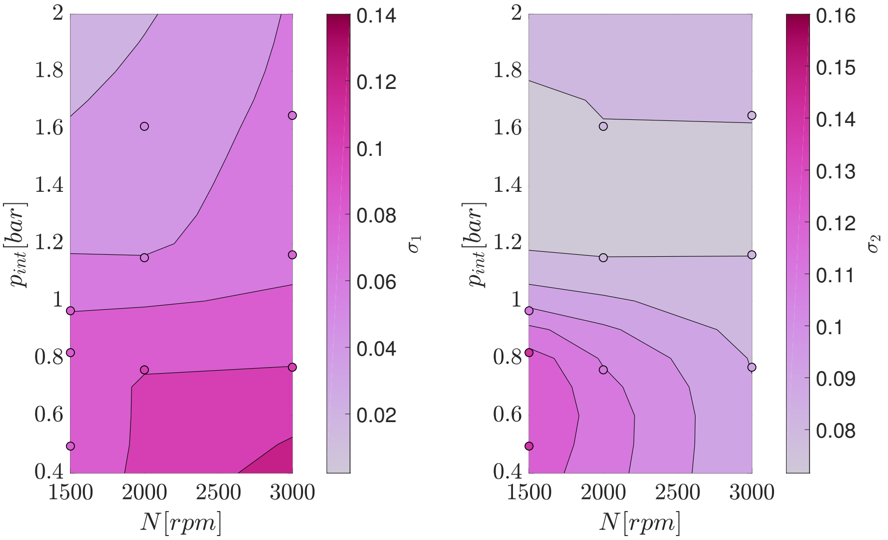

Figure 5.13: *Open loop map for σ_1 (left) and σ_2 (right).*

Nevertheless, in order to determine σ_1 and σ_2 a correction needs to be set when the SA is far away from the TDC since both parameters tend to be reduced. This correction has been only applied at low load condition where the SA was at early locations reducing hence the variability. The final value is obtained by:

$$\sigma_1 = \sigma_{OL1}(n, p_{int}) - f_{\sigma c1}(n, SA) \tag{5.13}$$

$$\sigma_2 = \sigma_{OL2}(n, p_{int}) - f_{\sigma c2}(n, SA) \tag{5.14}$$

The correction applied is shown in Figure 5.14.

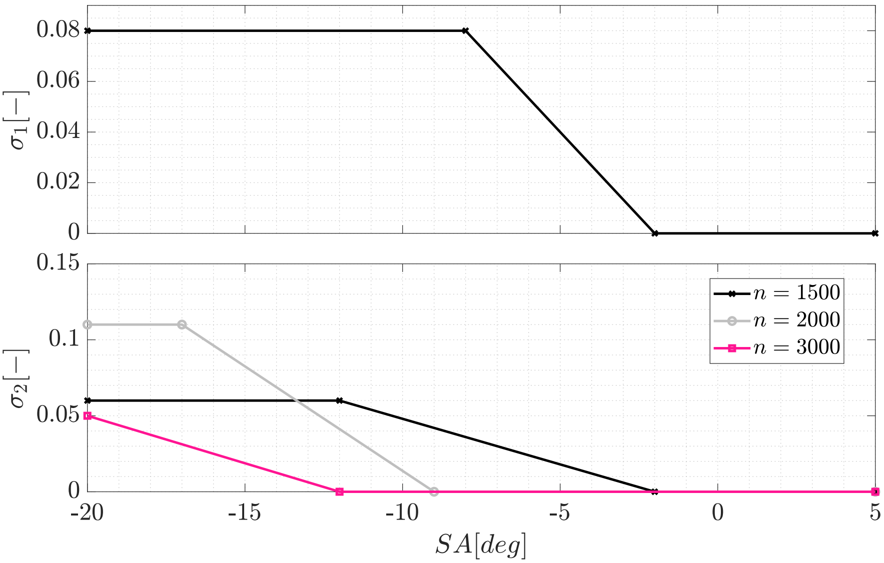

Figure 5.14: *Corrections applied to σ_1 and σ_2 in order to contemplate the effect of the SA.*

5.5 Validation

5.5.1 Training data-set

Figure 5.15 shows the mean absolute error (top) and the mean relative error (bottom) of the model, the variability propagation is computed at each % of the combustion evolution. The left plot shows the results from all operating points OP_A at 2000 rpm and right plot at 3000 rpm.

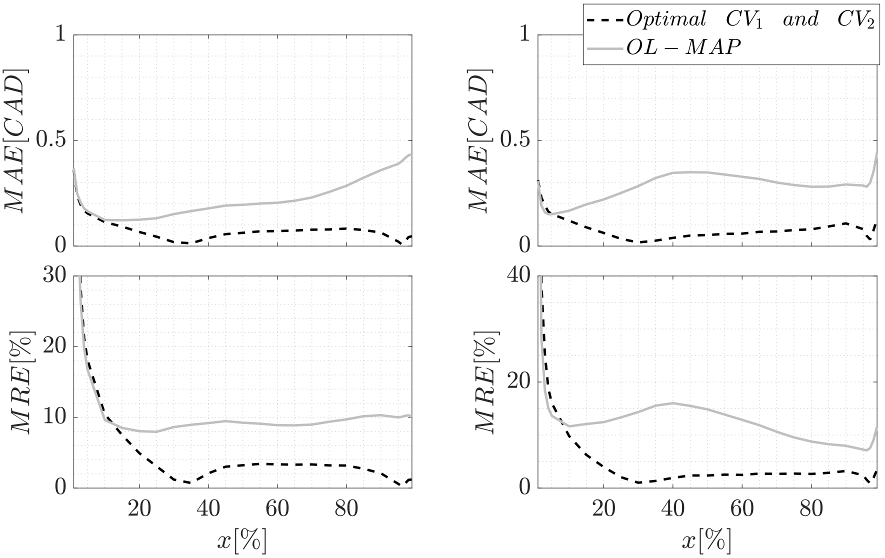

Figure 5.15: *Mean absolute error (top) and mean relative error (bottom) for the variability model at each % of the evolution for training data set: left 2000 rpm and right 3000 rpm.*

Note that for both cases, the model is able to reproduce the cycle-to-cycle variability with a relative error bellow 4% in cases where the noise is updated at each operating condition, on the other hand, if the noise is obtained from OL maps the error is less than 10 % for 2000 rpm cases, and less than 15 % for 3000 rpm cases. To obtain a better approximation, the operating conditions should be updated with at least three inputs (SA, n, p_{int}). The error between SOC and CA5 are above 20% because of the assumption that the SOC is located at the SA and no initial variability is considered for this parameter.

5.5.2 Transient data-set

The model was validated in transient conditions in engine A during transient $T12$. For a quantitative analysis, the average CAx and its variation have been quantified with two IIR filters, as:

$$\overline{CAx}_{k+1} = k_{fm}\overline{CAx}_k + (1 - k_{fm})CAx_{k+1} \quad (5.15)$$

$$\overline{\sigma}^2_{k+1} = k_{f\sigma}\overline{\sigma}^2_k + (1 - k_{f\sigma})\sigma^2_{k+1} \quad (5.16)$$

where k_{fm} and $k_{f\sigma}$ are fixed at 0.96 and 0.98 respectively, which are used to filter the CA_x and the variability measured from in-cylinder pressure sensors.

The variance at each cycle (σ^2) is obtained from:

$$\sigma_k^2 = (\overline{CAx}_k - CAx_k)^2 \tag{5.17}$$

In Figure 5.16 a portion of the test is shown: where the CA20 (top plot), CA50 (medium plot), and the CA90 (bottom plot) are represented. Cycle to cycle measurements are illustrated with magenta crosses, and the model output is represented with a black line.

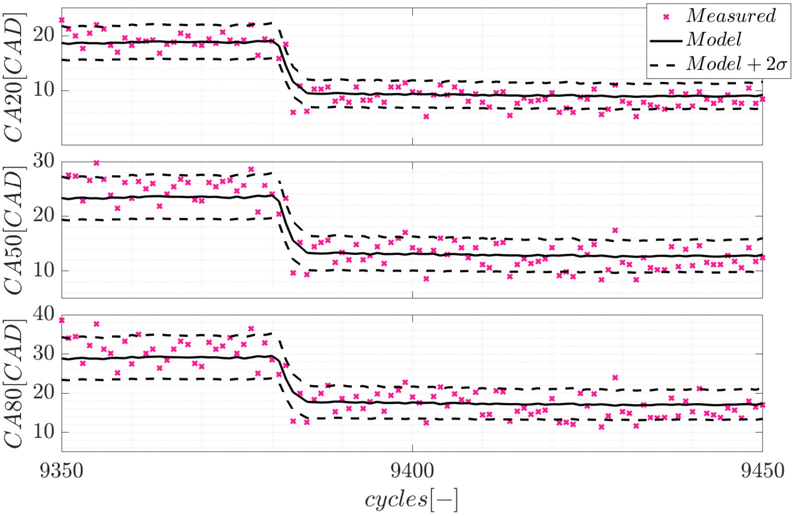

Figure 5.16: *Cycle-to-cycle evolution and model output of the CA20 (top plot), CA50 (medium plot), and CA80 (bottom plot).*

In Figure 5.17 the evolution of the CA50 (top plot) and its variability (bottom plot) during the complete transient test are shown. The experimental values are shown in black line, while the model output is represented in magenta line.

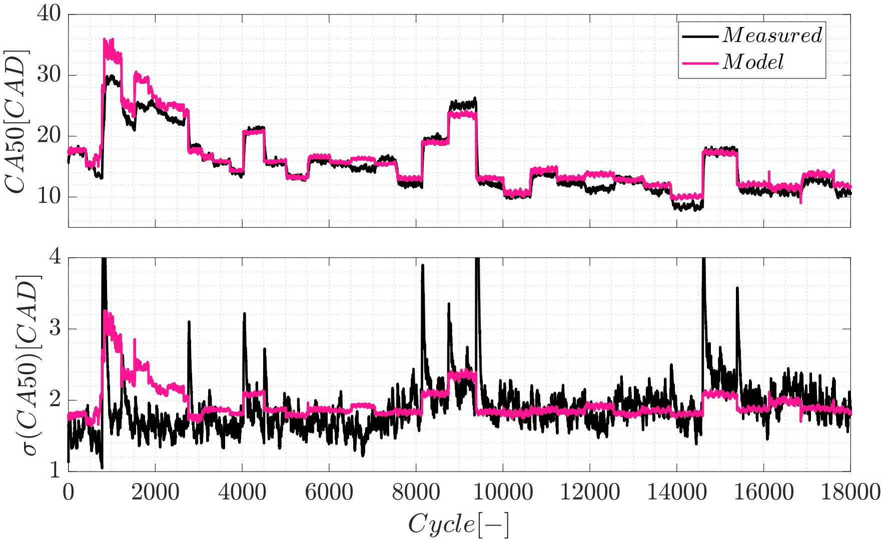

Figure 5.17: *CA50 evolution and its variability during the transient test.*

The mean relative error of the model at each % of the combustion is represented in Figure 5.18. During this transient test the combustion model was able to predict the mean value with an average error of 5% at each % of the combustion, while the error on the variability model predicted was of the 15 %.

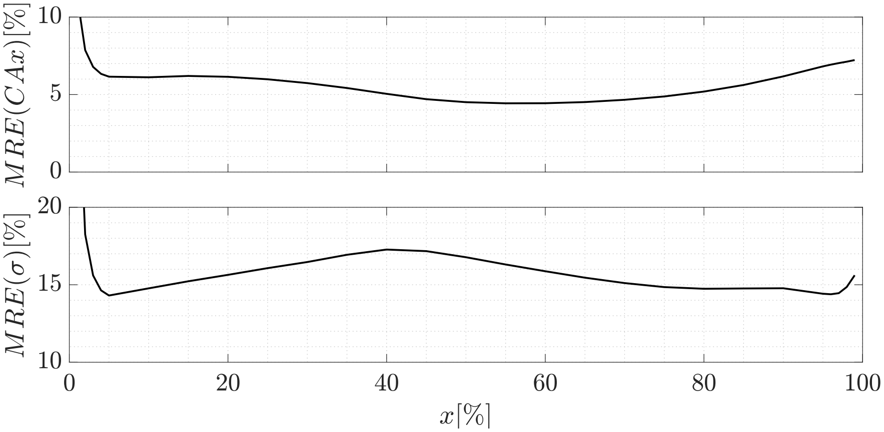

Figure 5.18: *Mean relative error of the CAx and its variation predicted by the model.*

5.6 Conclusions

In this Chapter the combustion variability has been analyzed and modeled. The first part of the Chapter analyzed experimental data, and the impact of fuel on cycle-to-cycle variability. Then, the combustion variability distribution in engine A was analyzed, concluding that the variability over training data set is normally distributed. Then, the combustion model for SI engines presented in Chapter 4 has been used to predict the average combustion phase evolution, and during this Chapter a variability model to predict the cycle-to-cycle variability at each % of the combustion has been developed.

The variability was modeled by the propagation of a probability distribution on the laminar flame speed, and a second one over the turbulent intensity of the model introduced in Chapter 4. The model was validated in engine A, where the engine speed, the SA, and the VGT were modified. The propagation of the variability is able to predict the cycle-to-cycle variability with a mean relative errors of 15% under transient and steady conditions.

5.A Hypothesis test

A normal distribution can be fitted at each combustion percentage for this operating points. The mean of the data and the variance can be estimated as:

$$M = \frac{1}{N}\sum_{i=1}^{N} A_i \tag{5.18}$$

$$\sigma = \sqrt{\frac{1}{N-1}\sum_{i=1}^{N} |A_i - M|^2} \tag{5.19}$$

For these tests two hypotheses are raised, the null hypothesis H_0, and the alternative hypothesis H_1, which can be described as:

$$\begin{array}{lll} H_0: & H=0 & : \text{ the distribution is normal} : X \sim \mathcal{N}(\mu, \sigma^2) \\ H_1: & H=1 & : \text{ the distribution is not normal} : X \nsim \mathcal{N}(\mu, \sigma^2) \end{array}$$

In this work a 5% significance level are chosen to evaluate the distributions.

$$
\begin{aligned}
p_{valor} &> \alpha : \text{does not reject } H_0 && (5.20)\\
p_{valor} &< \alpha : \text{reject } H_0 && (5.21)\\
& && (5.22)
\end{aligned}
$$

Bellow, each hypothesis test is explained in detail [12].

- Lilliefors: Is a normality test based on the Kolmogorov-Smirnov test. The statistic D_L is the largest absolute difference observed between the observed cumulative distribution function $S_n(X)$ and the normal cumulative distribution function $F^*(X)$, as:

$$D_L = max_{1 \leqslant j \leqslant n} |F^*(X_j) - S_n(X_j)| \tag{5.23}$$

$$
\begin{aligned}
\text{If } D_L &\leqslant D_\alpha : \text{does not reject } H_0 && (5.24)\\
\text{If } D_L &> D_\alpha : \text{reject } H_0 && (5.25)\\
& && (5.26)
\end{aligned}
$$

where D_α is tabulated, and for a normal distribution and $\alpha = 0.05$, $D_\alpha = 0.895$ [13].

- Anderson-Darling: The statistic is defined as:

$$A^2 = -n - S \tag{5.27}$$

where S is computed as:

$$S = \sum_{j=1}^{n} \frac{2j-1}{n} \left[ln(F(X_j) + ln(1 - F^*(X_{n+1-j})) \right] \tag{5.28}$$

where the expected cumulative distribution function of the specific distribution is $F^*(X_j)$.

If the test statistic A^2 is less than the critical value from the previous point, the null hypothesis H_0 cannot be rejected; otherwise, it is rejected. For a normal distribution and $\alpha = 0.05$, the critical value is A_α 0.752 [14].

$$\text{If } A \leqslant A_\alpha : \text{does not reject } H_0 \tag{5.29}$$
$$\text{If } A > A_\alpha : \text{reject } H_0 \tag{5.30}$$
$$\tag{5.31}$$

References

[1] Ozdor Nir, Dulger Mark and Sher Eran. "Cyclic variability in spark ignition engines a literature survey". *SAE transactions*, pp. 1514–1552, 1994. (cited in pp. 89 and 90)

[2] Heywood John B. *Internal combustion engine fundamentals*. McGraw-Hill Education, 2018. (cited in pp. 19, 26, 64, 66, 90, and 186)

[3] Galloni Enzo. "Analyses about parameters that affect cyclic variation in a spark ignition engine". *Applied Thermal Engineering*, Vol. 29 n^o 5-6, pp. 1131–1137, 2009. (cited in pp. 90 and 94)

[4] Maldonado Bryan P, Freudenberg James S and Stefanopoulou Anna G. "Stochastic feedback combustion control at high dilution limit". In *2018 annual American control conference (ACC)*, pp. 1598–1603. IEEE, 2018. (cited in p. 90)

[5] Maldonado Bryan P and Stefanopoulou Anna G. "Cycle-to-cycle feedback for combustion control of spark advance at the misfire limit". *Journal of Engineering for Gas Turbines and Power*, Vol. 140 n^o 10, 2018. (cited in p. 90)

[6] Novella Ricardo, Pla Benjamin, Bares Pau and Martinez-Hernandiz Pablo José. "Closed-Loop Combustion Control by Extremum Seeking with the Passive-Chamber Ignition Concept in SI Engines". Technical report, SAE Technical Paper, 2020. (cited in p. 90)

[7] Maldonado Bryan P, Bieniek Mitchell, Hoard John, Stefanopoulou Anna G, Fulton Brien and Nieuwstadt Michiel Van. "Modelling and estimation of combustion variability for fast light-off of diesel aftertreatment". *International Journal of Powertrains*, Vol. 9 n^o 1-2, pp. 98–121, 2020. (cited in p. 90)

[8] Ma Fanhua, Ding Shangfen, Wang Yu, Wang Yefu, Wang Junjun and Zhao Shuli. "Study on combustion behaviors and cycle-by-cycle variations in a turbocharged lean burn natural gas SI engine with hydrogen enrichment". *International journal of hydrogen energy*, Vol. 33 n^o 23, pp. 7245–7255, 2008. (cited in p. 91)

[9] López JJ, Novella R, Gomez-Soriano J, Martinez-Hernandiz PJ, Rampanarivo F, Libert C and Dabiri M. "Advantages of the unscavenged pre-chamber ignition system in turbocharged natural gas engines for automotive applications". *Energy*, Vol. 218, pp. 119466, 2021. (cited in pp. 91 and 92)

[10] Hua Jianxiong, Zhou Lei, Gao Qiang, Feng Zhonghui and Wei Haiqiao. "Effects on Cycle-to-Cycle Variations and Knocking Combustion of Turbulent Jet Ignition (TJI) with a Small Volume Pre-Chamber". Technical report, SAE Technical Paper, 2020. (cited in p. 92)

[11] Bares Pau, Selmanaj Donald, Guardiola Carlos and Onder Christopher. "Knock probability estimation through an in-cylinder temperature model with exogenous noise". *Mechanical Systems and Signal Processing*, Vol. 98, pp. 756–769, 2018. (cited in p. 97)

[12] Öner Metin and Deveci Kocakoç İpek. "JMASM 49: A compilation of some popular goodness of fit tests for normal distribution: Their algorithms and MATLAB codes (MATLAB)". *Journal of Modern Applied Statistical Methods*, Vol. 16 n^o 2, pp. 30, 2017. (cited in p. 110)

[13] Molin Paul and Abdi Hervé. "New Table and Numerical Approximations for Kolmogorov-Smirnov/Lilliefors/van Soest Normality Test". *Dijon: University of Bourgogne*, 1998. (cited in p. 110)

[14] Stephens Michael A. "The anderson-darling statistic". Technical report, Department of statics, Stanford University., 1979. (cited in p. 111)

CHAPTER 6

In-cylinder resonance modeling

Contents

6.1 Introduction

In-cylinder pressure oscillations are a consequence of different factors that must be controlled for safe and optimum operation of IC engines [1]. In SI engines, the auto-ignition of the end gas heavily excites resonance, what causes a reduction on the combustion efficiency and can damage the engine [2]. In compression ignited (CI) engines the in-cylinder resonance excitation is mostly caused by the amount of premixed combustion due to a long ignition delay [3]. A common strategy to reduce noise level in CI engines consists on using multiple injection to minimize the resonance excitation [1]. In new combustion modes, for example homogeneous charge compression ignition (HCCI), RCCI or TJI, combustion heavily excite resonance due to fast burning rates and normal combustion can be classified as knock [4].

In this chapter the in-cylinder resonance excitation in IC engines is analyzed and characterized in three different combustion modes: SI, TJI and RCCI. First, the resonance theory is presented, where Drapers equation is analyzed and a different approach that takes into account factors such as the viscosity of the fluid is investigated. Then, the in-cylinder pressure time-frequency analysis is explained, there the tools used are presented and in-cylinder pressure signal processing is described. Next, engines A and B are used to developed a model able to reproduce the amplitude evolution during knocking and normal combustion, by assuming a constant attenuation during the cycle. After, a different approach is presented: a pressure resonance attenuation model, where engines A, B and C are used to developed a model able to predict the attenuation evolution during a cycle of the in-cylinder resonance excitation.

6.2 Resonance theory

In-cylinder pressure oscillations are the product of complex phenomenon including the transport of pressure waves in the combustion chamber. In this sense, they can be studied by means of the so-called wave equation, which is derived from the conservation of momentum equation, where the following hypothesis are considered:

- No mass generation.
- Viscous effects are neglected.
- The process is isentropic: No heat transfer and no internal losses.

The wave equation is expressed as following:

$$\frac{\partial^2 p}{\partial t^2} = a^2 \nabla^2 p \tag{6.1}$$

where p represents the pressure, a the speed of sound in the combustion chamber, ∇^2 is the Laplacian operator and t is time.

In order to describe the in-cylinder resonance pressure oscillations in the combustion chamber, the 3D wave equation (6.1) can be written in the cylindrical coordinates, as following:

$$\frac{\partial^2 p}{\partial r^2} + \frac{1}{r}\frac{\partial^2 p}{\partial r^2} + \frac{1}{r^2}\frac{\partial^2 p}{\partial \phi^2} + \frac{\partial^2 p}{\partial z^2} = \frac{1}{a^2}\frac{\partial^2 p}{\partial t^2} \tag{6.2}$$

The analytic solution for Equation (6.2) was solved in [5], where the author gave a general solution with cylindrical contour conditions by introducing Bessel functions.

$$p = \sum A_{i,j,g} J_a(B_{i,j} r) e^{2\pi f t} \begin{Bmatrix} cos \\ sin \end{Bmatrix} (i\phi) cos(\frac{g\pi}{h} z) \tag{6.3}$$

$A_{i,j,g}$ are constant for every mode represented by sub indexes i, j and g. The proposed solution leads to the following expression for the resonance frequency:

$$f_{(i,j)} = a\sqrt{(\frac{B_{(i,j)}}{\pi D})^2 + (\frac{g}{2h})^2} \tag{6.4}$$

where g are the axial modes, which can be neglected near the TDC since the bore (D) is high compared with the height of the chamber (h) ($h <$ D) [6], a the speed of sound and $B_{(i,j)}$ are the Bessel constants of each mode (i,j), where i is the number of circumferential modes and j is the number of radial pressure modes [7]. Assuming ideal gas, the speed of sound can be computed from the trapped mass m_{cyl}, the in-cylinder pressure p_{cyl}, and estimating the instantaneous volume of the chamber V, as following:

$$a = \sqrt{\frac{\gamma p_{cyl} V}{m_{cyl}}} \tag{6.5}$$

where γ is the specific heat capacities ratio of the gases, which can be modeled such as suggested in [8], where polynomial expressions are use to represent the in-cylinder temperature .

Figure 6.1 shows the first 4 circumferential modes, Bessel constants for this modes are collected in Table 6.1.

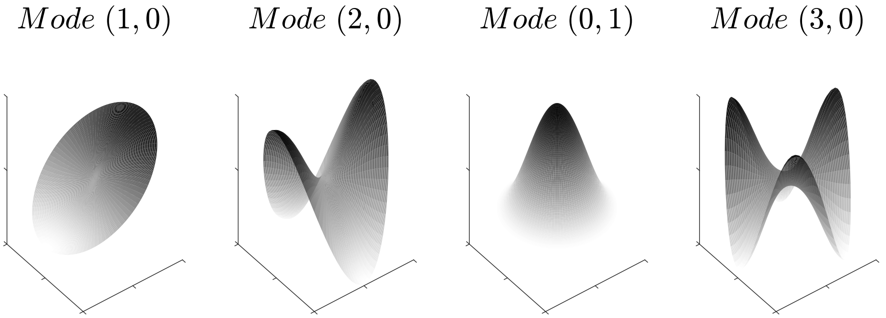

Figure 6.1: *Resonant mode shapes of first 4 modes.*

Table 6.1: *Bessel constants for first 4 resonant modes*

i	j	$B_{(i,j)}$
1	0	1.841
2	0	3.054
0	1	3.831
3	0	4.021

Figure 6.2 (bottom) shows the spectrograms of the in-cylinder pressure signal whose high-pass (f > 4000 Hz) filtered signal is shown in Figure 6.2 (top). The theoretical resonant frequency evolution of the first mode described by Equation (6.4) is represented in red dashed line.

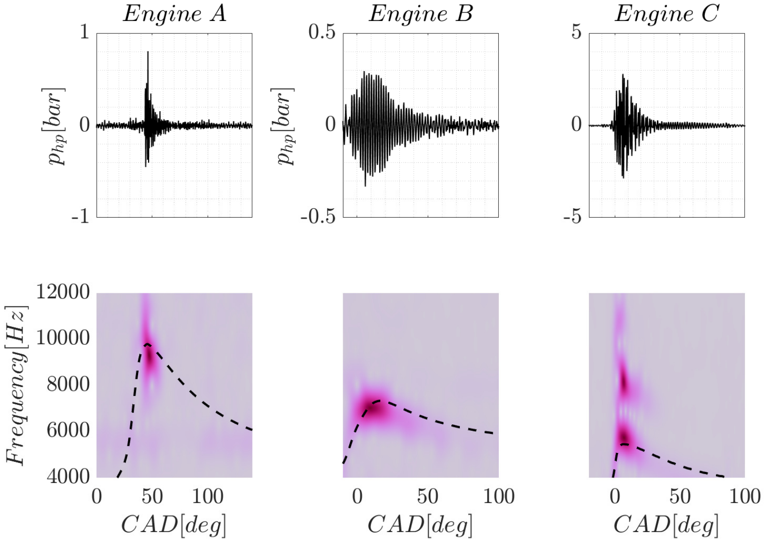

Figure 6.2: *In-cylinder signal. Top plot: High pass in-cylinder pressure. Bottom plot: Time-frequency spectrum of the in-cylinder pressure signal in engines: A (left), B (middle) and C (right).*

As can be seen in Figure 6.2, the most excited frequency in the pressure signal is the first mode for all engines, and please note that $D_A < D_B < D_C$ and this has an impact on the resonance frequency. Drapers equation is the most widely used method to analyze the knocking frequencies [9], but it must be noticed that Equation (6.4) only computes the resonance frequency, but not the amplitude of such oscillation. Such amplitude depends on how combustion excites the acoustic field inside the combustion chamber, and such oscillation is attenuated during the piston stroke because of the finite impedance of the walls and the viscosity of fluid. However, the resonance intensity evolution is an important parameter to take into account in order to analyze knock phenomenon [10].

In order to develop a model able to predict the evolution of the amplitude of the resonance, an approach to real frequency attenuation in ducts presented in [11] is analyzed. In [11], the viscous effect during the resonance attenuation has been studied, where the damping of the amplitude of such oscillation was modeled by a constant as a function of the oscillation frequency and the thermodynamic conditions of the gases. Nevertheless, this study analyzes the propagation of the wave along ducts and the real impedance of the walls was not considerated. In this case, the stationary wave solution was derived as a function of the distance to the source (z), such as:

$$p = Ae^{j\omega t}e^{j\beta z} \tag{6.6}$$

where A is the initial amplitude, ω the angular speed and the constant wave number. The constant wave number (β) is divided in a real part (k_0), representing the oscillation frequency, and a imaginary part (α), which represents the attenuation.

$$\beta = \pm k_0 + \alpha - j\alpha \tag{6.7}$$

When solving the equations (6.6) and (6.7) with the aforementioned assumptions the damping coefficient is obtained as:

$$\alpha = \frac{1}{ra}(\frac{\omega\mu}{2\rho})^{\frac{1}{2}} \tag{6.8}$$

where r is the radius of the duct, μ the viscosity, and ρ the density of the gas.

The approximation presented in Equation (6.6) will be used during followings sections to model the attenuation amplitude in the combustion chamber.

6.3 In-cylinder pressure time-frequency analysis

In this section the in-cylinder pressure time-frequency analysis is presented. The section is divided in two parts: first, time-frequency analysis tools used are presented and discussed, and then, the in-cylinder signal processing based on the tools previous introduced is described.

6.3.1 Time-frequency tools

The Fast Fourier Transform (FFT) is an extensively used tool used for the analysis of a signal in frequency domain, which decomposes the signal $s(t)$ in constant frequency harmonics $F(f)$ as:

$$F(f) = \int_{-\infty}^{\infty} s(t)e^{-j2\pi ft}dt \tag{6.9}$$

which can be discretized in the crank angle (θ) domain:

$$F(f) \approx \sum_{-\infty}^{\infty} s(t)(\theta) e^{-j2\pi f t(\theta)} \Delta t(\theta) \tag{6.10}$$

where $\Delta t(\theta)$ is defined as:

$$\Delta t(\theta) = \frac{\Delta\theta}{6n(\theta)} \tag{6.11}$$

where n is the engine speed, and $\Delta\theta$ the crank angle resolution.

In-cylinder pressure signal is not stationary, i.e the amplitude and spectrum of the signal change in time. If the spectrum of the signal is time dependent, sufficiently short elements needs to be used to analyze the spectrum, with the certainty that the spectrum is constant over each segment.

In order to separate these two phenomena time-frequency analysis is necessary, such as Short Time Fourier transform (STFT) or Wigner Distribution (WD). The STFT provides the amplitude for a given signal in the frequency domain at time or CAD position by windowing the in-cylinder pressure signal and moving the window along different CAD position. This permits to reduce the order of discontinuity at the boundary of the observation interval, more detail information about window function can be found in Appendix 6.A. The STFT is computed as:

$$P_{STFT}(\theta, f) = |F(f)|^2 = \sum_{\phi=-\infty}^{\phi=\infty} s(\theta)(\phi) w(\phi - \theta) e^{-j2\pi f t(\phi)} \Delta t(\phi) \tag{6.12}$$

However, high resolution in both, time and frequency, is not possible, i.e. for an adequate frequency analysis large windows are required, while such windows induce frequency components of the surrounding and as a consequence reduce the time resolution by filtering the estimation in time.

On the other hand, WD is a quadratic time-frequency distribution [12], which is defined as:

$$P_{WD}(\theta, f) = \sum_{\phi=-\infty}^{\phi=\infty} s(\theta - \frac{1}{2}\phi)s(\theta + \frac{1}{2}\phi)e^{-j2\pi f t(\phi)}\Delta t(\phi) \tag{6.13}$$

The issue with WD are the cross terms (interference terms) due to its quadratic nature. In Figure 6.3 two spectrograms computed by STFT and WD are compared: on the top plots STFT (left) and WD (right) spectrograms and on the bottom plot the band pass in-cylinder pressure. For STFT a $Blackman - Harris$ window is chosen for time-frequency analysis, the effect of the window is discussed in Apendix 6.A.

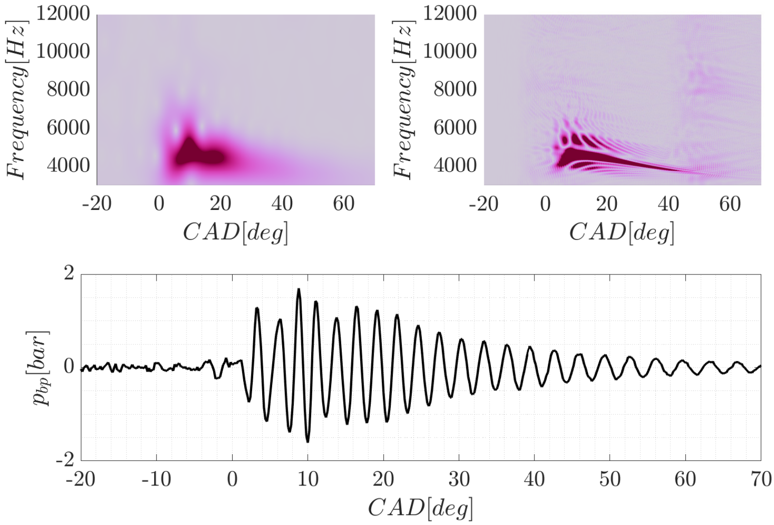

Figure 6.3: *Time frequency analysis of the in-cylinder pressure signal of engine C. Top left: spectrogram computed by STFT. Top right: spectrogram computed by WD. Bottom plot: Band-pass in-cylinder pressure.*

The WD provides the highest possible temporal-frequency resolution, but the computational burden for the WD distribution is higher than for the STFT, which discards the real-time application.

STFT and WD both present issues for real-time applications as the computation burden associated is high [13]. In order to characterize resonance evolution within the combustion chamber, a resonance indicator proposed in [14] is used. The authors propose a modified Fourier transform which contemplates the resonance theory by using a convolution with harmonics. Here, the indicator proposed is provided by widowed the in-cylinder pressure signal, and the intensity of the resonance is measured at each CAD position, and is defined as:

$$I_r(\theta) = \sum_{\theta=\theta_1}^{\theta=\theta_2} w(\theta-\theta_1)p_{bp}(\theta)e^{-2\pi \sum_{\psi=0}^{\psi=\theta} \frac{B\sqrt{\gamma(\psi)p_{lp}(\psi)V(\psi)}}{\pi D\sqrt{m}} T_s(\theta)} \tag{6.14}$$

where θ_1 and θ_2 define the CAD interval where the resonance analysis is performed, the window function w has a length of $\theta_2 - \theta_1$, $T_s(\theta)$ is the sampling period, which can be assumed as constant only in time-based acquisition or if the instantaneous engine speed fluctuations are negligible, B is the Bessel constant (1.842 for first radial mode), D is the cylinder bore, V the chamber volume, m the in-cylinder trapped mass, p_{lp} and p_{bp} are the low-pass and the band-pass in-cylinder pressure respectively. Here, a Blackman-Harris window function has been used.

The resonance amplitudes evolution computed from the STFT, WD and I_r are compared in Figure 6.4.

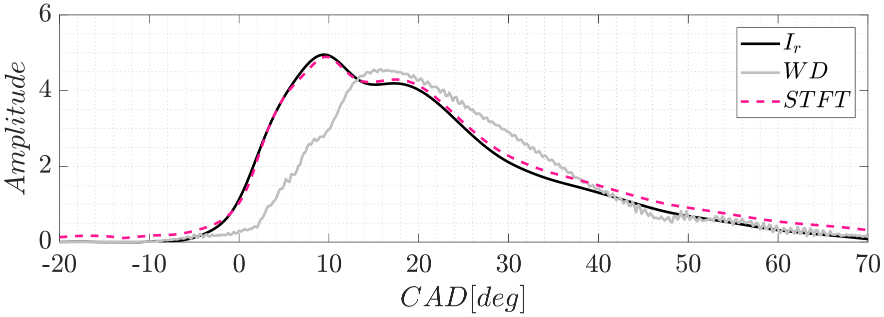

Figure 6.4: *Resonance attenuation evolution for case presented in Figure 6.3 computed by STFT, WD and Equation* (6.14)*.*

As shown in Figure 6.4, I_r case presented in Equation (6.14) and STFT has a simillar amplitude evolution, i.e the same window function was used for both analysis, but for WD the evolution is slightly different. In terms of computational time, the I_r is 4 times faster than the STFT, and the STFT 100 times faster than the WD.

6.3.2 In-cylinder pressure signal processing

The resonance amplitude evolution will be computed from in-cylinder pressure signal from Equation (6.14). STFT or WD are not selected since the computational burden is considerably higher than computed the resonance indicator [6].

Other parameter to be analyzed during this chapter is the attenuation of the resonance excitation. From in-cylinder pressure signal, the experimental resonance attenuation is computed following the scheme presented in Figure 6.5.

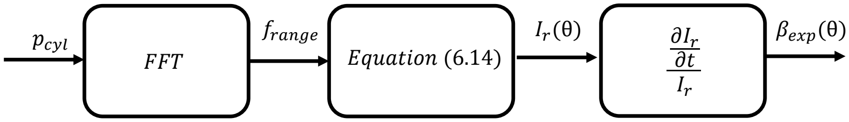

Figure 6.5: *Experimental attenuation procedure scheme.*

The first step is to compute the FFT in order to find the frequency range of the mode to analyze. A second step is added where the resonance indicator (I_r) is calculated, and finally the attenuation is obtained by deriving I_r and dividing by the amplitude. As example, the scheme procedure is shown in Figure 6.6.

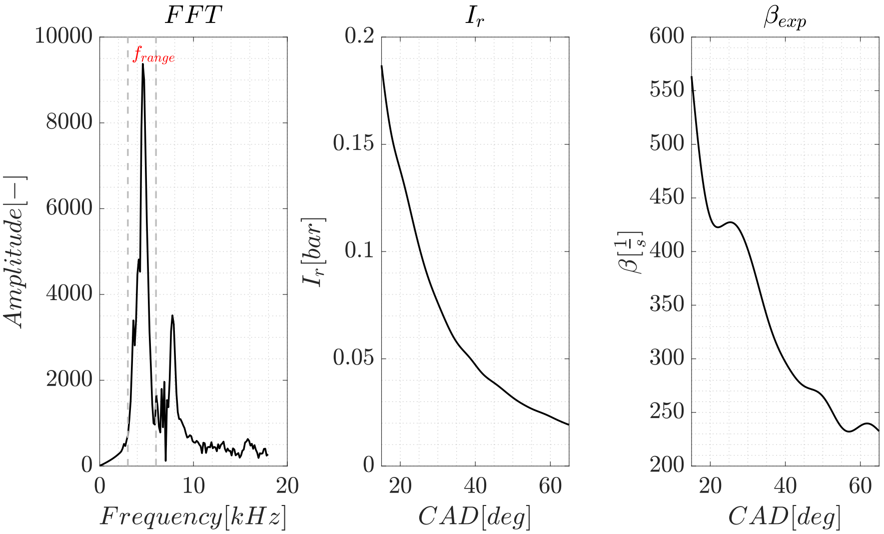

Figure 6.6: *Experimental attenuation procedure: STFT (left), I_r (middle) and α_{exp} (right).*

In Figure 6.6 left plot, the FFT of the in-cylinder pressure of engine C is shown, and in grey dashed line the frequency range f_{range} of the first radial mode is marked. The middle plot shows the resonance amplitude evolution computed by the Equation (6.14), and in right plot the experimental attenuation is represented.

6.4 Pressure resonance amplitude evolution model

This section is devoted to developed a model able to predict the amplitude of in-cylinder pressure resonance evolution over normal and knocking combustion by assuming a constant attenuation during a cycle. During the section two engine are used to developed the model: A and B engines.

6.4.1 Model description

In order to model the resonance evolution during normal and knocking combustion, the approximation found in [15] is analyzed. The attenuation introduced in Equation (6.7), which is used to represent the real acoustical evolution of the combustion chamber due to the impedance of the chamber walls, the movement of the piston, and the viscosity of the medium, among others. In this section, the value of the β is assumed to be constant during a given cycle. In order to model the resonance amplitude evolution, a first order system is used, which in discrete time domain can be described as [16]:

$$G_d[z] = \frac{z}{z - e^{\beta T_s}} = \frac{1}{1 - k_d z^{-1}} \tag{6.15}$$

where z^{-1} represents a unit delay, $k_d = e^{\beta T_s}$ is the parameter that characterizes the attenuation in the discrete domain, and T_s is the sampling period.

The resonance amplitude evolution can be computed from the transfer function in Equation (6.15), and the excitation of resonance $u(z)$, such as:

$$A(z) = G_d[z]u(z) \tag{6.16}$$

The amplitude of the pressure resonance depends on how combustion excites the acoustic field, for that reason, it is not possible to recognize the amplitude of the resonant mode in a concrete time step, nevertheless a diluted estimation after a window can be applied. From now on, it can be assumed that the estimation in Equation (6.14) is proportional to the intensity of the oscillation at the frequency of the oscillation in a time window.

$$I_r(z) \propto W[z]A(z) \tag{6.17}$$

where $W[z]$ is the window function which consists in a zero-phase filter with a Blackman-Harris window weighing as:

$$W[z] = \sum_{j=-J/2}^{J/2} w_j z^j \tag{6.18}$$

where J represents the window size in samples, and w_j the window factors that complies: $\sum w_j = 1$.

In Figure 6.7 an scheme of the amplitude resonance model is shown. The unknown variable is how the combustion excites the resonance field: $u(z)$, which should be modeled as a function of the cycle combustion parameters.

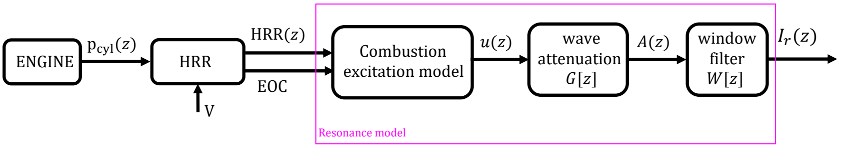

Figure 6.7: *Resonance model scheme.*

In order to model the the amplitude $u(z)$ two hypothesis are taken:

- For normal combustion, the combustion resonance excitation (u_C) is assumed to be produced by the heat fluctuations, so it was assumed to be proportional to the HRR. Which means that the highest resonance excitation is caused at the maximum HRR, and all the combustion process has a contribution to the final resonance amplitude evolution.

$$u_C(z) = C \cdot HRR(z) \tag{6.19}$$

- For knocking combustion, all the excitation, is assumed to be released in a small step located just after EOC. The intensity of the fluctuations cannot be measured online, which is mainly caused to the fuel burnt in auto ignition conditions. A step function of 0.5 CAD length with an intensity of $|u_A| = \hat{I}_r$ has been used to model the rapid pressure rise in knock event.

The attenuation constant of Equation (6.15), k_d, and the proportional relation between the HRR and C, might depend on the engine operating conditions, however its expected to be almost constant, and can be identified cycle-by-cycle on-line.

The final algorithm to compute the amplitude of the resonance excitation uses as an input cycle-to-cycle combustion data to update the C and k_d by using an infinite input response (IIR) filter, as following:

$$\begin{aligned} k_d^{k+1} &= k_d^k \alpha_{up} + \widehat{k}_d^k (1-\alpha_{up}) && (6.20) \\ C^{k+1} &= C^k \alpha_{up} + \widehat{C}^k (1-\alpha_{up}) && (6.21) \end{aligned}$$

where $\widehat{k}_d$ and $\widehat{C}$ are the identified damping and combustion excitation parameters, and α_{up} is the IIR filter coefficient weighting the impact of previous cycle value (k) and innovation $(k+1)$.

6.4.2 Adaptation of model parameters

Engines A and B are used to evaluate the parameters, k_d and C, under normal combustion over 500 consecutive cycles. In Figure 6.9 the histogram with the identified time constant (k_d) is represented, and in Figure 6.10 the proportional relation (C) between the HRR and the resonance intensity (I_r) is shown. Engine A was operated at $OP_A = 5$ and the MAPO average was of 0.18 bar. Engine B was operated at $OP_B = 10$ with an average MAPO of 0.48 bar. The average value and the variation, evaluated by the standard deviation, of both analysis has been summarized in Table 6.2. The characteristic time τ constant of both, engine A and B, was of 0.80 and 0.93 ms respectively (see Figure 6.8), and was computed from:

$$\tau = \frac{1}{\beta} = \frac{T_s}{\ln(k_d)} \tag{6.22}$$

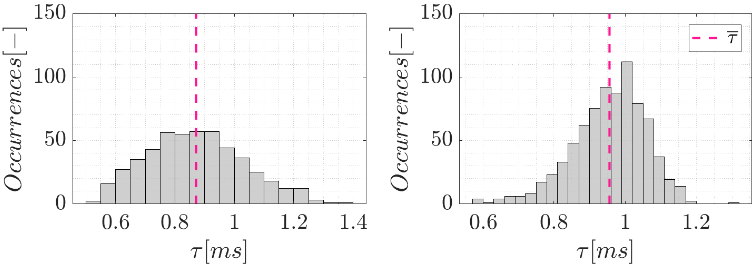

Figure 6.8: *Characteristic time τ identified at 500 cycles with conventional combustion. Left plot: Engine A $OP_A = 5$. Right plot: Engine B $OP_B = 10$.*

Notice that in Figure 6.9, the value of k_d for engines A and B is similar while the value of τ is not, this is because the sampling period T_s for both engines is different, since engine A in-cylinder pressure is sample every 0.2 CAD and in engine B case every 0.5 CAD.

Analyzing Figures 6.9 and 6.10, the shape of both histograms is not symmetrical, and has a small cue at lower values of attenuation and higher

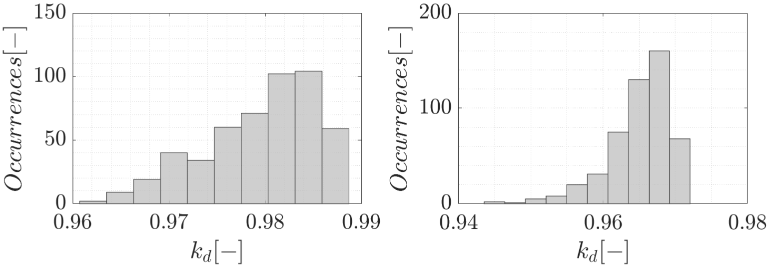

Figure 6.9: *Attenuation identified at 500 cycles with conventional combustion. Left plot: Engine A $OP_A = 5$. Right plot: Engine B $OP_B = 10$.*

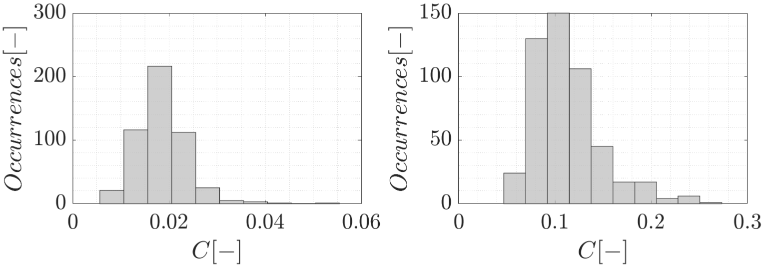

Figure 6.10: *Proportional relation between HRR and resonance intensity identified at 500 cycles with conventional combustion. Left plot: Engine A. Right plot: Engine B.*

values of the combustion excitation. This deviation can be attributed to cycles where the pressure oscillations are not completely caused by combustion excitation, and other sources such as noise interfered. According to Table 6.2, the obtained distributions also show that the variability of the attenuation can be neglected, in engine A represented a 0.6 % and in Engine B a 0.4 %. Besides, the combustion excitation variation ($\frac{\sigma(C)}{C}$) is estimated around a 30 %.

Table 6.2: *Model parameters*

	Engine A	Engine B
$\overline{k}_d$	0.9795	0.9651
$\sigma(k_d)$	0.0059	0.0043
$\overline{C}$	0.0184	0.1125
$\sigma(C)$	0.0051	0.0352

Moreover, the model has been evaluated under transient conditions in engine B, where the SA and throttle valve (X_{th}) were changed during transient $T13$. In Figure 6.11 the evolution of the model parameters: the attenuation (k_d) and the combustion excitation (C) characteristics have been continuously adapted by Equations (6.20) and (6.21), where $\alpha_{up} = 0.98$. However, note that this parameters are not sensitive to the operating engine condition.

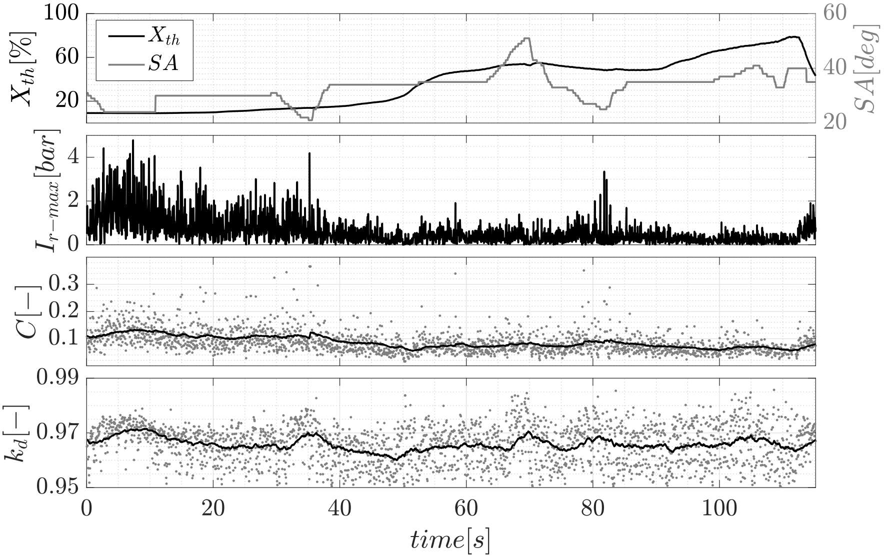

Figure 6.11: *Evolution of C and k_d during transient conditions. Engine B test number $T13$.*

6.4.3 Results and discussion

The model was validated in engines A and B during SA sweeps at operating condition $OP_A = 12$ and $OP_B = 20$. Each cycle the relative error of the model was computed as :

$$E_r = \frac{|\sum(I_r - I_{model})|}{I_r}100 \tag{6.23}$$

where I_{model} can be the resonance expected for combustion or for auto ignition.

The relative error of the models are represented in Figure 6.12 and 6.13, where the relative error for both, auto ignition and combustion model is shown on the left. Two cycles are highlighted: crosses are used to represent one cycle with relative error of auto ignition model lower than combustion model, and circles are used to represent the opposite case.

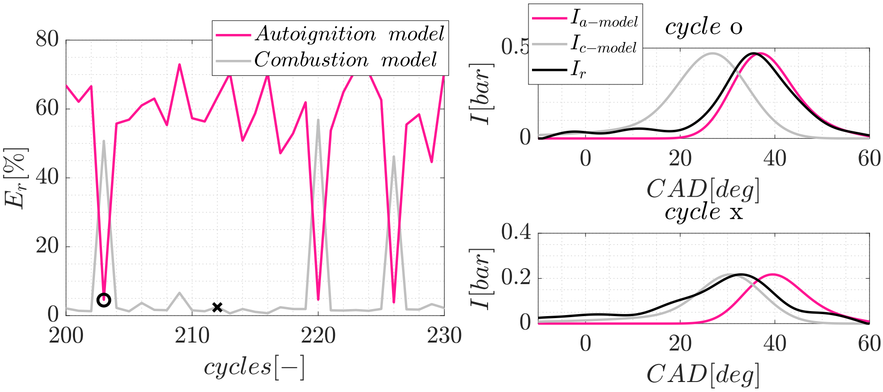

Figure 6.12: *Resonance model evolution results for engine A* $OP_A = 12$. *Left: Relative error of combustion and auto ignition models. Right: Detailed cycles.*

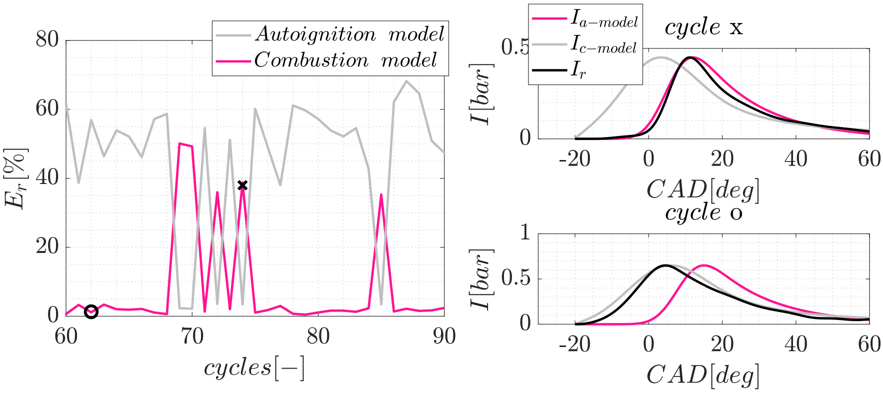

Figure 6.13: *Resonance model evolution results for engine B* $OP_B = 20$. *Left: Relative error of combustion and auto ignition models. Right: Detailed cycles.*

As can be seen in Figures 6.12 and 6.13 the estimated resonance evolution for normal combustion (I_r) looks closer to the combustion model ($I_{c-model}$) in no knocking conditions. Otherwise, when a knock event occurs ($'x'$ case) it seems more correlated with the auto ignition model ($I_{a-model}$). This approximation will be used during the following Chapter 7 to develop a knock recognition procedure.

6.5 Pressure resonance attenuation model

In the previous section the attenuation of the resonance excitation was assumed as constant during a cycle, this section aims to developed a model able to predict the attenuation of in-cylinder pressure resonance over a cycle. The experimental resonance attenuation is computed from in-cylinder pressure sensors following the scheme presented in Figure 6.5, and three combustion modes are used to analyzed and characterized the resonance damping: SI, TJI and RCCI.

6.5.1 Dimensional analysis

The attenuation over different operation points can be described as function of parameters in Equation (6.8) as:

$$\beta = K a^{c_1} \mu^{c2} \rho^{c_3} f^{c_4} D^{c_5} n^{c6} \tag{6.24}$$

where K is a constant value which must be calibrated, and c_j , with j from 1 to 6, are the exponents of the different parameters.

Applying dimensional analysis, Equation (6.24) in International System of units results as:

$$\frac{1}{s} = \left(\frac{m}{s}\right)^{c_1} * \left(\frac{kg}{ms}\right)^{c_2} * \left(\frac{kg}{m^3}\right)^{c_3} * \left(\frac{1}{s}\right)^{c_4} * m^{c_5} * \left(\frac{1}{s}\right)^{c_6} \tag{6.25}$$

During the expansion stroke, the evolution of all thermodynamic properties can be associated to the movement of the piston as:

$$\begin{aligned}
&\rho = \tfrac{P}{RT} = k_1 \tfrac{V^{-\gamma}}{V^{1-\gamma}} \\
&a = \sqrt{\gamma RT} = \sqrt{\gamma R k_2 V^{1-\gamma}} \\
&f = a\tfrac{B_{i,j}}{D} = \sqrt{\gamma R k_2 V^{1-\gamma}}\tfrac{B_{i,j}}{D} \\
&\mu = k_3 T^{0.7} = k_3 (V^{1-\gamma})^{0.7}
\end{aligned} \tag{6.26}$$

where R is the gas constant, k_i constant values, V the volume, T the in-cylinder temperature. The expression for the dynamic viscosity was computed according to [17]. In order to compensate energy losses, the adiabatic index (γ) will be replaced by a constant polytropic coefficient (κ).

Henceforth, according to Equations (6.8) and (6.26), in the expansion stroke, where a polytropic evolution is assumed, the attenuation of the resonance in a given cycle should be described in term of the volume evolution by:

$$\beta = K_1 V^{-c_0} \tag{6.27}$$

where K_1 is a constant in function of the gas conditions defined in Equations (6.26).

Constants relations must also satisfy (6.27). According to (6.26) and (6.27) the following relation is obtained:

$$c_0 = \frac{(1-\gamma)c_1}{2} + (1-\gamma)c_2 0.7 - c_3 + \frac{(1-\gamma)c_4}{2} \tag{6.28}$$

6.5.2 Calibration of the model parameters

The first step is to calibrate constants of Equation (6.27), namely K_1 and c_0, which were calibrated by least squares method as:

$$b = A * x \tag{6.29}$$

$$b = log(\beta) \tag{6.30}$$

$$A = [log(1) - log(V)] \tag{6.31}$$

$$[K1, c_0] = A\ b \tag{6.32}$$

In Figure 6.14, the mean variables K_1 and c_0 and 95 % confidence interval for the mean of the training points are shown.

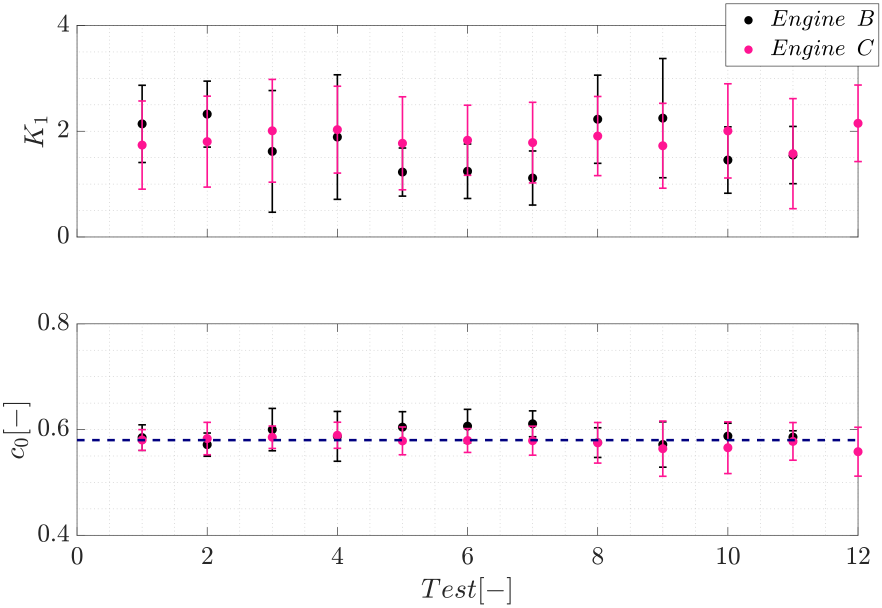

Figure 6.14: *Calibration β model for engine A and B: K_1 (top) and c_0 (bottom).*

As it can be seen in Figure 6.14, the operating condition has not significant impact on c_0 fitted value for both engines.

Taking a look to the system of Equations, (6.25) and (6.27), we have now x unknowns and y equations. In order to find a solution to the system of equations, two unknowns parameters must be determined. The effect of the speed and diameter are analyzed, by maintaining the rest of thermodynamic parameters constant.

First, the effect of the speed is analyzed in Figure 6.15 over the training points of engines A and B.

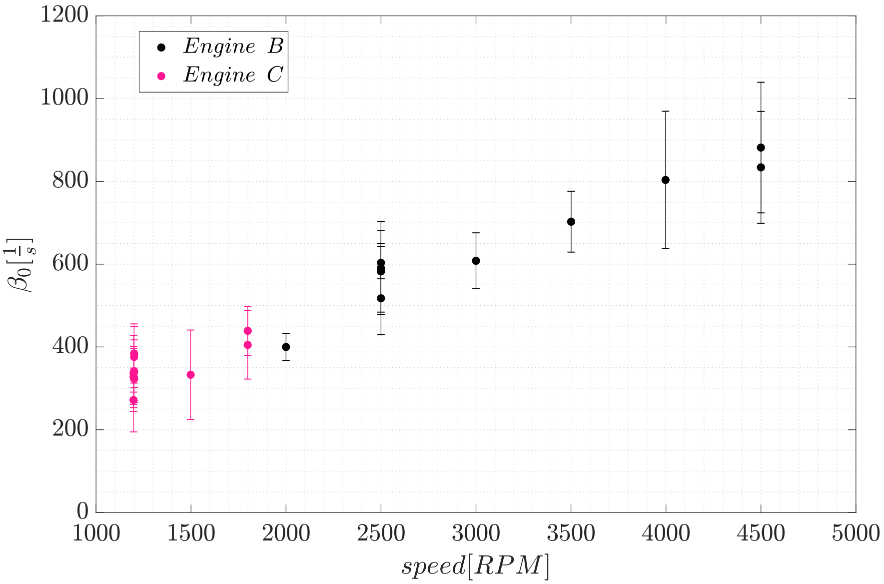

Figure 6.15: *Mean attenuation and 95% confidence interval for the mean at different engine speed of engine A and B.*

As can be seen in Figure 5 there is a linear relation between engine speed and attenuation, so the constant c_6 will be defined as 1.

In order to examine the cylinder size effect, and therefore the c_5 value, similar thermodynamic points were selected. In Figure 6.16 (left) the temperature and pressure for a $\theta_p = 40$ CAD are shown, the grey area shows the tests where similar conditions are achieved with both engines. Across this points the ratio between the attenuation is analyzed by defining a parameter χ as following:

$$\begin{aligned} \chi = \frac{\beta_A}{\beta_B} = (\frac{D_A}{D_B})^{\epsilon} \\ \epsilon = log_{\frac{D_A}{D_B}}(\frac{\beta_A}{\beta_B}) \end{aligned} \tag{6.33}$$

where ϵ quantify the effect of the diameter.

In Figure 6.16 (right), the mean ϵ value and 95% confidence interval is shown. Cases 1 and 2 correspond to operating points contained in grey area, while cases 3 to 8 corresponds to cases contained in pink area.

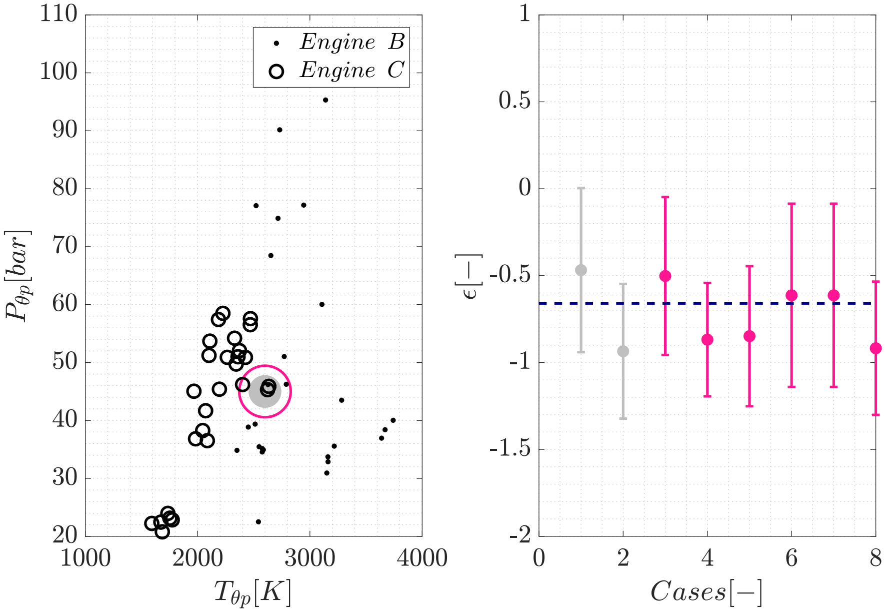

Figure 6.16: *Diameter effect for engine A and B: Temperature and pressure points (left), mean ϵ and standard deviation for 9 cases over 50 cycles.*

From Equations (6.25) and (6.28), using $c_0 = -0.58$, and assuming a linear effect of the speed from experimental analysis ($c_6 = 1$), the following relations are obtained:

$$\begin{aligned} c_1 &= -2c_2 - c_5 = 0.8298 - c_5 \\ c_2 &= -c_5 + c_4 - 2 = -0.4149 \\ c_3 &= -c_2 = 0.4149 \\ c_4 &= 1.58 + c_5 \end{aligned} \tag{6.34}$$

Figure 6.17 shows the fitting results for K constant (Equation (6.24) for all training points and both engines and both, engines A and B.

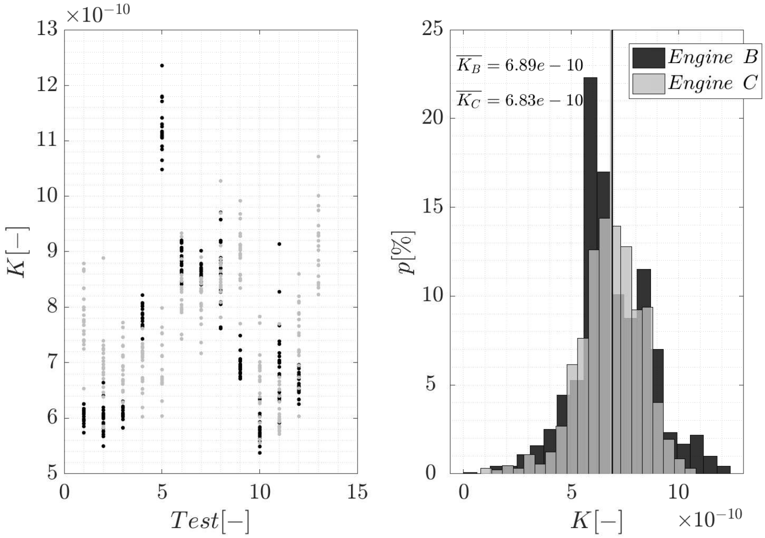

Figure 6.17: *K calibration. Left: Fitting results for each test. Right: Histogram for both engines calibration constant (right).*

Table 6.3: *Model calibration values*

Constant	Value
c_1	1.5
c_2	-0.42
c_3	0.42
c_4	0.92
c_5	-0.66
c_6	1
K	$6.86e^{-10}$

6.5.3 Results and discussion

In this section results of the attenuation resonance model are presented from three perspectives: firstly, the in-cycle results are shown, where the resonance attenuation model over a cycle is compared with the experimental attenuation. Secondly, the mean attenuation over several cycles results are presented, where one value is used to characterize the complete cycle attenuation. And finally, the engine diameter effect over engine A is analyzed.

6.5.3.1 In-cycle results

Figure 6.18 the resonance attenuation obtained from in-cylinder pressure signal and the model evolution are compared over one cycle.

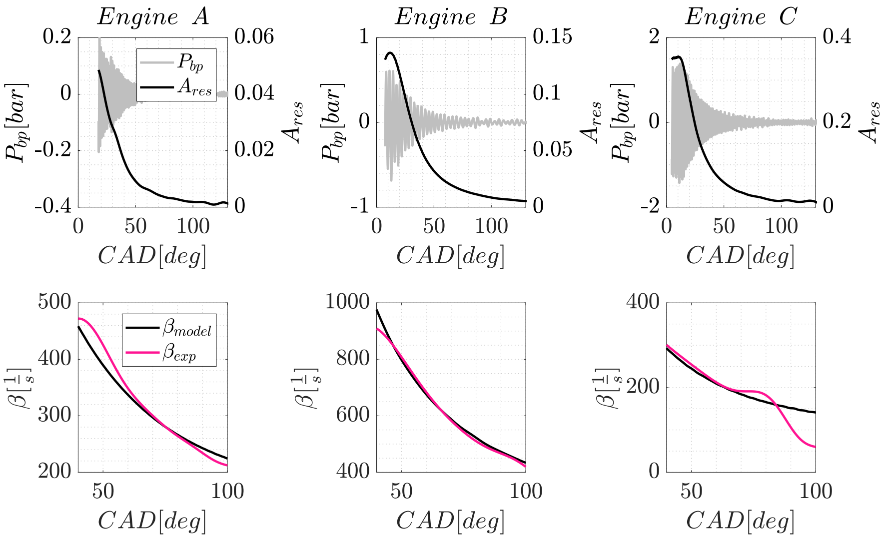

Figure 6.18: *Model in-cycle attenuation results: Engine A (left) , engine B (right). Resonance amplitude evolution (top) and resonance attenuation (bottom)*

Figure 6.18 (top) shows the band-pass in-cylinder pressure and A_{res}, in Figure 6.18 (bottom) the attenuation from experimental data (β_{exp}) and the model (β_{model}) are represented over the expansion stroke. Notice that when the oscillation drop below 200 $\frac{1}{s}$, there is insufficient sensitivity to calculate the attenuation and the model deviates from the measurement.

Figure 6.19 shows the mean relative error of the model evolution over 100 cycles. The relative error is computed as:

$$e_r[\%] = \frac{\beta_{model} - \beta_{exp}}{\beta_{exp}} * 100 \tag{6.35}$$

The analysis performed in Figure 6.19 is performed till 40 CAD the EOC, after that, β value is low and there is no sensibility on the measurement.

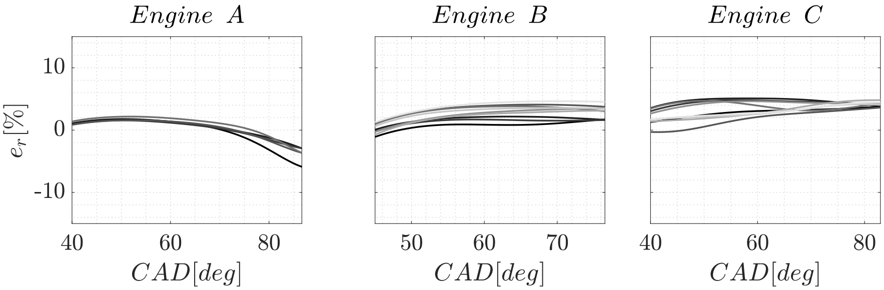

Figure 6.19: *Mean relative error between experimental in-cycle attenuation and model over 100 cycles (validation tests): Engine A (left), engine B (middle) and engine C (right).*

Note the the model is able to reproduce the evolution of the attenuation, not only for the calibration engines (A and B), but for engine C with an error of less than 10 %.

6.5.3.2 Mean attenuation

The mean value of attenuation obtained from experimental data was compared with the mean attenuation of the model, in Figure 6.20 the attenuation from training data (left) and validation data (right) are compared with the model results. Different colors are used to highlight engine A and B results, and validation results from engine C are marked with crosses. In continuous line the agreement is shown and in dashed line the expected error (10 %).

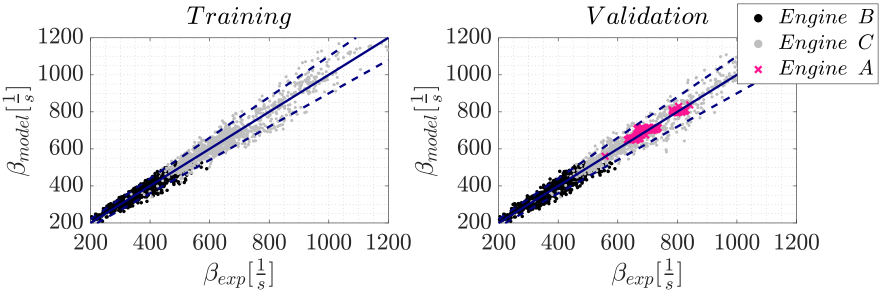

Figure 6.20: *Calculated attenuation: Training data (left) and validation data (right). – Agreement line, - - 10 % relative error*

As shown in Figure 6.20, the model is able to reproduce the mean attenuation over a cycle within a 10 % of error, in both engines used for calibration

(A and B) and a third engine used only in the validation section (engine C).

6.5.3.3 Engine diameter

In an attempt to compare the diameter effect with engine A, the attenuation cross-ratio (χ) from Equation (6.33) is used.

$$\chi_{exp} = \frac{\alpha_{exp-C}}{\alpha_{exp-A}} \tag{6.36}$$

$$\chi = \left(\frac{D_B}{D_C}\right)^{\epsilon} = 0.7821 \approx \chi_{exp} \tag{6.37}$$

In this section the analysis of the attenuation is performed at the same thermodynamic starting point (temperature and pressure). In Figure 6.21 the temperature and pressure at the same crank angle location for each case are represented. In pink, the area selected to compute the attenuation cross-ratio is shown.

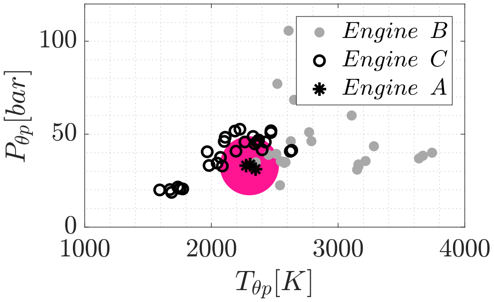

Figure 6.21: *Temperature and pressure points at 30 CAD ATDC.*

In Figure 6.22 (left) the relation χ_{exp} evolution between engines B and C over 100 cycles is represented, the mean of the model over the cycles is plotted in continuous black and dashed line is used to highlight the χ calculated with the model, based on the ratio between diameters. Figure 6.22 (right) shows the mean and the 95% confidence interval for the mean over 6 cases for B and C comparison, and 7 cases for A and C comparison.

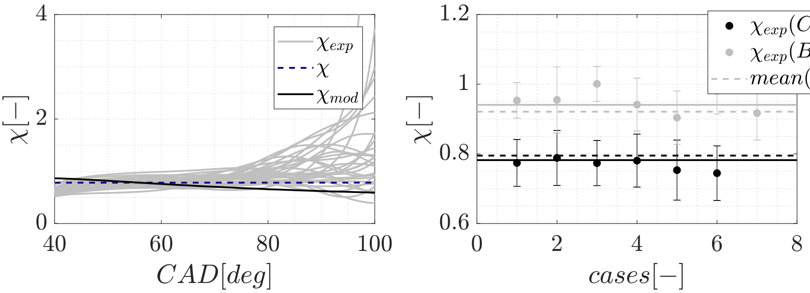

Figure 6.22: *Relation χ: In-cycle evolution of χ_{exp}, χ_{mod} and χ (left). Mean and 95% confidence interval for the mean of χ_{exp} for different cases and mean χ_{mod} (right)*

As shown in Figure 6.22, when comparing engine A and B with engine C, the model is able to predict the mean effect of the diameter on attenuation.

6.6 Resonance with different fuels

In this section results from engine B fueled with two different fuels (gasoline and CNG) will be shown.

First, the amplitude resonance model will be evaluated under the same operating condition in a normal combustion cycle. In Figure 6.23, the resonance indicator is shown in black line in two cases: engine fueled with gasoline (right) and fueled with CNG (left) during a normal combustion cycle. In grey line, the model for normal combustion case ($I_{model-c}$) is illustrated. In slight grey the high pass in-cylinder pressure is also represented. Both cases were computed with values shown in Table 6.2.

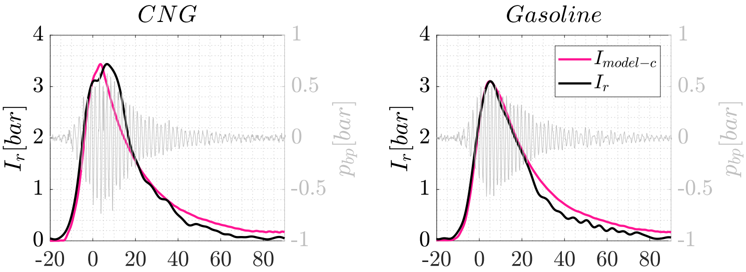

Figure 6.23: *Resonance model evolution results for engine B* $OP_B = 20$ *with the engine fueled with CNG (left) and gasoline (right).*

As it can be seen in Figure 6.23, the model is able to reproduce the resonance amplitude evolution in both cases, since the resonance evolution is modeled as a function of the HRR, which is affected by the fuel.

In the same operating condition, the attenuation was computed from the in-cylinder pressure signal. In Figure 6.24, the histogram of the mean attenuation obtained during 200 cycles is represented together with the value obtained from the model. On the left plot CNG cases, and on right plot gasoline.

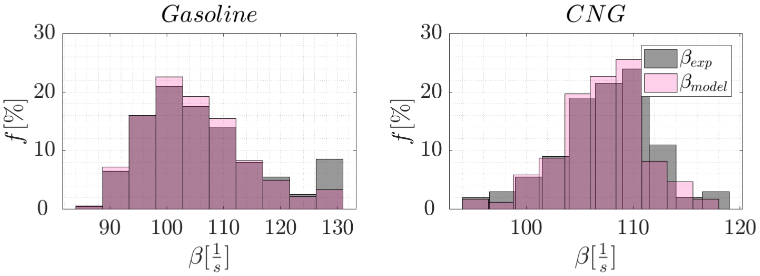

Figure 6.24: *Histogram of mean experimental and modeled attenuation during* $OP_B = 20$ *with the engine fueled with CNG (left) and gasoline (right).*

As shown in Figure 6.24, the attenuation of the resonance is independent of the used fuel, i.e depends on the operating conditions and the combustion chamber. In Figure 6.25, the attenuation from a cycle of Figure 6.23 is represented for both cases.

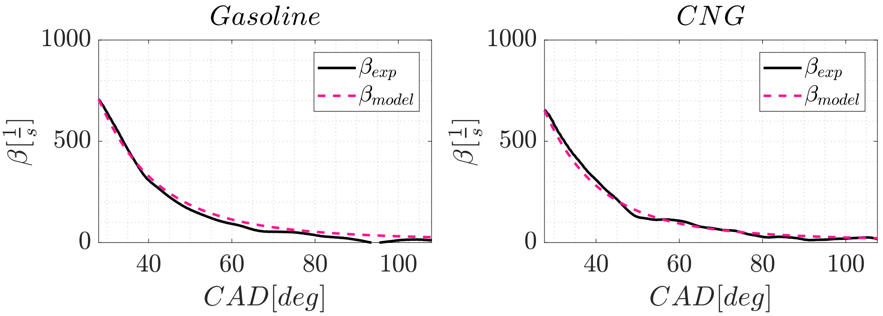

Figure 6.25: *Attenuation evolution during cycle of Figure 6.23 for CNG (left) and gasoline (right).*

In both cases analyzed in Figure 6.25 the model is able to reproduce the evolution of the attenuation in both, gasoline and CNG, thus the resonance evolution and the attenuation are independent of the fuel type. As a consequence, for a given engine and combustion mode, the models are able to reproduce the resonance in the combustion chamber.

6.7 Conclusions

In this chapter resonance amplitude evolution was analyzed. A resonance model evolution for combustion and knocking combustion is presented, considering an attenuation constant during a cycle. This model will be used in the following chapter to developed a knocking cycle recognition method. A second approach is presented, by modeling the attenuation during a cycle for engines A, B and C, demonstrating that the model is able to reproduce resonance attenuation evolution in three different combustion modes.

6.A Windows function

Windows are used in harmonic analysis to reduce the undesirable effects related to spectral leakage. There are several different types of window functions that can be applied depending on the signal. In Figure 6.26, four windows function are shown, on left plot in time domain and on right plot in frequency domain.

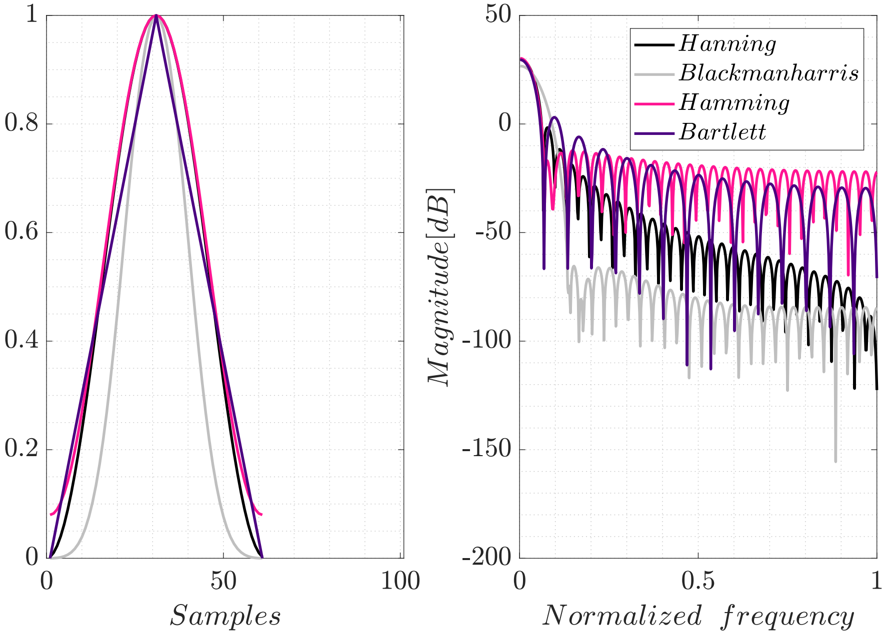

Figure 6.26: *Window functions. Left: time domain. Right: frequency domain.*

Note that Hamming window function does not reach zero, while the remaining three reach zero at both ends . This permits to eliminating all discontinuity when computing the STFT as is illustrated in Figure 6.27.

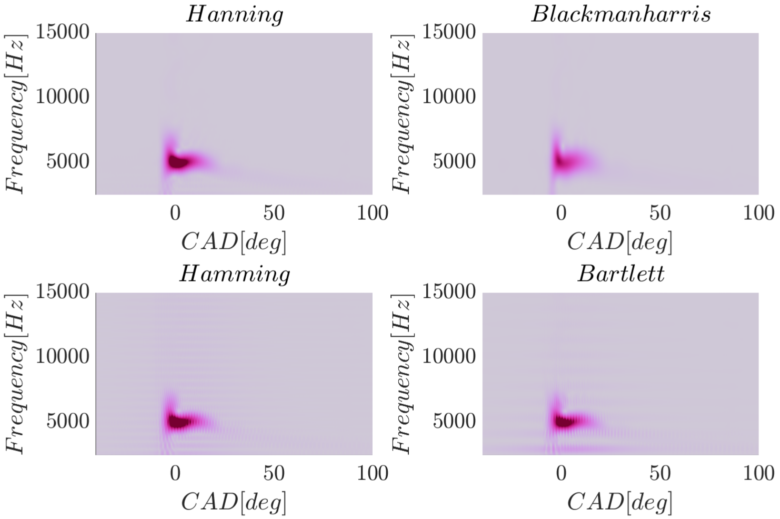

Figure 6.27: *Optimal window location over a transient.*

Following recommendations of window use in [18], the selected window for the frequency analysis is the Blackman-Harris window.

References

[1] Guardiola Carlos, Pla B, Bares P and Barbier A. "An analysis of the in-cylinder pressure resonance excitation in internal combustion engines". *Applied Energy*, Vol. 228, pp. 1272–1279, 2018. (cited in pp. 30 and 114)

[2] Xu Han, Yao Anren, Yao Chunde and Gao Jian. "Investigation of energy transformation and damage effect under severe knock of engines". *Applied Energy*, Vol. 203, pp. 506–521, 2017. (cited in p. 114)

[3] Kyrtatos Panagiotis, Hoyer Klaus, Obrecht Peter and Boulouchos Konstantions. "Apparent effects of in-cylinder pressure oscillations and cycle-to-cycle variability on heat release rate and soot concentration under long ignition delay conditions in diesel engines". *International Journal of Engine Research*, Vol. 15 n^o 3, pp. 325–337, 2014. (cited in p. 114)

[4] Attard William P, Blaxill Hugh, Anderson Eric K and Litke Paul. "Knock limit extension with a gasoline fueled pre-chamber jet igniter in a modern vehicle powertrain". *SAE International Journal of Engines*, Vol. 5 n^o 3, pp. 1201–1215, 2012. (cited in pp. 32 and 114)

[5] Draper Charles Stark. "The physical effects of detonation in a closed cylindrical chamber". 1935. (cited in pp. 50 and 115)

[6] Bares Moreno Pau. *In-cylinder pressure resonance analysis for trapped mass estimation in automotive engines.* PhD Thesis, Universitat Politècnica de València, 2017. (cited in pp. 19, 115, and 122)

[7] Luján José Manuel, Guardiola Carlos, Pla Benjamin and Bares Pau. “Estimation of trapped mass by in-cylinder pressure resonance in HCCI engines”. *Mechanical Systems and Signal Processing*, Vol. 66, pp. 862–874, 2016. (cited in pp. 115 and 181)

[8] Lapuerta Magin, Armas Oy and Hernández JJ. “Diagnosis of DI Diesel combustion from in-cylinder pressure signal by estimation of mean thermodynamic properties of the gas”. *Applied Thermal Engineering*, Vol. 19 n^o 5, pp. 513–529, 1999. (cited in pp. 22 and 116)

[9] Scholl David, Davis Craig, Russ Stephen and Barash Terry. “The volume acoustic modes of spark-ignited internal combustion chambers”. *SAE transactions*, pp. 1379–1386, 1998. (cited in p. 117)

[10] Li Ruixue C and Zhu Guoming G. “A real-time pressure wave model for knock prediction and control”. *International Journal of Engine Research*, p 1468087419869161, 2019. (cited in p. 117)

[11] Munjal ML. “Advances in the acoustics of flow ducts and mufflers”. *Sadhana*, Vol. 15 n^o 2, pp. 57, 1990. (cited in pp. 117 and 217)

[12] Cohen Leon. *Time-frequency analysis*, volume 778. Prentice Hall PTR Englewood Cliffs, NJ, 1995. (cited in p. 119)

[13] Shen Xun, Zhang Yahui and Shen Tielong. “Cylinder pressure resonant frequency cyclic estimation-based knock intensity metric in combustion engines”. *Applied Thermal Engineering*, Vol. 158, pp. 113756, 2019. (cited in p. 120)

[14] Broatch A., Guardiola C., Pla B. and Bares P. “A direct transform for determining the trapped mass on an internal combustion engine based on the in-cylinder pressure resonance phenomenon”. *Mechanical Systems and Signal Processing*, Vol. 62, pp. 480–489, 2015. (cited in pp. 120 and 217)

[15] Munjal Manchar Lal. *Acoustics of ducts and mufflers with application to exhaust and ventilation system design.* John Wiley & Sons, 1987. (cited in p. 123)

[16] Rohani Sohrab. *Coulson and Richardson’s Chemical Engineering: Volume 3B: Process Control.* Butterworth-Heinemann, 2017. (cited in p. 124)

[17] Mansouri SH and Heywood John B. “Correlations for the viscosity and Prandtl number of hydrocarbon-air combustion products”. *Combustion Science and Technology*, Vol. 23 n^o 5-6, pp. 251–256, 1980. (cited in p. 131)

[18] Harris Fredric J. “On the use of windows for harmonic analysis with the discrete Fourier transform”. *Proceedings of the IEEE*, Vol. 66 n^o 1, pp. 51–83, 1978. (cited in p. 143)

PART

IV

Applications to combustion diagnosis and control

CHAPTER

7

Combustion diagnosis

Contents

7.1 Introduction

In this chapter, the models developed in Chapters 4 and 6 will be used to develop tools for combustion diagnosis. This chapter is devoted to two applications, on the one hand, knock recognition methods, and on the other hand, in-cylinder trapped mass estimation.

First section present two knock recognition methods based on in-cylinder pressure signal, which makes use of the resonance evolution model presented in Chapter 6, and one method based on knock sensor signal, which combines the combustion model presented in Chapter 4 and one of the methods based on in-cylinder pressure signal. In addition, an application to different fuels of methods based on in-cylinder pressure is presented and results are analyzed.

Second section introduce an application of the attenuation model presented in Chapter 6 in order to improve the trapped mass estimation based on in-cylinder pressure signal.

Finally, in the last section, the main conclusions of the chapter are discussed.

7.2 Knock recognition

7.2.1 Low-knock recognition: MAPO limitations

As it was introduced in Chapter 2, one of the most extended indicator based on in-cylinder pressure signal for knock diagnosis in IC engines is MAPO [1]. In order to recognize knock events with MAPO criterion, a threshold must be previously calibrated for a given engine and different operating conditions [2]. In this sense, MAPO criteria consists of considering a maximum threshold for the high-pass filter of the in-cylinder pressure (p_{hp}), above which knocking conditions are considered, such as:

$$MAPO = max(p_{hp}) \tag{7.1}$$

In Figure 7.1 the high-pass in-cylinder pressure is shown for two cases, on the left a cycle with a low MAPO value (0.2 bar), and on the right a cycle with a high MAPO amplitude (0.9 bar). In order to analyze the excitation of the resonance, the HRR is also represented.

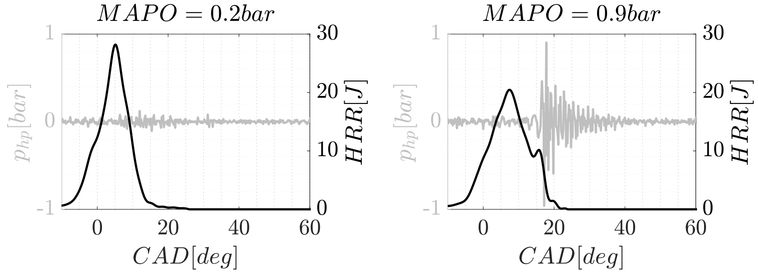

Figure 7.1: *High-pass in-cylinder pressure signal for two cases: Low MAPO (left) and high MAPO (right).*

Analyzing Figure 7.1, for left case, resonance is excited during the combustion, i.e. around the maximum of the HRR, on the other hand, for the right case, resonance is excited at the end of the combustion. Due to the auto-ignition process a second peak is observed in the HRR profile in the right case, which is associated with the fast burning rate of the end gas. As it can be seen in Figure 7.1, MAPO recognition is successful if the auto-ignition of the end gas produces an excitation of the resonance such that the amplitude of the phenomenon is high, however during this section the MAPO limitations are analyzed.

First, knocking and non-knocking events are analyzed in engines A and B in Figure 7.2. The spectrograms of the in-cylinder pressure signal for no-knocking cycles (left) and low-knocking cycles (right) are represented. The frequency spectrograms are computed by STFT using a Blackman-harris window of 30 CAD length, in dashed line the CA50 and CA90 are highlighted.

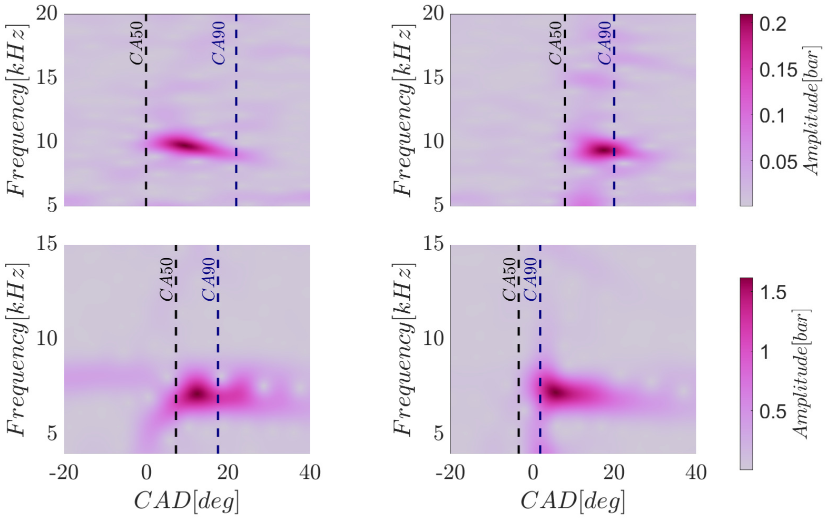

Figure 7.2: *Top plot: Engine A. Bottom plot: Engine B. CA50, CA90 and their spectrogram for two cycles: no-knocking cycle (left) and low-knocking cycle (right). Operation point:* $OP_A = 5$ *and* $OP_B = 12$.

The evolution of the high-pass in-cylinder pressure of Figure 7.2 are included in Figure 7.3, where the evolution of I_r introduced in Chapter 6 is also shown.

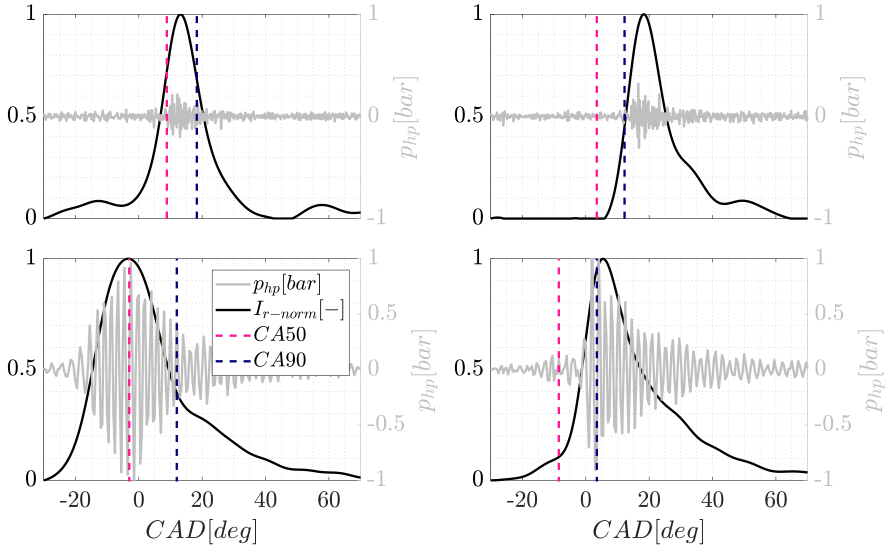

Figure 7.3: *Top plot: Engine A. Bottom plot: Engine B. HRR, CA50, CA90 and their spectrogram from two cycles: no-knocking cycle (left) and low-knocking cycle (right). Operation point:* $OP_A = 5$ *and* $OP_B = 12$.

Analyzing Figures 7.2 and 7.3, the maximum MAPO for both no-knocking and low-knocking cycles are similar for a given engine: 0.25 bar in engine A and 1.25 bar in engine B. Regardless similar MAPO amplitudes, in no-knocking cycles the resonance frequencies are excited near CA50, while in knocking cycles near CA90 which represents the end of combustion. Hence, if a low MAPO threshold is considered, normal combustion will be classified as knock (error type I), on the other hand, if a high MAPO threshold is chosen low-knocking cycle will be classified as normal combustion (error type II).

In order to analyzed SI and TJI combustion, MAPO probability distributions over 300 cycles at different SA settings is shown in Figure 7.4: left plot shows MAPO probability from Engine A, and right plot MAPO probability from Engine B.

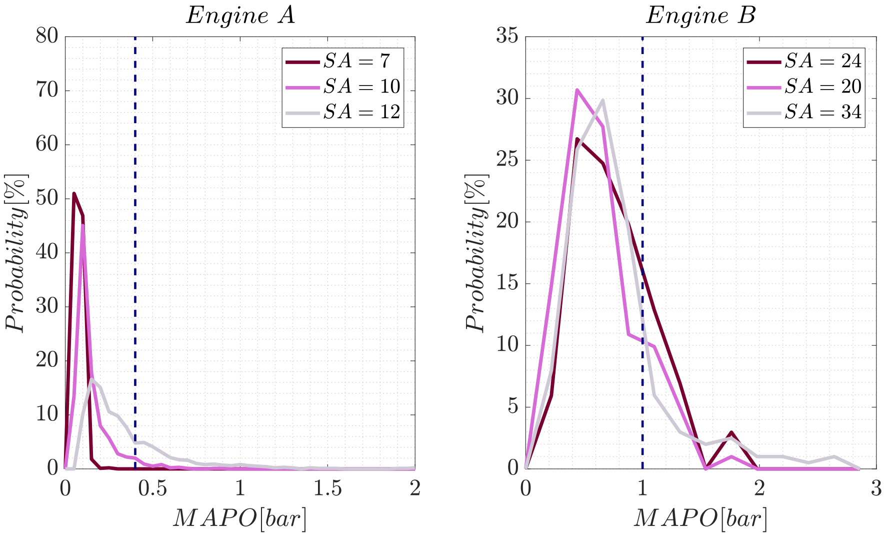

Figure 7.4: *Distribution of MAPO amplitude over SA sweeps. Left plot: Engine A ($OP_A = 5$). Right plot: Engine B ($OP_B = 12$).*

For TJI combustion (engine B), resonance levels are considerable higher, i.e. conventional combustion can achieve a MAPO level of 0.8 bar. In SI combustion, as SA is advanced MAPO distribution moves towards higher values. On the other hand, MAPO is less sensitive to SA in the TJI combustion. In dashed line, the MAPO threshold proposed for both engines is included, for engine A a MAPO threshold of 0.4 bar is chosen, and for engine B a MAPO threshold of 1 bar is chosen.

7.2.2 Methods based on in-cylinder pressure

In this section, two low-knock recognition methods based on in-cylinder pressure sensor will be presented by using the resonance indicator introduced in Chapter 6. First, a recognition method based on instantaneous combustion is presented. And after, a knock recognition method based on the amplitude resonance model presented in Chapter 6 is introduced. Both methods are validated in real-time operation in engine A at the end of this section.

7.2.2.1 Method 1: Recognition based on instantaneous combustion assumption

As discussed above, increasing the SA in a SI combustion produces higher temperature and pressure peaks in the combustion chamber, which leads to a higher knock probability. The parameter I_r introduced by Equation (6.14) was studied at different engine speeds, SA, and intake pressure conditions to analyze knocking events in engine A. In Figure 7.5, three cases are represented: normal combustion (left), low-knocking (middle) and knocking (right). The high-pass filtered in-cylinder pressured is represented on top plots, and I_r evolution is compared with the HRR evolution on bottom plots.

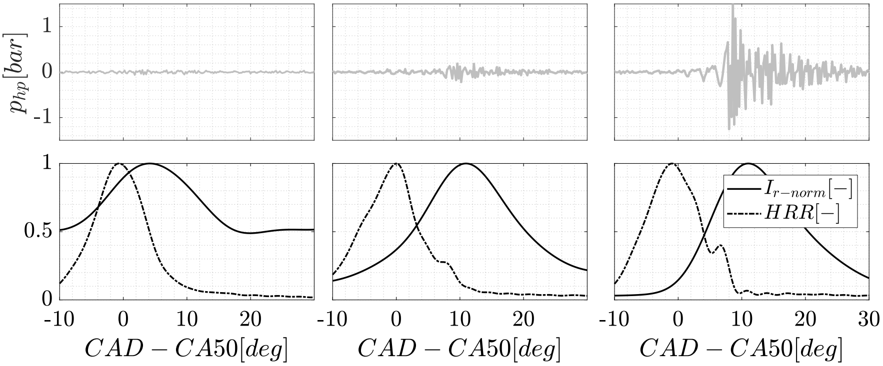

Figure 7.5: *Detail of three cycles at Engine A $OP_A = 5$. Left : No knock. Middle: low knocking cycle. Right: knocking cycle. Top plots high-pass filtered pressure and bottom plots normalized HRR plots I_r evolution.*

As it can be seen in Figure 7.5, the three cases show different locations where the cylinder resonance is excited with respect to the HRR evolution. Considering this effect, the resonance indicator (I_r) has been studied at two different CAD position: one at the CA50 (center of combustion) and the second one 10 CAD after CA50 which is assumed to be representative of the EOC. These two position were considerate since if the resonance is excited near the EOC, the source of such oscillation is the auto ignition process [1]. These positions are illustrated in Figure 7.6 for the third case of Figure 7.5 (right).

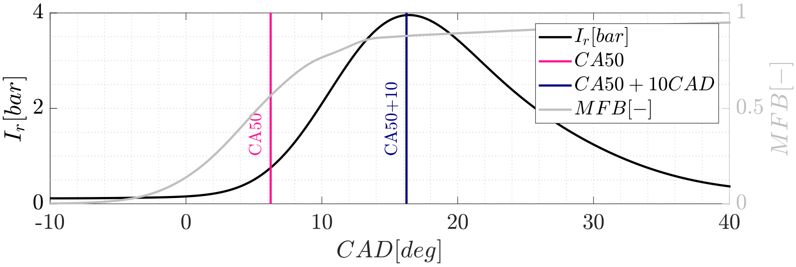

Figure 7.6: *Crank angle position of resonance analysis.*

In Figure 7.7 two groups of data of 1000 cycles length have been analyzed. Both groups have been recorded at $OP_A = 5$ at two different SA: 4 CAD-BTD (grey) and 12 CAD-BTD (black), i.e. low knocking and high knocking probability respectively. The value of the I_r at the main combustion (CA50) and EOC has been analyzed: on left plot the I_r value at CA50 is computed for both groups and on the right plot the value of I_r at CA50 + 10CAD is evaluated.

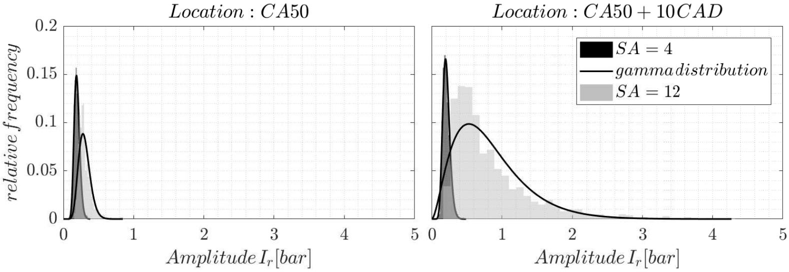

Figure 7.7: *Distribution of I_r in Engine A $OP_A = 5$ in two conditions: normal combustion and knock. Left plot: CA50. Right plot: CA50+10.*

Analyzing Figure 7.7, it may be noticed that at the CA50 (left plot) the amplitude of the indicator is similar in both SA settings with a small standard deviation, while in CA50+10 (right) the differences between the two groups is noticeable: the standard deviation for high knock probability data is considerably higher than for low-knock probability group. Thus, the maximum amplitude of I_r, as well as the location of the maximum seem to be both important parameters to identify knock.

Aiming to characterize resonance at different SA, a total of 1000 cycles at six SA settings have been examined. The maximum I_r amplitude and location calculated from the CA50, were computed for each cycle. The frequency in terms of number of events have been illustrated with grey color intensities in Figure 7.8: darker colors the most probable locations and amplitudes, and lighter colors the most improbable ones for each SA setting.

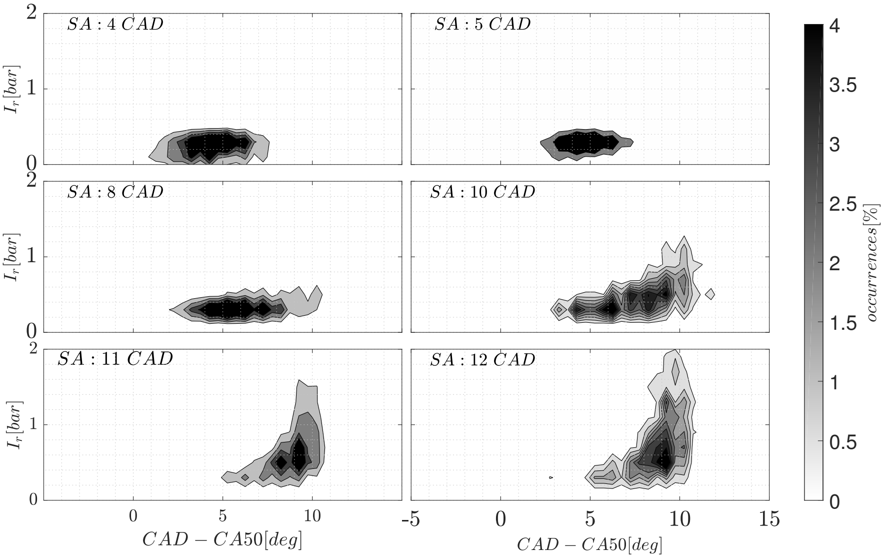

Figure 7.8: *Number of events of the maximum resonance indicator location and amplitude at different SA. Engine A* $OP_A = 5$.

In low probability setting, SA = 4 and SA = 5, the maximum I_r is located between 3 and 8 CAD after the main combustion (CA50), with a maximum amplitude above 0.4 bar. As SA advances, SA = 10, an additional shadow located 10 CAD after CA50 raise. These points represents knocking cycles, which excited resonance near EOC. When SA = 12, apart from being the percentage of knocking cycle higher, the maximum amplitude increases, which is a consequence of more auto ignited fuel. As a summary: in cycles with low knock probability, the maximum value of the resonance indicator is located near CA50 with low amplitude, as knock probability increases, the location of maximum indicator is located near EOC.

Minimum oscillation

Figure 7.8 analysis is used as starting point to develop a knocking criteria as a function of the amplitude and location of the resonance excitation phenomena. In order to establish the minimum oscillation in which the end gas auto ignites, the HRR is analyzed. The evolution of the heat in the combustion chamber (Q_c) can be expressed as:

$$Q_c = \frac{\kappa - 1}{\kappa} p_{cyl} dV + \frac{1}{\kappa - 1} V dp \tag{7.2}$$

where p_{cyl} the in-cylinder pressure, κ a constant, and V the instantaneous volume of the combustion chamber. The resonance intensity in a knocking cycle is related to the in-cylinder pressure rise rate due to the auto-ignition of the end gas, which can be considered as an instantaneous and therefore can be modeled as a constant volume combustion [3]. With this assumption, the heat released by the fuel (Q_f) during a knocking event can be computed as following:

$$Q_f = m_{f-a} H_p \tag{7.3}$$

where H_p is the lower heating power of the fuel (45 MJ/kg for gasoline), and m_{f-a} the fuel mass burnt by the auto-ignition of the end-gas.

Assuming complete combustion and no wall heat transfer, the pressure difference can be expressed from Equations (7.2) and (7.3) as:

$$dp = \frac{\kappa - 1}{V} m_{fa} H_p \tag{7.4}$$

where m_{fa}, i.e. represents the fuel left from the main combustion when knock occurs, and can be expressed as a function of the mass fraction burnt (MFB):

$$m_{fa} = m_f (1 - MFB) \tag{7.5}$$

If auto ignition takes place at CA80, 20% of the total fuel would be auto ignited, while if auto ignition takes place at CA99 a 1% will be auto ignited.

If we assume that the knock resonance amplitude excitation is proportional to the sudden rise of pressure due to the auto ignition event, the resonance amplitude can be expressed as a function of the MFB, p_{cyl}, V, and m_f, as following:

$$I_{r-minimum} = G \frac{\kappa - 1}{V} m_f H_p (1 - MFB) \tag{7.6}$$

where G represents the transference from the auto ignition event to the excitation of the resonance modes.

The mass fraction burnt, is calculated with the HRR introduced in Chapter 2, such as:

$$HRR \approx \frac{\kappa - 1}{\kappa} pdV + \frac{1}{\kappa - 1} Vdp \tag{7.7}$$

And MFB can be computed from HRR as:

$$MFB(\theta) = \frac{\int_{\theta_{SOC}}^{\theta} HRR(\theta)d\theta}{\int_{\theta_{SOC}}^{\theta_{TOC}} HRR(\theta)d\theta} \tag{7.8}$$

Knock recognition

In order to obtain a more precise recognition of knock, the minimum oscillation required to auto ignite the end gas is used as a threshold. If the I_r of a given cycle is higher than the expected resonance $I_{r-minimum}$ at the angle where I_r is maximum, then knock is detected as following:

$$if \quad \hat{I_r} \geqslant I_{r-minimum}(\theta_{(\hat{I_r})}) \text{ then knock} \tag{7.9}$$

where $\hat{I_r}$ is the maximum of I_r in the considered cycle.

Cases shown in Figure 7.5 (no knock, low knock, and knock cycles), are used to represent the knocking criteria of Equation 7.9 in Figure 7.9, where the I_r evolution is represented with a black line, and the threshold obtained by using a G of 0.08 with dashed line. G value was previously calibrated for engine A.

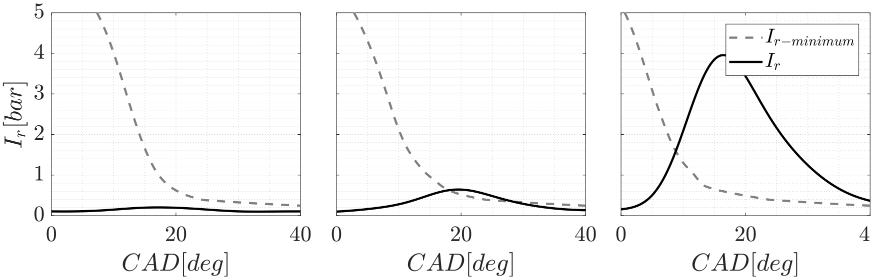

Figure 7.9: *I_r evolution and $I_{r-minimum}$ for three cases. Left: no knock cycle. Middle: low knock cycle. Right: a knock cycle. Cases in Figure 7.5.*

In low knocking and knocking cases, $\hat{I_r}$ is higher than the expected resonance, on the other hand, in normal combustion, $\hat{I_r}$ is bellow the expected resonance.

The method 1 knocking criteria is applied over 300 cycles at operating condition $OP_A = 5$ with SA = 11 CAD-BTDC in Figure 7.10, where the maximum amplitude of I_r is represented against the location referenced to the CA50. Different markers are used to highlight knocking recognition of method 1 (circles) and MAPO 0.4 (crosses). In order to illustrate the advantage of method 1 knocking recognition, three cycles have been marked with squares, and analyzed on the right side of the figure.

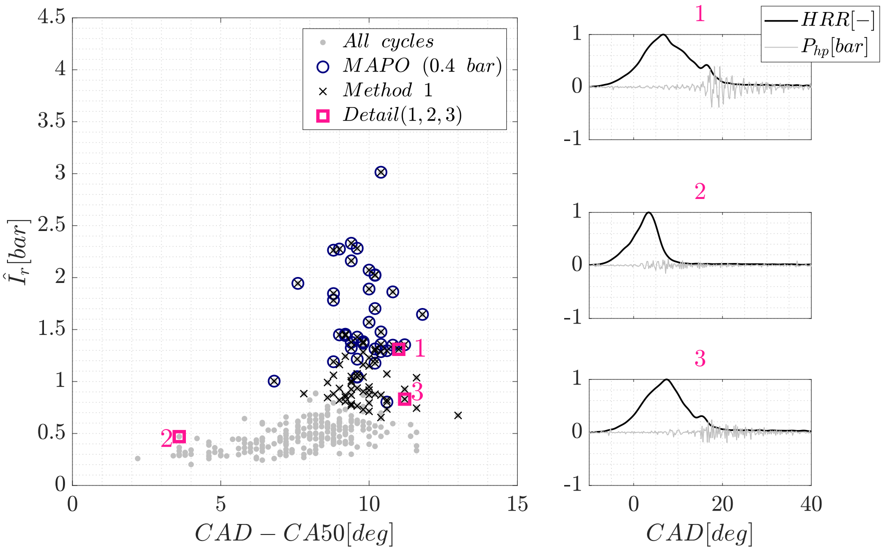

Figure 7.10: *Method 1 results in engine A. Left: the maximum I_r against its location for 300 cycles at $OP_A = 5$ (SA = 11 CAD-BTDC). Right: Detailed points are marked with squares and zoomed.*

Analyzing Figure 7.10, point number 1 is classified as knocking for a MAPO threshold of 0.4 bar and $\hat{I}_r$ is higher than points 2 and 3. Points number 2 and 3 have similar $\hat{I}_r$ amplitude but at different location with respect to the CA50. It must be notice that points 1 and 3 are knocking cycles: the HRR has second a peak at the EOC, but MAPO fails to detect cycle 3 as a knocking cycle while the proposed method is able to capture the low knocking intensity observed.

7.2.2.2 Method 2: Recognition based on resonance model

Method 2 knock recognition method is based on resonance model presented in Chapter 6. As explained above, in a given operating condition, the resonance excitation amplitude due to combustion (I_c) and auto ignition (I_a) are expected to be:

$$I_c(z) = W[z]G_d[z]u_C(z) \tag{7.10}$$

$$I_a(z) = W[z]G_d[z]u_A(z) \tag{7.11}$$

where the combustion excitation $u_C(z)$ is assumed to be proportional to the HRR: $u_C(z) = C \cdot HRR(z)$. The resonance excitation due to auto ignition is assumed to be located after the EOC as a step function of 0.5 CAD length, and with an intensity $|u_A|$.

As was introduced in Chapter 6, C is updated cycle-to-cycle, but due to the assumptions taken and uncertainties on the measurement of C a variability can be found. In this work, a Gaussian probability distribution is assumed for C: $\mathcal{N}(\overline{C}, \sigma(C))$, where $\overline{C}$ is the value updated cycle-to-cycle and $\sigma(C)$ is the measured variation of C. Hence, the expected maximum of the resonance excitation due to combustion is a value between I_c^- and I_c^+: $\overline{C} \pm 3\sigma(C)$.

In sever knocking cycles, the resonance excitation amplitude is much higher than I_c^+, therefore sever knock can be recognized as following:

$$\max(I_r^k) > \max(I_c^k)^+ \tag{7.12}$$

where k is the cycle number.

Even so, in cases where the $\hat{I}_r$ measured is in an uncertainty region, the evolution of the oscillation can give a comprehension about what triggered the resonance. In order to recognize knock in these cases, the resonance evolution estimated from in cylinder pressure I_r is normalized and compared with both, combustion and auto ignition models, also normalized. In this work, the error metric proposed is an euclidean distance along the crank angle such as:

$$\begin{array}{l} Ec(\theta_1 : \theta_2) = \sum_{\theta=\theta_1}^{\theta=\theta_2} \|I_{c-norm}(\theta) - I_{r-norm}(\theta)\| \\ Ea(\theta_1 : \theta_2) = \sum_{\theta=\theta_1}^{\theta=\theta_2} \|I_{a-norm}(\theta) - I_{r-norm}(\theta)\| \end{array} \tag{7.13}$$

where $\theta_1 : \theta_2$ the interval of analysis of resonance which corresponds to the main part of the combustion process: between CA10 and after CA90. In this work, a window of analysis from SA to SA+100 CAD is proposed.

In order to evaluate knock, both model errors are compared: if $E_a(\theta_2) < E_c(\theta_2)$, then knock is assumed, if not normal combustion is assumed. In Figure 7.11 the complete scheme for shape criteria proposed for knock recognition is shown.

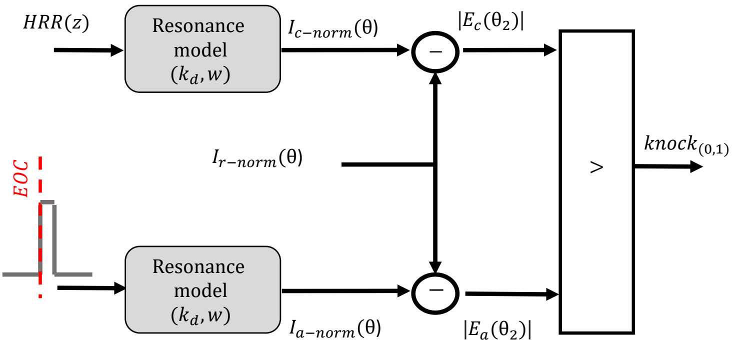

Figure 7.11: *Scheme of the shape criteria procedure for knock recognition.*

The complete knock recognition procedure involve a double criteria for the adaptation of the model parameters (C, k_d) and for knock classification. Resonance attenuation constant k_d is continuously updated, the combustion excitation is only updated when a cycle is classified as normal combustion. The complete scheme for knock recognition and adaptation of the model parameter is illustrated in Figure 7.12.

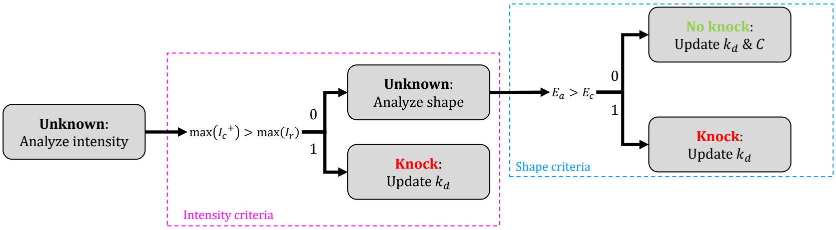

Figure 7.12: *Scheme of the complete procedure for knock recognition Method 2.*

Method 2 for knocking recognition was analyzed over 1000 cycles in engine B in TJI combustion, for that SA was varied from 25 to 40 CAD before TDC. In Figure 7.13 (left) the error E_a is represented against E_c, in dashed line the knocking criteria limit is illustrated: cycles bellow this limit are classified as normal combustion and above as knock. In black dots cycles with MAPO $>$ 0.6 bar are represented, and with crosses cycles with MAPO $>$ 1 bar. Pink squares are used to highlight three cycles which are detailed on the right side of the figure.

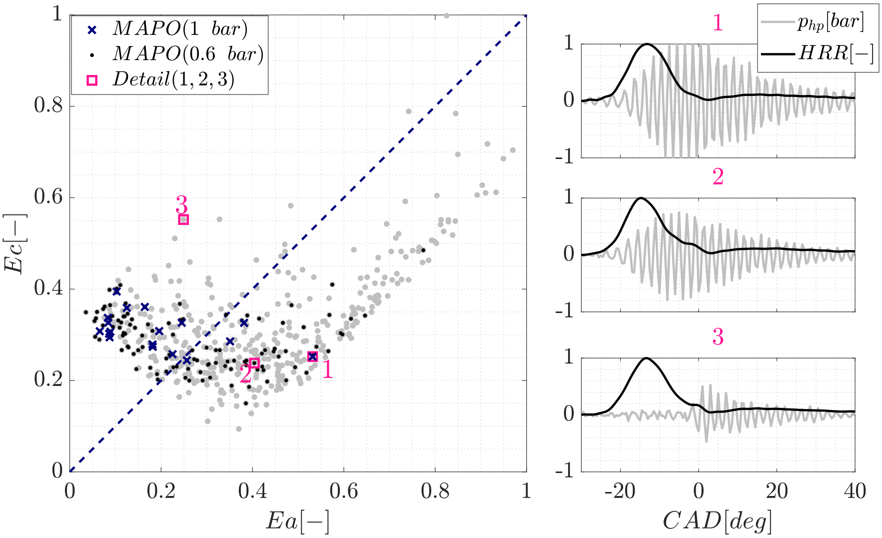

Figure 7.13: *In left side, E_a versus E_c for 1000 cycles at $OP_B = 10$ SA from 25 to 40 CAD BTDC. Detailed points are marked with blue circles and zoomed at the right side.*

Points 1 and 2 are classified as normal combustion with method 2 definition, but according to MAPO classification, they were classified as knock when a threshold of 0.6 bar is applied. Points 3, is not classified as knock for a MAPO threshold of 0.6 bar, but as it can be seen on the detailed plot (right side) this cycle is a knocking case: the resonance is excited at the end of combustion. As a summary, this method is able to recognize knocking cycles independently of the amplitude of the oscillation, which is a more precise definition for new combustion modes.

7.2.2.3 Validation results of methods 1 and 2

As discussed in Chapter 2,increasing the sensitivity of the knock detection used allows the SA control to work with higher knock probabilities, which finally leads to better control performance. In order to show this improvement. In this section the two low-knocking recognition methods based on in-cylinder pressure signal have been implemented in real time with a conventional knock controller in engine A. The conventional knock controller is characterized by setting the SA of the cycle k according to the result of the previous cycle as following:

$$SA^{k}_{conv} = \begin{cases} SA^{k-1}_{conv} - K_{ret} & if \quad Knock \\ SA^{k-1}_{conv} + K_{adv} & otherwise \end{cases} \tag{7.14}$$

where k is the cycle number, and K_{adv}, K_{ret} are the controller gains. K_{ret} is greater than K_{adv}: the SA is slowly advanced during normal combustion cycles, and it is rapidly retarded if a knock event is recognized. The gains of the conventional knock controller are associated by the knock probability (p_k) as:

$$K_{ret} = \frac{1 - p_k}{p_k} K_{adv} \tag{7.15}$$

Equation (7.15) shows how increasing the knock probability, reduces the asymmetry between the rate of SA advance and retard, then contributing to a lower SA variation. In order to set the controller knock probability, both methods are compared with MAPO knock probability when a threshold of 0.4 bar is applied. Results are illustrated in Figure 7.14, left side show the result for all SA sweeps and on the right plot a zoom between 0 and 2 % of MAPO is shown.

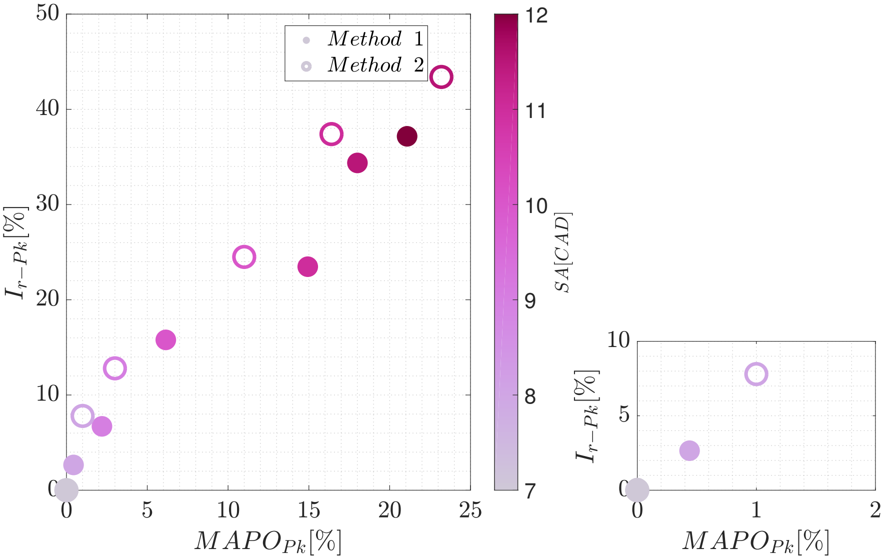

Figure 7.14: *Method 1 and 2 compared with MAPO during* $OP_A = 5$. *Left: Knock probability for different SA settings and methods. Right: MAPO (0.4 bar) probability versus Method 1 and 2 knock probability.*

For Method 1 a MAPO knock probability of 0.6 % is chosen, which correspond to a knock probability of method 1 of 2 %. For method 2, a MAPO probability of 1 % is selected, which represents a 8 % for method 2 criteria. The tests performed for each case are summarized in Table 3.5, where the characteristics of both controllers are shown.

In Figure 7.15 results for method 1 during tests $T1$ and $T2$ are shown. In black line the SA output when MAPO definition is applied, and continuos black line is used to represent SA output when using method 1 knock definition.

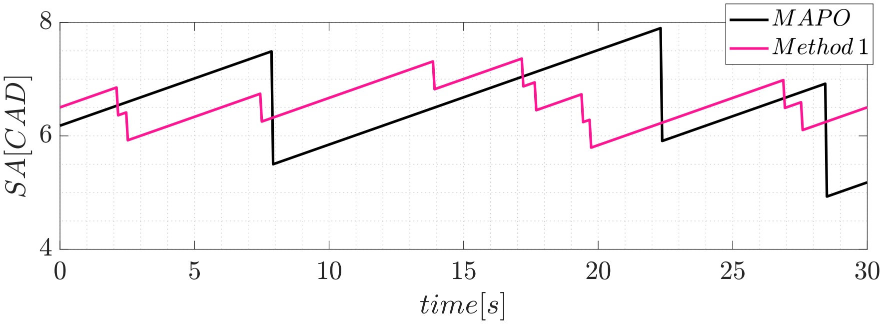

Figure 7.15: *SA control output using MAPO and method 1 definition in engine A. Top: Test number $T1$. Bottom plot: Test number $T2$.*

In Figure 7.16 the controller response for method 2 definition is compared with MAPO knock criteria during test $T3$.

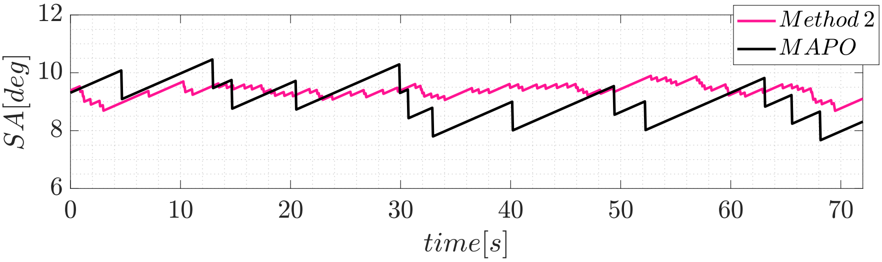

Figure 7.16: *SA control output using MAPO and method 2 definition. Engine A: Test number $T3$.*

A summary of results in terms IMEP, MAPO and SA is shown in Table 7.1 for both methods.

Table 7.1: *Results of tests performed with conventional knock control. Engine A*

	MAPO 0.4 bar		M1		MAPO 0.4 bar		M2	
TEST	T1	T2	T1	T2	T3	T4	T3	T4
$p[\%]$	0.6	0.6	2	2	1	1	8	8
$p_{MAPO}[\%]$	0.6	0.6	0.58	0.61	1	1	1.05	1
$SA_{mean}[deg]$	6.66	6.37	6.59	6.39	8.82	8.84	9.3	9.47
$SA_{max}[deg]$	10.84	10.82	9.88	9.9	10.84	10.82	9.88	9.9
σ_{SA}	0.66	1.44	0.37	0.45	0.57	0.97	0.2	0.3
$IMEP_{mean}[bar]$	11.62	11.60	11.59	11.63	11.4	11.58	11.62	11.78
$IMEP_{std}[bar]$	0.158	0.141	0.115	0.122	0.15	0.16	0.1	0.11
$MAPO_{max}[bar]$	0.783	1.411	0.399	0.406	0.95	0.98	0.45	0.57

The SA results for Tests $T1$, $T2$, $T3$ and $T4$, are represented with box plots in Figure 7.17, for MAPO definition and Method 1 ($M1$) and method 2 ($M2$) definitions. A higher SA average was achieved with both new knock event definitions, and the variability of the controller was significantly reduced. The higher averaged of SA imply a higher thermal efficiency, and the lower SA variability avoids dangerous SA conditions while reducing unnecessary vibrations.

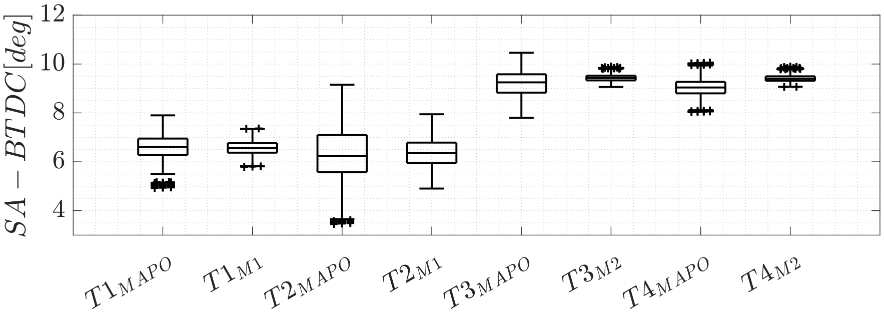

Figure 7.17: *SA values when using conventional knock control for MAPO and Method 1 and 2 knock recognition methods.*

The main advantage of being able to recognize low amplitude knocking cycles, thus allowing to set the controller with a higher probability than applying MAPO criteria, is that the higher sensitivity to knock allows the controller with the proposed methods to avoid SA areas where high knocking intensity (high MAPO values) can be reached. Maximum MAPO amplitudes in Table 7.1 confirm this benefit. Results of Table 7.1 highlights that the two new definition offers more information about knock, which is used to improve the controller performance, being able to reduced the SA variability, and therefore IMEP variability and achieving a more efficient average value. In MAPO case, where SA variability is higher, makes the controller to work in more advance SA values, which can lead to unsafe conditions. This is shown in maximum MAPO: 0.4 bar and 0.78 bar, for method 1 and MAPO criteria respectively, and 0.57 bar and 0.98 bar, for method 2 and MAPO criteria respectively.

7.2.3 Method based on knock sensor signal

Despite in-cylinder pressure signal is the most accurate method for knock diagnosis and widely used in research field, the application in production IC engines is limited due to factors such as durability and cost. Thereby, a knock recognition method based on knock sensor signal is presented in this section. Method 1 study is used to analyzed the knock sensor signal, and develop a method able to recognize knocking events as MAPO criteria.

7.2.3.1 Time-frequency analysis of knock sensor signal

This section presents the time-frequency analysis of the in-cylinder and knock signals. The main objective is to identify the information related to the knock phenomena from the engine block vibration. First, the vibration signal was referenced to the cylinder to be analyzed, for this case cylinder 2. Then, the referenced knock sensor and in-cylinder signals were windowed in order to separate the combustion from other cylinders. A window between 0 and 100 CAD was chosen to analyzed both signals. In Figure 7.18, the STFT spectrum of the in-cylinder pressure and knock sensor signals is represented (bottom plot) while the top plots show the band-pass filter of both signals.

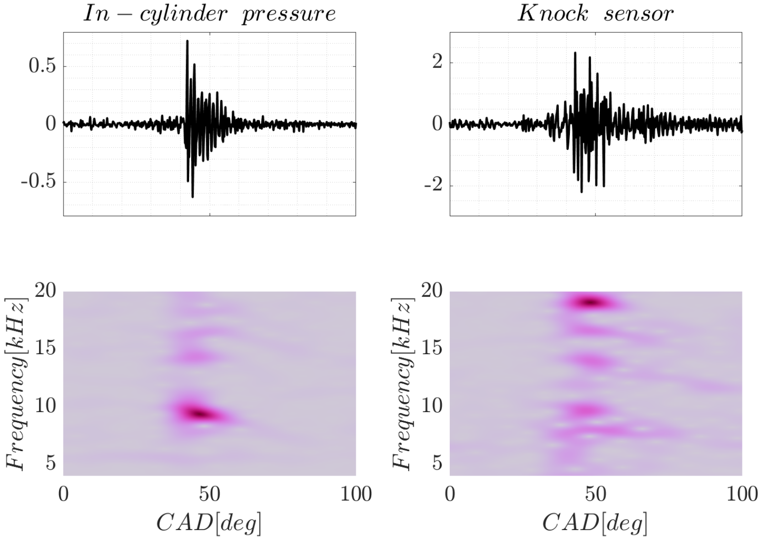

Figure 7.18: *Time-frequency analysis of pressure and knock signal. Top plots: In-cylinder band-pass pressure signal (left) and knock sensor signal (right). Bottom plots: Time-frequency analysis of pressure and knock signal STFT spectrum.*

In order to select the frequency band to examine knock phenomena the value of the coherence function between both signals is analyzed in Figure 7.19. The coherence function was defined in Chapter 2 Equation (2.29); the coherence is ranged from 0 (i.e. no correlated) to 1 (i.e. high correlated).

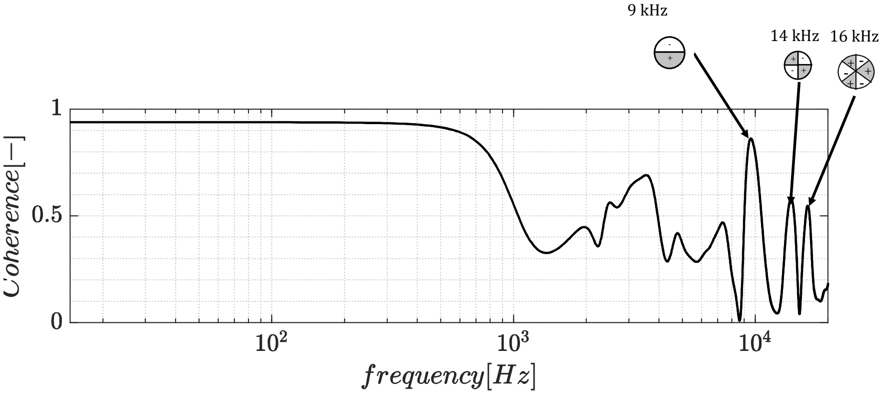

Figure 7.19: *Coherence function between in-cylinder pressure and knock signal.*

Three peaks are highlighted in Figure 7.19, one at 9 kHz, a second one at 14 kHz and a third at 16 kHz, which corresponds to the first, second and third circumferential modes described in Figure 6.1 (see Chapter 6). The coherence function between the in-cylinder pressure and the knock sensor signal was calculated over 200 cycles in engine A, results are shown in Figure 7.19.

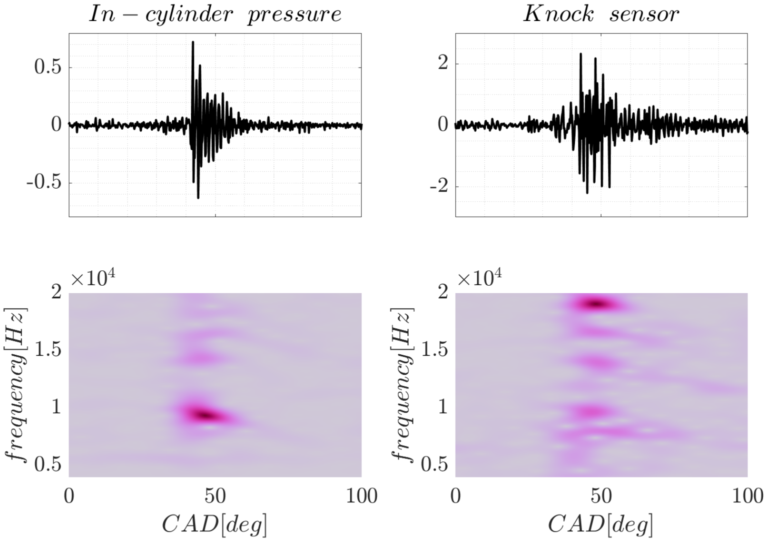

Figure 7.20: *In-cylinder pressure (left) and knock sensor (right) spectrograms.*

As can be seen in Figure 7.19, the coherence reach high values in specific frequency bands: peaks occurring between 200 Hz and 4 kHz are a direct results of combustion process, and higher frequencies with resonance modes of the combustion chamber. Then, showing that the knock sensor signal, specially in selected bandwidths, contain information related to the in-cylinder pressure resonance.

7.2.3.2 Method 3: knock recognition method based on knock sensor signal

In this section a knock recognition method based on knock sensor signal is performed by analyzing the resonance indicator computed from the knock sensor, and compared with the resonance indicator obtained from in-cylinder pressure sensor. The resonance indicator for knock sensor signal is computed as:

$$I_{r-k}(\theta) = \sum_{\theta=\theta_1}^{\theta=\theta_2} w(\theta-\theta_1) kn_{bp}(\theta) e^{-2\pi \sum_{\psi=0}^{\psi=\theta} \frac{B\sqrt{\gamma(\psi) kn_{lp}(\psi) V(\psi)}}{\pi D \sqrt{m}} T_s(\theta)} \tag{7.16}$$

where kn_{bp} and kn_{lp} are the band and low pass knock sensor signal respectively. In Figure 7.21 the resonance indicator evolution during a knocking cycle is computed from knock sensor is represented in grey line, and compared with the resonance indicator obtained from in-cylinder pressure in black line, both normalized.

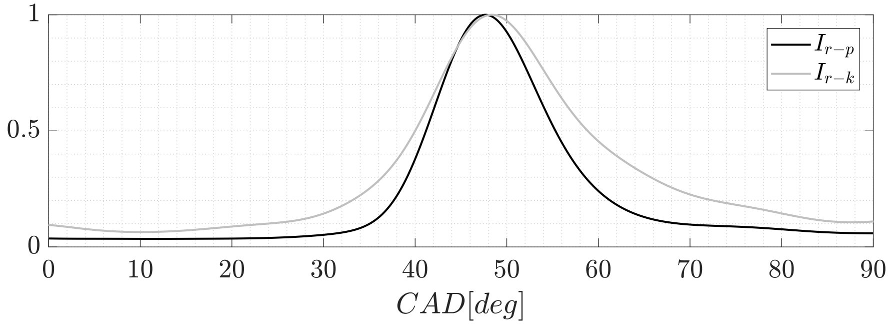

Figure 7.21: *Resonance indicator from in-cylinder pressure compared with knock sensor.*

As it is shown in Figure 7.21, the evolution of the I_r computed from both signals shows that despite some degradation (the I_r is distributed within a wider CAD range), it is still able to capture the cylinder pressure resonance phenomena and its location.

Figure 7.22 compares the resonance indicator maximum amplitude (left plot) and the resonance maximum amplitude location (right plot) from in-cylinder pressure sensor and knock sensor over 3000 cycles at operating point $OP_A = 15$. In Figure 7.22 (right) the amplitude of the resonance indicator from in-cylinder pressure is represented in grey scale color.

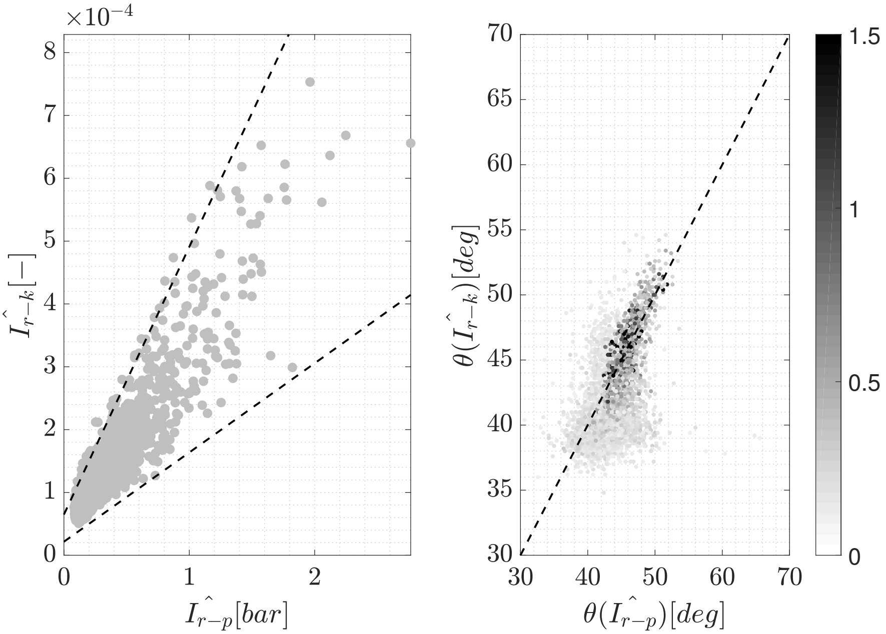

Figure 7.22: *Resonance indicator from in-cylinder pressure compared with knock sensor. Left: maximum resonance indicator amplitude. Right: maximum resonance indicator location.*

As it can be seen in Figure 7.22 (left) the dispersion of the amplitude obtained from knock sensor signal is maintained for all intensities. On the other hand, the location of the maximum amplitude (right plot) is only correlated in cases with high amplitude of resonance.

With the knock sensor signal it is possible to developed a recognition method, based on location and amplitude of resonance indicator, as method 1.

Because the location of the maximum obtained with the knock sensor is only correlated for cases where the maximum amplitude is high, it is not possible to detect low knocking cycles, but the detection is adequate for the case of the knocking cycles with sufficient excitation.

As it was shown in Chapter 4, it is possible to estimate the CA50 through the combination of the combustion model and the knock sensor signal. In Figure 7.23, the number of occurrences of the maximum I_r against the CA50 is shown for three SA settings: -2, -4 and -5 CAD. Top plots illustrates the number of occurrences by computing the resonance indicator and CA50 are equivalent but with in-cylinder pressure sensors, and bottom plots with the knock sensor and combustion model.

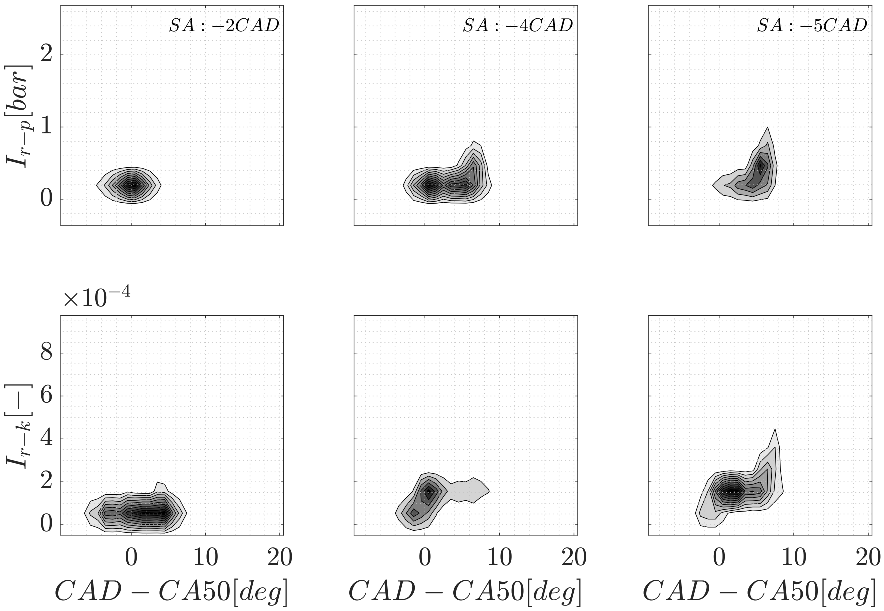

Figure 7.23: *Knock sensor resonance indicator: Number of occurrences of the maximum resonance indicator location and amplitude at different SA settings. Engine A* $OP_A = 15$*. Top plot: in-cylinder pressure sensor results. Bottom plot: knock sensor results.*

As is shown in Figure 7.23, in low probability knocking cycles, i.e SA = - 2 CAD, the maximum of the resonance indicator from in-cylinder pressure I_{r-p} is located between -5 and 5 CAD of the CA50. For the knock sensor case, I_{r-k}, and additional cloud of low intensity at 20 CAD after CA50 appears, this is associated with noise of the signal. When advancing the SA (SA = -4 and -5 CAD) a cloud located around 0 and 10 CAD after CA50 varying its intensity emerge for both cases. This additional cloud of points represents the knocking cycles, which are located near the EOC, and the intensity levels vary between low to high.

An approximation to method 1 based on in-cylinder pressure can be performed by using the combustion model presented in Chapter 4. The minimum oscillation required (Equation (7.6)) can be estimated through the MFB of the model as:

$$I_{r-k-minimum} = G_k \frac{\kappa - 1}{V} m_f H_p (1 - MFB_{model}) \tag{7.17}$$

where G_k is a constant to be calibrated and MFB_{model} the MFB from the combustion model presented in Chapter 4. In Figure 7.24 the scheme for method 3 recognition procedure based on knock sensor signal is presented.

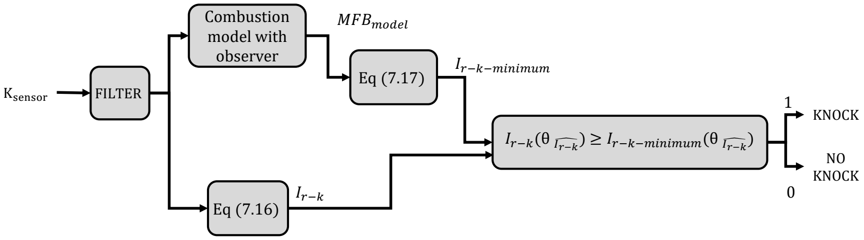

Figure 7.24: *Scheme of method 3 knock recognition procedure.*

In Figure 7.25 the resonance indicator computed from knock sensor signal is shown for 3 cases: no knock, low knock and high knock. In grey continuous line the high pass filtered in-cylinder pressure is represented. In black dashed line the minimum oscillation ($I_{r-k-minimum}$) is plot, and in grey dashed line the CA90.

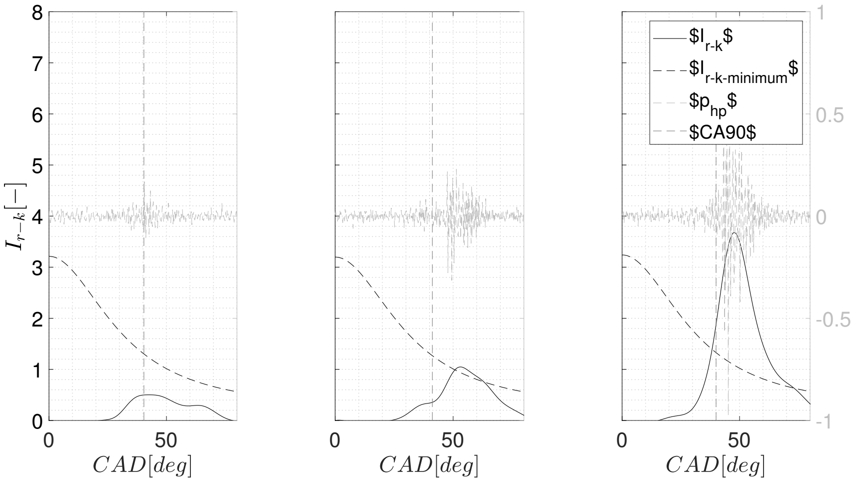

Figure 7.25: *Resonance indicator and minimum oscillation for knock sensor signal at $OP_A = 15$, two cases are illustrated: Left: normal combustion. Middle: low knock. Right: High knock.*

As shown in Figure 7.25, with the combination of knock sensor signal and the combustion model it is possible to recognize knocking events. Nevertheless, replacing an in-cylinder pressure sensor, by an indirect pressure resonance method such as the knock sensor leads to some performance penalty, in this case preventing the detection of some cycles with low knock intensity (see upper plots in Figure 7.25). The same analysis was performed over 5000 cycles in engine A, results are shown in Figure 7.26. In grey line the MAPO amplitude of each cycle is represented, with crosses the knock recognition by applying method 1 and in grey circles method 3.

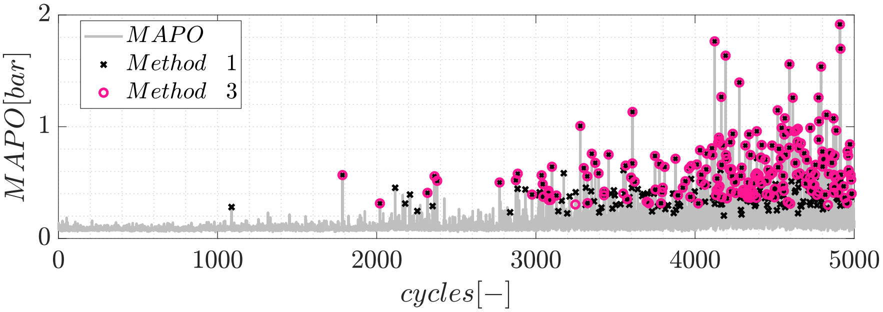

Figure 7.26: *Method 3 detection compared with MAPO amplitude and method 1 for engine A at $OP_A = 15$.*

In order to quantify results shown in Figure 7.26, a confusion matrix is performed by comparing the method based on knock sensor signal (method 3) and the method 1 based on in-cylinder pressure. Results are illustrated in Figure 7.27, where a confusion matrix is used to show the percentage of positives and negatives captured by the proposed method.

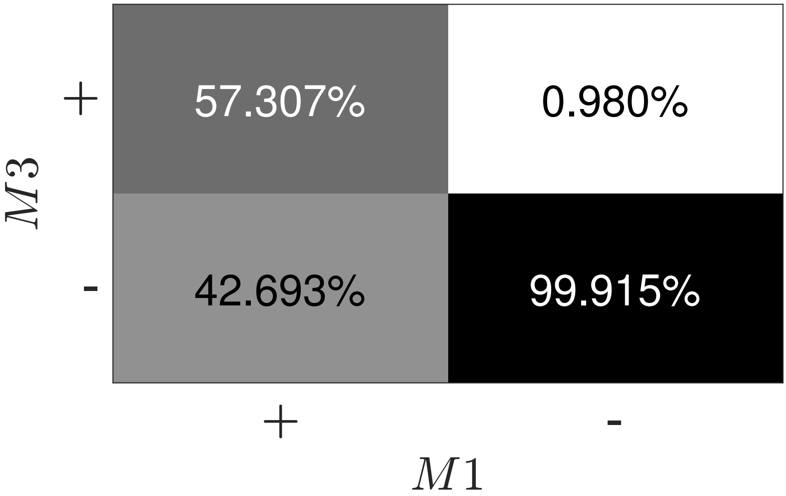

Figure 7.27: *Confusion matrix between methods 1, based on in-cylinder pressure, and 3 based on knock sensor.*

As is shown in Figure 7.27, method 3 is able to recognize a 57 % of the knocking cycles, based on the high sensitivity recognition, and the false negatives cycles are less than the 1 %.

7.2.4 Comparative of methods with MAPO

In this section methods 1 and 2, based on in-cylinder pressure sensor, and method 3, based on knock sensor, are compared with classical MAPO definition. Various steps of SA were performed in engine A in order to compared the different knock recognition methods. In Figure 7.28, the percentage of knocking cycles computed from several knock recognition criteria at each SA is shown for operating point $OP_A = 5$.

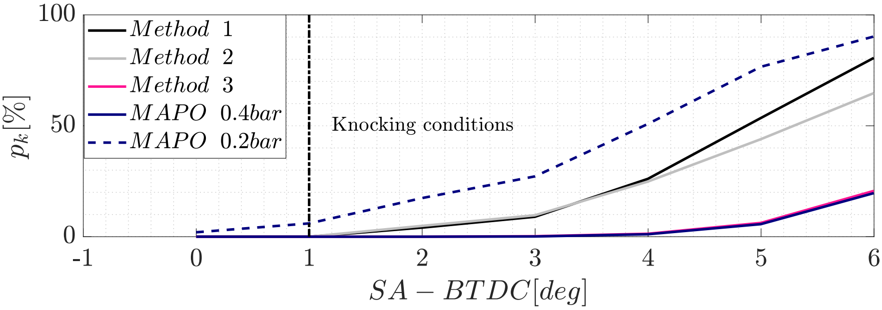

Figure 7.28: *Knock probability for different SA settings and methods.*

Notice that in SA = 1 a vertical line is representing the starting point of knocking conditions when methods 1 and 2 are taken as reference. As is shown in Figure 7.28, when MAPO threshold is set at 0.4 bar, only high knock events are recognized, while if MAPO threshold is set at a lower value, 0.2 bar, cycles at no knocking conditions are classified as knock. On the other hand, methods 1 and 2, are capable of recognizing knocking cycles with low amplitude, being the knock probability higher than for MAPO 0.4 and lower than MAPO 0.2. Besides, method 3 is able to detect cycles with a probability of MAPO 0.4 bar, but with the benefit that in-cylinder pressure is not required for this method.

In order to compare all the methods with MAPO 0.4 bar at different operating conditions, knock probability was computed for all SA sweeps at four operating conditions; results are illustrated in Figure 7.29.

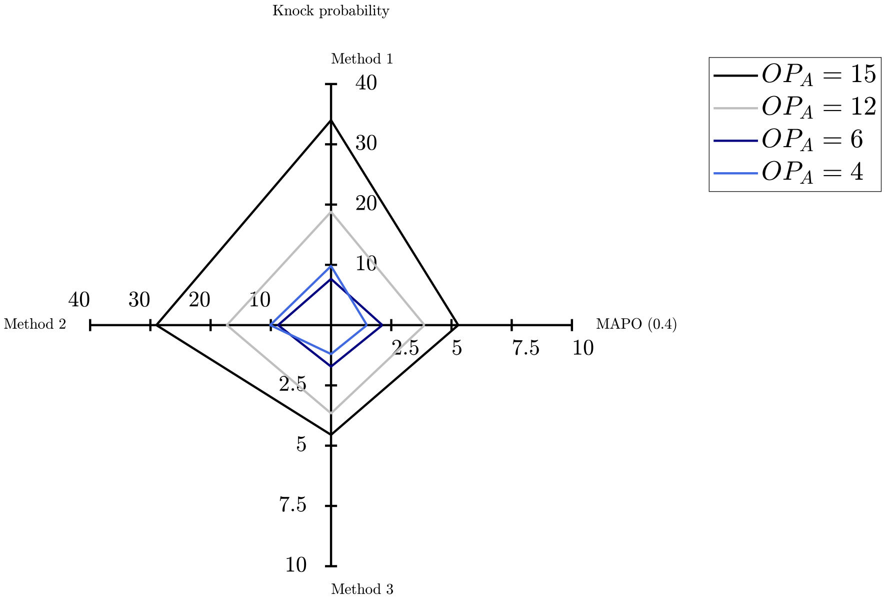

Figure 7.29: *Knock probability for MAPO 0.4 bar and methods 1, 2 and 3 at different operating conditions.*

As it can be seen in Figure 7.29, with methods 1 and 2 low knocking conditions are recognized, i.e a higher knock probability at each operating condition. Despite that method 3 is not capable of recognizing low knocking cycles, it is capable of recognizing a number of knocking events similar to MAPO criteria, thus being able to replace in-cylinder pressure sensor if the target is to detect only high knocking events.

MAPO definition has difficulty in recognition low knocking cycles without false recognition in SI engines. This is solved by being able to detect where resonance is excited by the proposed two in-cylinder pressure methods. If low knocking cycles is not required for the application, method 3 is able to detect high knocking events without in-cylinder pressure sensors.

7.2.5 Application to different fuels

Knock detection methods based on in-cylinder pressure sensor was also validated for different fuels in engine B. First, the effect of the fuel on the resonance indicator was analyzed in Figure 7.30, where the number of events of the maximum resonance indicator location against the amplitude at different

SA is shown: on top cases with the engine fueled with gasoline and on bottom cases fueled with CNG.

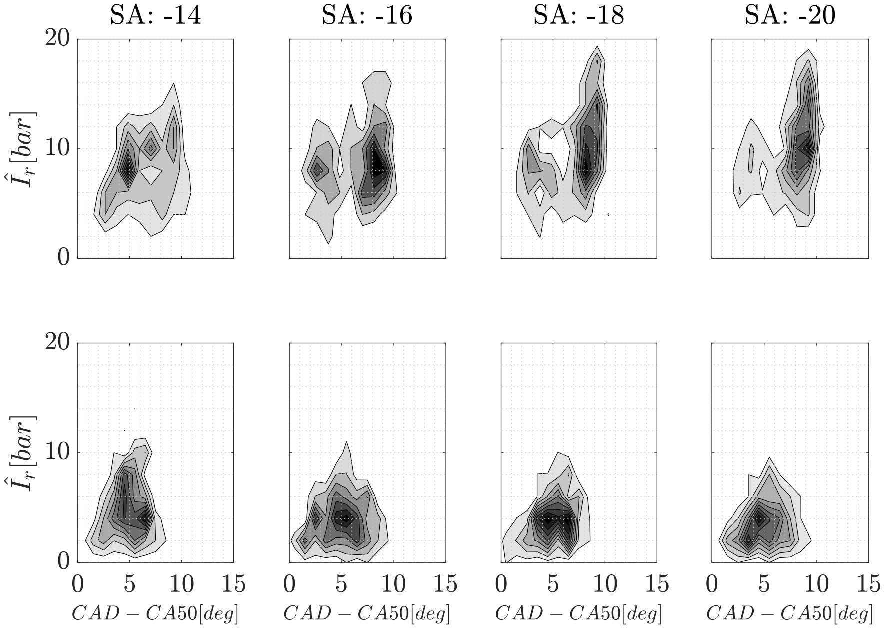

Figure 7.30: *Number of events of the maximum resonance indicator location against amplitude at different SA settings and fuels. Operating condition* $OP_B =$*. Top: Gasoline. Bottom: CNG.*

As expected, knock tendency, i.e resonance intensities are lower for CNG cases. This is thanks to the higher knock resistance for gaseous fuels compared with gasoline, which is due to the higher RON of CNG [4, 5].

As it was explained above, both knock recognition methods 1 and 2 are independent on the fuel type, i.e the recognition method is based on the cylinder pressure signal (independently of the fuel that has lead to this evolution). In Figure 7.31 the knock threshold for method 1 criteria is shown for gasoline (left) and CNG (right) when SA = -20 CAD over 200 cycles.

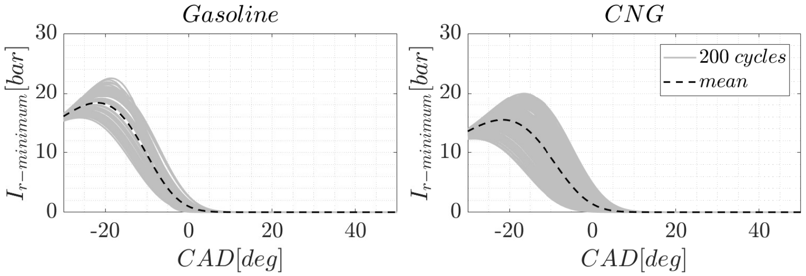

Figure 7.31: *Minimum expected resonance for knock occurrence. Left: Gasoline. Right: CNG. Operating condition OP_B = SA = -20 CAD.*

As introduced in Equation (7.6), the minimum oscillation required for the end gas to auto ignite is a function of the lower calorific value of the fuel and the evolution of the MFB, therefore, the method is independent on the fuel type.

Both knock recognition methods based on in-cylinder pressure signal are analyzed at engine B over $OP_B =$ in Figure 7.32. In grey the cycles fueled with gasoline and the threshold is represented, and in black cases fueled with CNG.

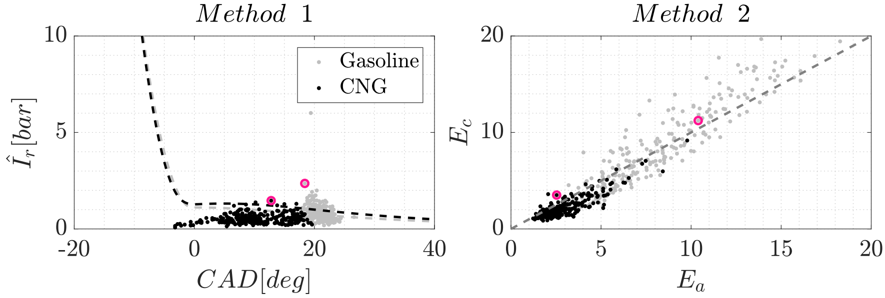

Figure 7.32: *Methods 1 and 2 over all SA settings at OP_B =. Left: Method 1. Right: Method 2. Two cycles classified as knock for both methods are highlighted.*

As it can be seen in Figure 7.32, over the same operating conditions, cases fueled with gasoline exhibit more knocking cycles. In blue two cycles are highlighted, one for gasoline and another one for CNG. These cycles are represented in Figure 7.33, where the high-pass pressure and HRR are shown on top plot, and the resonance indicator is compared with resonance models for combustion and auto ignition on bottom plots.

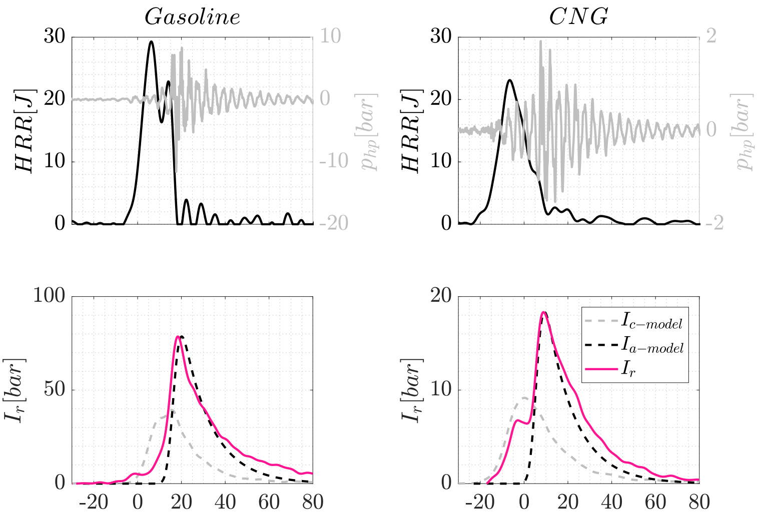

Figure 7.33: *Detail cycle for Gasoline (left) and CNG (right). Bottom plots: HRR and high pass pressure. Top plots: Resonance indicator compared with resonance model for combustion and auto ignition.*

For both cases resonance model fit better with the resonance evolution in the combustion chamber in a knocking case independently on the fuel type. As it was demonstrated during this section, both methods based on in-cylinder pressure are capable of adapting not only to different types of combustion, but also to different fuels without the need to re-calibrate the models.

7.3 In-cylinder trapped mass estimation

In-cylinder pressure resonance excitation has been extensively used for knock analysis and recognition, nevertheless, in recent years an algorithm to estimate the trapped mass has been developed in [6], by using signal analysis techniques. The method used to determine the trapped mass from resonance might be erratic if no sufficient resonance exist or if some noise is analyzed. In order to overcome this, the attenuation model can be used as a tool to identify the optimal range to analyze the pressure oscillations for a trapped mass estimation by detecting normal resonance damping from other noise sources [6].

In Figure 7.34 (left) the experimental attenuation is compared with the model during the expansion stroke in a cycle at 1500 rpm of engine B, on right plot the relative error is represented.

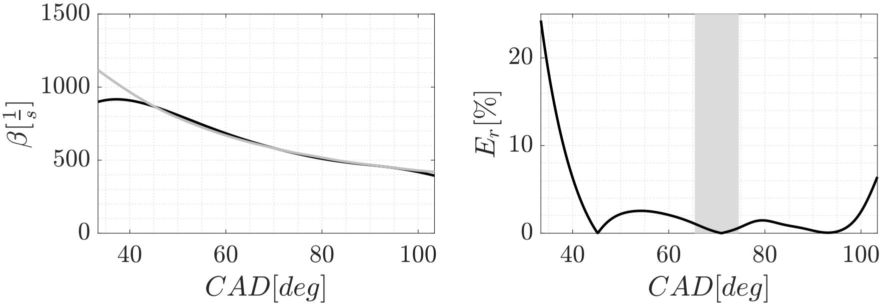

Figure 7.34: *Optimal window for trapped mass estimation: Attenuation evolution and model (left), relative error of the model during expansion stroke (right).*

The relative error between the attenuation and the model indicates the optimal window where resonance is more clear over background noise. Therefore, the optimal window can be obtained by finding the range with minimum error by computing the mean error at different window range (w_a) as:

$$E_{range} = mean(|\beta_{mode}(w_a) - \beta_{exp}(w_a)|) \tag{7.18}$$

The optimal window location procedure scheme proposed is shown in Figure 7.35, where w_{opt} represents the CAD at the center of the window for the calculations. In this work the initial window size was of 40 CAD.

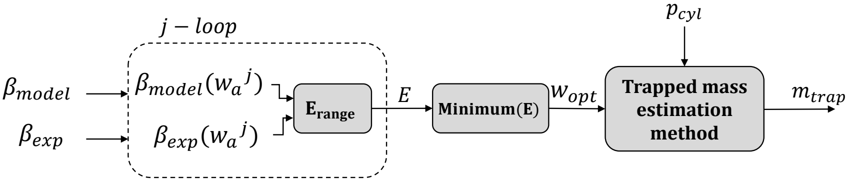

Figure 7.35: *Optimal window procedure for trapped mass estimation.*

The optimal window location will be the range with the minimum error. This criteria was also implemented over a IMEP transient, by computing the trapped mass as shown [7]. The trapped mass results over the transient are shown in Figure 7.36, where the mass calculated from air mass flow sensor and injected fuel is compared with that obtained from the resonance method. The moving average (M_m) over 20 cycles and the moving standard deviation (σ_m) are highlighted in points and dashed line respectively.

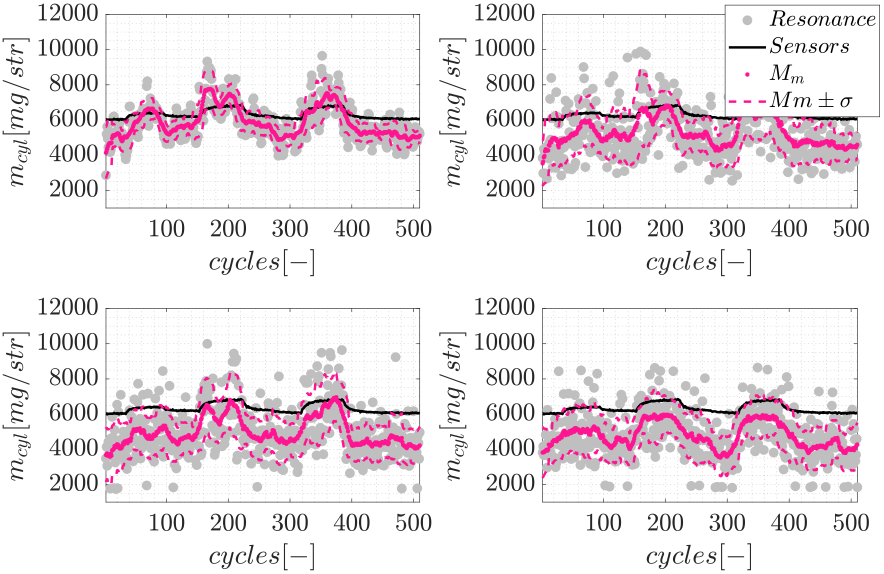

Figure 7.36: *Optimal window procedure for trapped mass estimation.*

Additionally, in Figure 7.37, the evolution of the optimal window location for each cycle is represented. Three locations are highlighted with dashed line: 40, 30 and 20 CAD.

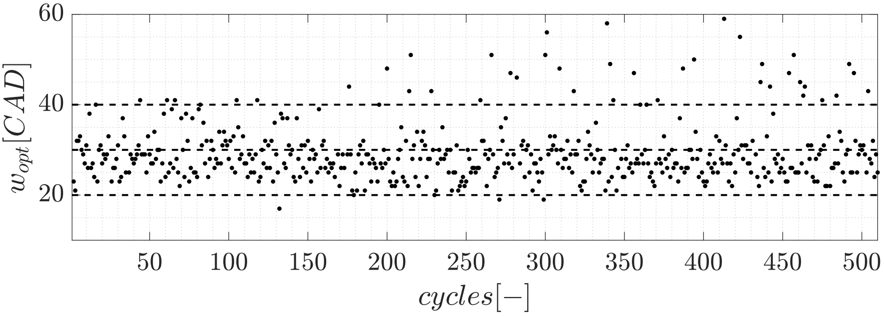

Figure 7.37: *Optimal window location over a transient.*

As it can be seen in Figure 7.37, a moving window provides a better approximation of the trapped mass estimation, since permits to differentiate resonance from other noise sources, which depends on the combustion and the attenuation evolution.

7.4 Conclusions

In this chapter the models developed in the second part of the dissertation were used for different combustion diagnosis applications: on the one hand, for knock recognition methods, and on the other hand, to improve the estimation of the trapped mass from the resonance excitation.

In the first part of the chapter 3 knock recognition methods had been developed, two based on in-cylinder pressure signal and one based on knock sensor signal:

Method 1 defines a minimum oscillation required based on the constant volume combustion of the fuel mass that is not burnt by the SI flame development.

Method 2 is based on a resonance evolution model capable to distinguish normal combustion from auto ignition, this method is based on the shape of the resonance evolution, and not only its intensity, will permit the recognition of knock in new combustion modes, where the resonance is highly excited by combustion, while it will facilitate the recognition of low-knocking cycles in SI engines.

Method 3 is based on the combustion model presented in chapter 4 and the method 1. This method aims to make use of knock sensor signal to estimate the minimum oscillation and compared with the resonance indicator from the knock sensor.

It has been demonstrated that methods 1 and 2 are able to recognize low knocking cycles in SI combustion, which is use full to update online models based on knock observation. Moreover, the methods are able to differentiate combustion from resonance in new combustion modes where normal combustion heavily excites resonance, such as TJI combustion. One of the great advantages of methods 1 and 2 is the flexibility that provides for different fuels and combustion type, such as gasoline or CNG, and SI or TJI combustion.

Regarding method 3, knock sensor based, results show that this method is not able to detect low-knocking cycles, but is capable of recognized knocking cycles with a MAPO criteria of 0.4 bar. One of the major advantages of this method is that it does not make use of in-cylinder pressure sensors.

In the second part of the chapter, an optimization of the window to compute the trapped mass from the resonance is presented, where the attenuation model can be used to identify resonance from other noise sources, identifying the optimal range for resonance analysis. Results shows that the model gives more information about resonance, allowing a better estimation of the trapped mass.

References

[1] Bares Pau, Selmanaj DONALD, Guardiola Carlos and Onder Christopher. “A new knock event definition for knock detection and control optimization”. *Applied Thermal Engineering*, Vol. 131, pp. 80–88, 2018. (cited in pp. 31, 33, 148, and 153)

[2] Kefalas Achilles, Ofner Andreas B, Pirker Gerhard, Posch Stefan, Geiger Bernhard C and Wimmer Andreas. “Detection of Knocking Combustion Using the Continuous Wavelet Transformation and a Convolutional Neural Network”. *Energies*, Vol. 14 n^o 2, pp. 439, 2021. (cited in p. 148)

[3] McKenzie Jacob and Cheng Wai K. “The anatomy of knock”. Technical report, SAE Technical Paper, 2016. (cited in p. 156)

[4] Pipitone Emiliano and Genchi Giuseppe. “Experimental Determination of Liquefied Petroleum Gas–Gasoline Mixtures Knock Resistance”. *Journal of Engineering for Gas Turbines and Power*, Vol. 136 n^o 12, 2014. (cited in p. 177)

[5] Pipitone Emiliano and Beccari Stefano. “Performances improvement of a SI CNG bi-fuel engine by means of double-fuel injection”. Technical report, SAE Technical Paper, 2009. (cited in p. 177)

[6] Broatch Alberto, Guardiola Carlos, Pla Benjamín and Bares Pau. “A direct transform for determining the trapped mass on an internal combustion engine based on the in-cylinder pressure resonance phenomenon”. *Mechanical Systems and Signal Processing*, Vol. 62, pp. 480–489, 2015. (cited in p. 179)

[7] Luján José Manuel, Guardiola Carlos, Pla Benjamin and Bares Pau. “Estimation of trapped mass by in-cylinder pressure resonance in HCCI engines”. *Mechanical Systems and Signal Processing*, Vol. 66, pp. 862–874, 2016. (cited in pp. 115 and 181)

CHAPTER 8

Combustion control

Contents

8.1 Introduction

Two of the most fundamental issues related to IC engines are the energy efficiency and emissions performance, which are influenced by the combustion quality [1]. In order to optimize IC engine performance many actuators are used, such as SA or VVT, between others [2]. One of the main combustion control parameters in SI engines is the SA [3], since it allows to modify the combustion timing and therefore combustion efficiency, avoiding knocking conditions. Additionally, RGF, which is defined as the ratio of the residual gas mass to the total gas burned in a cycle [4], is an important parameter for managing the combustion quality since influences in emissions, stability and volumetric efficiency.

Chapter 4 has presented a combustion model with an observer, which makes use of signals available in the ECU and a knock sensor. Chapter 7 proposed two low-knocking cycles recognition based on in-cylinder pressure. This chapter is devoted to point out the potential of such models: first, method 1 knock criteria is used to update a map-based model for SA knock control, this controller is compared with the conventional knock controller in steady and transients conditions. Then, the combustion model presented in Chapter 4 is implemented in real-time, where two control variables are used: SA and VVT, with the aim to control the RGF and optimizing the combustion with the SA; RGF may be controlled with VVT actuation.

8.2 Fuzzy logic knock control

Knock control can be divided in two main groups: feedback and model based methods. The issue with feedback methods is the high variation of the spark timing and the slow response of these controllers [5]. On the other hand, model based controllers can rely on physical models, which are very complex, or map-based models, which required a high amount of cycles to adapt under transient conditions.

In this section a knock control combining both feedback and adaptive methods is presented. In order to update the map-based model fast, the low-knocking recognition method presented in Chapter 7 is used, since recognize low-knocking cycles permits to shorten the time to identify stochastic properties, and hence, adapt the model faster [6].

In order to achieve this purpose, a SA control based on map learning technique combined with a conventional knock controller (see Chapter 2) for SA control is proposed. Figure 8.17 shows the general scheme of such control algorithm.

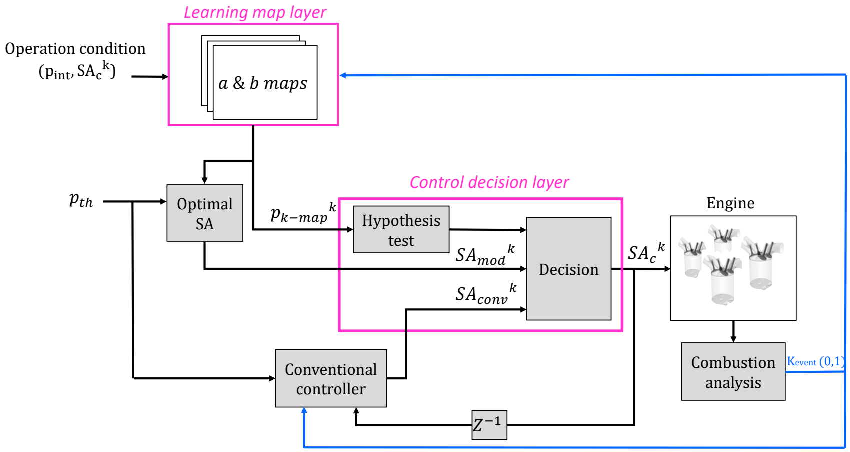

Figure 8.1: *SA knock controller based on map learning and conventional controller proposed.*

The proposed control structure has two main layers: learning and control. The first layer consist of two maps, namely a and b, which are probability distribution maps. The distribution maps are modeled as a function of the intake pressure (p_{int}) and the SA. The output of the learning layer is the predicted knock probability over the different operating conditions modeled as a function of p_{int} and SA. Then, the optimal SA module, estimates the SA leading to the desired knock probability (p_{th}).

The second layer, the control layer, is used to evaluate the knock probability model. This layer consist of two parts: a hypotheses test and a decision. In the first part, the hypotheses test, the knock probability expected obtained from the model is contrasted with the probability computed from most recent knocking events. The second part, the decision, determines the control action: if the probability of the model is near the observed probability during the recent past, the control action used is SA_{mod}, on the other hand, if there is a discrepancy between both probabilities, the control action used is the SA from a conventional knock controller SA_{conv}. Between both extremes, a combination between model and conventional control is applied. During next sections both layers will be introduced in detail.

8.2.1 Learning map layer

As introduced in [7], no matter the knock amplitude probability density function, knocking events are binomial distributed. The binomial signal of knock is computed from detection method 1, described in Chapter 7, and the distribution of knock probability is learned by using Bayes theorem as is introduced in [8]. The distribution learned is a beta distribution with a and b parameters: $Beta(p \mid a, b)$. Where a represents knocking events, and b normal combustion. The probability that a given cycle is classified as knock, $Pr\{knock = 1\}$, is denoted as p_k.

Knock event distribution is learned from the Bayesian learning process [9], where p_k, in this case, adopts a beta distribution, so the mean and the variation can be estimated as:

$$M[p_k] = \frac{a}{a+b} \tag{8.1}$$

$$Var[p_k] = \frac{ab}{(a+b)^2(a+b+1)} \tag{8.2}$$

The calculation process is illustrated in Figure 8.2: on the left the events from cycle k to $k+2$ are represented, crosses are used for cycles classified as knocking and filled circles for cycles classified as normal combustion. On the right plot, the distribution for each cycles is shown. In cycle k, 10 cycles had been passed: 3 knocking ($a^k = 3$) and 7 with normal combustion ($b^k = 7$). One cycle after, $k+1$, a knocking event is observed, then $a^{k+1} = 4$ and $b^{k+1} = 7$, and a modification on the distribution is observer on the right side. The same for cycle $k+2$, where the cycle is classified as normal combustion, so $a_{k+2} = a_{k+1}$ and $b_{k+2} = 8$.

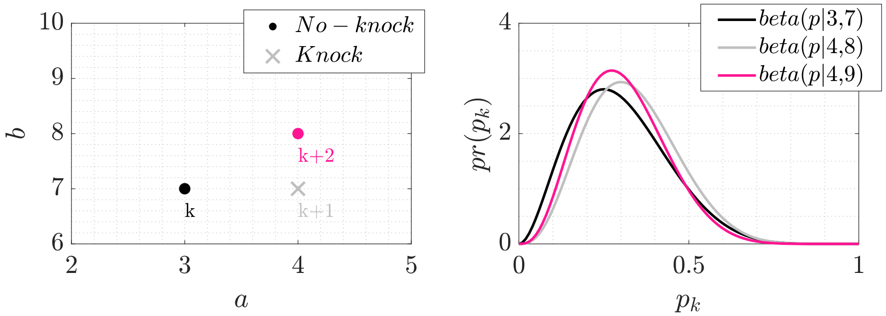

Figure 8.2: *Map learning process for SA control. Left plot: a and b parameters evolution. Right plot: Beta distribution of cases on left plot.*

The engine operating conditions can be characterized in a two dimensional grid (x_1,x_2) for every engine speed. Where x_1 is the intake pressure p_{int} and x_2 the combustion phasing represented by the SA. The grid to characterize the engine operating condition is represented on the left side of Figure 8.3, where a grey dot are used to highlight the actual operating condition characterized by $x_{1,op}, x_{2,op}$.

Because the engine does not always work precisely on the grid points, the grid should be updated following an adaptation method. Several adaptation methods can be found on literature: Kalman filter [10], Gaussian filter [11], etc. In this work, a Gaussian filter is applied to update knock probability distribution map, where the weight (ϕ) for each grid point X ($X : [x_{1,op}, x_{2,op}]$) is updated as following:

$$\phi = \frac{1}{\sqrt{2\pi}\sigma_{x_1}} e^{-\frac{1}{2}\frac{(x_1 - x_{1,op})^2}{\sigma_{x_1}^2}} + \frac{1}{\sqrt{2\pi}\sigma_{x_2}} e^{-\frac{1}{2}\frac{(x_2 - x_{2,op})^2}{\sigma_{x_2}^2}} \tag{8.3}$$

σ_{x_1} and σ_{x_2} determines the smoothness of map. In Figure 8.3 (right plot) the effect of increasing σ_{x_1,x_2} is represented: in grey the updated with $\sigma_{x_1,x_2} = 1$ and in blue for $\sigma_{x_1,x_2} = 2$.

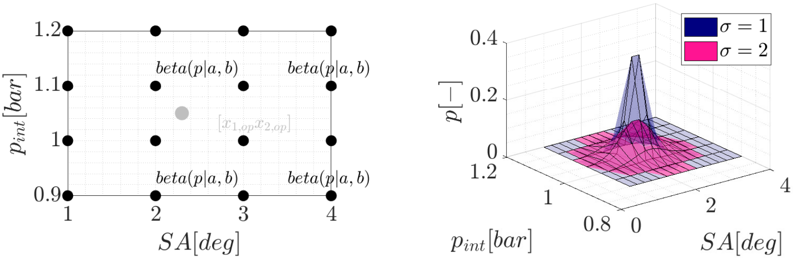

Figure 8.3: *Proposed probability map learning algorithm for knock control.*

The parameters of beta distribution, a and b, are updated as:

$$\begin{aligned} a^{k+1} &= a^k + \phi \qquad if \quad knock \\ b^{k+1} &= b^k + \phi \qquad otherwise \end{aligned} \tag{8.4}$$

A normalization needs to be applied to these parameters [8]:

$$a + b = N_s \tag{8.5}$$

where N_s is the normalization magnitude, if N_s is high, the effect of new data on learning is slow, otherwise, the effect of innovation is fast. In the present work a normalization size of 200 is used.

After parameters a and b are computed, the knock probability at each grid point can be calculated by Equation (8.3). The σ value in each dimension should not be very high: an elevated number could lead to overestimate knock probability at points near the operating point. In the present work, the smoothness chosen is $\sigma_{x1,x2} = ([2,1])$.

Another aspect to consider is that knock probability for a given operating condition is never decreasing for increasing SA points [12], i.e. advancing the SA leads to higher knock probability points. This phenomenon is considerate to calculate the optimal SA, but is not taken into account to update the distributions models a and b. In Figure 8.4 the knock probability map and the map with the constraint is represented: magenta map is the updated knock probability map and grey map is the model to calculate the SA for a given knock probability.

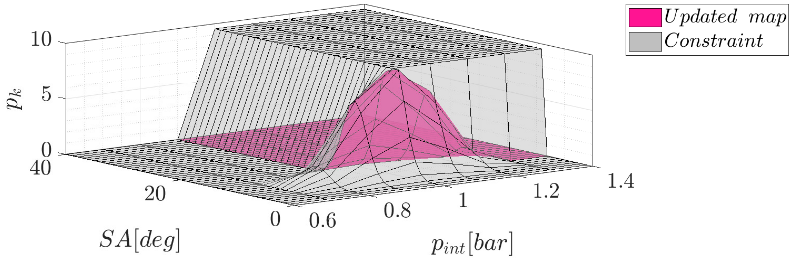

Figure 8.4: *Proposed probability constraint map learning for spark advance control.*

8.2.2 Control decision layer

As explained above, the decision layer is divided in two parts. In this section both, hypothesis test and decision blocks, will be introduced.

8.2.2.1 Hypothesis test

The hypothesis test block in Figure 8.17 is used to compare the knock probability modeled and observed knock probabilities. The probability of detecting k_i knocking events in k_n cycles is calculated as proposed in [13]:

$$p_{kn}^{k_i} = \binom{a}{b} p_{ki}^{ki}(1 - p_{ki})^{(kn-k_i)} \tag{8.6}$$

where p_{ki}^{ki} is the probability of observing ki knocking cycles and p_{ki} the knock probability.

The likelihood ratio test L_h is largely employed in knock control, some examples can be found in [13, 14]. L_h is used to evaluate evaluate two statistical models, for this particular case the expected knock probability, p_0, compared with the observed knock probability, p_{obs}. The observed knock probability can be computed as: $p_{obs} = k_i/kn$. The Likelihood ratio is calculated as:

$$L_h = \frac{L(p_0 \mid N_{kn})}{L(p_{obs} \mid N_{kn})} = \frac{p_0^{kn}(1 - p_0)^{(kn-k_i)}}{p_{obs}^{k_i}(1 - p_{obs})^{(kn-k_i)}} \tag{8.7}$$

k_i represents the number of knock events in kn cycles. N_{kn} is the observed sequence of knocking cycles. An illustration of the likelihood ratio as a function of kn is represented in Figure 8.5 for a knock probability $p_0 = 0.1$.

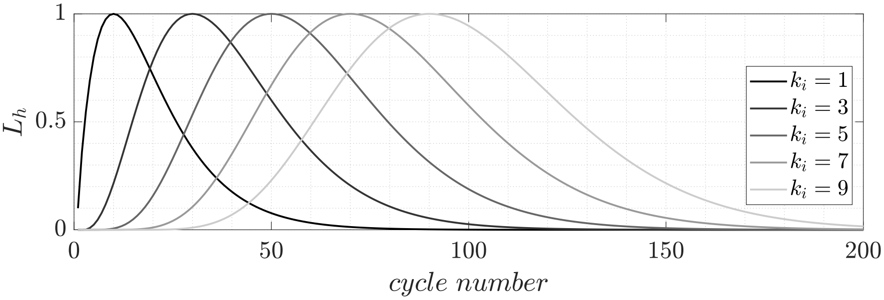

Figure 8.5: *Example of likelihood ratio for different number of knocking events ($p_0 = 0.1$).*

A value of $L_h = 1$ shows that the expected probability p_0 perfectly match with the observation knocking rate p_{obs}, on the other hand, L_h close to zero indicates a mismatch. For example, as is shown in Figure 8.5, the maximum of L_h at each k_i case match with the knock probability p_0, i.e. after 50 cycles ($kn = 50$) and five knocking cycle ($k_i = 5$), the maximum L_h for that case is located at $\frac{k_i}{k_n} = 10$ cycles.

In order to compute the observed knock probability First In First Out (FIFO) buffers are used. In this case, two FIFO buffers are used: 100 cycles and 5 cycles length. The first buffer is used to calculate the knock probability of a given operating condition, and the second buffer is used to detect consecutive knocking events. The observed probability of both FIFO buffers is computed as following:

$$p_{buffer} = \frac{\sum_{j=1}^{N_{buffer}} k_i^j}{N_{buffer}} \tag{8.8}$$

where k_i^j is the boolean (true = 1/false = 0) knock signal, and N_{buffer} is the length of the buffer.

Therefore, the L_h defined in Equation (8.7) is calculated as:

$$L_h = \frac{p_{k-map}^{k}(1 - p_{k-map})^{(kn-k_i)}}{p_{buffer}^{k_i}(1 - p_{buffer})^{(kn-k_i)}} \tag{8.9}$$

where p_{k-map} represents the probability obtained from the model, and p_{buffer} is the observed probability over the FIFO buffers.

8.2.2.2 Decision block

The second block define the control action of SA, where a combination of the model and conventional controller is implemented in a fuzzy logic control system. If knock probability from the model, p_{k-map}, match with the observed knock probability, p_{buffer}, then the SA command will be obtained from the model. Otherwise, the SA output will be a combination of model and conventional controller.

The final SA is a fuzzy set between model and conventional knock controller, which is supervised by a gain α_c as:

$$SA_c^k = (1-\alpha_c)SA_{conv}^k + \alpha_c SA_{mod}^k \tag{8.10}$$

α_c will be 1 when the model matches the observation, and 0 if mismatch.

As explained above, two values of likelihood ratio are computed, one from the long buffer (L_{hL}) and from the short buffer (L_{sL}). Both L_h are used to compute α_c as is illustrated in Figure 8.6.

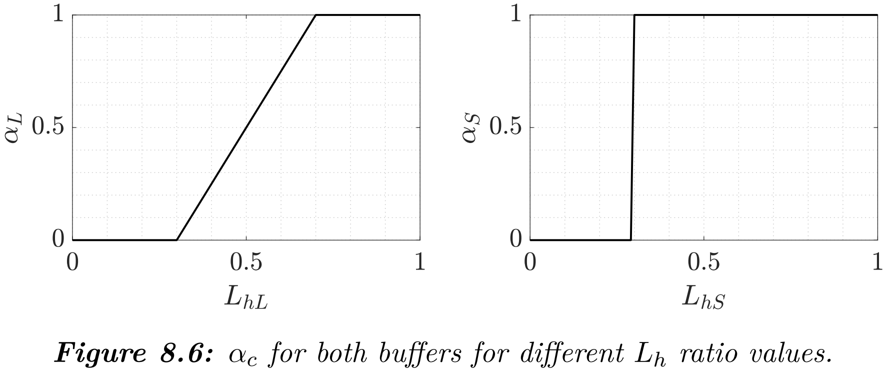

Figure 8.6: *α_c for both buffers for different L_h ratio values.*

The L_{hS} limit value was calibrated by observing how consecutive knocking cycles affect to the likelihood ratio from the short buffer, while the function L_{hL} was fetermine as an arbitrary function between 1 and the limit from the

L_{hS}.

The final fuzzy logic value to control the transition between model and conventional controller, α_c, is computed as the product between both α values, α_L and α_S.

8.2.3 Simulation of map learning process

In order to show the learning process a simulation over transient $T6$ in engine A is performed. During transient test $T6$, the SA was controlled by a conventional knock control with a set knock probability of 8 %. In Figure 8.7, the knock probability from the buffer of 100 cycles, the control knock probability (p_{k-c}) and the map knock probability for each cycle are represented.

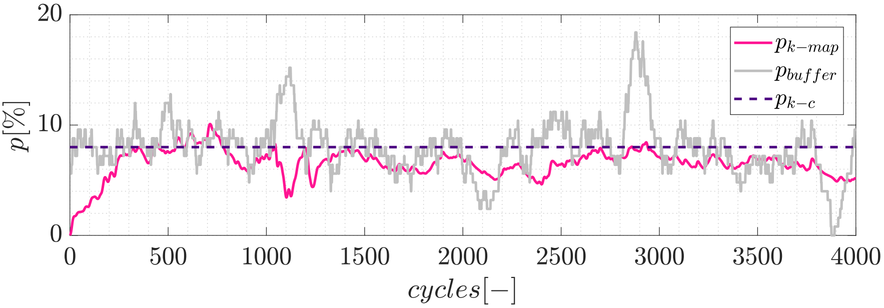

Figure 8.7: *Knock probability during transient* $T6$*: from the map* p_{k-map}*, from the long buffer* p_{buffer} *and the controller set probability* p_{k-c}.

Note that p_{k-map} initial number is zero, while knocking events are detected the map probability increase up to a probability around the probability set at the conventional controller. In Figure 8.8 (left), the updated grid points during the transient are shown for four sets of cycles, and right plot shows the trajectory over the 2000 cycles of the knock probability over the grid.

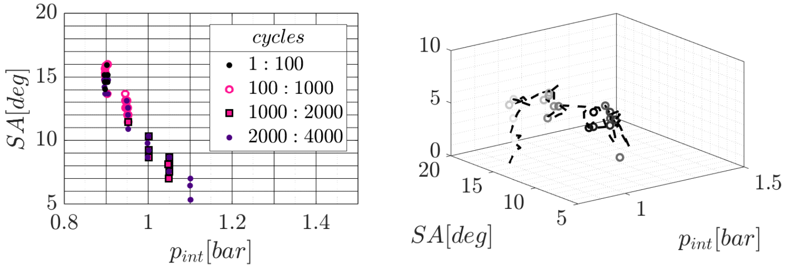

Figure 8.8: *Updated grid points during transient $T6$. Left: grid points updated over each set cycles. Right: knock probability trajectory over the grid points.*

The updated maps at the end of each set cycles shown in Figure 8.8 are represented in Figure 8.4.

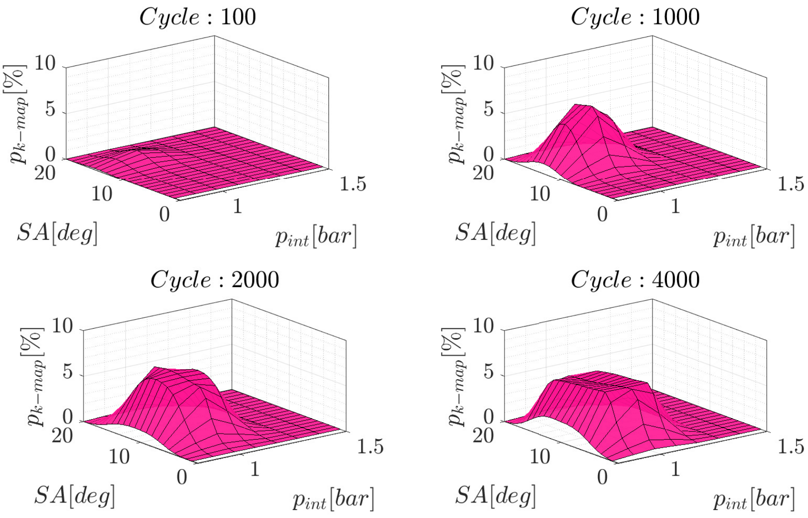

Figure 8.9: *Knock updated map of cycle: 100 (left top), 1000 (right top), 2000 (left bottom) and 4000 (right bottom).*

As shown in Figure 8.4, on cycle 100 the map is basically empty, after 1000 cycles, the map is mainly updated at 0.9 bar intake pressure, which is the mean in-cylinder pressure during first 1000 cycles during transient $T6$. Afterwards, in cycle 2000 more points of in-cylinder pressure and SA are updated. Note that at the end of the transient test, the map is updated around all transient operating points (p_{int},SA).

In Figure 8.10 the same SA sweeps were performed in engine A over operating condition $OP_A = 5$, two cases are plotted: with and without EGR.

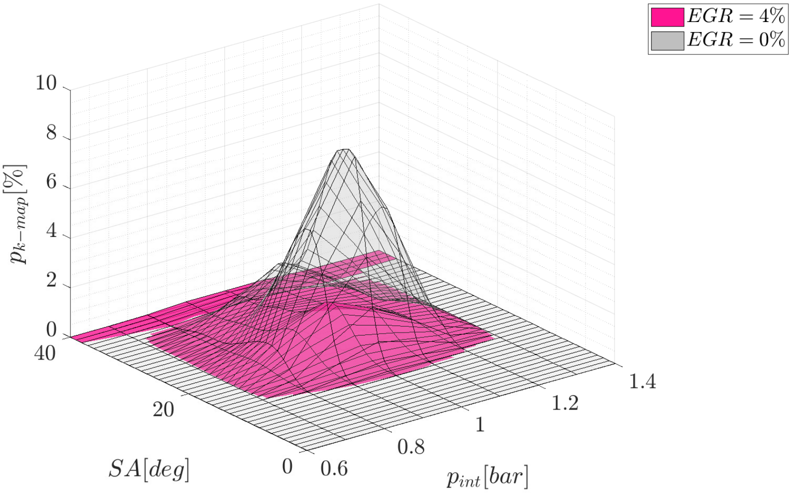

Figure 8.10: *Knock updated map with and without EGR.*

As is shown in Figure 8.10, the knock probability model is able to update under different operating conditions over the same grid points. As expected, for the EGR case, the knock probability becomes considerably lower than in the case without EGR.

8.2.4 Validation results and discussion

8.2.4.1 Learning

Initially, the knock probability maps are empty, so the SA output is controlled by the conventional knock control, i.e. $\alpha_c = 0$. In the learning process, the knock probability map is cycle by cycle updated. In order to illustrate this process, the engine operating conditions were maintained constant at operating point $OP_A = 5$. In Figure 8.11 results are represented: top plot shows the control action, SA_c and the optimal SA obtained from the model, SA_{mod}. In the middle plot, the knock probability updated of the model is represented with the knock probability set at the controller, p_{th}. In the bottom plot, the decision gain α_c and the likelihood ratio of the 100 cycles buffer are plotted.

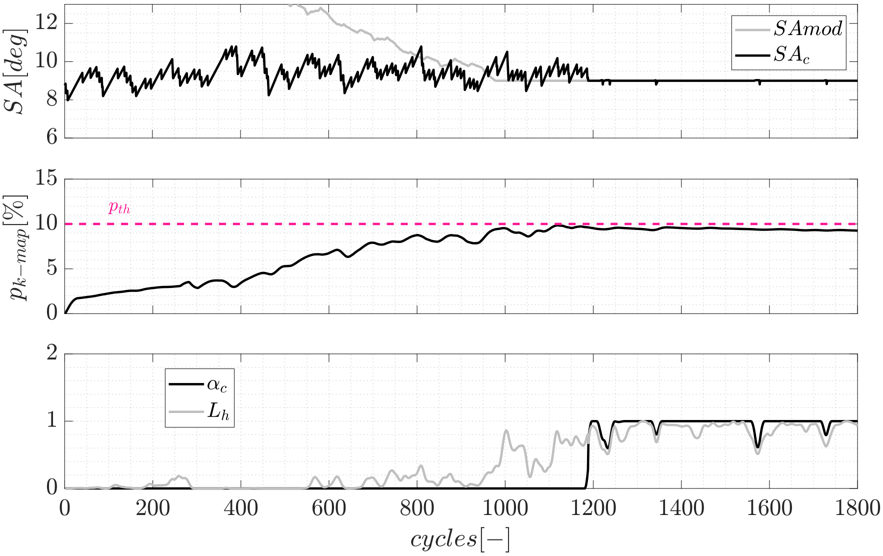

Figure 8.11: *Learning process results. Top plot: SA controller output. Middle plot: knock probability from model. Bottom plot: Likelihood ratio from long buffer and* α_c *value.*

As it can be seen in Figure 8.11, along the learning process the knock probability of the model reaches the threshold of the controller p_{th}, and once the model is updated, the likelihood ratio takes values near to 1, and the model is able to represent the actual knock probability. Hence, the control action of SA will be a combination between model and conventional knock control according to α_c value. The cycles required to fill the model are 1200 cycles with the engine running at 2000 rpm, what is translated into 80 seconds.

8.2.4.2 Steady state results

The performance of the fuzzy logic controller is validated in steady state condition and contrasted with a conventional knock control strategy. In Figure 8.13 the response of both controllers are shown in two operating conditions: $OP_A = 4$ (left) and $OP_A = 12$ (right). The controller gain K_{ret} was set at 0.5 CAD. Note that for $OP_A = 4$ case at cycle 140 the SA is delayed, this is a consequence of consecutive knocking cycles observed, what lead to α_c near zero.

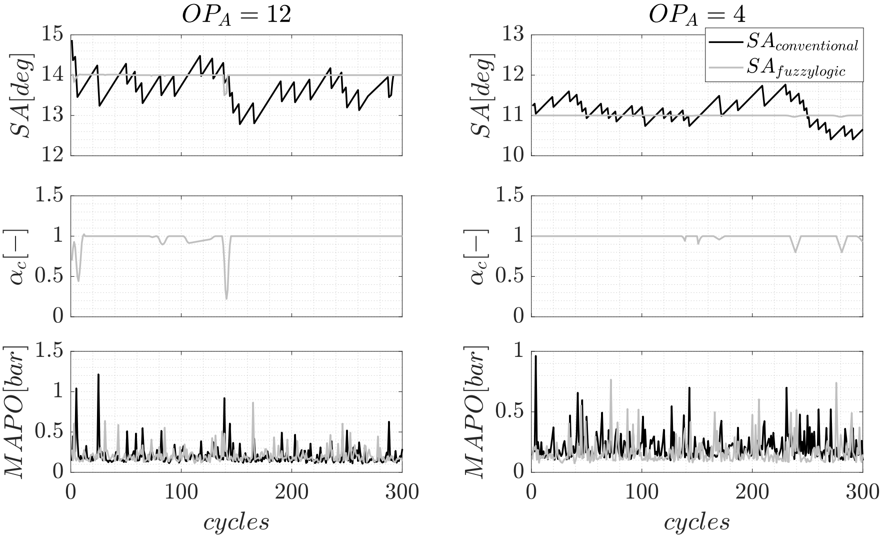

Figure 8.12: *Control performance at different load conditions. Left plot:* $OP_A = 12$ *. Right plot* $OP_A = 4$ *. Top plot: SA controller output. Middle plot* α_c *value. Bottom plot: MAPO.*

In Table 8.1 the mean and the variation of SA and IMEP, the maximum MAPO value, and the knock probability computed for a MAPO threshold of 0.4 bar with the conventional controller (p_{k-M}), and method 1 criteria presented in Chapter 7 combined with the Fuzzy Logic Controller (p_{k-I}) are shown. Comparing both, conventional knock controller and fuzzy logic at the same operating condition, similar mean SA value is found. Nevertheless, the variation of SA is considerably higher for conventional controller, which might lead to dangerous SA zones. The variation of SA is also reflected in IMEP standard deviation, which for $OP_A = 4$ case is three times higher.

Table 8.1: *Control performance at 2000 rpm and operating conditions.*

	Conventional		Fuzzy logic	
OP_A	12	4	12	4
$K_{ret}[deg]$	0.5	0.5	0.5	0.5
σ_{SA}	0.34	0.31	0.1	0.006
$\overline{SA}[deg]$	13.77	10.86	13.86	11.07
σ_{IMEP}	0.13	0.12	0.12	0.09
$\overline{IMEP}[bar]$	9.18	10.4	9.4	10.66
$M\hat{A}PO[bar]$	1.2	0.96	0.86	0.7
$p_{k-MAPO}[\%]$	3.98	2.72	1.99	1.7
$p_{k-M1}[\%]$	10.6	10.4	10.1	9.97

In order to evaluate the proposed controller under different operating conditions, a summary of six points is represented in Figure 8.13, where the thermal efficiency (left) and the maximum MAPO (right) are compared for both controllers. The conventional controller results are represented against fuzzy logic results. Knock probability was set at 10 % and the gain K_{ret} was set at 0.5 CAD, thermal efficiency was computed from in-cylinder pressure as:

$$\eta_{th} = \frac{\S p_{cyl}\, dV}{m_f q_{LHV}} \tag{8.11}$$

m_f is the fuel amount injected during one combustion cycle, q_{LHV} is the lower heating power of the fuel, which takes a value of 45 MJ/kg for gasoline, p_{cyl} is the in-cylinder pressure, dV is the rate of the volume change.

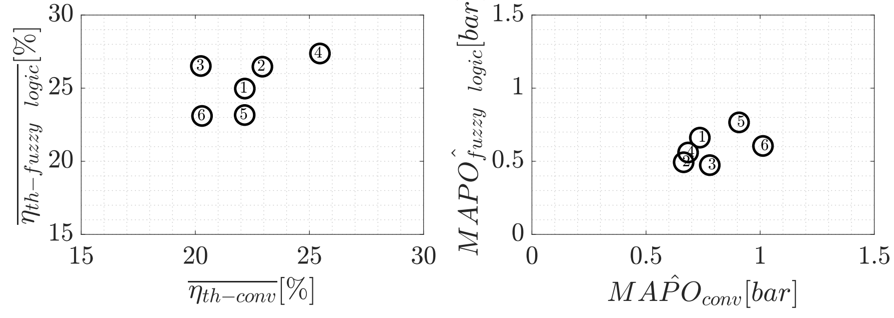

Figure 8.13: *SA comparison for six operating points at steady condition.*

A box and whiskers plot of the SA-BTDC corresponding to each steady point is represented in Figure 8.14. Where the letter C is used to represent results from conventional controller and FL results from fuzzy logic controller.

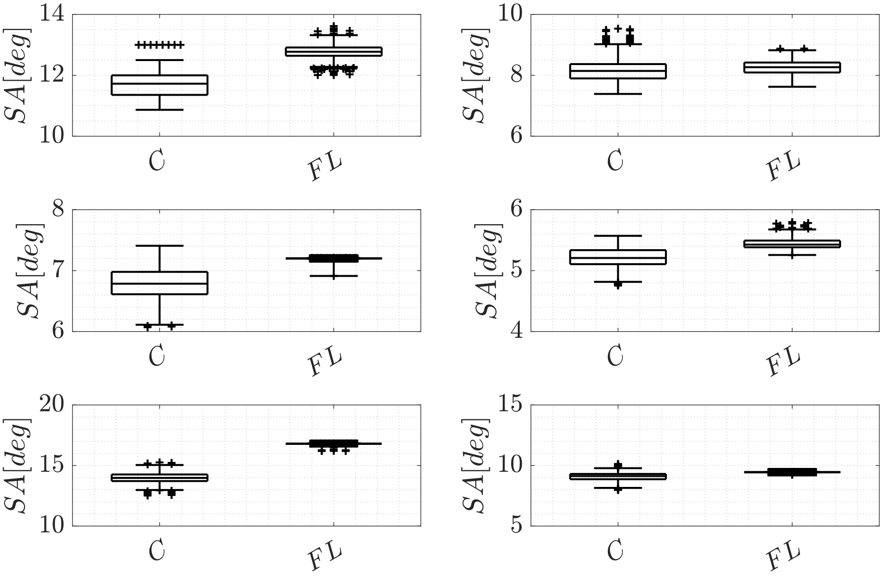

Figure 8.14: *MAPO comparison for six operating points at steady condition.*

Analyzing Figure 8.13, while comparing the same operating conditions, fuzzy logic controller exhibit an improvement in terms of η_{th} and safety (lower maximum MAPO). Results from Figure 8.14 show that the controller proposed achieved a higher SA average and significantly reduced the variability of the control for the six steady points.

8.2.4.3 Transient state results

Fuzzy logic controller is validated in transient conditions: transients tests $T6$ and $T7$. The knock probability of the controller was set at 10 %. In Figure 8.15 results from test $T7$ are shown. Analyzing Figure 8.15, during the first throttle step, around cycle 800, various cycles with MAPO over 1 bar are observed. This is because the conventional controller (only feedback control) is slower when delaying SA than fuzzy logic controller. During the second throttle step, around cycle 1200, the SA controlled by conventional strategy takes more time to reach an optimum value, which is translated in less performance during the transient.

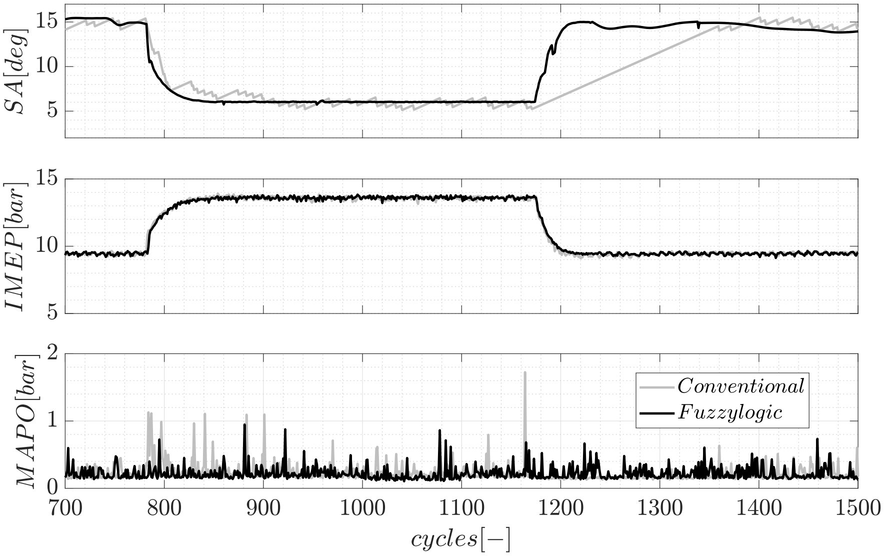

Figure 8.15: *Control performance of Test $T7$. Top plot: SA. Middle plot: IMEP. Bottom plot: MAPO*

The 100 size buffer knock probability during transient $T6$ is represented in Figure 8.16 for both controllers. As it can be seen, the observed probability for conventional controller case achieves a 6 % of knock probability (for MAPO criterion) during the load transient. Since the variability of the SA is higher for the conventional controller case, and the knock probability of 6 %, the controller output might lead to dangerous operating conditions.

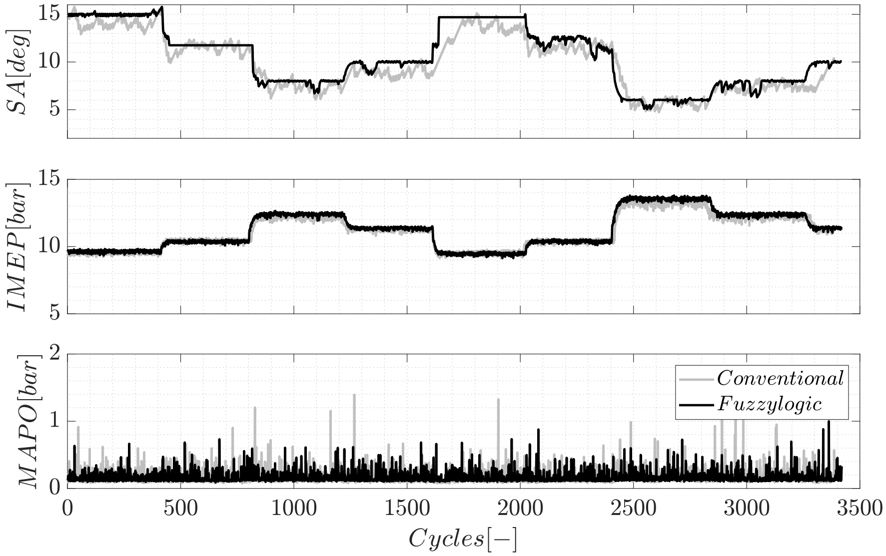

Figure 8.16: *Knock probability observed for conventional and fuzzy logic controllers during transient $T6$.*

In Table 8.2 results from transients $T6$ and $T7$ are summarized, where the mean value of SA and IMEP, the maximum MAPO, percentage of cycles with MAPO over 0.4 bar (p_{k-MAPO}), percentage of cycles computed as knock with method 1 (p_{k-M1}), and the thermal efficiency for both controllers is shown.

Table 8.2: *Control performance: Test T6 & T7.*

	Conventional		Fuzzy logic	
$Test$	T7	T6	T7	T6
$\overline{SA}$	10.6	9.9	10.95	10.53
$\overline{IMEP}[bar]$	10.8	11.1	11.18	11.4
$M\hat{A}PO[bar]$	1.72	1.4	0.86	0.9
$p_{k-MAPO}[\%]$	6	4	2.4	2
$p_{k-M1}[\%]$	17.8	15.6	10.3	10.2
$\eta_{th}[\%]$	24.22	24.97	25.17	25.33

Fuzzy logic controller is able to reach higher IMEP while MAPO maximum is lower than conventional control strategy. The improvement of the thermal efficiency was of 2 % for the proposed strategy for both, test $T6$ and $T7$.

8.3 Model based control for residual gas fraction with combustion optimization control.

Residual gas fraction and combustion phase are two important variables in SI engines since affect thermal efficiency, emissions and combustion stability. In-cylinder pressure sensors are the most extended signal used as feedback for closed loop SA and RGF control. However, pressure sensors are still affected by challenges such as durability and cost. This section presents a model-based RGF control with SA optimization: first the controller design is presented, where the application of the combustion model presented in Chapter 4 is explained. And then, experimental results in steady and transient conditions are shown.

8.3.1 Controller design

The controller proposed in this work is shown in Figure 8.17. Where, the combustion model presented in Chapter 4 is used to estimate the in-cylinder pressure each cycle k. Then, the in-cylinder pressure obtained from the combustion model is used for two purposes: first, to obtain the optimal SA for a given operation point (U_k), and a second one to estimate the RGF and predict the VVT of the exhaust required for a given set-point. The RGF set-point are arbitrary values in order to evaluate the performance of the controller.

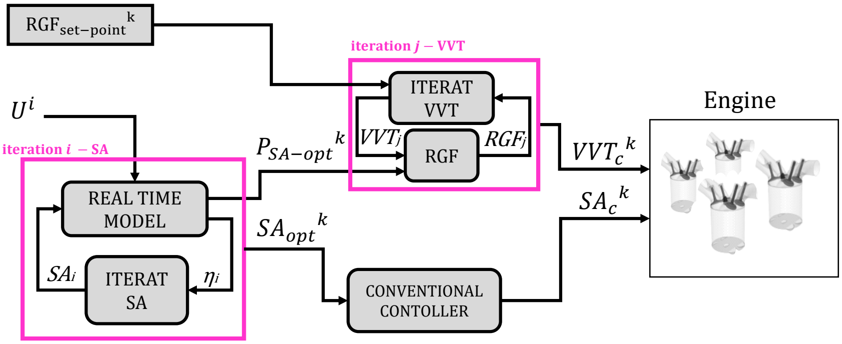

Figure 8.17: *Controller scheme proposed.*

In the iteration loop $i-SA$, the thermal efficiency (η_i) is estimated from the combustion model at different SA SA_i through Eq8.12. When the iteration loop reach the maximum efficiency stops, and the optimal value SA^{k}_{opt} is obtained. The iteration loop $j - VVT$, is used to estimate the VVT needed for a RGF set-point.

Then, a conventional knock controller is applied to delay SA if knock is recognized. Knock detection is performed by knock sensor signal, applying the recognition procedure introduced in Chapter 2.

8.3.1.1 Iterative algorithm

In this section, thee algorithms used for each iteration loop presented Figure 8.17 are introduced.

- *Iteration* $i - SA$: In order to find the maximum efficiency each cycle, each iteration i the thermal efficiency is computed as:

  $$\eta_i = \frac{\S p(SA_i)dV}{m_f q_{LHV}} \tag{8.12}$$

  Each iteration i, a value of SA is computed by an iterative fixed point algorithm, which is shown in Figure 8.18. The value SA_i is used as an input in the combustion model to evaluate η_i, when the maximum is reached the iteration loop stop, and the optimal value of SA is obtained.

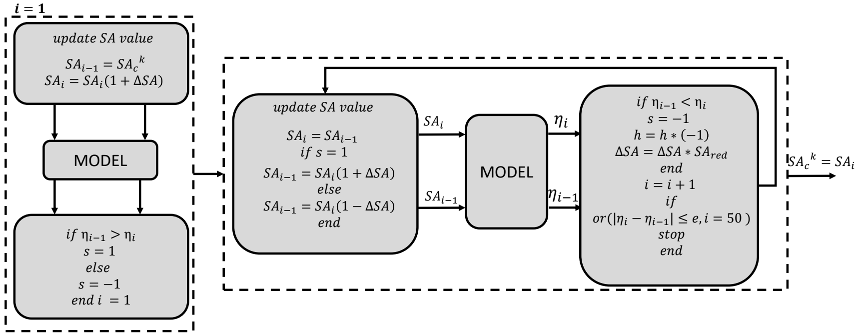

Figure 8.18: Iteration proposed for SA optimization.

- *Iteration* $j - VVT$: The method presented in [15] is used to estimate the RGF from the combustion model as following :

$$RGF_j = \left(\frac{P^k_{SA-opt}(EVC_j)}{P^k_{SA-opt}(EVO_j)} \right)^{\gamma} \frac{V(EVC_j)}{V(EVO_j)} \tag{8.13}$$

where $P^k_{SA-opt}(EVC_j)$ is the in-cylinder pressure from the model at the EVC position, $P^k_{SA-opt}(EVO_j)$ is the in-cylinder pressure from the model at the EVO position.

The VVT_j is computed by a bisection iterative algorithm as it is shown in Figure 8.19.

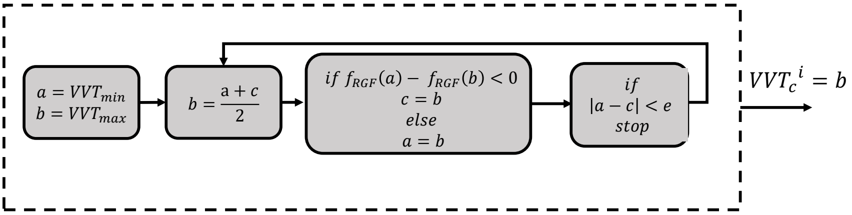

Figure 8.19: *Iteration proposed for RGF control.*

8.3.2 Experimental results

This section is divided in two parts: the first part, the optimal SA computed through the model is compared against the thermal efficiency during a SA sweep. The second part, the validation of the controller is shown in both, steady and transient conditions.

8.3.2.1 Optimization of SA obtained from the model

The optimal SA computed from the iteration i loop is compared against the efficiency obtained at different SA sweeps for three different engine speeds in Figure 8.20.

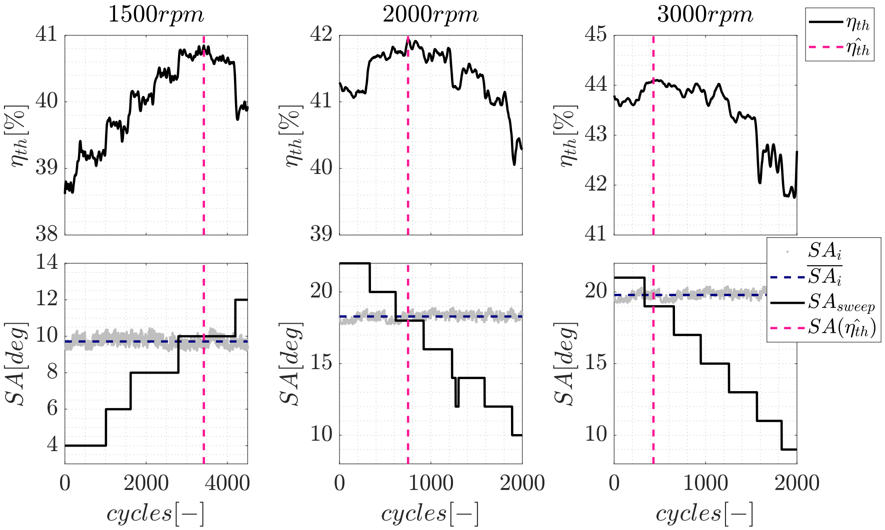

Figure 8.20: *Spark advance sweeps: Thermal efficiency at three engine speeds compared with the model optimal value.*

As it can be seen in Figure 8.20, the optimal SA obtained by the iteration loop proposed is correlated with the experimental value for maximum combustion efficiency.

8.3.2.2 Controller validation

The controller was validated during steady and transient conditions. In Figure 8.21 a steady test at operating point $OP_A = 2$ is shown, where the RGF target is arbitrary changed during the test to check the performance of the controller.

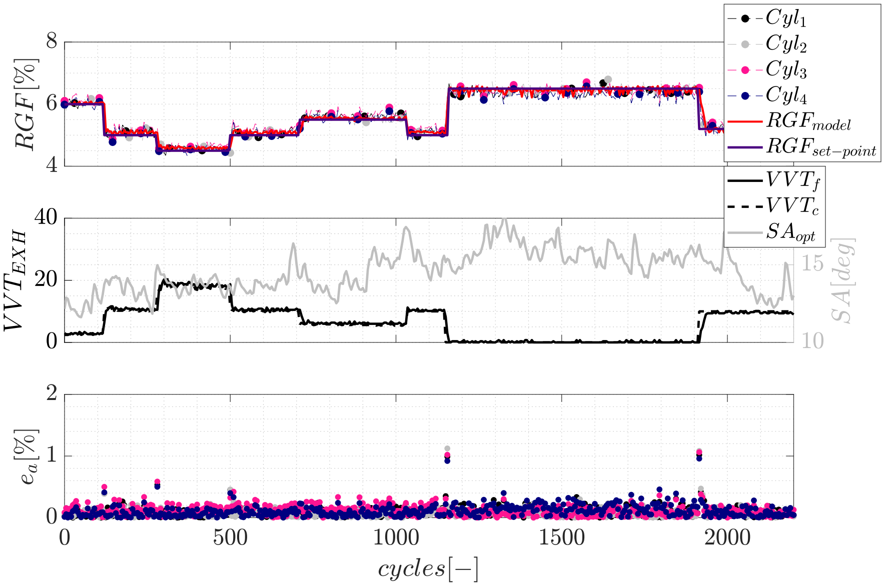

Figure 8.21: *Steady test validation (operating condition $OP_A = 2$). Top plot: RGF evolution. Middle plot: VVT and SA controller output. Bottom plot: Absolute error between $RGFset-point$ and $RGF_{measured}$*

Analyzing Figure 8.21, note that the maximum absolute error (1 % of RGF) is reached during VVT changes, nevertheless in steady conditions the absolute error is maintained below 0.5 %. Also must be noticed that the SA controller output is the one obtained from the model, since no knocking conditions are reached.

The proposed controller was also validated in transients conditions (tests: $T5$ and $T10$), results are shown in Figure 8.22. During this tests the RGF target was maintained at 5 % by controlling the VVT and optimizing the SA. The top plots shows the RGF computed through each in-cylinder pressure sensor, the RGF target is highlighted in red line, the bottom plots shows the controller outputs, i.e VVT and SA commands.

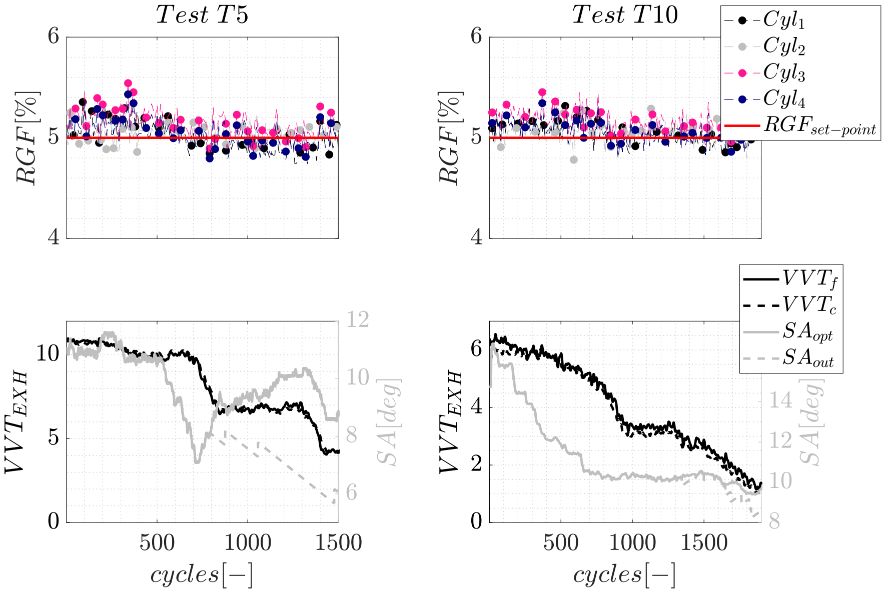

Figure 8.22: *Transient test validation. Left plot: Test $T5$ (load transient). Right plot: test $T10$ (speed transient).*

As it can be seen in Figure 8.22, in $T5$ case, the SA controller out put corresponds to the optimal value until medium load its reached ($p_{int} = 0.9$ bar). After this points, knocking conditions are reached, and the SA is delayed by the conventional knock controller. In Figure 8.23, the mean RGF and the standard deviation during the transient tests is represented.

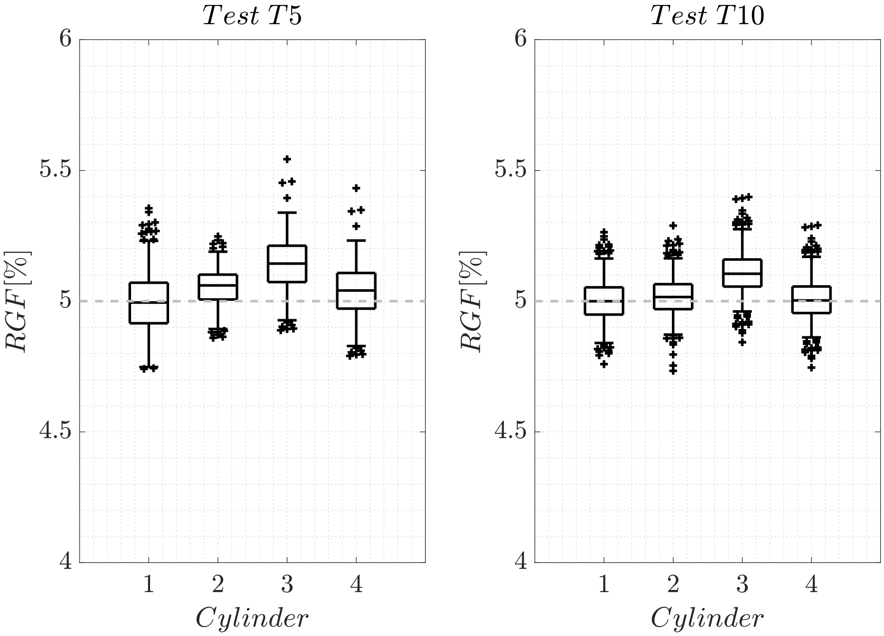

Figure 8.23: *Mean RGF and standard deviation for tests $T5$ and Test $T10$.*

As it can be seen in Figure 8.23, during both tests the controller is able to keep the mean value of the RGF for all the cylinders close to the target value of 5 %.

In Figure 8.24 the transient corresponding to test $T8$ is shown. In this test the RGF target value was changed. On the top plot the RGF evolution is represented, and on the bottom plot the controller out puts.

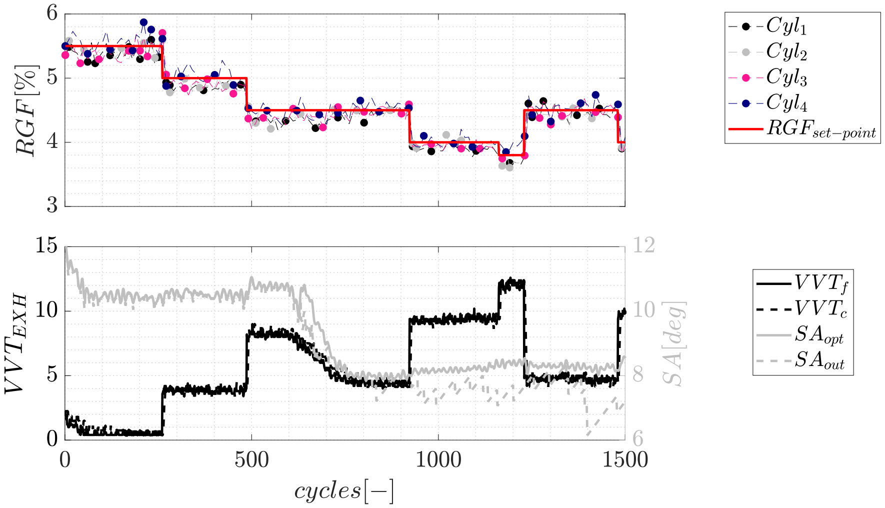

Figure 8.24: *Transient test validation (test T8). Top plot: RGF value from in-cylinder pressure signals and model. Bottom: VVT and SA commands.*

It must be noticed that even if the operating conditions change, all the cylinders follows the RGF set point. The error during the transient test $T8$ is evaluated in Figure 8.25 for all cylinders.

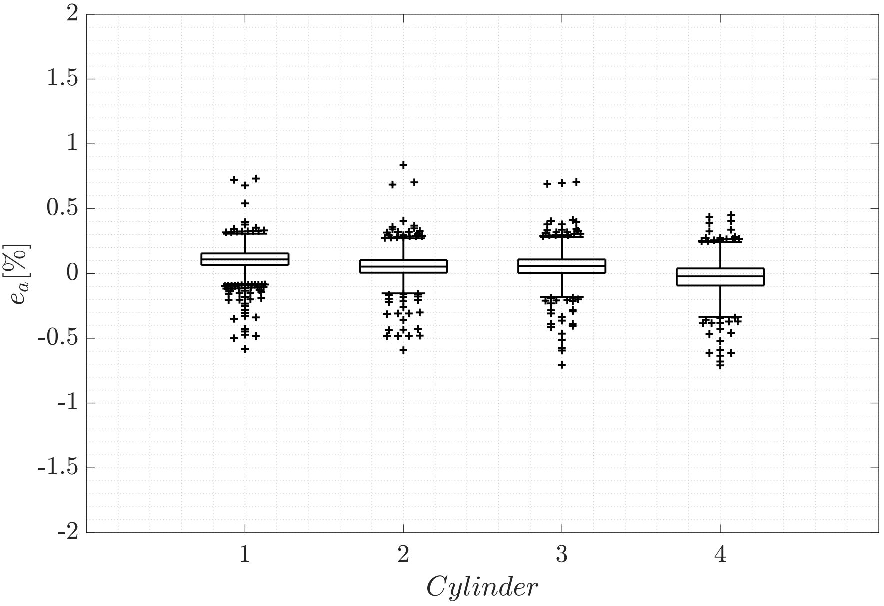

Figure 8.25: *Error between RGF target and RGF from each cylinder: Test T8.*

As it can be seen in Figure 8.25, the mean absolute error of cylinders 1, 2, and 3 is near zero, while cylinder 4 shows a slight deviation.

8.4 Conclusions

This chapter presents two combustion control applications of the combustion diagnosis and model developed in previous Chapters. First, method 1 knocking recognition criteria is used to update a knock probability model to control the SA. And then, an application for the combustion model presented in Chapter 4 is developed, where the RGF is controlled by the command of the VVT while the SA is optimized at the optimal value.

From this study, the following conclusions can be point out:

- Fuzzy logic knock controller: With this control strategy an improvement of the thermal efficiency between 1%– 6.2% in steady conditions was achieved, while MAPO value was maintained at safe levels. One of the advantages of this method is no need of initial calibration. Under transient conditions, the controller was able to achieve a faster response than conventional controller, and presented less SA variability which leads to a more stable operation.

- RGF model based-controller: The controller was able to estimate the optimal combustion phasing while controlling the RGF with a maximum absolute error of 1 %. During this work the potential to replace in-cylinder pressure sensors by a combustion model was shown.

References

[1] Gao Jinwu, Zhang Yahui, Zhang Jiangyan and Shen Tielong. “Adaptive Internal Model Based Control of the RGF Using Online Map Learning and Statistical Feedback Law”. *IEEE/ASME Transactions on Mechatronics*, Vol. 25 n^o 2, pp. 1117–1128, 2019. (cited in pp. 10 and 186)

[2] Sen Asok K, Zheng Jianjun and Huang Zuohua. “Dynamics of cycle-to-cycle variations in a natural gas direct-injection spark-ignition engine”. *Applied Energy*, Vol. 88 n^o 7, pp. 2324–2334, 2011. (cited in p. 186)

[3] Heywood John B. *Internal combustion engine fundamentals*. McGraw-Hill Education, 2018. (cited in pp. 19, 26, 64, 66, 90, and 186)

[4] Wang Yuanfeng. “A Novel Two-Zone Thermodynamic Model for Spark-Ignition Engines Based on an Idealized Thermodynamic Process”. *Energies*, Vol. 13 n^o 15, pp. 3801, 2020. (cited in p. 186)

[5] Jones James C Peyton, Muske Kenneth R, Frey Jesse and Scholl David. “A stochastic knock control algorithm”. Technical report, SAE Technical Paper, 2009. (cited in p. 186)

[6] Jones James C Peyton and Frey Jesse. “Threshold optimization and performance evaluation of a classical knock controller”. *SAE International Journal of Engines*, Vol. 8 n^o 3, pp. 1021–1028, 2015. (cited in p. 186)

[7] Frey Jesse, Jones James C Peyton and Shayestehmanesh Saeed. “Stochastic simulation of a cumsum knock controller”. *IFAC-PapersOnLine*, Vol. 49 n^o 11, pp. 210–216, 2016. (cited in p. 188)

[8] Zhang Yahui, Shen Xun, Wu Yuhu and Shen Tielong. “On-board knock probability map learning–based spark advance control for combustion engines”. *International Journal of Engine Research*, Vol. 20 n^o 10, pp. 1073–1088, 2019. (cited in pp. 10, 34, 188, and 190)

[9] Neal Radford M. *Bayesian learning for neural networks*, volume 118. Springer Science & Business Media, 2012. (cited in p. 188)

[10] Guardiola Carlos, Pla B, Blanco-Rodriguez David and Eriksson Lars. “A computationally efficient Kalman filter based estimator for updating look-up tables applied to NOx estimation in diesel engines”. *Control Engineering Practice*, Vol. 21 n^o 11, pp. 1455–1468, 2013. (cited in p. 189)

[11] Gao Jinwu, Zhang Yahui and Shen Tielong. “An on-board calibration scheme for map-based combustion phase control of spark-ignition engines”. *IEEE/ASME Transactions on Mechatronics*, Vol. 22 n^o 4, pp. 1485–1496, 2017. (cited in p. 189)

[12] Cavina Nicolo, Brusa Alessandro, Rojo Nahuel and Corti Enrico. “Statistical Analysis of Knock Intensity Probability Distribution and Development of 0-D Predictive Knock Model for a SI TC Engine”. Technical report, SAE Technical Paper, 2018. (cited in p. 190)

[13] Jones James C Peyton, Spelina Jill M and Frey Jesse. “Likelihood-based control of engine knock”. *IEEE Transactions on Control Systems Technology*, Vol. 21 n^o 6, pp. 2169–2180, 2013. (cited in p. 191)

[14] Spelina Jill M, Peyton Jones James C and Frey Jesse. “Stochastic simulation and analysis of a classical knock controller”. *International Journal of Engine Research*, Vol. 16 n^o 3, pp. 461–473, 2015. (cited in p. 191)

[15] Yun HJ and Mirsky William. “Schlieren-streak measurements of instantaneous exhaust gas velocities from a spark-ignition engine”. *SAE transactions*, pp. 3143–3158, 1974. (cited in p. 205)

PART

V

Conclusions and future work

Chapter

9

Conclusions and future work

Contents

9.1 Main contributions

This work presented a set of combustion diagnosis indicators oriented to combustion control. For that purpose, different topics have been covered along this dissertation:

- A control oriented combustion model for SI combustion able to predict the average and expected combustion variability was developed. The combustion model provides a continuous estimation of combustion parameters such as: CAx, IMEP, RGF, with no need from information currently available in the Engine Control Unit and without dependence of in-cylinder pressure measurement. The model estimation was improved with an observer of the knock sensor signal and an EKF.

- Resonance was analyzed and modeled for three different combustion types: SI, TJI and RCCI. Two models of the amplitude of resonance evolution where presented. The first model was calibrated for SI and TJI combustion by assuming a constant attenuation during a cycles, where two cases were analyzed: normal and knocking combustion. The second model aims to reproduce the attenuation over a cycle, this model can be used to improve algorithms that makes use of resonance, such as trapped mass estimation.
- An application of the first resonance model was developed by using the model to recognize knocking cycles for SI and TJI combustion. The model is able to distinguish between normal combustion, even when normal combustion heavily excites resonance.
- A low-knocking cycle recognition method was developed by using a crank angle dependent threshold. This model was validated in SI combustion, demonstrating the improvement in control applications.
- Two control applications of the combustion indicators were presented. First, one of the previously developed methods for knock recognition based on in-cylinder pressure signal was used to update a map-based model. Secondly, an application of the combustion model for SA optimization and RGF control has been developed. Both control applications have shown to improve the performance of conventional controllers in the tested cases.

Following, an overview of these points and the main conclusions are presented.

9.1.1 Combustion modeling

The combustion process was modeled by a two zone model. The inputs of the model are available signals in commercials ECU. The average combustion model is composed of three OL tables, two variables for HRR calculation and one to characterize the combustion model, as a function of the engine speed and the intake pressure. And the variability model propagates two probability distributions over two variables of the combustion model, i.e the laminar flame speed and turbulent intensity.

Both, average and variability combustion models, were validated over the training and the validation data sets in engine A. The complete model can be used off-line to simulate the real combustion and to implement control strategies with no need to carry out experimental tests, or implemented in real time to estimate combustion parameters and use it for control feedback information.

An observer was designed, allowing a better estimation of the mean combustion parameters under transient conditions. The observer corrects the laminar flame speed by the use of the knock sensor signal, and uses this estimation, and information from the combustion model, to improve the in-cylinder pressure estimation. When comparing the combustion model and the observer, with the later an improvement of the relative error over a 10 % was achieved over the estimated CAx, IMEP and RGF, and their values can be adapted to the different cylinders. Despite the improvements of the estimations, one of the disadvantages of the model with observer is the need of a knock sensor signal with a fast acquisition.

In addition, the variability model was able to predict the cycle-to-cycle variation with an error bellow a 20 % after the CA5, before CA5 the error found over transient and steady points was higher to the assumption of the start of combustion at the spark advance.

9.1.2 In-cylinder resonance characterization

The resonance indicator I_r proposed in [1], was used to described the resonance evolution in the combustion chamber in three different combustion modes: SI, TJI and RCCI.

Taking as starting point the expression of the amplitude resonance evolution found in [2], two resonance models have been developed.

Model of amplitude evolution: This model was developed by assuming a constant attenuation of the resonance amplitude for a given cycle. The resonance amplitude was modeled for two cases: normal and abnormal combustion. For normal combustion, the resonance excitation source has been assumed from the HRR. For knocking combustion, the resonance source has been modeled to be released in a small step. Results shows that, independently of the combustion type, the model is able to reproduce the resonance amplitude evolution with an error bellow 10 %. This model was used in a later chapter to develop a knock recognition method.

Model of attenuation evolution: An additional model was developed in order to predict the attenuation over a cycle. The model was calibrated in engines B and C, and validated in all, engines A, B and C. Results shows that the attenuation of the resonance excitation is independently of the source of the combustion, i.e depends on thermodynamic properties and the dimension of the combustion chamber. In larger engines, the resonance is damped slower. An application of the model for trapped mass estimation was performed over engine C, where the model is used to estimate the best window location for the calculation of the trapped mass from resonance method.

9.1.3 Knock recognition methods

Three knock recognition methods, two based on in-cylinder pressure and one on knock sensor signal, were developed in this work.

Knock recognition based on in-cylinder pressure sensors: Two methods were developed in this work: the first method was based on a threshold as a function of the mass fraction burned, the second method was based on a resonance model which is able to predict the resonance amplitude evolution under normal and abnormal combustion. For engine A case, both methods were able to recognized low-knocking cycles under SI combustion. And for engine B case, the methods were able to recognized knock in TJI combustion, where normal combustion heavily excites resonance. Both models were online validated in engines A, where an improvement in terms on efficiency, safety and cycle-to-cycle variability was achieved. With low-knocking cycles recognition the controller can be set at a higher knock probability, being able to obtain lower SA variability, i.e lower IMEP variation, and avoiding high knock probability areas. Because both methods depend on parameters obtained from the in-cylinder pressure sensor and how combustion evolves, they are applicable to different fuels.

Knock recognition based on vibration signal: A knock recognition method that combines the combustion model and the knock sensor signal was developed. The method was validated in engine A over different operating conditions and SA settings, where the knock probability obtained was comparable to a MAPO threshold of 0.4 bar. The main advantage of this method is does not rely on in-cylinder pressure sensors, as is based on a model and knock sensor signal.

9.1.4 Combustion control applications

Part of the work presented along this dissertation was used to develop combustion control applications.

Model based knock controller: One of the low-knocking cycles recognition method based on in-cylinder pressure was used to update a map-based knock probability model. The model was used to obtain the optimal SA setting, and a conventional knock controller was employ in case the probability of the model does not agree with the real one measured through a FIFO buffer. The controller was validated in engine A, and compared with a full conventional knock controller. An improvement in terms of efficiency and variability was achieved, i.e the model-based control maintain an optimal SA level without performing delays of SA in necessary. During transient conditions, the proposed controller was able to maintain the MAPO values under safety values.

Model based RGF control and combustion optimization: The combustion model developed in this work was used to obtain cycle-by-cycle the optimal SA and the VVT position for a given RGF set-point. A conventional knock controller was used in case knock was detected through the vibration measurement. Results show that the RGF was controlled in all four cylinders under steady and transient operation, with an absolute error bellow 2 % during transient and bellow 1 % at steady state.

9.2 Future work

As it was demonstrated, the aim of this work is to present algorithms which can be embedded in on-board ECUs.

Improvement of the combustion model: With the measurement of the instantaneous engine speed, is possible to obtain more information from the combustion process. With this information, more complex observers can be developed in order to improve the combustion estimation.

Model based RGF control: This controller can be implemented in order to control the RGF to control emissions, as well as control knock probability, since knock is not only affected by the SA, but also by the VVT timming.

Test cell implementation: The attenuation model developed can be implemented in real time to improve the estimation of the trapped mass from the in-cylinder resonance method. This estimation can be implemented in close-loop control strategies of EGR, RGF, etc. Besides, the knock recognition methods based on in-cylinder pressure are reliable techniques to implement in real time on a test bench. Moreover, both knock recognition methods have been implemented in real time in the prototyping system of engine A introduced in Chapter 3.

On-board implementation of knock recognition methods: The implementation of low-knocking cycles recognition methods in commercial ECUs has to face two points: first the in-cylinder pressure acquisition above 15 kHz in order to capture resonance excitation, and second the computational cost of method 2 may overcome the ECU capabilities. This last point must be studied to determine the viability of such implementation. For the method based on vibration measurement, the only point to face is the signal acquisition: also a frequency above 15kHz is required to analyzed resonance from the knock sensor signal.

Virtual engine: By combining the combustion and the variability model, with air path models, and knock model, is possible to model the complete engine operation, and use it for testing during the early development of control algorithms.

Close loop control: Some of the systems in the engine ECUs are controlled by open-loop or adaptive tables, such as VVT or SA. In order to improve this adaptation, the combustion model can be implemented for those control strategies in production engines. Actually, the knock sensor signal is used to retard the calibrated optimal value of SA, one possibility is the application of the knock sensor based knock recognition method to control the SA with a conventional knock controller.

References

[1] Broatch A., Guardiola C., Pla B. and Bares P. “A direct transform for determining the trapped mass on an internal combustion engine based on the in-cylinder pressure

resonance phenomenon". *Mechanical Systems and Signal Processing*, Vol. 62, pp. 480–489, 2015. (cited in pp. 120 and 217)

[2] Munjal ML. "Advances in the acoustics of flow ducts and mufflers". *Sadhana*, Vol. 15 n^o 2, pp. 57, 1990. (cited in pp. 117 and 217)

References

Alphabetic Index of Authors

streak measurements of instantaneous exhaust gas velocities from a spark-ignition engine Schlieren. (cited in p. 4)

streak measurements of instantaneous exhaust gas velocities from a spark-ignition engine Schlieren. (cited in p. 5)

A Aziz A Rashid, Firmansyah Firmansyah and Raja Shahzad Raja Shahzad. "Combustion analysis of a CNG direct injection spark ignition engine". *International Journal of Automotive and Mechanical Engineering (IJAME)*, Vol. 2, pp. 157–170, 2010. (cited in p. 9)

Agency International Energy. "Global Energy Review: CO2 Emissions in 2020". https://www.iea.org/. Accessed: 2021-03-12. (cited in pp. 5 and 6)

Akimoto Kenji, Komatsu Hirotaka and Kurauchi Atsushi. "Development of pattern recognition knock detection system using short-time Fourier transform". *IFAC Proceedings Volumes*, Vol. 46 n^o 21, pp. 366–371, 2013. (cited in p. 32)

Armas Octavio, Ballesteros Rosario and Cardenas María Dolores. "Thermodynamic diagnosis of diesel and biodiesel combustion processes during load-increase transient sequences". *Applied energy*, Vol. 97, pp. 558–568, 2012. (cited in p. 7)

Armas Octavio, Yehliu Kuen and Boehman André L. "Effect of alternative fuels on exhaust emissions during diesel engine operation with matched combustion phasing". *Fuel*, Vol. 89 n^o 2, pp. 438–456, 2010. (cited in p. 7)

Arnone L, Manelli S, Chiatti G and Chiavola O. "In-cylinder pressure analysis through accelerometer signal processing for diesel engine combustion optimization". Technical report, SAE Technical Paper, 2009. (cited in p. 28)

Association European Automobile Manufacturers. "Fuel types of new cars 2019-2020". https://www.acea.be/. Accessed: 2021-03-17. (cited in pp. 7 and 8)

Attard William P, Blaxill Hugh, Anderson Eric K and Litke Paul. "Knock limit extension with a gasoline fueled pre-chamber jet igniter in a modern vehicle powertrain". *SAE International Journal of Engines*, Vol. 5 n^o 3, pp. 1201–1215, 2012. (cited in pp. 32 and 114)

Bares Pau, Selmanaj Donald, Guardiola Carlos and Onder Christopher. "Knock probability estimation through an in-cylinder temperature model with exogenous noise". *Mechanical Systems and Signal Processing*, Vol. 98, pp. 756–769, 2018. (cited in p. 97)

Bares Pau, Selmanaj DONALD, Guardiola Carlos and Onder Christopher. "A new knock event definition for knock detection and control optimization". *Applied Thermal Engineering*, Vol. 131, pp. 80–88, 2018. (cited in pp. 31, 33, 148, and 153)

Bares Moreno Pau. *In-cylinder pressure resonance analysis for trapped mass estimation in automotive engines.* PhD Thesis, Universitat Politècnica de València, 2017. (cited in pp. 19, 115, and 122)

Ben Livier, Raud-Ducros Nathalie, Truquet Remy and Charnay Georges. "Influence of air/fuel ratio on cyclic variation and exhaust emission in natural gas SI engine". Technical report, SAE Technical Paper, 1999. (cited in p. 86)

Benajes J, Novella R, Gomez-Soriano J, Martinez-Hernandiz PJ, Libert C and Dabiri M. "Evaluation of the passive pre-chamber ignition concept for future high compression ratio turbocharged spark-ignition engines". *Applied Energy*, Vol. 248, pp. 576–588, 2019. (cited in pp. 8 and 30)

Bi Fengrong, Li Xin, Liu Chunchao, Tian Congfeng, Ma Teng and Yang Xiao. "Knock detection based on the optimized variational mode decomposition". *Measurement*, Vol. 140, pp. 1–13, 2019. (cited in p. 30)

Bi Fengrong, Ma Teng and Wang Xu. "Development of a novel knock characteristic detection method for gasoline engines based on wavelet-denoising and EMD decomposition". *Mechanical Systems and Signal Processing*, Vol. 117, pp. 517–536, 2019. (cited in p. 30)

Blizard Norman C and Keck James C. "Experimental and theoretical investigation of turbulent burning model for internal combustion engines". *SAE Transactions*, pp. 846–864, 1974. (cited in p. 62)

Broatch A., Guardiola C., Pla B. and Bares P. "A direct transform for determining the trapped mass on an internal combustion engine based on the in-cylinder pressure resonance phenomenon". *Mechanical Systems and Signal Processing*, Vol. 62, pp. 480–489, 2015. (cited in pp. 120 and 217)

Broatch Alberto, Guardiola Carlos, Pla Benjamín and Bares Pau. "A direct transform for determining the trapped mass on an internal combustion engine based on the in-cylinder pressure resonance phenomenon". *Mechanical Systems and Signal Processing*, Vol. 62, pp. 480–489, 2015. (cited in p. 179)

Brunt M. F. J. and Emtage A. L. "Evaluation of burn rate routines and analysis errors". *SAE Technical Papers*, 1997. (cited in p. 25)

Businaro Andrea, Cavina Nicolò, Corti Enrico, Mancini Giorgio, Moro Davide, Ponti Fabrizio and Ravaglioli Vittorio. "Accelerometer Based Methodology for Combustion Parameters Estimation". *Energy Procedia*, Vol. 81, pp. 950–959, 2015. (cited in pp. 28, 29, and 71)

Butts Kenneth Roy and Jaikamal Vivek. “Model-based verification and validation of electronic engine controls”. Technical report, SAE Technical Paper, 2012. (cited in p. 10)

Caton Jerald A. “The thermodynamics of internal combustion engines: examples of insights”. *Inventions*, Vol. 3 n^o 2, pp. 33, 2018. (cited in p. 19)

Cavina Nicolo, Brusa Alessandro, Rojo Nahuel and Corti Enrico. “Statistical Analysis of Knock Intensity Probability Distribution and Development of 0-D Predictive Knock Model for a SI TC Engine”. Technical report, SAE Technical Paper, 2018. (cited in p. 190)

Ceviz MA and Kaymaz I. “Temperature and air–fuel ratio dependent specific heat ratio functions for lean burned and unburned mixture”. *Energy Conversion and Management*, Vol. 46 n^o 15-16, pp. 2387–2404, 2005. (cited in p. 22)

Chao Yuedong, Lu Haifeng, Dong Guangyu, Deng Jun and Li Liguang. “Abnormal Combustion Diagnosis and Combustion Period Based Phase Estimation with a Modified Form Tandem Ion Current Detection System on SI Gasoline Engines”. *Energy Procedia*, Vol. 158, pp. 2098–2105, 2019. (cited in p. 32)

Chiatti Giancarlo, Chiavola Ornella, Recco Erasmo, Magno Agnese, Mancaruso Ezio and Vaglieco Bianca M. “Accelerometer measurement for MFB evaluation in multi-cylinder diesel engine”. *Energy*, Vol. 133, pp. 843–850, 2017. (cited in p. 29)

Chiavola Ornella, Chiatti Giancarlo, Arnone Luigi and Manelli Stefano. “Combustion characterization in diesel engine via block vibration analysis”. Technical report, SAE Technical Paper, 2010. (cited in p. 28)

Chiavola Ornella, Chiatti Giancarlo and Recco Erasmo. “Accelerometer measurements to optimize the injection strategy”. Technical report, SAE Technical Paper, 2012. (cited in p. 28)

Cohen Leon. *Time-frequency analysis*, volume 778. Prentice Hall PTR Englewood Cliffs, NJ, 1995. (cited in p. 119)

comission European. “2030 Climate target plan”. https://ec.europa.eu/info. Accessed: 2021-03-16. (cited in p. 5)

Corti Enrico and Forte Claudio. “A statistical approach to spark advance mapping”. *Journal of Engineering for Gas Turbines and Power*, Vol. 132 n^o 8, 2010. (cited in p. 34)

Corti Enrico, Forte Claudio, Mancini Giorgio and Moro Davide. “Automatic combustion phase calibration with extremum seeking approach”. *Journal of Engineering for Gas Turbines and Power*, Vol. 136 n^o 9, pp. 091402, 2014. (cited in pp. 33 and 46)

Costa Rodrigo C and Sodré José R. “Compression ratio effects on an ethanol/gasoline fuelled engine performance”. *Applied Thermal Engineering*, Vol. 31 n^o 2-3, pp. 278–283, 2011. (cited in p. 9)

Del Re Luigi, Allgöwer Frank, Glielmo Luigi, Guardiola Carlos and Kolmanovsky Ilya. *Automotive model predictive control: models, methods and applications*, volume 402. Springer, 2010. (cited in p. 10)

Demirbas Ayhan. "Fuel properties of hydrogen, liquefied petroleum gas (LPG), and compressed natural gas (CNG) for transportation". *Energy Sources*, Vol. 24 n^o 7, pp. 601–610, 2002. (cited in p. 9)

Desantes Jose Maria, Novella Ricardo, De La Morena Joaquin and others. "Achieving ultra-lean combustion using a pre-chamber spark ignition system in a rapid compression-expansion machine". Technical report, SAE Technical Paper, 2019. (cited in p. 30)

Draper Charles Stark. "The physical effects of detonation in a closed cylindrical chamber". 1935. (cited in pp. 50 and 115)

Dues Steven M, Adams Joseph M and Shinkle George A. "Combustion knock sensing: Sensor selection and application issues". *SAE transactions*, pp. 1192–1202, 1990. (cited in p. 32)

Earth Berkeley. "Global Temperature Report for 2020". http://berkeleyearth.org/global-temperature-report-for-2020/. Accessed: 2021-03-12. (cited in p. 5)

Egnell R. "Combustion diagnostics by means of multizone heat release analysis and NO calculation". *SAE Technical Papers*, 1998. (cited in p. 23)

Eguchi Makoto, Fukuda Naoki, Ohmori Hiromitsu, Takahashi Motoki, Yamasaki Yudai and Kaneko Shigehiko. "Diesel Engine Combustion Control with Onboard Calibration by Using Feedback Error Learning". Technical report, SAE Technical Paper, 2019. (cited in p. 10)

Finesso Roberto, Hardy Gilles, Mancarella Alessandro, Marello Omar, Mittica Antonio and Spessa Ezio. "Real-time simulation of torque and nitrogen oxide emissions in an 11.0 L heavy-duty diesel engine for model-based combustion control". *Energies*, Vol. 12 n^o 3, pp. 460, 2019. (cited in p. 18)

Frey Jesse, Jones James C Peyton and Shayestehmanesh Saeed. "Stochastic simulation of a cumsum knock controller". *IFAC-PapersOnLine*, Vol. 49 n^o 11, pp. 210–216, 2016. (cited in p. 188)

Galloni E, Fontana G and Palmaccio R. "Effects of exhaust gas recycle in a downsized gasoline engine". *Applied Energy*, Vol. 105, pp. 99–107, 2013. (cited in p. 8)

Galloni Enzo. "Analyses about parameters that affect cyclic variation in a spark ignition engine". *Applied Thermal Engineering*, Vol. 29 n^o 5-6, pp. 1131–1137, 2009. (cited in pp. 90 and 94)

Galloni Enzo. "Dynamic knock detection and quantification in a spark ignition engine by means of a pressure based method". *Energy conversion and management*, Vol. 64, pp. 256–262, 2012. (cited in p. 31)

Gao Jinwu, Zhang Yahui and Shen Tielong. “An on-board calibration scheme for map-based combustion phase control of spark-ignition engines”. *IEEE/ASME Transactions on Mechatronics*, Vol. 22 n^o 4, pp. 1485–1496, 2017. (cited in p. 189)

Gao Jinwu, Zhang Yahui, Zhang Jiangyan and Shen Tielong. “Adaptive Internal Model Based Control of the RGF Using Online Map Learning and Statistical Feedback Law”. *IEEE/ASME Transactions on Mechatronics*, Vol. 25 n^o 2, pp. 1117–1128, 2019. (cited in pp. 10 and 186)

Gatowski JA, Balles En N, Chun Kwang Min, Nelson FE, Ekchian JA and Heywood John B. “Heat release analysis of engine pressure data”. *SAE Transactions*, pp. 961–977, 1984. (cited in p. 22)

Gerardin Rodrigo Ceccatto, Alves Marco Aurélio Faleiros, de França Arruda Jose Roberto and others. “Analysis of Spark Ignition Engine Knock Signals using Fourier and Discrete Wavelet Transform”. Technical report, SAE Technical Paper, 2009. (cited in p. 31)

Giglio V., Iorio B., Police G. and Rispoli N. “In-cylinder Pressure Measurement for Control and Diagnostics in Spark Ignition Engines”. *SAE Technical Papers*, 2005. (cited in p. 25)

Göktaş Meltem, Balki Mustafa Kemal, Sayin Cenk and Canakci Mustafa. “An evaluation of the use of alcohol fuels in SI engines in terms of performance, emission and combustion characteristics: A review”. *Fuel*, Vol. 286, pp. 119425, 2021. (cited in p. 9)

Gómez Arántzazu, Fernández-Yáñez Pablo, Soriano José A, Sánchez-Rodríguez Luis, Mata Carmen, García-Contreras Reyes, Armas Octavio and Cárdenas M Dolores. “Comparison of real driving emissions from Euro VI buses with diesel and compressed natural gas fuels”. *Fuel*, Vol. 289, pp. 119836, 2021. (cited in p. 9)

Gu Fengshou, Li W, Ball AD and Leung AYT. “The condition monitoring of diesel engines using acoustic measurements part 1: acoustic characteristics of the engine and representation of the acoustic signals”. Technical report, SAE Technical Paper, 2000. (cited in p. 27)

Guardiola Carlos, Olmeda P, Pla B and Bares P. “In-cylinder pressure based model for exhaust temperature estimation in internal combustion engines”. *Applied Thermal Engineering*, Vol. 115, pp. 212–220, 2017. (cited in p. 24)

Guardiola Carlos, Pla B, Bares P and Barbier A. “An analysis of the in-cylinder pressure resonance excitation in internal combustion engines”. *Applied Energy*, Vol. 228, pp. 1272–1279, 2018. (cited in pp. 30 and 114)

Guardiola Carlos, Pla B, Blanco-Rodriguez David and Eriksson Lars. “A computationally efficient Kalman filter based estimator for updating look-up tables applied to NOx estimation in diesel engines”. *Control Engineering Practice*, Vol. 21 n^o 11, pp. 1455–1468, 2013. (cited in p. 189)

Guardiola Carlos, Pla Benjamin, Bares Pau and Stefanopoulou Anna. "Cylinder charge composition observation based on in-cylinder pressure measurement". *Measurement*, Vol. 131, pp. 559–568, 2019. (cited in pp. 46 and 74)

Gundlapally Santhosh R, Papadimitriou Iakovos, Wahiduzzaman Syed and Gu Tian. "Development of ECU capable Grey-box models from detailed models—application to a SCR reactor". *Emission Control Science and Technology*, Vol. 2 n^o 3, pp. 124–136, 2016. (cited in p. 46)

Harris Fredric J. "On the use of windows for harmonic analysis with the discrete Fourier transform". *Proceedings of the IEEE*, Vol. 66 n^o 1, pp. 51–83, 1978. (cited in p. 143)

Hellring Magnus and Holmberg Ulf. "An ion current based peak-finding algorithm for pressure peak position estimation". Technical report, SAE Technical Paper, 2000. (cited in p. 27)

Hellström Erik, Lee Donghoon, Jiang Li, Stefanopoulou Anna G and Yilmaz Hakan. "On-board calibration of spark timing by extremum seeking for flex-fuel engines". *IEEE Transactions on control systems technology*, Vol. 21 n^o 6, pp. 2273–2279, 2013. (cited in p. 10)

Heywood John B. *Internal combustion engine fundamentals*. McGraw-Hill Education, 2018. (cited in pp. 19, 26, 64, 66, 90, and 186)

Hirsch Markus, Alberer Daniel and Del Re Luigi. "Grey-box control oriented emissions models". *IFAC Proceedings Volumes*, Vol. 41 n^o 2, pp. 8514–8519, 2008. (cited in p. 46)

Hua Jianxiong, Zhou Lei, Gao Qiang, Feng Zhonghui and Wei Haiqiao. "Effects on Cycle-to-Cycle Variations and Knocking Combustion of Turbulent Jet Ignition (TJI) with a Small Volume Pre-Chamber". Technical report, SAE Technical Paper, 2020. (cited in p. 92)

Isermann Rolf. "Engine modeling and control". *Berlin: Springers Berlin Heidelberg*, Vol. 1017, 2014. (cited in p. 9)

Jia Libin, Naber Jeffrey D and Blough Jason R. "Review of sensing methodologies for estimation of combustion metrics". *Journal of Combustion*, Vol. 2016, 2016. (cited in pp. 18, 27, and 28)

Jiang J, Gu Fengshou, Gennish R, Moore DJ, Harris G and Ball AD. "Monitoring of diesel engine combustions based on the acoustic source characterisation of the exhaust system". *Mechanical Systems and Signal Processing*, Vol. 22 n^o 6, pp. 1465–1480, 2008. (cited in p. 27)

Jones James C Peyton and Frey Jesse. "Threshold optimization and performance evaluation of a classical knock controller". *SAE International Journal of Engines*, Vol. 8 n^o 3, pp. 1021–1028, 2015. (cited in p. 186)

Jones James C Peyton, Frey Jesse and Shayestehmanesh Saeed. "Stochastic simulation and performance analysis of classical knock control algorithms". *IEEE Transactions on Control Systems Technology*, Vol. 25 n^o 4, pp. 1307–1317, 2016. (cited in p. 33)

Jones James C Peyton, Muske Kenneth R, Frey Jesse and Scholl David. "A stochastic knock control algorithm". Technical report, SAE Technical Paper, 2009. (cited in p. 186)

Jones James C Peyton, Shayestehmanesh Saeed and Frey Jesse. "A Bayesian knock event controller". *IEEE Transactions on Control Systems Technology*, Vol. 28 n^o 5, pp. 1627–1637, 2019. (cited in p. 34)

Jones James C Peyton, Spelina Jill M and Frey Jesse. "Likelihood-based control of engine knock". *IEEE Transactions on Control Systems Technology*, Vol. 21 n^o 6, pp. 2169–2180, 2013. (cited in p. 191)

Keck James C. "Turbulent flame structure and speed in spark-ignition engines". In *Symposium (International) on Combustion*, volume 19, pp. 1451–1466. Elsevier, 1982. (cited in p. 63)

Kefalas Achilles, Ofner Andreas B, Pirker Gerhard, Posch Stefan, Geiger Bernhard C and Wimmer Andreas. "Detection of Knocking Combustion Using the Continuous Wavelet Transformation and a Convolutional Neural Network". *Energies*, Vol. 14 n^o 2, pp. 439, 2021. (cited in p. 148)

Kurihara N, Suzuki J, Shirayama Y, Borg J and Oho S. "An accurate method of knock detection using wavelet transform for spark-ignition (SI) engine". In *14th International Congress on Sound and Vibration*, 2007. (cited in p. 32)

Kyrtatos Panagiotis, Hoyer Klaus, Obrecht Peter and Boulouchos Konstantions. "Apparent effects of in-cylinder pressure oscillations and cycle-to-cycle variability on heat release rate and soot concentration under long ignition delay conditions in diesel engines". *International Journal of Engine Research*, Vol. 15 n^o 3, pp. 325–337, 2014. (cited in p. 114)

Lagana Armando AM, Lima Leonardo L, Justo João F, Arruda Benedito A and Santos Max MD. "Identification of combustion and detonation in spark ignition engines using ion current signal". *Fuel*, Vol. 227, pp. 469–477, 2018. (cited in p. 30)

Lapuerta Magin, Armas Oy and Hernández JJ. "Diagnosis of DI Diesel combustion from in-cylinder pressure signal by estimation of mean thermodynamic properties of the gas". *Applied Thermal Engineering*, Vol. 19 n^o 5, pp. 513–529, 1999. (cited in pp. 22 and 116)

Leach Felix, Kalghatgi Gautam, Stone Richard and Miles Paul. "The scope for improving the efficiency and environmental impact of internal combustion engines". *Transportation Engineering*, p 100005, 2020. (cited in p. 3)

Li Ning, Yang Jianguo, Zhou Rui and Liang Caiping. "Determination of knock characteristics in spark ignition engines: An approach based on ensemble empirical mode decomposition". *Measurement Science and Technology*, Vol. 27 n^o 4, pp. 045109, 2016. (cited in p. 32)

Li Ruixue C and Zhu Guoming G. “A real-time pressure wave model for knock prediction and control”. *International Journal of Engine Research*, p 1468087419869161, 2019. (cited in p. 117)

Livengood JC and others. “Correlation of autoignition phenomena in internal combustion engines and rapid compression machines”. 1955. (cited in p. 34)

López JJ, Novella R, Gomez-Soriano J, Martinez-Hernandiz PJ, Rampanarivo F, Libert C and Dabiri M. “Advantages of the unscavenged pre-chamber ignition system in turbocharged natural gas engines for automotive applications”. *Energy*, Vol. 218, pp. 119466, 2021. (cited in pp. 91 and 92)

Luján José Manuel, Guardiola Carlos, Pla Benjamin and Bares Pau. “Estimation of trapped mass by in-cylinder pressure resonance in HCCI engines”. *Mechanical Systems and Signal Processing*, Vol. 66, pp. 862–874, 2016. (cited in pp. 115 and 181)

Ma Fanhua, Ding Shangfen, Wang Yu, Wang Yefu, Wang Junjun and Zhao Shuli. “Study on combustion behaviors and cycle-by-cycle variations in a turbocharged lean burn natural gas SI engine with hydrogen enrichment”. *International journal of hydrogen energy*, Vol. 33 n^o 23, pp. 7245–7255, 2008. (cited in p. 91)

Maldonado Bryan P, Bieniek Mitchell, Hoard John, Stefanopoulou Anna G, Fulton Brien and Nieuwstadt Michiel Van. “Modelling and estimation of combustion variability for fast light-off of diesel aftertreatment”. *International Journal of Powertrains*, Vol. 9 n^o 1-2, pp. 98–121, 2020. (cited in p. 90)

Maldonado Bryan P, Freudenberg James S and Stefanopoulou Anna G. “Stochastic feedback combustion control at high dilution limit”. In *2018 annual American control conference (ACC)*, pp. 1598–1603. IEEE, 2018. (cited in p. 90)

Maldonado Bryan P and Kaul Brian C. “Control-oriented modeling of cycle-to-cycle combustion variability at the misfire limit in SI engines”. In *Dynamic Systems and Control Conference*, volume 84287, p V002T26A001. American Society of Mechanical Engineers, 2020. (cited in p. 8)

Maldonado Bryan P and Stefanopoulou Anna G. “Cycle-to-cycle feedback for combustion control of spark advance at the misfire limit”. *Journal of Engineering for Gas Turbines and Power*, Vol. 140 n^o 10, 2018. (cited in p. 90)

Mansouri SH and Heywood John B. “Correlations for the viscosity and Prandtl number of hydrocarbon-air combustion products”. *Combustion Science and Technology*, Vol. 23 n^o 5-6, pp. 251–256, 1980. (cited in p. 131)

Maurya Rakesh Kumar. “In-cylinder pressure measurement in reciprocating engines”. In *Reciprocating Engine Combustion Diagnostics*, pp. 37–121. Springer, 2019. (cited in p. 18)

Mauss Jakob and Simons Matthias. “Chip simulation of automotive ECUs”. In *9th symposium Steuerungssysteme fur automobile Antriebe*, 2012. (cited in p. 46)

McKenzie Jacob and Cheng Wai K. “The anatomy of knock”. Technical report, SAE Technical Paper, 2016. (cited in p. 156)

Mocanu Florin and Taraza Dinu. “Estimation of main combustion parameters from the measured instantaneous crankshaft speed”. Technical report, SAE Technical Paper, 2013. (cited in p. 27)

Molin Paul and Abdi Hervé. “New Table and Numerical Approximations for Kolmogorov-Smirnov/Lilliefors/van Soest Normality Test”. *Dijon: University of Bourgogne*, 1998. (cited in p. 110)

Moshrefi Amirhossein. “Weighted-EMD to Increase Knock Detection Accuracy”. (cited in p. 32)

Munjal Manchar Lal. *Acoustics of ducts and mufflers with application to exhaust and ventilation system design.* John Wiley & Sons, 1987. (cited in p. 123)

Munjal ML. “Advances in the acoustics of flow ducts and mufflers”. *Sadhana*, Vol. 15 n^o 2, pp. 57, 1990. (cited in pp. 117 and 217)

Narayan S, Milojevic Sasa and Gupta Vipul. “Combustion monitoring in engines using accelerometer signals”. *Journal of Vibroengineering*, Vol. 21 n^o 6, pp. 1552–1563, 2019. (cited in p. 27)

Neal Radford M. *Bayesian learning for neural networks*, volume 118. Springer Science & Business Media, 2012. (cited in p. 188)

Netzer Corinna, Seidel Lars, Ravet Frederic and Mauss Fabian. “Assessment of the validity of RANS knock prediction using the resonance theory”. *International Journal of Engine Research*, Vol. 21 n^o 4, pp. 610–621, 2020. (cited in p. 30)

Novella Ricardo, Pla Benjamin, Bares Pau and Martinez-Hernandiz Pablo José. “Closed-Loop Combustion Control by Extremum Seeking with the Passive-Chamber Ignition Concept in SI Engines”. Technical report, SAE Technical Paper, 2020. (cited in p. 90)

of the Petroleum Exporting Countries Organization. “2020 World Oil Outlook 2045”. https://www.opec.org/. Accessed: 2021-03-12. (cited in pp. 6 and 9)

Öner Metin and Deveci Kocakoç İpek. “JMASM 49: A compilation of some popular goodness of fit tests for normal distribution: Their algorithms and MATLAB codes (MATLAB)”. *Journal of Modern Applied Statistical Methods*, Vol. 16 n^o 2, pp. 30, 2017. (cited in p. 110)

Ozdor Nir, Dulger Mark and Sher Eran. “Cyclic variability in spark ignition engines a literature survey”. *SAE transactions*, pp. 1514–1552, 1994. (cited in pp. 89 and 90)

Park Sung Tae and Yang Jinguo. “Engine knock detection based on wavelet transform”. In *Proceedings. The 8th Russian-Korean International Symposium on Science and Technology, 2004. KORUS 2004.*, volume 3, pp. 80–83. IEEE, 2004. (cited in p. 31)

Parra Andres Felipe Sierra and Torres Adalberto Gabriel Diaz. “Improvement of a knock model for natural gas SI engines through heat transfer evaluation”. *International Journal on Interactive Design and Manufacturing (IJIDeM)*, Vol. 12 n^o 4, pp. 1423–1433, 2018. (cited in p. 31)

Payri F, Broatch A, Tormos B and Marant V. “New methodology for in-cylinder pressure analysis in direct injection diesel engines—application to combustion noise”. *Measurement Science and Technology*, Vol. 16 n^o 2, pp. 540, 2005. (cited in p. 18)

Payri F, Luján José M, Guardiola Carlos and Pla B. “A challenging future for the IC engine: new technologies and the control role”. *Oil & Gas Science and Technology–Revue d’IFP Energies nouvelles*, Vol. 70 n^o 1, pp. 15–30, 2015. (cited in p. 9)

Peyton Jones James C, Spelina Jill M and Frey Jesse. “Optimizing knock thresholds for improved knock control”. *International Journal of Engine Research*, Vol. 15 n^o 1, pp. 123–132, 2014. (cited in p. 31)

Pipitone Emiliano and Beccari Stefano. “Performances improvement of a SI CNG bi-fuel engine by means of double-fuel injection”. Technical report, SAE Technical Paper, 2009. (cited in p. 177)

Pipitone Emiliano and Genchi Giuseppe. “Experimental Determination of Liquefied Petroleum Gas–Gasoline Mixtures Knock Resistance”. *Journal of Engineering for Gas Turbines and Power*, Vol. 136 n^o 12, 2014. (cited in p. 177)

Pischinger Stefan. “Current and future challenges for automotive catalysis: engine technology trends and their impact”. *Topics in Catalysis*, Vol. 59 n^o 10, pp. 834–844, 2016. (cited in pp. 7 and 8)

Police Giuseppe, Diana Salvatore, Giglio Veniero, Iorio Biagio and Rispoli Natale. “Downsizing of SI engines by turbo-charging”. In *Engineering Systems Design and Analysis*, volume 42517, pp. 463–476, 2006. (cited in pp. 8 and 9)

Ponti Fabrizio, Ravaglioli Vittorio and De Cesare Matteo. “Development of a methodology for engine performance investigation through double crankshaft speed measurement”. *Journal of Engineering for Gas Turbines and Power*, Vol. 138 n^o 10, 2016. (cited in p. 27)

Ponti Fabrizio, Ravaglioli Vittorio, Moro Davide and Serra Gabriele. “MFB50 on-board estimation methodology for combustion control”. *Control Engineering Practice*, Vol. 21 n^o 12, pp. 1821–1829, 2013. (cited in p. 27)

Ponti Fabrizio, Ravaglioli Vittorio, Serra Gabriele and Stola Federico. “Instantaneous engine speed measurement and processing for MFB50 evaluation”. *SAE International Journal of Engines*, Vol. 2 n^o 2, pp. 235–244, 2010. (cited in p. 27)

Poulos Stephen G and Heywood John B. “The effect of chamber geometry on spark-ignition engine combustion”. *SAE transactions*, pp. 1106–1129, 1983. (cited in p. 63)

Rohani Sohrab. *Coulson and Richardson's Chemical Engineering: Volume 3B: Process Control.* Butterworth-Heinemann, 2017. (cited in p. 124)

Rugland Christian and Stenlaas Ola. "Knock Sensor Based Virtual Cylinder Pressure Sensor". Technical report, SAE Technical Paper, 2019. (cited in p. 27)

Saraswati Samir and Chand Satish. "Reconstruction of cylinder pressure for SI engine using recurrent neural network". *Neural Computing and Applications*, Vol. 19 n^o 6, pp. 935–944, 2010. (cited in p. 27)

Scholl David, Davis Craig, Russ Stephen and Barash Terry. "The volume acoustic modes of spark-ignited internal combustion chambers". *SAE transactions*, pp. 1379–1386, 1998. (cited in p. 117)

Selmanaj Donald, Panzani Giulio, Van Dooren Stijn, Rosgren Jonatan and Onder Christopher. "Adaptive and unconventional strategies for engine knock control". *IEEE Transactions on Control Systems Technology*, Vol. 27 n^o 4, pp. 1838–1845, 2018. (cited in p. 34)

Sen Asok K, Zheng Jianjun and Huang Zuohua. "Dynamics of cycle-to-cycle variations in a natural gas direct-injection spark-ignition engine". *Applied Energy*, Vol. 88 n^o 7, pp. 2324–2334, 2011. (cited in p. 186)

Serrano Jose Ramon, Novella Ricardo and Piqueras Pedro. "Why the development of internal combustion engines is still necessary to fight against global climate change from the perspective of transportation", 2019. (cited in p. 6)

Shen Tielong, Kang Mingxin, Gao Jinwu, Zhang Jiangyan and Wu Yuhu. "Challenges and solutions in automotive powertrain systems". *Journal of Control and Decision*, Vol. 5 n^o 1, pp. 61–93, 2018. (cited in p. 33)

Shen Xun, Zhang Yahui and Shen Tielong. "Cylinder pressure resonant frequency cyclic estimation-based knock intensity metric in combustion engines". *Applied Thermal Engineering*, Vol. 158, pp. 113756, 2019. (cited in p. 120)

Shu Gequn, Pan Jiaying and Wei Haiqiao. "Analysis of onset and severity of knock in SI engine based on in-cylinder pressure oscillations". *Applied Thermal Engineering*, Vol. 51 n^o 1-2, pp. 1297–1306, 2013. (cited in pp. 30 and 31)

Siano D and D'agostino D. "Knock detection in SI engines by using the discrete wavelet transform of the engine block vibrational signals". *Energy Procedia*, Vol. 81, pp. 673–688, 2015. (cited in p. 62)

Siano Daniela, Bozza Fabio, D'Agostino Danilo and Panza Maria Antonietta. "The use of vibrational signals for on-board knock diagnostics supported by in-cylinder pressure analyses". Technical report, SAE Technical Paper, 2014. (cited in p. 32)

Sjeric Momir, Taritas Ivan, Tomi Rudolf, Bla Mislav, Kozarac Darko and Luli Zoran. "Efficiency improvement of a spark-ignition engine at full load conditions using exhaust gas recirculation and variable geometry turbocharger–Numerical study". *Energy conversion and management*, Vol. 125, pp. 26–39, 2016. (cited in p. 7)

Spelina Jill M, Peyton Jones James C and Frey Jesse. “Stochastic simulation and analysis of a classical knock controller”. *International Journal of Engine Research*, Vol. 16 n^o 3, pp. 461–473, 2015. (cited in p. 191)

Stephens Michael A. “The anderson-darling statistic”. Technical report, Department of statics, Stanford University., 1979. (cited in p. 111)

Tabaczynski Rodney J, Ferguson Colin R and Radhakrishnan Krisna. “A turbulent entrainment model for spark-ignition engine combustion”. *SAE transactions*, pp. 2414–2433, 1977. (cited in pp. 63 and 64)

Taglialatela F, Cesario N, Porto M, Merola SS, Sementa P and Vaglieco BM. “Use of Accelerometers for spark advance control of SI engines”. *SAE International Journal of Engines*, Vol. 2 n^o 1, pp. 971–981, 2009. (cited in pp. 18 and 28)

Thomasson Andreas, Shi Haoyun, Lindell Tobias, Eriksson Lars, Shen Tielong and Jones James C Peyton. “Experimental validation of a likelihood-based stochastic knock controller”. *IEEE Transactions on Control Systems Technology*, Vol. 24 n^o 4, pp. 1407–1418, 2015. (cited in p. 34)

Tong Qiang, Xie Hui, Song Kang and Zou Dong. “A Control-Oriented Engine Torque Online Estimation Approach for Gasoline Engines Based on In-Cycle Crankshaft Speed Dynamics”. *Energies*, Vol. 12 n^o 24, pp. 4683, 2019. (cited in p. 27)

Vibe Ivan I and Meißner Franz. *Brennverlauf und kreisprozess von verbrennungsmotoren.* Verlag Technik, 1970. (cited in p. 25)

Wang Shu, Zhu Qilun, Prucka Robert, Prucka Michael and Dourra Hussein. “Input adaptation for control oriented physics-based SI engine combustion models based on cylinder pressure feedback”. *SAE International Journal of Engines*, Vol. 8 n^o 4, pp. 1463–1471, 2015. (cited in p. 62)

Wang Yuanfeng. “A Novel Two-Zone Thermodynamic Model for Spark-Ignition Engines Based on an Idealized Thermodynamic Process”. *Energies*, Vol. 13 n^o 15, pp. 3801, 2020. (cited in p. 186)

Wong Victor W and Hoult David P. “Rapid distortion theory applied to turbulent combustion”. *SAE Transactions*, pp. 1243–1262, 1979. (cited in p. 64)

Woschni G. “A universally applicable equation for the instantaneous heat transfer coefficient in the internal combustion engine”. *SAE Technical Papers*, 1967. (cited in p. 23)

Wu Hao. “Study of spark ignition engine combustion model for the analysis of cyclic variation and combustion stability at lean operating conditions”. 2013. (cited in p. 64)

Xu Han, Yao Anren, Yao Chunde and Gao Jian. “Investigation of energy transformation and damage effect under severe knock of engines”. *Applied Energy*, Vol. 203, pp. 506–521, 2017. (cited in p. 114)

Yeo GwonKoo, Kil JeongKi, Youn YoungKee, Kim ChangDae and Kim NamHyuk. "Three-way catalysts for partial lean-burn engine vehicle". Technical report, SAE Technical Paper, 2000. (cited in p. 8)

Yoshiyama Sadami, Tomita Eiji and Hamamoto Yoshisuke. "Fundamental study on combustion diagnostics using a spark plug as ion probe". Technical report, SAE Technical Paper, 2000. (cited in p. 27)

Yu Shui and Zheng Ming. "Future gasoline engine ignition: A review on advanced concepts". *International Journal of Engine Research*, p 1468087420953085, 2020. (cited in p. 8)

Yun HJ and Mirsky William. "Schlieren-streak measurements of instantaneous exhaust gas velocities from a spark-ignition engine". *SAE transactions*, pp. 3143–3158, 1974. (cited in p. 205)

Zadnik Martin, Vincent François, Vingerhoeds R and Galtier Frederic. "SI engine knock detection method robust to resonance frequency changes". Technical report, SAE Technical Paper, 2007. (cited in p. 32)

Zhang Yahui and Shen Tielong. "On-Board map learning-based combustion phase control in spark ignition engines". In *2017 IEEE Conference on Control Technology and Applications (CCTA)*, pp. 287–292. IEEE, 2017. (cited in p. 9)

Zhang Yahui, Shen Xun and Shen Tielong. "A survey on online learning and optimization for spark advance control of SI engines". *Science China Information Sciences*, Vol. 61 n^o 7, pp. 70201, 2018. (cited in p. 34)

Zhang Yahui, Shen Xun, Wu Yuhu and Shen Tielong. "On-board knock probability map learning–based spark advance control for combustion engines". *International Journal of Engine Research*, Vol. 20 n^o 10, pp. 1073–1088, 2019. (cited in pp. 10, 34, 188, and 190)

Zhao Kai and Shen Tielong. "Boundary Learning for Spark-Ignition Engine Control". In *2020 15th IEEE Conference on Industrial Electronics and Applications (ICIEA)*, pp. 241–246. IEEE, 2020. (cited in p. 10)

Zhao Kai, Wu Yuhu and Shen Tielong. "Stochastic Knock Control with Beta Distribution Learning for Gasoline Engines". *IFAC-PapersOnLine*, Vol. 51 n^o 31, pp. 125–130, 2018. (cited in p. 34)

Zhen Xudong, Wang Yang, Xu Shuaiqing, Zhu Yongsheng, Tao Chengjun, Xu Tao and Song Mingzhi. "The engine knock analysis–An overview". *Applied Energy*, Vol. 92, pp. 628–636, 2012. (cited in pp. 30 and 31)